ELASTO-PLASTIC IMPACT OF FINE PARTICLES AND FRAGMENTATION OF SMALL AGGLOMERATES

Zemin Ning, BSc, MSc

Doctor of Philosophy

THE UNIVERSITY OF ASTON IN BIRMINGHAM

April 1995

The University of Aston in Birmingham

ELASTO-PLASTIC IMPACT OF FINE PARTICLES AND FRAGMENTATION OF SMALL AGGLOMERATES

Zemin Ning, BSc, MSc

Thesis submitted for the degree of Doctor of Philosophy
1995

SUMMARY

Surface deposition of dense aerosol particles is of major concern in the nuclear industry for the safety assessment. This study presents theoretical investigations and computer simulations of single gas-born U_3O_8 particles impacting with the in-reactor surface and the fragmentation of small agglomerates.

A theoretical model for elasto-plastic spheres has been developed and used to analyse the force-displacement and force-time relationships. The impulse equations, based on Newton's second law, are applied to govern the tangential bouncing behaviour. The theoretical model is then incorporated into the Distinct Element Method code TRUBAL in order to perform computer simulated tests of particle collisions. A comparison of simulated results with both theoretical predictions and experimental measurements is provided. For oblique impacts, the results in terms of the force-displacement relationship, coefficients of restitution, trajectory of the impacting particle, and distribution of kinetic energy and work done during the process of impact are presented. The effects of Poisson's ratio, friction, plastic deformation and initial particle rotation on the bouncing behaviour are also discussed.

In the presence of adhesion an elasto-plastic collision model, which is an extension to the JKR theory, is developed. Based on an energy balance equation the critical sticking velocity is obtained. For oblique collisions computer simulated results are used to establish a set of criteria determining whether or not the particle bounces off the target plate. For impact velocities above the critical sticking value, computer simulated results for the coefficients of restitution and rebound angles of the particle are presented.

Computer simulations of fracture / fragmentation resulting from agglomerate-wall impact have also been performed, where two randomly generated agglomerates (one monodisperse , the other polydisperse), each consisting of 50 primary particles are used. The effects of impact angle, local structural arrangements close to the impact point, and plastic deformation at the contacts on agglomerate damage are examined. The simulated results show a significant difference in agglomerate strength between the two assemblies. The computer data also shows that agglomerate damage resulting from an oblique impact is determined by the normal velocity component rather than the impact speed.

Key words:
Elasto-plastic deformation
Surface adhesion
Impact
Distinct element method
Agglomerates
Fracture / Fragmentation

This thesis is dedicated to

Zi Jiang River

which passes by my hometown.

ACKNOWLEDGEMENTS

I would like to express my sincere gratitude to my research supervisor, Dr. Colin Thornton who introduced me to Particle Technology. I am grateful to him for his support, guidance, and constructive comments throughout the course of this work. The benefit from his optimistic attitudes towards research and persistence in chasing scientific solutions is as important as the knowledge gained during the research period.

I would also like to thank Dr. Michael Reeks, Nuclear Electric plc, Berkeley Nuclear Labs, for his enthusiasm in organising the project and invaluable advice. The financial support provided by Nuclear Electric plc is very much appreciated.

A special acknowledgement goes to Dr. David Kafui who provided the technical assistance in computer facilities. I am also grateful to my colleagues: Dr. Guoping Lian, Dr. Gexin Sun, Teo Ciomocos, and Leon Toland for their encouragement, support, and help. The final draft of the thesis was finished at the University of Surrey. I would like to take this opportunity to thank Dr. Mojtaba Ghadiri for his understanding and support.

Finally, my sincere thanks are expressed to my wife Xiaoping, who gives me constant loving support. The encouragement and understanding from my parents and members of my family always furnish the extra energy for my work and I hope that what I have done partly fulfils their expectations.

Contents

List of Figures

List of Tables

Chapter 1 Introduction

1.1 Background of the project

The understanding of the behaviour of particles upon impact with a surface arouses interests in many fields of engineering and technology. The particle-surface impact behaviour is determined by many factors. Variations of initial conditions and material properties lead to different results. Factors involved in an impact process can be classified into three main categories: impact parameters (particle velocity, impact angle); particle / target properties (particle size, shape and density; surface friction, adhesion and roughness; the bulk mechanical properties of the two colliding bodies); environmental factors (temperature, properties and flow rate of the surrounding medium). The diversity of these parameters makes the impact process particularly complex.

The whole process of an impact can be regarded as an evolution of energy transfer. During loading the initial kinetic energy is transformed into the elastic strain energy stored in both contacting bodies and then released to furnish the movement of the particle upon rebound. However, energy is also dissipated during a collision. The mechanisms of energy loss involved in an impact are multiple and plastic deformation, energy required to overcome attractive surface forces, interfacial and internal friction, and elastic wave propagation are among them.

Numerous experimental observations of particle-particle or particle-wall collisions have been reported and, since the establishment of classical theory of elastic contact mechanics by

Hertz (1882), there have been many developments in the theoretical understanding of contact interactions and impact mechanisms. However, none of the current theoretical models can fully answer the questions of capture and rebound of single particles impacting a target surface.

The main objective of the work reported in this thesis is to provide a comprehensive theoretical examination of the impact behaviour of non-adhesive and adhesive elasto-plastic spheres impacting a target. The approach adopted for the research is to perform computer simulated experiments using the Distinct Element Method (DEM) in which the contact interaction rules, used in the program, are based on theoretical contact mechanics. In order to achieve this objective new theories have been developed to model elasto-plastic spheres.

The motivation of the work presented is related to safety assessment in nuclear reactor plants. In the nuclear industry, the gas-borne aerosol particles present many operational and environmental problems which may affect the maintenance, safety, and efficiency of the plant. It is of great importance to know the mechanisms which determine whether a particle bounces off or sticks to the in-reactor surface. When radioactivity is released into the flow route of a nuclear reactor in an accident, the oxidation of exposed nuclear fuel UO_2 creates U_3O_8 particles and agglomerates (Payne & Butterworth 1986). Within the transport rigs of the cooling system the gas-borne U_3O_8 agglomerates may be broken up into fragments either by turbulent shear or upon impact with a surface and this will result in a size distribution of smaller particles or agglomerates. Experimental observations suggest that surface deposition is a particle size dependent phenomenon. Agglomerate fragmentation and the resulting size distribution of the clusters could lead to a significant increase of retention within the containment. A set of criteria for whether an impacting particle bounces or adheres to a surface needs to be established and a better understanding of fragmentation behaviour is also required for the safety assessment. Therefore, a special goal of the research program is to provide data on particle/wall interactions which may be incorporated into Computational Fluid Dynamics (CFD) codes used to model the gas flow regime.

Since the project was funded by Nuclear Electric plc, Berkeley Laboratories, the results presented in this thesis include special data relating to U_3O_8 particles impacting a stainless steel target. For these impact simulations the particle/target properties were provided by Nuclear Electric plc and are given in Table 1.1.

Table 1.1 Particle and target properties

Materials / Properties	U_3O_8	Stainless steel
Young's modulus (GPa)	215	215
Poisson's ratio	0.3	0.3
Density (kg m^{-3})	8300	7830
Elastic yield limit (GPa)	>1.9	>1.9
Adhesive energy (J m^{-2})	0.2	0.2
Coefficient of friction	0.35	0.35

1.2 Order of presentation

Chapter 2 presents a review of the previous research on theoretical impact models and experimental observations. The factors involved in a particle-surface collision and their effects on the impact behaviour, such as plastic deformation, surface adhesion and surface roughness are discussed. This chapter also gives a brief introduction to recent developments in computer simulated experiments, using the Distinct Element Method developed by Cundall (1971). A more detailed discussion of the methodology is deferred until Chapter 7.

Normal and oblique impacts of non-adhesive elasto-plastic spheres are examined in

Chapters 3 and 4 respectively. In Chapter 3, a new theoretical model is presented to describe the normal contact force-displacement relationships during plastic loading and elastic unloading. Based on this model, computer simulated impact experiments are reported and compared with an analytical solution for the coefficient of restitution. Using the computer simulated data the effect of impact velocity on the contact duration is also examined. Chapter 4 deals with oblique impacts, in which the normal contact interaction law is based on the theory described in Chapter 3. The evolution of contact forces and various energy components during a collision are examined. The rebound conditions obtained from oblique impact simulations are presented in terms of the tangential coefficient of restitution, the rebound angle, the particle centroid and the reflection angle of the contact patch. From the results obtained, the effects of impact angle, friction, elastic properties and plastic deformation are demonstrated. The effect of initial particle rotation is also considered.

Adhesive spheres are considered in Chapter 5 and Chapter 6. The theoretical basis of the normal interaction behaviour is presented in Chapter 5. Based on an energy balance equation, an analytical solution is obtained for the critical impact velocity below which elastic spheres adhere to the target. For elasto-plastic spheres the theory is more complicated and computer simulated tests are used to provide information on the stick/bounce behaviour. An attempt is also made to simulate the impact of ammonium fluorescein particles. In order to obtain agreement with experimental data reported by Wall et al (1989, 1990), it is necessary to incorporate the concept of a dynamic yield stress. In Chapter 6 results of computer simulated oblique impacts of adhesive spheres are presented. The effect of impact angle on both the sticking criterion and the motion of rebounding particles is examined, for both elastic and elasto-plastic spheres.

The Distinct Element Method is discussed in Chapter 7. The methodology and main structure of the program TRUBAL is described. The necessary modifications to the code in order to incorporate plastic deformation at the interparticle contacts are explained and

PAGE MISSING IN ORIGINAL

Chapter 2 Literature review

2.1 Introduction

Since Hertz (1882) pioneered the classical theory of impact between two frictionless elastic bodies considerable advances in the theoretical understanding of the impact mechanisms and the experimental observations of the behaviour of particle-particle or particle -wall collisions have been made by many researchers. The interaction laws of two contacting bodies have been extended to include aspects such as the influence of friction at the interface (McEwen 1949, Smith and Liu 1953), tangential loading and sliding contact (Mindlin 1949, Mindlin and Deresiewicz 1953), the kinetic energy loss due to elastic wave propagation (Hunter 1957, Reed 1985a, 1985b), the effect of surface energy (Johnson et al 1971, Johnson 1976, Savkoor and Briggs 1977), elasto-plastic deformation (Bitter 1953, Rogers and Reed 1984), surface roughness (Greenwood and Williamson 1966, Fuller and Tabor 1975, Cheng et at 1987), and the effect of dynamic yield stress (Wall et al 1989). Also, a number of experimental investigations have been reported to test the theoretical models (Zener 1941, Tillett 1954, Maw et al 1976, 1981, Sundararajan and Shewmon 1987, Borzone et al 1990, and Sondergaard et al 1990, etc.). For an account of the earlier development of impact theory and experiments the reader is directed to the book by Goldsmith (1960) and for recent developments in contact mechanics theory reference should be made to the book by Johnson (1985).

The literature review presented in this Chapter is concerned mainly with impact models under different situations, experimental observations, and the influence of factors involved in particle-wall collisions. A review of elastic impacts on smooth surfaces with and without adhesion will be presented first. Following an introduction to the interactions of non-adhesive spheres under elasto-plastic deformation, Section 2.4 then briefly discusses some

previously published elasto-plastic adhesion models. Although the study reported in the following chapters will not consider the effect of surface roughness on the impact behaviour, a brief introduction in Section 2.5 may benefit future studies. Finally previous computer simulations of particle impact are discussed, in Section 2.6.

2.2 Elastic impact without adhesion

2.2.1 Normal impact

Hertz (1882) first used his static theory of elastic contact to analyse the impact between frictionless elastic bodies. The assumption made in this quasi-static theory is that the deformation is restricted to the vicinity of the contact area. The theory also assumes that the energy loss due to elastic wave propagation can be ignored and the total mass of each body moves at any instant with the velocity of its centre of mass. A particular consequence of the quasi-static nature of the Hertzian approximation is that the elastic energy of the two bodies acquired during the collision process is entirely reversible, the impact and rebound velocities are identical and the coefficient of restitution is therefore unity.

Consider two elastic spheres of radii R_i (i = 1,2), with masses m_i and elastic properties E_i and ν_i, moving at velocity V_i along their line of centres when there is no particle spin. The relative velocity V is

$$V = V_2 - V_1 = \frac{d\alpha}{dt} \qquad (2.1)$$

where α is the relative approach of the two centroids. The force between the two spheres once contact has been established is

$$P = m_1 \frac{dV_1}{dt} = - m_2 \frac{dV_2}{dt} \qquad (2.2)$$

If we let $1/m^* = 1/m_1 + 1/m_2$ then we have

$$P = - m^* \frac{dV}{dt} = - m^* \frac{d^2\alpha}{dt^2} \qquad (2.3)$$

For a static elastic contact the Hertzian relationship between the normal force and the relative approach is

$$P = \frac{4}{3} E^* R^{*1/2} \alpha^{3/2} \qquad (2.4)$$

where

$$1/R^* = 1/R_1 + 1/R_2, \qquad 1/E^* = (1 - \nu_1^2) / E_1 + (1 - \nu_2^2) / E_2 \qquad (2.5)$$

For a single particle with mass m and radius R impacting a half-space, $m^* = m$ and $R^* = R$. In this study we are mainly concerned with the case of particle-wall collisions and, therefore m and R will normally be used in the equations rather than m^* and R^*. From (2. 3) and (2. 4) we have

$$m \frac{d^2\alpha}{dt^2} = - \frac{4}{3} E^* R^{*1/2} \alpha^{3/2} \qquad (2.6)$$

Integrating with respect to α gives

$$\frac{m}{2} [V_i^2 - (\frac{d\alpha}{dt})^2] = \frac{8}{15} E^* R^{1/2} \alpha^{5/2} \qquad (2.7)$$

where the impact velocity V_i is the velocity of approach at t = 0. When the displacement reaches the maximum value there is no relative motion between the two bodies and then

$$\alpha_{max} = (15 m V_i^2 / 16 E^* R^{1/2})^{2/5} \qquad (2.8)$$

Further integration of (2. 6) provides the time evolution of the displacement given by

$$t = \frac{\alpha_{max}}{V_i} \int d (\alpha / \alpha_{max}) / [1 - (\alpha / \alpha_{max})^{5/2}]^{1/2} \qquad (2.9)$$

The numerical solution of this integral has been obtained by Deresiewicz (1968) and the compression-time curve has been converted into a force-time curve using (2.4). Further studies can be found in the papers presented by Tsai (1968) and Graham (1973). In this analysis the spheres are assumed to be perfectly elastic and frictionless at the interface. The

energy absorbed in the wave motion is neglected so that the deformation is perfectly reversible. The total impact time is then given as

$$t_c = \frac{2\alpha_{max}}{V_i} \int_0^1 d\,(\alpha / \alpha_{max}) / [\, 1 - (\alpha / \alpha_{max})^{5/2} \,]^{1/2}$$

$$= 2.94\, \alpha_{max} / V_i = 2.87\, (m^2 / RE^{*2} V_i)^{1/5} \qquad (2.10)$$

The assumption of the static theory is valid if the distance travelled by the elastic waves during impact is very long compared with the dimension of the contact area (Love 1944, see Johnson 1985). In this case there is no energy loss in an impact between two perfectly elastic bodies. However, in an impact between a sphere and a thin plane body in which the elastic wave will travel more times from the top to the bottom of the plate, and some energy will be converted into the form of flexural vibration, the mechanism of energy loss due to elastic wave propagation must be considered.

The effect of elastic waves within solid bodies was first mentioned by Saint-Venant (1867) for the impact of long rods, who argued that even perfectly elastic materials would have a coefficient of restitution less than unity. Sears (1908) and Wagstaff (1924) took into account the kinetic energy loss due to elastic waves within the bars and their results showed a good agreement with the experiments. Some other experimental investigations of impacting elastic spheres on plates were reported by Raman (1920), Zener (1941), Tillett (1954), and Sondergaard et al (1990) etc. A theoretical evaluation of energy dissipated due to elastic motion in an impact of a sphere with a massive plane body was given by Hunter (1957). The same problem was analysed by Reed (1985a, 1985b) who also compared his prediction with that of Hunter and the experimental results of Tillett (1954).

According to Hunter (1957) the total energy loss in the form of elastic wave motion is

$$W = \frac{8\Omega(1 + \nu_2)}{\rho_w C_0^3} \left(\frac{1 - \nu_2^2}{1 - 2\nu_2} \right)^{1/2} \int_0^\infty \omega^2 |f(\omega)|^2 d\omega \qquad (2.11)$$

where Ω is the imaginary part of

$$\int_0^{\infty} [\xi(\xi^2 - 1)^{1/2} / F_0(\xi)]\, d\xi$$

and

$$F_0(\xi) = (2\xi^2 - \gamma^2)^2 - 4\xi^2 [(\xi^2 - 1)(\xi^2 - \gamma^2)]^{1/2}$$

$$\gamma = [2(1 - \nu_2)/(1 - 2\nu_2)]^{1/2}$$

$$C_0 = (E_2/\rho_w)^{1/2}$$

ρ, ρ_w = density of the sphere and the target wall respectively;

$f(\omega)$ = the Fourier transform of the force-time history.

The fraction of initial energy lost given by Hunter (1957) is

$$\lambda_H = \frac{W}{mV_i^2/2} = \frac{2.255\,\Omega(1+\nu_2)}{\rho_w C_0^3} \left(\frac{1-\nu_2^2}{1-2\nu_2}\right)^{1/2} \rho^{-1/5} E^{*6/5} V_i^{3/5} \qquad (2.12)$$

where V_i is the impact velocity, and the fraction given by Reed (1985a) is

$$\lambda_R = \frac{10.263\,\Omega(1+\nu_2)}{\rho_w C_0^3} \left(\frac{1-\nu_2^2}{1-2\nu_2}\right)^{1/2} \rho^{-1/5} E^{*6/5} V_i^{3/5} \qquad (2.13)$$

which is larger than Hunter's estimation.

As discussed by Reed (1985a) neither of the two theoretical values of restitution coefficient agrees well with the experimental measured value given by Tillett (1954) because the energy loss is underestimated. Some other energy loss mechanisms, such as strain rate effect and plastic deformation of surface asperities, may have been involved in the impact process.

Experimental investigations in the field of impact have been performed for a variety of

purposes. A number of tests have been conducted with the object of assessing the validity of a proposed theory or the accuracy of an assumed model of material behaviour. For normal impact, experiments are specially designed to minimise the fraction of energy removed from the contact region by stress wave propagation relative to the initial kinetic energy of the system. The results of these experiments, therefore, are mainly concerned with the observed values of coefficient of restitution, impact velocity, duration of collision, and the diameter of the impinging indentations.

A definite value for the coefficient of restitution cannot be assigned to the impact of spheres unless their size, material, and impact velocity are specified initially. Raman (1920) measured the coefficient of restitution for different materials of the same particle size (Fig. 2. 1) while for different sizes experiments were reported by Zener (1941), Tillett (1954) and Sondergaard et al (1990). Using the premise of Hertz, Zener (1941) measured the amount of energy transferred from the ball to the plate. Tillett (1954) examined the factors

Fig. 2. 1 Coefficient of restitution as a function of impact velocity for spheres of the same size and different materials (Raman 1920).

which affected the coefficient of restitution while Andrews (1930) and Lifshitz and Kolsky (1964) measured the contact time with variations in impact velocities. Recently Sondergaard et al (1990) reported the influence of the ratio of the particle diameter to the plate thickness on the particle rebound resulting from a normal impact. The major observations of the above researchers are summarised below.

In all instances the magnitude of the coefficient of restitution decreases monotonically from unity with increasing impact velocity. The dependence of the coefficient on impact velocity is weak at low velocities while for impacts with significantly higher velocities in which fully plastic deformation occurs the coefficient of restitution decreases like $V_i^{-1/4}$ with increasing impact velocity (Brenner et al 1981 and Sondergaard et al 1990). It has also been reported that, when the target plates are thick relative to the diameter of the ball, there is only a small variation in the restitution coefficient with velocity of the impact, which is of the order of 0.5% over a velocity range of 0.2 - 3.0 m/s (Tillett 1954); with thin plates the variation is much greater.

Plate thickness is one of the significant factors involved in affecting the kinetic energy loss in the process of impact. As the thickness of the plate is decreased a longitudinal wave will travel more times from the top to the bottom of the plate before contact is terminated and a significant proportion of energy will be converted into flexural vibration of the plate. As a consequence, the magnitude of the coefficient of restitution should be reduced relative to that for a thick target, a conclusion which has been substantiated by all the experimental results.

It was reported by Sondergaard et al (1990) that by dropping the sphere to impact the plate at various distances from either of the clamped edges, the coefficient of restitution decreased with an increase in the distance of the impact point from the clamped edges until, at a certain critical distance, it then became independent of the distance from the support. The dependence of the critical distance on the ball diameter was also examined in their experiments and was found to be independent of the plate thickness.

The dependence of contact time on impact velocity was reported by Sears (1908) and Lifshitz and Kolsky (1964). With an increase in impact velocity the contact time decreased not only when the mode of impact would be expected to be elastic, but also in cases when plastic deformation of the specimens was clearly seen to have taken place. Experimental results measured by Andrews (1930), shown in Fig. 2.2, indicate that there probably exists a power law relationship between the contact duration and impact velocity when plastic deformation dominates the impact process.

Variation of temperature leads to changes in material properties. The experimental data indicated that the coefficient of restitution would decrease with an increase of temperature.

The effect of surface roughness on the behaviour of particle bounce for normal impacts has been examined by Lifshitz and Kolsky (1964). It was experimentally revealed that both the magnitude and repeatability of the coefficient of restitution were affected by surface roughness. When the target had a finely ground surface the magnitudes obtained for the coefficient of restitution for elastic rebound were very scattered and never exceeded 0.82. If the surface was polished and the measurements were repeated, the values were very much less scattered and a maximum value of 0.87 was obtained. When the surface was then highly polished for a considerable time the measurements of the coefficient of restitution were found to be quite consistent at a value of 0.95. The effect of surface roughness on impact involves very complicated mechanisms; a more detailed discussion will be given in Section 2.5.

In general, it can be concluded that the analysis based on a combination of the elastic wave propagation theory and the static contact law provides an excellent description of the phenomenon in the velocity range considered and is well supported by the experimental results. The Hertzian theory by itself, whilst not rigourously correct, still yields an acceptable approximation of the impact process. At higher impact velocities, the theory needs to be modified to account for the effects of local plastic deformation.

Fig. 2.2 Variations of contact duration with impact velocity when plastic deformation dominates the process of impact (Andrews, 1930).

2.2.2 Oblique impact

Oblique impact with the possibility of micro-slip and sliding at the contacting surfaces involves complicated mechanics at the microscale. This also makes the prediction of appropriate macroscopic collision characteristics quite difficult. The tangential traction and micro-slip behaviour arising from simultaneous variations in tangential and normal forces have been analysed by Mindlin and Deresiewicz (1953) while the no-slip solution was given by Mindlin (1949). The traction at any time during the collision depends not only upon the current forces, but also upon the history of loading. The relationship between tangential traction and normal motion has also been investigated and it has been shown that even for dissimilar material the effect of tangential traction on the normal motion is very small and may reasonably be neglected (Johnson 1985). This means that the tangential load / displacement and normal load / displacement relationships can be treated separately.

Therefore, the variation of contact radius and contact pressure throughout the impact are given by the Hertzian theory, independent of the friction forces.

For the interactions between an elastic sphere and a wall with elastic properties of E_i, G_i, ν_i (i = 1, 2), the normal force P, the relative normal approach α, and the contact radius a, are provided by the classical theory of Hertz

$$\alpha^3 = 9P^2 / 16RE^{*2} \qquad (2.14)$$

$$a^3 = 3PR / 4E^* \qquad (2.15)$$

and

$$\alpha = a^2 / R \qquad (2.16)$$

From (2.14) and (2.15) the normal contact stiffness is given as

$$\frac{dP}{d\alpha} = 2E^* (R\alpha)^{1/2} = 2E^*a \qquad (2.17)$$

As Mindlin and Deresiewicz (1953) showed, the deformation under the action of tangential forces is related to micro-slip and the history of the loading forces. The tangential contact stiffness depends on whether the system is loading, unloading or reloading. Slip is initiated at the circumference of the circular contact area and when the tangential force increases, an annular area of slip develops spreading radially inwards until the adhered area of contact is zero and rigid body sliding occurs. At this moment the tangential force reaches its limiting value of $T = \mu P$. If the maximum tangential force T is then reduced, slip in the opposite direction spreads radially inwards from the perimeter of the contact area. Because the tangential reversal load does not result in a recession of the existing slip annulus the tangential stiffness is dependent upon the loading history. According to Thornton and Randall (1988) the tangential incremental force under the circumstance of loading, unloading, and reloading can be expressed as

$$\Delta T = 8G^*a\Theta\Delta\delta \pm \mu\Delta P (1 - \Theta) \qquad (2.18)$$

where

$\Delta\delta$ = incremental tangential displacement;

a = contact radius;

ΔP = incremental normal force;

$$1/G^* = (2 - \nu_1) / G_1 + (2 - \nu_2) / G_2 \qquad (2.19)$$

and

$$\Theta^3 = 1 - (T + \mu\Delta P) / \mu P \qquad \text{(loading)} \qquad (2.20a)$$

$$\Theta^3 = 1 - (T^* - T + 2\mu\Delta P) / 2\mu P \qquad \text{(unloading)} \qquad (2.20b)$$

$$\Theta^3 = 1 - (T - T^{**} + 2\mu\Delta P) / 2\mu P \qquad \text{(reloading)} \qquad (2.20c)$$

Only for unloading is the negative sign in (2.18) used. The parameters T* and T** define the load reversal points.

Maw et al (1976, 1981) examined, both numerically and experimentally, the oblique impact of an elastic sphere on a half space. Hertzian impact theory was used for the normal force and normal component of impact velocity while numerical procedures provided by Mindlin and Deresiewicz (1953) were used to investigate the tangential traction and slip behaviour. The area of contact was assumed to be divided into areas of stick and slip. Another assumption made was that the coefficient of friction was constant over an area of slip and friction was the only source of energy dissipation.

In order to study the relationship between reflection velocity and impact velocity of the contact patch, Maw et al (1976) proposed two non-dimensional parameters. One is related to the radius of gyration of the sphere

$$\chi = (1 - \nu) (1 + mR^2 / I) / (2 - \nu) \qquad (2.21)$$

where I is the moment of inertia of the sphere about its centre. The other parameter is related to the impact velocity

$$\psi = [2(1 - \nu) / \mu(2 - \nu)] (V_{ti} / V_{ni}) \qquad (2.22)$$

where V_{ni} is the initial normal velocity of the contact point, V_{ti} is the corresponding tangential velocity and

$$V_{ti} / V_{ni} = \tan \theta \qquad (2.23)$$

where θ is the angle of incidence.

Figure 2.3 illustrates the variations in tangential force throughout the impact process for different incident conditions. For angles of incidence which are small compared with the angle of friction ($\psi \leq 1$) there is no sliding at the start of the impact. For larger angles of impact ($1 < \psi \leq 4\chi - 1$) the impact starts and finishes with sliding, with partial slip occurring in between. Finally, if the impact angle is sufficiently high ($\psi > 4\chi - 1$) sliding occurs throughout the impact process and the tangential displacement does not reverse. It can also be clearly seen from Fig. 2.3 that if the angle of incidence is not too large the tangential force T undergoes a reversal during the impact, whereas the normal force completes a half cycle only. Figure 2.4 shows the variations of the reflection angle of the contact patch under different incident situations. The tangential reflection velocity V_{tr} of the contact patch is found to be mainly negative except when $\psi > 4\chi$. This phenomenon has been substantiated by experiment, Maw et al (1981). The investigations of Maw et al were concentrated on the vicinity of the impact point, and the normal and tangential behaviour of the local contact area was then presented. However, some characteristics of the particle itself, such as the trajectory of the particle centre and particle spin around its centre, were neglected. Although the particle rotation upon departure can be clearly seen in the photograph presented by Maw et al (1981), both of Maw et al 's papers did not mention it.

An experimental investigation of solid spheres bouncing off flat plates was reported by Sondergaard et al (1990). The particle-wall system was designed to take the form that the particle diameter was greater than the plate thickness. Glass and steel balls of different sizes were dropped from various heights to impact an aluminium target plate obliquely. The entire trajectory was photographed, and both the components of the impact and departure velocities

Fig. 2.3 Nondimensional tangential force plotted against nondimensional time for different angles of incidence for a sphere (Maw et al. 1976).

Fig. 2.4 Nondimensional local angle of reflection against that of incidence for a sphere (Maw et al. 1976).

of the particle centre were ascertained from these trajectories. These velocities then were used to calculate normal and tangential coefficients of restitution. Also a non-dimensional parameter, the impulse ratio f, was proposed:

$$f = (1 - e_t) \tan \theta / (1 + e_n) \qquad (2.24)$$

where e_t is the tangential coefficient of restitution; e_n is the normal coefficient of restitution; θ is the angle of incidence. The experiments revealed that the data for e_n were quite consistent and repeatable while the data for e_t exhibited a significant scatter which could not be eliminated by carefully cleaning all the surfaces for every test. It was also reported that the impulse ratio f increased systematically with the incident angle until a critical angle was reached. The critical angle, which was about 45° for Pyrex glass and 35° for steel spheres, was found roughly consistent with the critical angle for complete sliding estimated by Maw et al (1976, 1981) as being in the range of 45° - 55°. The impulse ratio data for angles less than the critical values were quite consistent. However, above the critical angles, the data were found to be very scattered and inconsistent. It was suggested that collisions at impact angles above the critical value may be very sensitive to variations in the effective friction of the surfaces in the vicinity of the contact point.

Thornton and Randall (1988) and Thornton and Yin (1991) reported computer simulated experiments of oblique impact for two elastic spheres. The effect of impact angle on both the angle of reflection of the contact patch and the rebound angle of the particle centre was investigated and the results, illustrated in Fig. 2.6, were in good agreement with the work of Maw et al (1981). The effect of impact angle on the reduction in linear kinetic energy, gain in rotational kinetic energy and the proportion of the initial kinetic energy which was dissipated was also examined, see Fig. 2.5. It was observed that the kinetic energy never reduced to zero because the normal and tangential velocities reversed direction at different times. For small angles there was a recovery of linear kinetic energy during the rebound stage. This did not occur at large impact angles due to rigid body sliding occurring throughout the impact duration.

Fig. 2.5 Effect of impact angle on linear and rotational kinetic energies and dissipated energy (impact of two elastic spheres with parameters: R = 100 μm; ρ = 2.65 mg/m^3; E = 70 GPa; ν = 0.3; μ = 0.35 and the normal component of the approaching velocity is 0.05 m/s for each particle, Thornton and Yin 1991).

2.3 Interactions of adhesive spheres

2.3.1 Adhesion between elastic bodies

Two ideally flat clean surfaces, when pressed into intimate contact, should adhere due to the action of van der Waals intermolecular forces of attraction. There is ample evidence to suggest that the adhesion at the contact area is responsible for the resistance offered to the separation of bodies under the action of normal or tangential forces. The surface forces were first explained by London and soon after they were applied by Bradley (1932), Derjaguin (1934), de Boer (1936) and Hamaker (1937) to the problems of the forces between macroscopic bodies. Johnson et al (1971) (the JKR model) extended the Hertzian model to two elastic adhering spheres in normal contact by using an overall energy balance

approach. It is assumed in the JKR model that the adhesion between the two spheres results only in a change of surface energy over the contact area and thus the attractive interparticle forces are of infinitely short range. The contact area predicted by the JKR model is therefore larger than that by Hertz, with an infinite tensile stress at the perimeter. Another theoretical model was provided by Derjaguin et al (1975) (the DMT model) considering the attractive forces to have a finite range outside the contact area. The DMT model assumes that the adhesion forces have no effect on the shape of the particles and hence the contact area exerts a Hertzian compressive pressure; only outside the contact area is there a tensile stress which decreases with surface separation. Some discussions and comments for both the JKR and DMT model were given by Tabor (1977). Savkoor and Briggs (1977) made an extension of the JKR theory to analyse the effect of a tangential force upon the size of the contact area, which showed that the contact area of two elastic adhering spheres under a given normal load is reduced when a tangential force is applied.

In the JKR model the total energy U_T can be divided into three components: the stored elastic energy U_E, the mechanical potential energy U_M, and the surface energy U_S, which can be expressed as

$$U_E = (P_1^{5/3}/15 + P_0^2 P_1^{-1/3}/3) / (16E^{*2}R / 9)^{1/3} \qquad (2.25)$$

$$U_M = -P_0 (P_1^{2/3}/3 + 2P_0 P_1^{-1/3}/3) / (16E^{*2}R / 9)^{1/3} \qquad (2.26)$$

$$U_S = -\Gamma\pi a_1^2 = -\Gamma\pi (3RP_1 / 4E^*)^{2/3} \qquad (2.27)$$

where P_1 is the effective Hertzian normal force; P_0 is the applied normal force; Γ is the Dupre energy of adhesion, which is equal to $\gamma_1 + \gamma_2 - \gamma_{12}$ (γ_1 and γ_2 are the surface energies of each contacting bodies and γ_{12} is the interfacial energy). Satisfying equilibrium, $dU_T / dP_1 = 0$, the effective Hertzian normal force is obtained as

$$P_1 = P_0 + 3\pi\Gamma R \pm \sqrt{6\pi\Gamma R P_0 + 9\pi^2\Gamma^2 R^2}$$

$$= P_0 + 2P_c \pm \sqrt{4P_0 P_c + 4P_c^2} \qquad (2.28)$$

where

$$P_c = \frac{3}{2}\pi\Gamma R \qquad (2.29)$$

The contact radius is defined by

$$a^3 = 3RP_1 / 4E^* \qquad (2.30)$$

which is larger than that given by Hertz since $P_1 > P_0$. When the applied load is made negative the contact radius decreases and separation of the two bodies will occur if $P_0 = -P_c$, which defines the pull-off force.

2.3.2 Adhesive peeling and interfacial sliding

It was argued by Savkoor and Briggs (1977) that the tangential stress distribution over the contact area would be prescribed by the " no-slip " solution of Mindlin (1949) when the effect of oblique loading was considered in the presence of adhesion. Under increasing tangential force T there is a reduction in the contact radius which can be expressed by

$$a^3 = (3R / 4E^*) (P_0 + 2P_c \pm \sqrt{4P_0 P_c + 4P_c^2 - T^2 E^* / 4G^*}) \qquad (2.31)$$

Savkoor and Briggs suggested that this reduction would relate to a " peeling " mechanism which continues in a stable manner until a critical tangential force is reached. When the relative tangential displacement reaches that corresponding to the critical tangential force the peeling process is complete. If the critical value of tangential force

$$T_c = 4\sqrt{(P_0 P_c + P_c^2) G^* / E^*} \qquad (2.32)$$

is reached, the contact radius will reduce to

$$a^3 = (3R / 4E^*) (P_0 + 2P_c) \qquad (2.33)$$

Thornton and Yin (1991) examined the tangential behaviour after peeling and concluded that the contacting surfaces must peel before an interfacial sliding can occur. Assuming the transition from peeling to sliding to be smooth a new sliding criterion was proposed

$$T = \mu (P_0 + 2P_c) \qquad P_0 \geq -0.3\, P_c \qquad (2.34a)$$

$$T = \mu\, P_1 [\, 1 - (P_1 - P_0) / 3P_1 \,]^{3/2} \qquad P_0 < -0.3P_c \qquad (2.34b)$$

Thornton and Yin argued that Savkoor and Briggs's model suggested two failure criteria, the peeling failure defined by (2.32) and the sliding failure defined by (2.34). The relationship of tangential force-displacement would change when the normal load P_0 reaches the value

$$P_t = 2P_c [\, (\Psi - 1) \pm \sqrt{\Psi (\Psi - 1)} \,] \qquad (2.35)$$

where

$$\Psi = 4G^* / \mu^2 E^*$$

Taking the positive square root in (2.35), if $P_0 < P_t$ the tangential force at the end of peeling is greater than that necessary for sliding and hence, when the tangential displacement reaches the corresponding value, T drops to the value given by (2.34a) or (2.34b). If $P_0 > P_t$, peeling is followed by the development of a slip annulus which spreads radially inwards until sliding occurs; there is not a sudden change of the tangential force. The reported theoretical model for tangential behaviour in the presence of adhesion was validated by the experimental observations for polyethylene-terephthalate monofilaments, Briscoe and Kremnizer (1979) (see Thornton and Yin 1991).

The effect of adhesion on oblique impact of identical particles has been examined by computer simulated experiments. It was reported by Thornton and Yin (1991) that the rebound angle, velocity and particle spin were all functions of the total history of the impact duration following an oblique impact. The results also showed that, although adhesion affected the dissipation and redistribution of energy for all angles of impact, the effect was most pronounced when peeling was completed at the end of the impact. One of the significant consequences of the effect of adhesion was reported to be the possible bouncing back of a particle along the initial impact trajectory, as shown in Fig. 2.6 (a). However, investigations concerning the effect of impact angle, impact velocity, and magnitude of

Fig. 2.6 Rebound angles for different impact angles (with and without adhesion): (a). rebound angle of the particle centre; (b). angle of reflection for the contact patch (Impact of two elastic spheres with surface energy $\Gamma = 0.4$, Thornton and Yin 1991).

surface energy on the particle bouncing behaviour were not given. For relatively large impact angles at which gross sliding occurs during the whole process of the impact, the relationship between the interfacial friction and surface adhesion was also not examined in previous investigations.

In respect of surface deposition, due to the effect of surface adhesion, there is a range of impact velocities for which a particle will remain adhered to the target and rebound will not occur. Johnson (1986) argued that the critical sticking velocity, V_c, below which sticking would occur, could be obtained by relating the initial kinetic energy of the particle to the work done by the adhesive force. He suggested that the work done could be calculated as the area under the JKR force-displacement curve where $\alpha < 0$, which was approximately equal to $P_c\alpha_c$, where α_c is the relative approach at separation. More details will be provided in Chapter 5.

2.4 Elasto-plastic impact

Bitter (1963) analysed three stages of an elasto-plastic indentation process and used an energy balance method to study the phenomena of erosion. A simple energy balance model with adhesion energy estimated from the classical theory for the point contact was proposed by Dahneke (1971, 1972, 1973 and 1974). The proportion of energy lost was assumed in his analysis to be a constant degree during the plastic deformation, so that the energy loss was overestimated at high impact velocities. Plastic deformation was also included in the adhesion theory by Brenner et al (1981) to explain the energy loss during an impact of large metal particles with a hard surface. Other investigations of elasto-plastic impact were reported by Wempner et al (1984) and Follansbee and Sinclair (1984). Based on Bitter's work, Rogers and Reed (1984) presented a theoretical model which considered both elastic and plastic deformations occurring during particle-surface impacts, and in which a good agreement with experimental results was found for low and moderate impact velocities. A

similar model to that used by Rogers and Reed was proposed by Fichman and Pnueli (1985) in the case of two particles holding together because of adhesion forces.

2.4.1 Elasto-plastic impact without adhesion

As described by Bitter (1963) the whole process of an elasto-plastic impact can be divided into three stages. The first stage of interaction between the bodies starts at the moment of initial contact of the bodies and ends when the peak pressure reaches the elastic yield limit of the softer of the two bodies. In this elastic deformation stage the Hertzian theory may be applied. The second stage commences at the onset of plastic deformation and ends when the impacting bodies have zero relative velocity. The area of plastic deformation grows from the centre of the contact zone and is surrounded by an annulus in which only elastic deformation occurs. In the third stage of impact the stored elastic energy is recovered and the motion of the particle depends on the incident velocity, surface adhesion, and surface roughness, etc.

According to Davies (1949) the elastic yield limit is reached only if the impact velocity is greater than a limiting elastic velocity

$$V_y = \left(\frac{\pi}{2E^*}\right)^2 \left(\frac{2}{5\rho}\right)^{1/2} \sigma_y^{5/2} \qquad (2.36)$$

where ρ is the density of the impacting particle and σ_y is the elastic yield limit. The energy stored in elastic deformation at the end of the first stage is $mV_y^2 / 2$. Also the relative approach of the two bodies during this stage can be obtained from the Hertz equations as

$$\alpha_y = R \left(\frac{\pi\sigma_y}{2E^*}\right)^2 \qquad (2.37)$$

Bitter showed that for small deformations the area of the annulus of elastic deformation is always the same during the second stage and equal to the value at the end of the first stage of impact. It was argued that when the particle approaches the maximum compression there are

two types of elastic strain energies, the energy stored in the region of elastic deformation U_e and the energy stored in the area of plastic deformation U_{pe}, and

$$U_e = \frac{1}{2} m V_y^2 \qquad (2.38)$$

$$U_{pe} = \frac{1}{2} \alpha_y \sigma_y \pi a_p^2 \qquad (2.39)$$

By assuming $a_p^2 \approx 2R\alpha_p = 2R(\alpha^* - \alpha_y)$ the energy loss in terms of plastic deformation is

$$U_p = \int_0^{\alpha^* - \alpha_y} \sigma_y \pi a_p^2 \, d\alpha \approx \pi R \sigma_y (\alpha^* - \alpha_y)^2 \qquad (2.40)$$

where α^* and α_p are the total maximum compression and plastic deformation respectively. Bitter (1963) identified the relationship

$$U_{pe} = \sqrt{15 U_e U_p / 4} \qquad (2.41)$$

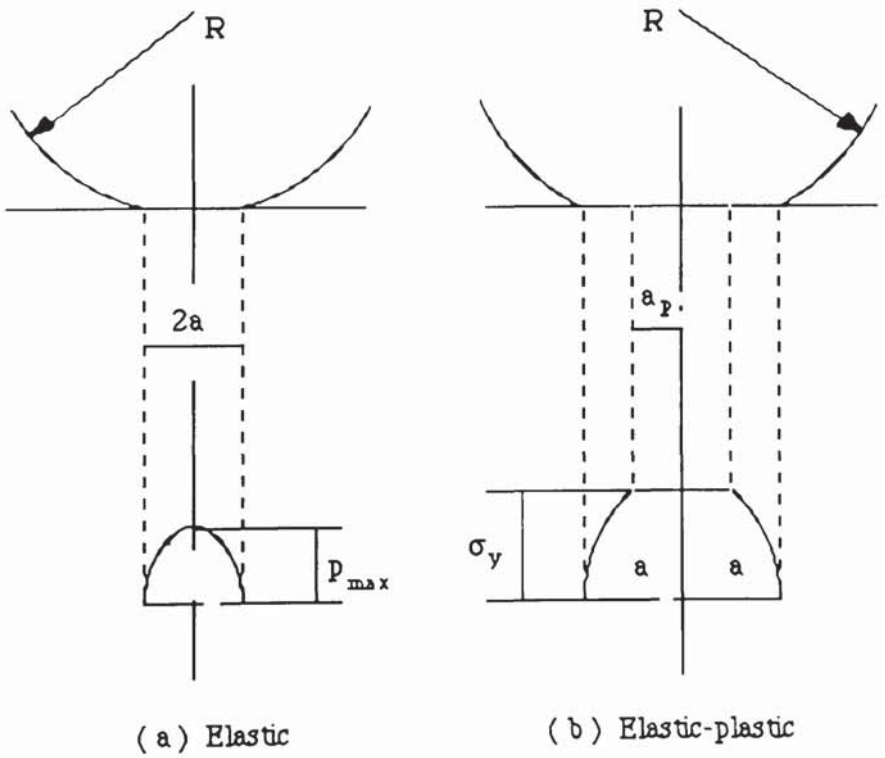

Fig. 2.7 Pressure distribution at contact area: (a) elastic impact - Hertz; (b) elasto-plastic impact.

and gave the energy balance equation during the loading process as

$$\frac{1}{2} mV_i^2 = U_e + U_{pe} + U_p = U_e + \sqrt{15U_e U_p / 4} + U_p \qquad (2.42)$$

However, the energy equation governing the unloading process was not presented and the coefficient of restitution cannot be determined from his analysis.

An impact model which deals with fully plastic indentation was proposed by Johnson (1985) to calculate the coefficient of restitution and its dependence on impact velocity. It was assumed that when the fully plastic state is approached the relationship between the contact radius and the total (elastic and plastic) compression can be described as $\alpha = a^2 / 2R$ according to the experimental results. The energy balance equation during plastic loading is

$$\frac{1}{2} mV_i^2 = \int_0^{a^*} \pi a^2 \sigma_y (a / R) da = \frac{\pi \sigma_y a^{*4}}{4R} \qquad (2.43)$$

The unloading process is purely elastic and the stored elastic strain energy is gradually released and converted into kinetic energy of the particle. The force-contact radius relationship is provided by the Hertzian equations during elastic recovery, but at the transition point from loading to unloading the maximum contact force is $P^* = \pi \sigma_y a^{*2}$. The kinetic energy of rebound can be expressed as

$$\frac{1}{2} mV_r^2 = \frac{3P^{*2}}{10E^* a^*} = \frac{3\pi^2 \sigma_y^2 a^{*3}}{10E^*} \qquad (2.44)$$

The normal coefficient of restitution is obtained from

$$e_n^2 = \frac{\frac{1}{2} mV_r^2}{\frac{1}{2} mV_i^2} = \frac{6\pi \sigma_y R}{5E^* a^*} \qquad (2.45)$$

Substituting for a* using (2.43) there results

$$e_n = 1.72 \sigma_y^{5/8} E^{*-1/2} \rho^{-1/8} V_i^{-1/4} \qquad (4.46)$$

It is expected, as demonstrated by Johnson (1985), that the coefficient of restitution gradually falls with increasing velocity after the initial elastic yield limit is exceeded. When a fully plastic indentation is obtained e_n is proportional to $V^{-1/4}$. Experimental results taken from Goldsmith (1960) show the same behaviour and the power law relationship between coefficient of restitution and impact velocity approximately has an exponent of -1/4.

Fig. 2.8 Ricochet behaviour of particles upon impacts: the ricochet curve delimits the regions of ricochet and indentation (Bulantsev et al 1985).

Most theoretical and experimental studies of plastic impact have been mainly concerned with the erosion of metal. Hutchings et al (1976) developed a computer model of oblique impact for a rigid sphere against an ideal rigid-plastic solid surface. The model was implemented by Rickerby and Macmillan (1980) and Hutchings et al (1981) for different impact velocities and impact angles. Their results indicated that the model successfully predicted the energy absorbed during an impact, and the rebound velocity. The dependence of the crater volume on impact velocity was reasonably predicted. However, neglecting elastic forces the model cannot account for the particle rebound from a normal impact, nor can it be expected to remain valid at very low impact velocities. A theoretical and experimental investigation of particle ricochet upon impact at high speeds (200 - 1500 m /

sec) was reported by Bulantsev et al (1985). Using a modified finite-element model, the process of rebound of a sphere upon impact along the normal to the plate and the process of collision at an angle against an aluminium plate were investigated. A simple relationship, concerning the behaviour of particle ricochet, between impact velocity and impact angle θ, was experimentally established (Fig. 2.8). It was also reported that, for normal impacts, particles with high impact velocity would not bounce off the softer plate at any velocity. Sundararajan and Shewmon (1987) presented some experimental observations of oblique impact for a hard ball against ductile plates in which the behaviour of six ductile materials was examined over a range of impact velocities and impact angles. The dimensions of the resulting impact craters and the rebound velocity and angle were also experimentally measured.

2.4.2 Elasto-plastic adhesion models

The surface adhesion acting over the contact area and its effect on particle interactions have been extensively investigated and, in the literature, there are quite a few reported adhesion models which deal with elasto-plastic deformation for different purposes. No attempt is made to cover all of the relevant literature. The following models are relatively well-known and particularly somewhat relevant to this study.

Brenner et al (1981) presented an energy balance model in which the stored elastic energy and the energy required to break the bonding had been taken into account to deal with the onset of bounce. In this model the deformation in the incoming stage of impact process was assumed to be predominantly plastic and the stored elastic energy furnished the kinetic energy of rebound in the recovery stage. If the impacting bodies are of the same material the energy balance model is given as

$$\frac{1}{2} m V_r^2 = U_e - U_b \qquad (2.47)$$

where V_r is the particle velocity in the recovery stage, U_e is the stored elastic energy and U_b is the energy required to break the bond, and

$$U_e = \frac{3\pi^2 (1 - \nu^2) \sigma_y^2 a^3}{5E} \qquad (2.48)$$

$$U_b = c\Gamma\pi a^2 \qquad (2.49)$$

where E and ν are the elastic properties of the target; a is the maximum contact radius; σ_y is the pressure under which the metal flows plastically during the impact and can be obtained from the normal force divided by the projected impact area at maximum penetration; Γ is the adhesion energy per unit of contacting area and c is the fraction of the impact area over which interactive bonds are created between the two bodies.

Assuming that the deformation was predominantly plastic Brenner et al (1981) developed the relationship between the particle radius R and the radius a of the contact area as

$$a^2 / R^2 = 1.1 (\rho / \sigma_y)^{1/2} V_i \qquad (2.50)$$

where ρ and σ_y are the density and the elastic yield limit of the target surface respectively; V_i is the initial or impact velocity of the particle. Using (2.50), the particle velocity in the recovery stage obtained from (2.47) is

$$V_r^2 = \frac{1.038\,\pi(1 - \nu^2)\,\sigma_y^{5/4} V_i^{3/2}}{\rho^{1/4} E} - \frac{3.3\,c\Gamma V_i}{2R\rho^{1/2}\sigma_y^{1/2}} \qquad (2.51)$$

By letting $V_r = 0$ the critical velocity V_c above which the particle bounces off the target surface is given as

$$V_c = \frac{0.256 c^2 \Gamma^2 E^2}{R^2 \rho^{1/2} \sigma_y^{7/2} (1 - \nu^2)^2} \qquad (2.52)$$

It is worth noting that the equations for the rebound velocity and the critical velocity in the paper by Brenner et al (1981) contain errors. The above equations based on their analysis are correct.

Based on the analysis of Bitter (1963), Rogers and Reed (1984) considered a sphere impacting with a plane surface. They assumed that plastic deformation was the only energy loss mechanism and proposed the following criterion for the particle rebounding from the surface

$$\frac{1}{2} mV_i^2 - U_p > U_A \qquad (2.53)$$

where U_p is the energy dissipated due to plastic deformation and U_A is the total adhesive energy available at the end of the impact. During loading the effect of surface energy was ignored and, following the analysis of Bitter (1963), Rogers and Reed (1984) defined U_p by the equation

$$U_p = \frac{1}{2} [(2mV_i^2 - \frac{1}{8} mV_y^2)^{1/2} - (\frac{15}{8} mV_y^2)^{1/2}]^2 \qquad (2.54)$$

Using the JKR theory, the total adhesive energy U_A was defined as

$$U_A = P_0 (P_1^{2/3} + 2P_0 P_1^{-1/3}) / [3 (4E^*/3)^{2/3} R_c^{1/3}] + \pi\Gamma (3R_c P_1 / 4E^*)^{2/3} \qquad (2.55)$$

with

$$P_1 = P_0 + 3\pi\Gamma R_c + \sqrt{(P_0 + 3\pi\Gamma R_c)^2 - P_0^2} \qquad (2.56)$$

where $P_0 = mg$ is the gravitational force due to the mass of the sphere and $R_c > R$ accounts for the flattening of the sphere as a result of plastic deformation.

In order to calculate R_c, Rogers and Reed (1984) assumed that the unloading behaviour was elastic and the radius of the total contact area at the end of the loading phase could be expressed as

$$a = (\frac{3PR_c}{4E^*})^{1/3} \qquad (2.57)$$

where P is the sum of the forces in the plastic and elastic regions of the contact area and is given by

$$P = \pi a_p^2 \sigma_y + \frac{4}{3} E^* R^{1/2} \left(\frac{15 m V_y^2}{16 E^* R^{1/2}} \right)^{3/5} \qquad (2.58)$$

Assuming Bitter' s (1963) postulate

$$a^2 = a_y^2 + a_p^2 \qquad (2.59)$$

the effective particle radius R_c is defined as

$$R_c = 4E^* (a_y^2 + a_p^2)^{3/2} / 3P \qquad (2.60)$$

where the projected radius of elastic deformation at initial yield a_y and the radius of plastic deformation a_p are

$$a_y = \left(\frac{15 m V_y^2 R^2}{16 E^*} \right)^{1/5} \qquad (2.61)$$

$$a_p = \left(\frac{2 U_{pe}}{\pi R \sigma_y} \right)^{1/2} \left(\frac{2E^*}{\pi \sigma_y} \right) \qquad (2.62)$$

Wall et al (1989) compared the model of Rogers and Reed (1984) with experimental measurements of the coefficient of restitution for ammonium fluorescein particles impacting a silicon target. They found that the decrease in restitution coefficient with increasing impact velocity, indicative of plastic deformation, occurred at much lower velocities than observed experimentally. They attributed this to the fact that the model assumed a constant yield limit, independent of impact velocity. Consequently, they modified the Rogers and Reed model by replacing the static yield limit σ_y with the dynamic yield limit σ_y^d which is strain rate dependent. The dynamic yield limit σ_y^d according to Malvern (1951) was defined by

$$\sigma_y^d = \sigma_y [1 + m \ln(1 + n \dot{\varepsilon}_p)] \qquad (2.63)$$

where m and n are empirical fitting constants and the plastic strain rate was expressed as

$$\dot{\varepsilon}_p \approx (2 / \pi) (1 / V_y) (V_i^2 - V_y^2)^{1/2} \qquad (2.64)$$

where V_i and V_y are the impact velocity and the yield limit velocity respectively. Figure 2.9 shows a comparison between the predictions of the Rogers and Reed (1984) model and the

experimental data measured by Wall et al (1989). It is seen that the model of Rogers and Reed (1984) can only match the experimental data at impact velocities close to the sticking velocity. For high impact velocities, however, the model underestimated the velocity ratio by a great amount. The results of the modified Rogers and Reed (1984) model in which the dynamic yield limit was taken into account, also shown in Fig. 2.9, indicate that the modified model agrees better with the experimental measurements over a range of impact velocities.

Wall et al (1989) also examined the effect of the target properties and particle size on the particle bouncing behaviour. It is seen from Fig. 2.10a that the experimental measurements of the velocity ratio (V_r / V_i) depend on target materials at low impact velocities, but there is not a material dependence at high velocity when the plastic deformation dominates the impact process. The same behaviour was observed for the effect of particle size and the phenomenon is diagrammatically illustrated in Fig. 2.10b.

Fig. 2.9 Comparisons between the measurements of velocity ratio and predictions of Rogers and Reed (1984), and modified Rogers and Reed for 2R = 4.9 μm ammonium fluorescein particles impacting a silicon target surface (Wall et al 1989).

Fig. 2.10 Experimental measurements of the effect of target properties (a) and particle size (b) on the velocity ratio over a full range of impact velocities (Wall et al 1989).

2.5 Surface roughness and its effect on impact

2.5.1 Nature of surface roughness

Real surfaces are never smooth. When two surfaces are pressed into contact they touch at the tips of the surface irregularities, so that the real area of contact is only a fraction of the normal area. Instead of the continuous force and resulting continuous pressure distribution, the force between rough solids must be considered to be the sum of a set of individual forces transmitted through an array of discrete contact spots. Over each small area of the surface the collective effect of these individual forces can be treated statistically as a pressure. Higher pressure may correspond to a higher density of contact spots or to larger individual spots.

There is considerable evidence that asperities on real surfaces can have any shape whatever and any distribution of heights. Providing basic solutions for the governing equations exist for these shapes, the effect of surface roughness on contact phenomena can be predicted by combining these solutions with a probability distribution function for the asperity parameters. A number of physical surface models have been proposed. Some of them are based upon individual model asperities which are assumed to deform elastically or plastically; others are based on the random nature of the surface profile.

Greenwood and Williamson (1966) proposed a quantitative roughness model with the assumption that the summit height distribution of surfaces is Gaussian and all summits have a constant radius of curvature. The simplification in using a constant radius of curvature was removed by Whitehouse and Archard (1970). Greenwood and Williamson's theoretical model has also been applied to the point contact of spheres by Greenwood and Tripp (1967) and Mikic (1974), and to the line contact of cylinders by Lo (1969).

Nayak (1971) proposed a two-dimensional random process model of surface roughness based on the theory of statistical geometry developed by Longuet-Higgins (1957

) for the analysis of ocean surfaces. It was assumed in this theory that the surface heights, slopes, and curvature possessed a multi-Gaussian probability density. Nayak's model was used to analyse the plastic contact of rough surfaces and a similar analysis was performed by Onions and Archard (1972). Cheng et al (1987) presented an elasto-plastic asperity model which was based on volume conservation of an asperity control volume during plastic deformation. Numerical results obtained from the model were compared with other existing purely elastic and purely plastic models. One of the criteria by which the validity of these models can be assessed is whether they predict proportionality between true contact area and load. An introduction to rough surface models and their applications can be found in the book of Thomas (1982).

2.5.2 The effect of surface roughness with and without adhesion

The behaviour of rough surfaces is determined by the statistical distribution of asperity heights and secondarily by their mode of deformation. If the deformation is within the limit of elasticity of the material for a given pressure distribution the deformation laws can be found from elasticity theory. A relationship between separation and pressure can then be established.

In an axi-symmetric case the contact of a smooth sphere of radius R with a nominally flat rough surface can be simplified. The asperities are taken to have spherical caps of uniform radius k_s, whose heights above a mean datum have a statistical distribution $\Phi(Z_s)$ and standard deviation σ_s, which deform elastically and independently according to the theory of Hertz. The force required to compress an individual asperity by an amount α_a and the contact area A_1 are given by

$$P_a = \frac{4}{3} E^* k_s^{1/2} \alpha_a^{3/2} \qquad (2.65)$$

$$A_1 = \pi k_s \alpha_a \qquad (2.66)$$

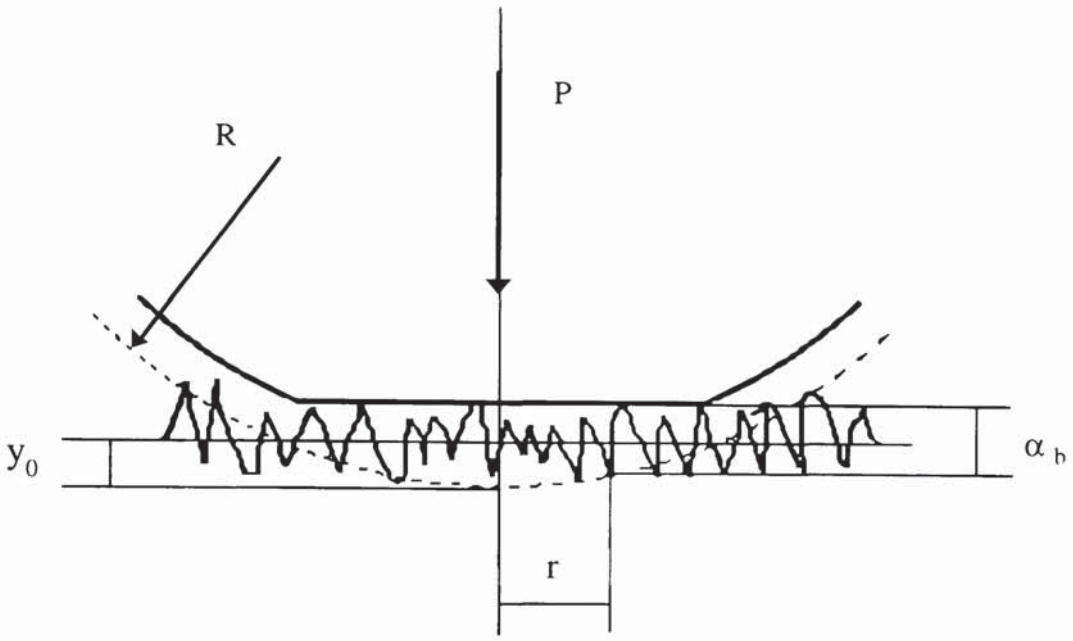

Fig. 2.11 Contact of a smooth elastic sphere with a nominally flat randomly rough surface.

Referring to Fig. 2.11, the profile of the undeformed sphere relative to a datum which is taken at the mean level of the rough surface is

$$y = y_0 - r^2 / 2R \qquad (2.67)$$

With a bulk displacement α_b and an asperity displacement α_a, the separation d between the two surfaces is

$$d(r) = \alpha_b(r) - y(r) = -y_0 + (r^2 / 2R) + \alpha_b(r) \qquad (2.68)$$

The asperity displacement $\alpha_a = Z_s - d$, where Z_s is the height of the asperity summit above the datum. The effective pressure and the expected total area of contact over radius r were given by Greenwood and Williamson (1966) as

$$p(r) = \frac{4\eta_s E^* k_s^{1/2}}{3} \int_d^{\infty} [Z_s - d(r)]^{3/2} \Phi(Z_s) dZ_s \qquad (2.69)$$

$$A(r) = \pi\eta_s k_s \int_d^\infty (Z_s - d(r))\Phi(Z_s)dZ_s \qquad (2.70)$$

where η_s is the number of asperities per unit area. Greenwood and Tripp (1967) defined an effective contact radius by

$$\bar{a} = 3\pi \int_0^\infty rp(r)dr \,/\, 4 \int_0^\infty p(r)dr \qquad (2.71)$$

The effect of surface roughness on the distribution of normal pressure, for low loads and high loads, is illustrated in Figs.2.12a and 2.12b respectively. The non-dimensional parameter β is defined as

$$\beta = \frac{\sigma_s}{\alpha_0} = \frac{\sigma_s R}{a_0^2} = \sigma_s \left(\frac{16RE^{*2}}{9P^2} \right)^{1/3} \qquad (2.72)$$

where α_0 is the bulk compression and a_0 is the contact radius for smooth surfaces under the load P, as calculated from the Hertzian theory. It can be seen from Fig. 2.12a that surface roughness is very significant at low loads. Compared with the Hertzian pressure distribution for the same applied load, the maximum pressure at the centre is greatly reduced by surface roughness and the load is distributed over a much larger apparent area of contact. At high loads, shown in Fig. 2.12b, the differences become insignificant.

It has been experimentally found that the measured adhesion decreases drastically when the surface of rubber or glass is roughened. The extent of adhesion decrease cannot be accounted for solely as the reduction in real area of contact. Johnson (1976) suggested that if the force required to separate the individual asperity is

$$P_c = -\frac{3}{2}\pi\Gamma k_s \qquad (2.73)$$

the total contact force per unit area $\underline{P}$ between two contacting surfaces due to adhesion under load P is the sum of the forces exerted by all the asperities whose height exceeds d, i.e.

$$\underline{P} = \eta_s P_c \int_{d-\alpha_c}^\infty F(\alpha/\alpha_c)\Phi(Z)d(Z) \qquad (2.74)$$

Fig. 2.12 Effect of surface roughness on contact pressure distribution without adhesion: solid line - effective pressure distribution p (r); broken line - Hertzian pressure distribution (Johnson 1985).

where α_c is the maximum separation of the asperity before the adhesion breaks and

$$F(\alpha/\alpha_c) = \frac{3(P_a/P_c) + 2 + 2(1 + P_a/P_c)^{1/2}}{3^{2/3}[P_a/P_c + 2 + 2(1 + P_a/P_c)^{1/2}]^{1/3}} \qquad (2.75)$$

where P_a is the force at an individual asperity contact. In the presence of adhesion, Johnson (1976) defined an elastic adhesion index β_λ, and

$$\beta_\lambda = \frac{\sigma_s}{\alpha_c} = \left(\frac{16RE^{*2}\sigma_s^3}{3P_c^2}\right)^{1/3} = \frac{4}{3}\left(\frac{E^{*2}\sigma_s^3}{\pi^2\Gamma^2 R}\right)^{1/3} \qquad (2.76)$$

The maximum tensile force per unit area required to separate the surface was defined as $\underline{P}_c$. The reduction in adhesion with surface roughness was illustrated by Johnson (1976) by plotting $\underline{P}_c/\eta_s P_c$ against β_λ, as shown in Fig. 2.13. Experimental measurements by Fuller and Tabor (1975) supported the trend shown in the figure.

Fig. 2.13 Reduction in adhesion with surface roughness: broken line - as suggested by Johnson (1974), adhesion ceases when $\beta_\lambda > 1.6$; solid line - as measured by Fuller and Tabor (1975).

As discussed before, the surface roughness affects the consistency and repeatability of the coefficient of restitution in the cases of normal collisions. Brenner et al (1981) presented an investigation of normal impact adhesion in which the effect of surface roughness of both the target plate and the particle on the critical velocity for bounce was examined. In order to compare the results of different experiments they defined a critical velocity statistically in terms of a sticking probability which is the fraction of impinging particles that adhere permanently to the surface for a constant set of experimental conditions. The critical velocity was defined as the velocity at which the sticking probability was 0.5. It was reported that for both the plate and the ball, surface roughness resulted in an increase in the sticking probability compared to smooth plates and balls (Fig. 2.14). The critical velocity at a temperature of 973 K, for example, was 0.2 m / s for the smooth balls, but about 1.4 m / s for the rough balls.

Recently, Borzone et al (1990) experimentally investigated the tangential behaviour of

particle-wall interactions on rough surfaces. Particle impact and rebound parameters were determined by using a high-speed photographic technique in which single particles were targeted, using an eductor, onto a ceramic surface. The particles then were fed into the eductor and their trajectories were photographed (Fig. 2.15). A considerable number of points were measured in order to obtain the correlations for rebound angles and velocities because of the dispersion in the data.

Rebound angle and velocity were correlated with impact angle. It was reported that, for smooth surfaces, the ratio of rebound velocities to impact angle showed less scatter than the ratio of rebound angle to impact angle. This means that measurements of kinetic energy were more reliable than trajectories. For rough surfaces, it was reported that the dispersion of the data was too great to establish any reliable correlation with impact angle.

Fig. 2.14 Effect of ball and plate roughness on the sticking probability of iron balls striking iron plates at 973 K at various impingement velocities (Brenner et al 1981).

Fig. 2.15 Trajectory dispersion of 2 mm diameter alumina particles upon impact on a). Rough wall; b). Smooth wall; for an impact velocity of 2 m/s (Borzone et al. 1990).

2.5.3 Plastic deformation and surface roughness

The deformation of an asperity will cease to be purely elastic beyond a certain load. Plastic flow starts within an asperity, and as the load increases the zone of plastic flow increases until eventually the entire asperity deforms plastically. In their earlier work Bowden and Tabor (1954) suggested that the contact pressures were equal to the flow pressure of the softer of two contacting materials and the normal load was then supported by the plastic flow of the asperities. Later, Greenwood and Williamson (1966), Whitehouse and Archard (1970), and Onions and Archard (1973) argued that the surface contact must often involve an appreciable proportion of asperity contacts at which the deformation is entirely elastic. It is now generally recognised that, under conditions of multiple contacts even if the deformations are entirely elastic, the true area of contact can increase almost proportionally with the load.

A non-dimensional plasticity index, a combinational parameter of surface statistics and material constants which determines whether the contact will be essentially elastic or elasto-plastic, has been proposed by different authors in different ways. It has already been mentioned that the plastic deformation starts at a point within an asperity while the surrounding material continues to deform elastically. Fully plastic deformation occurs when the mean contact pressure over the contact zone is about three times the value at the onset of plastic flow. At this stage the deformation is described by the ideal plastic contact theory where the interfacial pressure is constant and equal to the indentation hardness, and there is no surface deformation outside the contact zone.

The form of the plasticity index presented by Greenwood and Williamson (1966) is

$$\psi = \frac{E^*}{H} \left(\frac{\sigma^*}{k_s} \right)^{1/2} \qquad (2.77)$$

where H is the hardness of the material; σ^* is the standard deviation of the asperity peak distribution; and k_s is the radius of curvature of the asperities (assumed to be constant).

The plasticity index given by Whitehouse and Archard (1970) is

$$\psi = \frac{E^*}{H} (\sigma / \beta^*) \qquad (2.78)$$

where σ is the standard deviation of the asperity height distribution and β^* is the correlation distance.

Johnson (1976) considered the case of fully plastic deformation in the presence of adhesion and proposed a plastic adhesion index ψ_λ where

$$\psi_\lambda = \frac{\sigma}{\alpha_s} = \pi^2 H^4 k_s \sigma / 2\Gamma^2 E^{*2} \qquad (2.79)$$

He also defined a " coefficient of adhesion " as the ratio of the force required to separate the surface to the force which pressed them together; which was related to the plastic adhesion index by the equation

$$\frac{P_s}{P} = -1 + \frac{1 + \psi_\lambda}{\psi_\lambda} \exp (-1 / \psi_\lambda) \qquad (2.80)$$

The corresponding reduction in adhesion due to surface roughness is shown in Fig. 2.16 clearly indicating that very small adhesion occurs if $\psi_\lambda > 2$.

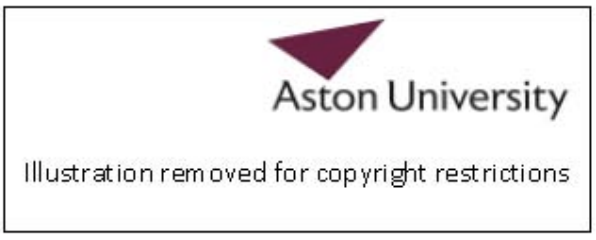

Fig. 2.16 Reduction in adhesion with surface roughness (plastic) (Johnson 1976).

2.6 Computer simulated impact experiments

While physical experiments to confirm the theoretical models of particle collisions under different conditions have been conducted for more than one hundred years since Hertz (1882), only in recent years has computer simulation been used to investigate particle impacts. For rigid particles against a ductile target surface, mainly relating to the erosion of metal, previous computer simulated impact tests include Hutchings et al (1976), Rickerby and Macmillan (1980), Hutchings et al (1981), and Bulantsev et al (1985). The results of their simulations and experimental observations have been discussed in Section 2.4.

Computer simulation of assemblies of contiguous solid particles was initiated by Cundall (1971, 1974), who developed the so called Distinct Element Method (DEM) in which the interaction of the particles is considered as a transient problem with states of equilibrium developing whenever the internal forces balance. The normal and tangential force-displacement behaviour in the original program was modelled by linear springs. The DEM can also be used to simulate single particle impacts with the incorporation of particle interaction laws based on contact mechanics theories.

The simulation of an impact process consists of a series of calculation cycles in which the evolution of the collision is advanced over a small increment of time. The wall is assumed to be stationary during impact. In order to eliminate the effect of gravity on particle velocity, the particle is placed in a position which is very close to the target wall. In the first calculation cycle the incremental normal and tangential displacements of the sphere are obtained by multiplying the prescribed initial particle velocity components by a very small time step. Adding the incremental displacements to the co-ordinates of the particle centre gives the new position of the particle. The forces and force increments established in the first cycle or time step are determined from the initial conditions of the theoretical equations. The tangential forces at the contact point contribute to the relative spin and the moment components are stored to calculate the rotational velocity and update the angular position in

the next time step.

In the second and subsequent cycles the current particle velocity components are used to provide the relative normal and tangential displacements increments, from which the new particle position is obtained according to the current position. The current contact normal and tangential stiffness, provided by the theoretical contact mechanics, are multiplied by the normal and tangential incremental displacements to obtain contact force increments. The motion of the particle is governed by the equations according to Newton's second law, in which the components of the out of balance force and momentum furnish the linear and rotational movements respectively. For the linear motion, the components of particle acceleration are obtained by dividing the components of the newly updated out of balance force on the particle by the particle mass, while taking account the effect of gravity. The accelerations are multiplied by the small time step to provide velocity increments which are used to update the particle velocities. Finally the new incremental displacements, obtained by multiplying the velocity components by time step, are used to record the new position of the particle. The rotational movements of the particle is modelled in the same way as the linear motion. The above calculation cycle is repeated until the end of the impact.

Randall (1989) conducted computer simulated normal and oblique impacts of non-adhesive elastic spheres against a wall. The coefficient of restitution was examined and the relationship between rebound angle and impact angle was reported to be a good agreement with that given by Maw et al (1976, 1981). The effect of surface adhesion forces, according to Johnson et al (1971) and Johnson (1976) in normal interactions and Savkoor and Briggs (1977) and Thornton (1992) in tangential interactions, was implemented into the program by Yin (1992). The results of computer simulated particle-particle interactions of oblique impacts with and without adhesion, reported by Thornton and Yin (1991), have been discussed in Sections 2.2 and 2.3.

2.7 Concluding remarks

Using the JKR theory, surface adhesion was incorporated into the impact model proposed by Rogers and Reed (1984), and the dynamic yield limit, as defined by Malvern (1951), was used to modify the model of Rogers and Reed by Wall et al (1989). The most advanced theoretical treatment to date is that of Wall et al (1989), but this is restricted to normal impacts and the effect of surface energy during the impact process is neglected. Therefore, it is necessary to extend the work by Thornton and Yin (1991) to incorporated plastic deformation and the work of Wall et al (1989) to oblique impacts in order to examine the mechanisms of energy loss due to oblique collisions which are still little understood. For the case of no adhesion the most relevant model is that of Johnson (1985), which deals with fully plastic impact. However, for relatively small impact velocities at which the colliding particle undergoes elasto-plastic deformations the model is not able to provide reasonable solutions.

The basic asperity model of Greenwood and Williamson (1966) has been extended to include such aspects as curved surfaces (Greenwood and Tripp 1967), two rough surfaces with misaligned asperities (Greenwood and Tripp 1971), non-uniform radii of curvature of asperity peaks (Hisakado 1974), elliptic paraboloidal asperities (Bush et al 1975), asperities of plastic deformation (Nayak 1971), and asperities of elasto-plastic deformation (Cheng et al 1987). However, the experimental investigations of contacting rough surfaces are far behind the considerable developments of theoretical work. Experimental studies aimed at measurements of the asperity properties are understandably limited by the great difficulties involved in trying to measure the precise value of the parameters which the theoretical model are based on, such as mean curvature of asperity peaks, standard deviation of asperity heights, and area density of asperities. These factors create major difficulties when attempting to numerically simulate impact with rough surfaces. Consequently, in this study, the effect of surface roughness will not be considered.

Chapter 3 Normal impact of elasto-plastic spheres

3.1 Introduction

This chapter considers the elastic-plastic impact behaviour of a sphere impacting orthogonally with a wall. The initial, pre-yield, behaviour is described by Hertzian theory which was presented in Section 2.2. Assuming the absence of strain hardening or strain rate effects, the post-yield behaviour is described by modifying the Hertzian pressure distribution to account for the limiting normal pressure, σ_y, due to plastic deformation at the contact. The modified Hertzian theory is then used to obtain analytical expressions for the coefficient of restitution, the contact force evolution and the contact duration. Finally, results of computer simulated normal impacts are presented and compared with theory and previous experimental results.

3.2 Yield

When a sphere of radius R impacts the target surface all the kinetic energy is absorbed and transformed into elastic energy provided that yield does not occur. If the impact velocity is just large enough to initiate yield, using (2.14) and (2.16) we have

$$\frac{1}{2} mV_y^2 = \int_0^{\alpha_y} P d\alpha = \frac{8E^*}{3R^2} \int_0^{a_y} a^4 da = \frac{8E^* a_y^5}{15R^2} \qquad (3.1)$$

from which

$$a_y = \left(\frac{15R^2 mV_y^2}{16E^*} \right)^{1/5} = \left(\frac{5\pi\rho R^5 V_y^2}{4E^*} \right)^{1/5} \qquad (3.2)$$

where ρ is the density of the particle and V_y, which we define as the yield velocity, is the velocity below which the interaction behaviour is assumed to be elastic. From Hertzian theory, the maximum contact pressure at the centre of the contact area is

$$p_0 = \frac{3P}{2\pi a^2} = \frac{2E^* a}{\pi R} \qquad (3.3)$$

We now define a " contact yield stress " $\sigma_y = p_0 (a_y)$ and from (3.2) and (3.3) there results

$$\sigma_y = \frac{2E^*}{\pi} \left(\frac{5\pi\rho V_y^2}{4E^*} \right)^{1/5} \qquad (3.4)$$

from which

$$V_y = \left(\frac{\pi}{2E^*} \right)^2 \left(\frac{2}{5\rho_1} \right)^{1/2} \sigma_y^{5/2} \qquad (3.5)$$

which corresponds to (2.36) originally derived by Davies (1949).

3.3 Force-displacement relationship

For elastic spheres the Hertzian pressure distribution and normal contact force are

$$\sigma(r) = \frac{3P}{2\pi a^3} (a^2 - r^2)^{1/2} \qquad (3.6)$$

$$P = 2\pi \int_0^a \sigma(r) r dr \qquad (3.7)$$

If plastic deformation occurs we assume a Hertzian pressure distribution with a cut-off corresponding to the contact yield stress σ_y (Fig. 3.1) which is constant for a given impact velocity. After yield the normal force P is given by

$$P = P_c - 2\pi \int_0^{a_p} (\sigma(r) - \sigma_y) r \, dr \qquad (3.8)$$

where P_e is the effective elastic force given by (3.7) and a_p is the radius of the contact area under plastic deformation. Integrating (3.8) we obtain

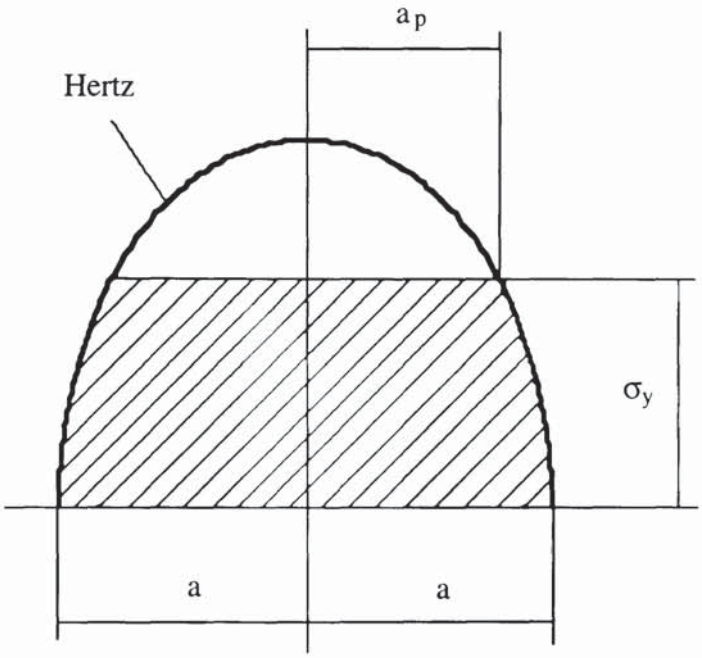

Fig. 3.1 Pressure distribution with plastic deformation.

$$P = \pi a_p^2 \sigma_y + P_e [\, 1 - (a_p/a)^2 \,]^{3/2} \qquad (3.9)$$

Using (3.6), σ_y may be defined as

$$\sigma_y = \frac{3P_y}{2\pi a_y^2} \qquad (3.10)$$

or, with reference to Fig. 3.1,

$$\sigma_y = \frac{3P_e}{2\pi a^2} [\, 1 - (\frac{a_p}{a})^2 \,]^{1/2} \qquad (3.11)$$

The contact radius is obtained from

$$a^3 = (3R/4E^*) P_e \qquad (3.12)$$

Hence, using (3.10), (3.11) and (3.12) we find that

$$1 - \left(\frac{a_p}{a}\right)^2 = \left(\frac{a_y}{a}\right)^2 \qquad (3.13)$$

or

$$a^2 = a_p^2 + a_y^2 \qquad (3.14)$$

which corresponds to the assumption of Bitter (1963) that the area of the annulus of elastic deformation remains equal to the total contact area at yield. Using (3.13) we may rewrite (3.9) as

$$P = \pi\sigma_y (a^2 - a_y^2) + P_e \left(\frac{a_y}{a}\right)^3$$

$$= P_y + \pi\sigma_y (a^2 - a_y^2) \qquad (3.15)$$

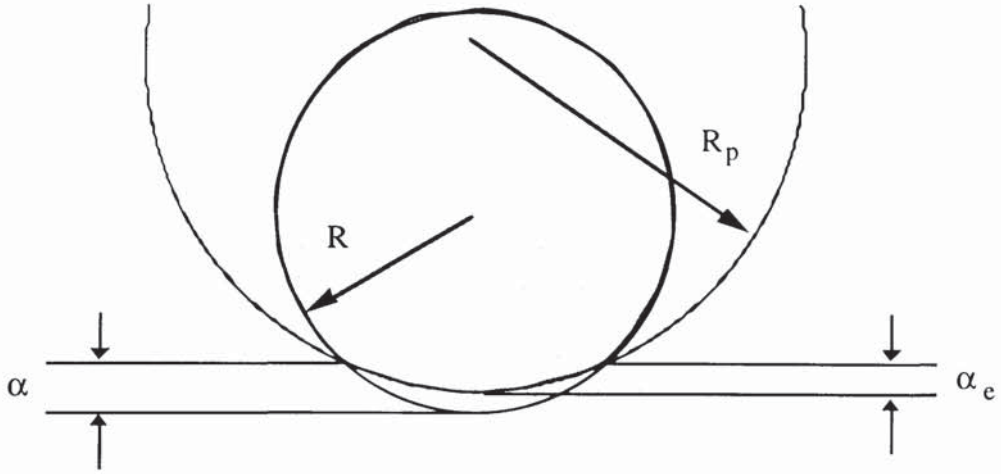

Fig.3.2 Flatted contact surfaces under plastic deformation.

Experimental observations indicate that the contact curvature reduces during plastic deformation and varies from (1/R) at initial yield to ~(1/2R) at the fully plastic state, Johnson (1985). As shown diagrammatically in Fig.3.2, during plastic deformation the elastic compression α_e at the centre of the contact area is less than the relative approach α and the contact curvature is reduced from 1/R to $1/R_p$, where R_p may be considered to be the radius of an equivalent elastic sphere. Hence, the contact radius may be defined as

$$a^2 = R\alpha \qquad \text{or} \qquad a^2 = R_p\alpha_e \qquad (3.16)$$

But, since the variations of R_p and α_e during plastic loading remain uncertain, it is necessary to substitute (3.16a) into (4.15) to obtain

$$P = P_y + \pi\sigma_y (R\alpha - a_y^2) \qquad (3.17)$$

from which the plastic normal contact stiffness is defined as

$$k^n = \frac{dP}{d\alpha} = \pi R\sigma_y = 2E^* a_y \qquad (3.18)$$

During elastic recovery the force-displacement relationship is assumed to be elastic and is provided by the classic Hertzian equations but with a contact curvature R_p, corresponding to the point of unloading. At the transition point from loading to unloading the contact area generated by the actual maximum contact force P^* is the same as that developed by the maximum equivalent elastic force P_e^* for a contact curvature of 1/R. Hence, using (3. 12),

$$a^{*3} = \frac{3R}{4E^*} P_e^* = \frac{3R_p}{4E^*} P^* \qquad (3.19)$$

which leads to

$$R_p = \frac{RP_e^*}{P^*} \qquad (3.20)$$

where the equivalent elastic force is

$$P_e^* = \frac{4E^*}{3R} a^{*3} = \frac{4}{3} E^* R^{1/2} \alpha^{*3/2} \qquad (3.21)$$

The complete force-displacement curve for elastic-plastic loading and elastic unloading is diagrammatically illustrated in Fig.3.3. It is seen from Fig.3.3 that the linear plastic loading curve is tangential to the Hertzian curve at the yield point y and intersects the vertical axis at $P_0 < 0$. Using (3.18) we may write

$$2E^* a_y = \frac{P_y - P_0}{\alpha_y} = \frac{P^* - P_0}{\alpha^*} \qquad (3.22)$$

from which

$$P_o = P_y - 2E^* a_y \alpha_y = P_y - \frac{2E^*}{R} a_y^3$$

$$= P_y - \frac{3}{2} P_y = -\frac{P_y}{2} \qquad (3.23)$$

and the maximum relative approach is

$$\alpha^* = \frac{P^* - P_o}{\pi R \sigma_y} = \frac{2P^* + P_y}{2\pi R \sigma_y} \qquad (3.24)$$

Substituting (3.24) into (3.21) we have

$$P_e^* = \frac{4E^*}{3R} \left(\frac{2P^* + P_y}{2\pi\sigma_y} \right)^{3/2} \qquad (3.25)$$

from which the maximum contact radius is given as

$$a^* = \left(\frac{2P^* + P_y}{2\pi\sigma_y} \right)^{1/2} \qquad (3.26)$$

Consequently, from (3.20) the equivalent particle radius during elastic recovery is

$$R_p = \frac{4E^*}{3P^*} \left(\frac{2P^* + P_y}{2\pi\sigma_y} \right)^{3/2} \qquad (3.27)$$

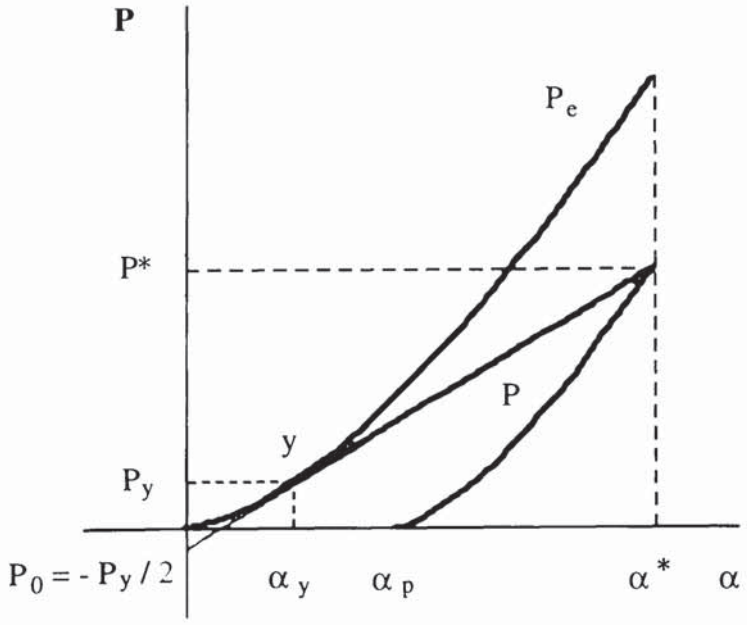

Fig. 3.3 Force-displacement curve for loading and unloading.

3.4 Particle bounce and coefficient of restitution

The impact process may conveniently be considered as divided into three distinct stages (Bitter, 1963). The first stage starts at the moment of initial contact of the bodies and the deformations in both bodies remain purely elastic until the peak pressure reaches the elastic yield limit of the softer of the two contacting bodies. In this stage the classic Hertzian theory can be used. The second stage commences at the onset of plastic deformation and ends when the impacting bodies have zero relative velocity. The area of plastic deformation grows from the centre of the contact zone and is surrounded by an annulus in which only elastic deformation occurs. In the third stage of impact the stored elastic energy is gradually released and transformed into kinetic energy of the particle. After impact the motion of the particle depends on the energy dissipated during the elastic-plastic impact.

The coefficient of restitution, e, is generally viewed as an experimentally determined parameter which in some way represents the effect of inelastic material behaviour, where part of the initial energy has been lost during the impact. It is defined as a ratio of the departure velocity to the approach velocity. The mechanisms of energy loss during impact involve many aspects, such as plastic deformation, elastic wave propagation, surface adhesion forces, internal friction, surface roughness, electrostatic effects, etc. Theoretical and experimental investigations indicate that plastic deformation is the dominant factor which dissipates initial kinetic energy and determines bounce of the particle when the impact velocity becomes relatively high or fully plastic deformation is achieved. The energy loss in elastic waves during plastic impact will be discussed in the next section. As we can find later the amount of energy loss in elastic waves is small and we are justified to concentrate on the mechanism of plastic deformation while ignoring other minor affecting factors.

From Fig.3.3 up to the instant of maximum compression part of the initial kinetic energy is dissipated during plastic loading while a certain amount of energy is transformed into stored elastic strain energy with maximum contact radius a* and contact force P*. The

energy transfer equation is

$$\frac{1}{2}mV_{ni}^2 = \int_0^{\alpha^*} P d\alpha = \int_0^{\alpha_y} P d\alpha + \int_{\alpha_y}^{\alpha^*} P d\alpha$$

$$= \frac{2}{5} P_y \alpha_y + \frac{1}{2} (P_y + P^*) (\alpha^* - \alpha_y)$$

$$= \frac{2}{5} P_y \alpha_y + \frac{1}{2} (P_y + P^*) (\frac{2P^* + P_y}{2\pi R\sigma_y} - \alpha_y)$$

$$= \frac{(P_y + P^*) (2P^* + P_y)}{4\pi R\sigma_y} - \frac{1}{10} P_y \alpha_y - \frac{1}{2} P^* \alpha_y \qquad (3.28)$$

where

$$\alpha_y = \frac{\pi^2 R^2 \sigma_y^2}{4E^{*2}} \quad \text{and} \quad P_y = \frac{\pi^3 R^2 \sigma_y^3}{6E^{*2}} \qquad (3.29)$$

If the particle bounces off the surface there is a residual displacement α_p corresponding to permanent plastic deformation. The process of elastic unloading corresponds to one in which a particle with a radius of R_p undergoes an equivalent displacement $\alpha_e = \alpha^* - \alpha_p$. The kinetic energy of rebound is equal to the work done during elastic recovery

$$\frac{1}{2} mV_{nr}^2 = \int_{\alpha_p}^{\alpha^*} P d\alpha = \int_0^{\alpha^* - \alpha_p} P d\alpha = \frac{2}{5} P^* (\alpha^* - \alpha_p) = \frac{2}{5} P^* \alpha_e \qquad (3.30)$$

where the equivalent displacement according to the Hertzian theory is

$$\alpha_e = \frac{a^{*2}}{R_p} = \frac{1}{R_p} (\frac{3R_p P^*}{4E^*})^{2/3} = (\frac{1}{R_p})^{1/3} (\frac{3P^*}{4E^*})^{2/3} \qquad (3.31)$$

Substituting α_e and R_p from (3. 27) the energy balance equation during rebound becomes

$$\frac{1}{2} mV_{nr}^2 = \frac{3P^{*2}}{10E^*} (\frac{2\pi\sigma_y}{2P^* + P_y})^{1/2} \qquad (3.32)$$

At very high impact velocities when $a_y << a^*$, $\alpha_y << \alpha^*$ and $P_y << P^*$ the maximum contact force may be approximated as

$$P^* = \pi\sigma_y a^{*2} \qquad (3.33)$$

and (3.28) and (3.32) may be rewritten as

$$\frac{1}{2} mV_{ni}^2 = \frac{P^{*2}}{2\pi R\sigma_y} = \frac{\pi\sigma_y a^{*4}}{2R} \qquad (3.34)$$

and

$$\frac{1}{2} mV_{nr}^2 = \frac{3P^{*2}}{10E^*} \left(\frac{\pi\sigma_y}{P^*}\right)^{1/2} = \frac{3P^{*2}}{10E^* a^*} = \frac{3\pi^2 \sigma_y^2 a^{*3}}{10E^*} \qquad (3.35)$$

The coefficient of restitution defined as the ratio of rebound velocity to impact velocity is therefore obtained from

$$e_n^2 = \frac{\frac{1}{2} mV_{nr}^2}{\frac{1}{2} mV_{ni}^2} = \frac{3\pi\sigma_y R}{5E^* a^*} \qquad (3.36)$$

Using (3.34) we have

$$a^* = \left(\frac{RmV_{ni}^2}{\pi\sigma_y}\right)^{1/4} \qquad (3.37)$$

therefore

$$e_n = \left(\frac{3\pi\sigma_y R}{5E^*}\right)^{1/2} \left(\frac{\pi\sigma_y}{RmV_{ni}^2}\right)^{1/8}$$

$$= 1.324\, \sigma_y^{5/8} E^{*-1/2} \rho_1^{-1/8} V_{ni}^{-1/4} \qquad (3.38)$$

It is clear that the coefficient of restitution is not a material property, but depends upon the severity of the impact. Johnson (1985) conducted an analysis of a particle bouncing upon plastic impact. He argued that in a fully plastic indentation the relationship between the compression α and the contact radius a is $\alpha = a^2 / 2R$, so that the loading slope is $2\pi R\sigma_y$, which is twice that used in this study. The coefficient of restitution at high impact velocities according to Johnson (1985) is

$$e_n = \left(\frac{6\pi\sigma_y R}{5E^* a^*} \right)^{1/2} = 1.72\, \sigma_y^{5/8} E^{*-1/2} \rho^{-1/8} V_{ni}^{-1/4} \qquad (3.39)$$

which is 1.3 times of that given in (3.38) since twice the stored elastic strain energy exists at the end of the loading process.

During the preparation of this thesis, Thornton (1994) obtained a complete analytical solution for the coefficient of restitution based on the theoretical treatment described in Section 3.3. The theoretical derivation is presented below. Rewriting (3.28) there results

$$\frac{1}{2} m V_{ni}^2 = \frac{2}{5} P_y \alpha_y + \frac{1}{2} (P_y + P^*) \left(\frac{P^* - P_y}{\pi R \sigma_y} \right)$$

$$= \frac{1}{2} m V_y^2 + \frac{P^{*2}}{4E^* a_y} - \frac{P_y^2}{4E^* a_y} \qquad (3.40)$$

Since

$$P_y = \frac{5R}{4a_y^2} m V_y^2 = \left(\frac{5E^* a_y}{3} m V_y^2 \right)^{1/2} \qquad (3.41)$$

we may rewrite (3.40) as

$$\frac{1}{2} m V_{ni}^2 = \frac{P^{*2}}{4E^* a_y} + \frac{1}{12} m V_y^2 \qquad (3.42)$$

from which the maximum contact force is given as

$$P^{*2} = 4E^* a_y \left(\frac{1}{2} m V_{ni}^2 - \frac{1}{12} m V_y^2 \right) \qquad (3.43)$$

Therefore (3.35) may be expressed as

$$\frac{1}{2} m V_{nr}^2 = \frac{6a_y}{5a^*} \left(\frac{1}{2} m V_{ni}^2 - \frac{1}{12} m V_y^2 \right) \qquad (3.44)$$

The coefficient of restitution can be obtained from

$$e_n^2 = \frac{\frac{1}{2} m V_{nr}^2}{\frac{1}{2} m V_{ni}^2} = \frac{6a_y}{5a^*} \left(1 - \frac{1}{6} \frac{V_y^2}{V_{ni}^2} \right) \qquad (3.45)$$

Since

$$a_y^2 = \frac{3P_y}{2\pi\sigma_y} \qquad \text{and} \qquad a^{*2} = \frac{2P^* + P_y}{2\pi\sigma_y} \tag{3.46}$$

we have

$$\left(\frac{a_y}{a^*}\right)^2 = \frac{3P_y}{2P^* + P_y} = \frac{3}{1 + 2P^*/P_y} \tag{3.47}$$

Using (3.41) and (3.43) there results

$$\left(\frac{P^*}{P_y}\right)^2 = \frac{6}{5}\left(\frac{V_{ni}^2}{V_y^2} - \frac{1}{6}\right) \tag{3.48}$$

or

$$\frac{P^*}{P_y} = \sqrt{\frac{6}{5}\left(V_{ni}/V_y\right)^2 - \frac{1}{5}} \tag{3.49}$$

Substituting (3.47) and (3.49) into (3.45) we have

$$e_n^2 = \frac{6\sqrt{3}}{5}\left[\frac{1}{1 + 2\sqrt{\frac{6}{5}\left(V_{ni}/V_y\right)^2 - \frac{1}{5}}}\right]^{1/2}\left[1 - \frac{1}{6}\left(\frac{V_y}{V_{ni}}\right)^2\right]$$

$$= \frac{6\sqrt{3}}{5}\left[\frac{V_y/V_{ni}}{\left(V_y/V_{ni}\right) + 2\sqrt{\frac{6}{5} - \frac{1}{5}\left(V_y/V_{ni}\right)^2}}\right]^{1/2}\left[1 - \frac{1}{6}\left(\frac{V_y}{V_{ni}}\right)^2\right] \tag{3.50}$$

from which the coefficient of restitution is obtained

$$e_n = \left[\frac{108}{25}\frac{V_y/V_{ni}}{\left(V_y/V_{ni}\right) + 2\sqrt{\frac{6}{5} - \frac{1}{5}\left(V_y/V_{ni}\right)^2}}\right]^{1/4}\left[1 - \frac{1}{6}\left(\frac{V_y}{V_{ni}}\right)^2\right]^{1/2} \tag{3.51}$$

If $V_{ni} = V_y$, equation (3.51) gives $e_n = 1$. At very high impact velocities when $V_y << V_{ni}$, (3.51) can be simplified as

$$e_n = \left[\frac{108}{25}\frac{V_y/V_{ni}}{2\sqrt{6/5}}\right]^{1/4} = 1.185\left(\frac{V_y}{V_{ni}}\right)^{1/4} \tag{3.52}$$

Since V_y is a material related parameter, alternatively, we may substitute (3.5) into (3.52) and the expression for the coefficient of restitution is given as

$$e_n = 1.324\,\sigma_y^{5/8} E^{*-1/2} \rho^{-1/8} V_{ni}^{-1/4} \tag{3.53}$$

which is in agreement with (3.38).

3.5 Force-time relationship and energy dissipation in elastic waves

In order to estimate the contact duration for an elastic-plastic impact the force-time relationship during elastic-plastic loading and elastic unloading must be known. The Hertzian treatment of elastic impact gives an expression for the time of contact between the two colliding bodies which has been found to be dependent on the velocity of approach. The contact force during elastic-plastic impact is also related to the severity of impact. For the simplicity of analysis the yield stress of material is assumed to be constant during the loading process and the effect of a dynamic yield stress is ignored. Referring to (3.15) the contact force in the loading process is

$$P = P_y + \pi\sigma_y (a^2 - a_y^2) = \pi\sigma_y R (\alpha - \frac{1}{3}\alpha_y) \qquad (3.54)$$

The equation governing the motion of the sphere with mass m is given by

$$m\ddot{\alpha} = -P = -\pi\sigma_y R (\alpha - \frac{1}{3}\alpha_y) \qquad (3.55)$$

The expression of the response frequency in the solution of the above differential equation will be very complicated. To simplify the mathematical treatment, it is assumed that there is negligible elastic deformation at initial yield and also in material surrounding the contact point. This is only valid for high impact velocities, but by using this assumption we may rewrite (3.55) as

$$m\ddot{\alpha} = -\pi\sigma_y a^2 = -\pi\sigma_y R\alpha \qquad (3.56)$$

The solution of this differential equation is

$$\alpha = \alpha^* \sin \varpi_p t \qquad 0 \le t \le \pi/2\varpi_p \qquad (3.57)$$

where α^* and ϖ_p are the maximum approach and the response frequency for plastic loading respectively, and

$$\dot{\alpha} = \alpha^* \varpi_p \cos \varpi_p t \qquad (3.58)$$

$$\ddot{\alpha} = -\alpha^* \varpi_p^2 \sin \varpi_p t = -\varpi_p^2 \alpha \qquad (3.59)$$

or

$$m\ddot{\alpha} = -\varpi_p^2 \alpha m = -\pi\sigma_y R\alpha \qquad (3.60)$$

$$\varpi_p^2 = \pi\sigma_y R / m \qquad (3.61)$$

$$\varpi_p = \left(\frac{3\sigma_y}{4\rho_1 R^2}\right)^{1/2} \qquad (3.62)$$

where ρ_1 is the density of the sphere. Up to the instant of maximum compression the kinetic energy is absorbed in local elastic and plastic deformation of the two colliding bodies

$$\frac{1}{2} m V_{ni}^2 = \int_0^{\alpha^*} P d\alpha = \frac{1}{2} \pi\sigma_y R \alpha^{*2} \qquad (3.63)$$

and therefore

$$\alpha^* = \left(\frac{m}{\pi\sigma_y R}\right)^{1/2} V_{ni} = \left(\frac{4\rho_1 R^2}{3\sigma_y}\right)^{1/2} V_{ni} \qquad (3.64)$$

From (3.60) the expression for the time dependent contact force is

$$P(t) = -m\ddot{\alpha} = \pi\sigma_y R\alpha^* \sin \varpi_p t = P^* \sin \varpi_p t \qquad 0 \le t \le \pi/2\varpi_p \qquad (3.65)$$

and the maximum contact force is

$$P^* = \pi\sigma_y R\alpha^* = \pi R^2 \left(\frac{4\rho_1\sigma_y}{3}\right)^{1/2} V_{ni} \qquad (3.66)$$

With respect to (3.45), under the same assumption as above, we have

$$e_n^2 = \frac{6a_y}{5a^*} = \frac{3\pi\sigma_y R}{5E^*a^*} = \frac{4}{5}\frac{\pi\sigma_y R}{m}\frac{1}{4E^*a^*/3m}$$

$$= \frac{4}{5}\frac{\varpi_p^2}{4E^*a^*/3m} = \frac{4}{5}\varpi_p^2/\varpi_e^2 \qquad (3.67)$$

Since as demonstrated in Appendix A

$$\varpi_e = \sqrt{\frac{4E^*a^*}{3m}} = \sqrt{\frac{4}{5}}\frac{\varpi_p}{e_n} \qquad (3.68)$$

is the response frequency during elastic recovery in an elastic-plastic impact and the first part of (3.68) is valid for purely elastic impacts as well. It is seen that the elastic frequency is dependent on the severity of impact. At the point of transition from loading to unloading the force function and its time derivative must be continuous and the force-time relationship can be given by

$$P(t) = P^* \cos \varpi_e (t - \pi/2\varpi_p) \qquad \pi/2\varpi_p \le t \le \pi/2\varpi_p + \pi/2\varpi_e \qquad (3.69)$$

where P^* is the value of the maximum force at the transition point and is given by (3.66). The total contact time including plastic loading time t_L and elastic recovery or unloading duration t_U is therefore given as

$$t = t_L + t_U = \frac{\pi}{2\varpi_p} + \frac{\pi}{2\varpi_e} = \frac{\pi}{2}\left(\frac{1}{\varpi_p} + \frac{1}{\varpi_e}\right) = \frac{\pi}{2\varpi_p}\left(1 + \sqrt{5/4}\, e_n\right)$$

$$= \frac{\pi R}{2}\left(1 + \sqrt{5/4}\, e_n\right)\left(\frac{4\rho_1}{3\sigma_y}\right)^{1/2} = \pi R \left(1 + \sqrt{5/4}\, e_n\right)\left(\frac{\rho_1}{3\sigma_y}\right)^{1/2} \qquad (3.70)$$

The complete loading-unloading history as described in equations (3.65) and (3.69) is shown in Fig. 3.4.

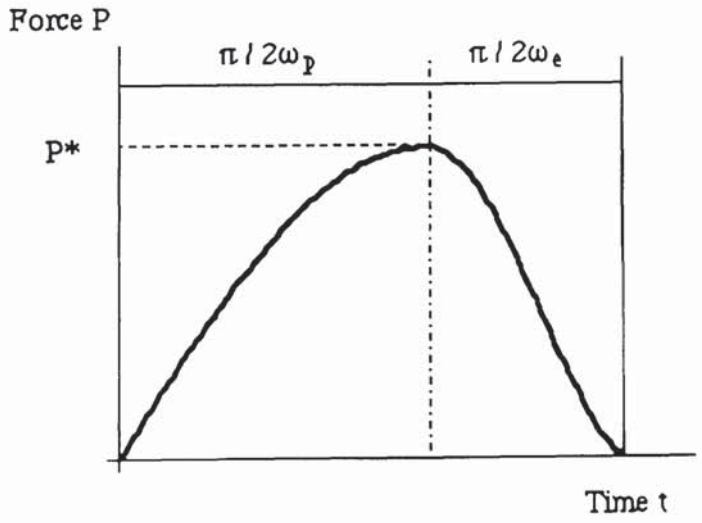

Fig. 3.4 Force-time relationships defined by (3.65) and (3.69).

As demonstrated in Section 2.2.1, for purely elastic impacts the power law relationship between the contact duration and impact velocity has an exponent of -1/5 and the force-time curve is symmetric. It is seen from (3.62) and (3.70) that the time of collision during plastic loading is independent of impact velocity, however the total contact time varies with impact velocity due to the involvement of the coefficient of restitution which is proportional to $V_i^{-1/4}$ as demonstrated in (3.38). Numerous collision experiments (Andrews, 1931; Tabor, 1951) have shown that the asymmetric type of force-time curve is of general occurrence, if plastic flow occurs. As the impact velocity is increased further, the coefficient of restitution e_n falls and the elastic unloading time t_U becomes a smaller proportion of the total time of impact t.

It is worth noting that the contact time at initial yield given by (3.70) is not exactly equal to that given by (2.10). The reason for this may correspond to the assumption that the elastic deformation in the initial stage of loading is ignored and (3.56) is valid for the whole range of impact velocities whether they be below or above the yield velocity. Under this assumption an asymmetry of the force-time curve occurs at initial yield, and it is seen from (3.70) that the time of elastic recovery is slightly longer than that for the loading process when $e_n = 1.0$. Substituting V_y of (3.9) into (2.10) the minimum elastic impact time is

$$t_{e,min} = 2.87 \left(\frac{m^2}{RE^{*2}V_y} \right)^{1/5} = 4.66\, R \left(\frac{\rho_1}{\sigma_y} \right)^{1/2} \qquad (3.71)$$

and the maximum plastic impact time by letting $e_n = 1$ in (3.70) is

$$t_{p,max} = 3.84\, R \left(\frac{\rho_1}{\sigma_y} \right)^{1/2} \qquad (3.72)$$

which is less than the value of $t_{e,min}$.

The energy dissipation in elastic waves during plastic impact was estimated by Hutchings (1979), who analysed the force-time relationship during plastic loading and elastic unloading separately. The relationship between the plastic and elastic response

frequency was assumed to be related to the coefficient of restitution, which is close to this study as demonstrated in (3.68). A complete analysis of the initial kinetic energy radiated to the free surface of semi-infinite solid during plastic impact is given in Appendix A. The major results of the analysis are presented below.

Under a transient time dependent force which has the pulse shape of $\sin\varpi t$ or $\cos\varpi t$ the total energy loss in elastic wave propagation according to Hunter (1957) is

$$W = \frac{\zeta(\nu_2)}{\rho_2 C_0^3} P^{*2} \varpi_0 \qquad (3.73)$$

where

$$C_0 = (E^* / \rho_2)^{1/2} \qquad (3.74)$$

$$\zeta(\nu_2) = \beta(1 + \nu_2)\left(\frac{1 - \nu_2^2}{1 - 2\nu_2} \right)^{1/2} \qquad (3.75)$$

which is only related to the Poisson's ratio of the substrate ν_2; ρ_2 is the density of the target surface; P^* and ϖ_0 are the maximum contact force and the response frequency respectively. The maximum force is unique in both loading and unloading process due to the smooth loading and unloading transition. However, the frequency in elastic recovery is no longer equal to the previous one in the plastic loading process. An equivalent frequency was defined by Hutchings (1979) and then used to calculate the total energy dissipation in elastic wave motion. It is at this point the present analysis differs from that of Hutchings. From physical arguments, the total energy loss can be subdivided into two parts: the energy loss in the plastic loading process W_p and the energy dissipation during elastic recovery W_e, and

$$W_p = \frac{\zeta(\nu_2)}{\rho_2 C_0^3} \pi^2 R^3 \left(\frac{\rho_1 \sigma_y}{3} \right)^{3/2} V_{ni}^2 \qquad (3.76)$$

$$W_e = \frac{\zeta(\nu_2)}{\rho_2 C_0^3} P^{*2} \varpi_e = \sqrt{\frac{4}{5}} \frac{W_p}{e_n} \qquad (3.77)$$

The total radiated energy is then given by

$$W = W_p + W_e = \frac{\zeta(\nu_2)}{\rho_2 C_0^3} \pi^2 R^3 \left(\frac{\rho_1 \sigma_y^3}{3} \right)^{1/2} V_{ni}^2 \left(1 + \sqrt{\frac{4}{5}} \frac{1}{e_n} \right) \qquad (3.78)$$

and the fraction of the initial kinetic energy loss is

$$W^* = \frac{W}{\frac{1}{2} m V_{ni}^2} = \frac{\zeta(\nu_2)}{\rho_2 C_0^3} \pi \left(\frac{3\sigma_y^3}{4\rho_1} \right)^{1/2} \left(1 + \sqrt{\frac{4}{5}} \frac{1}{e_n} \right) \qquad (3.79)$$

For U_3O_8 particles striking a steel plate, at an impact velocity of V_{ni} = 1.0 m/s, which is slightly above the yield velocity, the percentage energy loss W* is 0.818%; when V_{ni} = 10 m/s equation (3.79) predicts that W* = 1.07%; and at V_{ni} = 100 m/s we have W* = 1.564%. In the previous analysis we assume that there is no effect of the dynamic yield stress during impact. If this factor is going to be included the situation would be much more complicated. As the fraction of energy loss is very low we are justified to ignore the energy loss in terms of elastic wave propagation during elastic and elastic-plastic impacts irrespective of whether or not we take into account the effects of a dynamic yield strength.

3.6 Computer simulation results

Numerical simulations of normal impact of elasto-plastic spheres with a plane smooth wall have been performed using the computer program TRUBAL. Detailed information about the computer code, and the modifications that have been made to incorporate the new theories described in this thesis, will be presented in Chapter 8. Typical simulations will be illustrated for the case of U_3O_8 particles impacting a stainless steel surface. The particle and target properties used in the simulations were provided in Table 1.1. The particle radius used in the computer simulated experiments is R = 10 μm.

Figure 3.5 shows the normal force-displacement curves obtained for impact velocities of 5.0, 10.0 and 20.0 m/s. After plastic yield the slope of the loading curves is unique, in agreement with (3.18). At different impact velocities the elastic unloading curves are not parallel to each other since the contact curvature decreases with an increase in impact velocity. Consequently, the slope of unloading curve at the transition point becomes stiffer as the severity of plastic indentation increases.

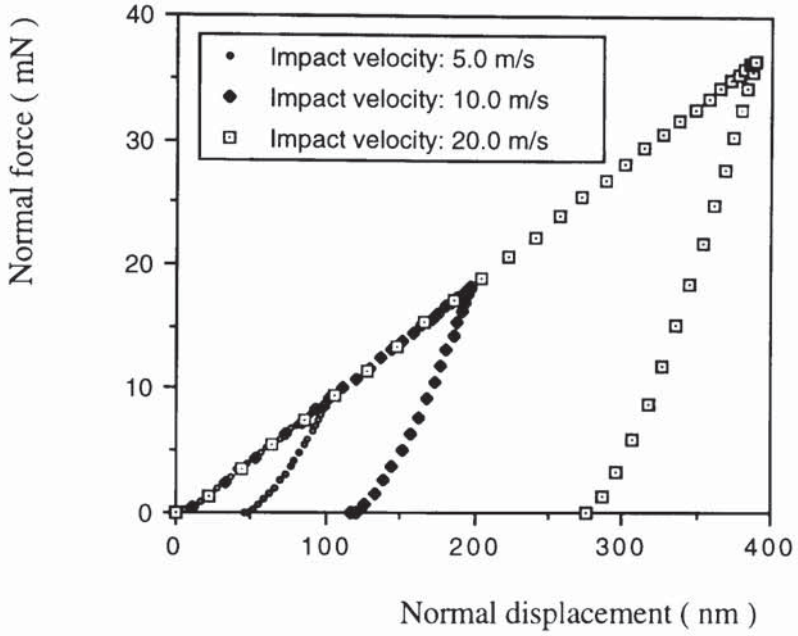

Fig. 3.5 The normal force-displacement relationship at different impact velocities.

Coefficients of restitution, obtained from the simulations, are plotted against impact velocity in Fig.3.6 . It is seen that there are three ranges of behaviour: elastic impact, elasto-plastic impact and fully plastic impact. If other mechanisms of energy dissipation such as elastic wave propagation, surface roughness, and internal friction, etc., are ignored, the elastic collision process is entirely reversible and the impact and rebound velocities are identical. The coefficient of restitution, therefore, is unity. At high impact velocities the plastic deformation dominates the loading process and the initial plastic yield force P_y is insignificant compared with the maximum contact force generated. It can be seen from Fig.3.6 that the results of the computer simulations in this high velocity range match the

theoretical power law relationship given by (3.38) very well. However, in the range $V_y < V_{ni} < 10V_y$, the difference between the simulation results and the predictions of (3.38) are significant. The differences are of major concern since this is a region which is commonly encountered in process engineering problems.

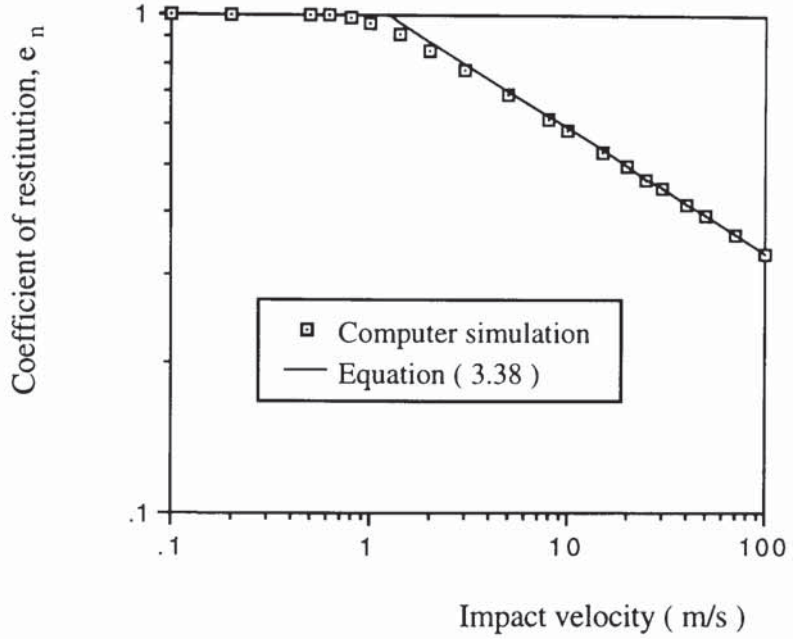

Fig. 3.6 Computer simulated normal coefficient of restitution in the full range of impact velocity and theoretical predictions given by (3.38).

The simulated results and the power law relationship (3.38) are replotted in Fig. 3.7 to emphasise the difference. Superimposed on the figure is an alternative prediction recently suggested by Stronge (1994b) which, for a sphere impacting a wall, takes the form

$$e_n = \frac{V_y}{V_{ni}} \left[\frac{8}{5} \left(\frac{V_{ni}}{V_y} \right)^2 - \frac{3}{5} \right]^{3/8} \qquad (3.80)$$

Inspection of (3.80) shows that, for $V_{ni} >> V_y$, the equation degenerates to

$$e_n = 1.193 \left(\frac{V_y}{V_{ni}} \right)^{1/4} \qquad (3.81)$$

and that, for $V_{ni} = V_y$, $e_n = 1$. However, Stronge's (1994b) equation (3.80) also predicts $e_n > 1$ for $V_y < V_{ni} < 1.59V_y$, as shown in Fig. 3.7.

In Fig. 3.8 the coefficient of restitution obtained from computer simulated experiments are compared with the analytical solution (3.51) provided by Thornton (1994). It is seen that there is an exact agreement between the analytical predictions and the simulation data. Since the analytical solution is based on the theoretical assumptions incorporated into the computer code, Fig. 3.8 provides the verification that the computer program has been correctly coded.

The evolution of the normal contact force with time is shown in Fig. 3.9 for an elastic impact and an elasto-plastic impact. In both cases of computer simulation an impact velocity of 50.0 m/s was used. In order to simulate the elastic impact a very high yield stress was prescribed to ensure that no plastic deformation occurred. It can be seen that for the elasto-plastic impact the force evolution is asymmetric, in agreement with Fig. 3.4, the rebound period being significantly shorter than the loading period. It is also noted that the total impact duration is larger than that of the equivalent elastic impact. For comparison, the evolution of the equivalent elastic force P_e during the loading period of the elasto-plastic impact is also shown.

Figure 3.10 shows how the contact duration varies with impact velocity, indicating the total contact time t, the loading period t_L and the unloading period t_U. For an impact velocity equal to the yield velocity $V_y = 0.625$ m/s, the computer simulation gave $t_L = t_U = 0.0384$ μs which may be compared with the theoretical prediction of 0.0385 μs according to (2.10). As the impact velocity increases both the loading period and the unloading period decrease. However, as can be seen from Fig. 4.10, at impact velocities $V_{ni} > 5.0$ m/s the loading period tends to a constant value of $t_L = 0.0297$ μs as predicted by (3.70). Therefore, it is concluded that the computer simulated results agree very well with the theoretical predictions.

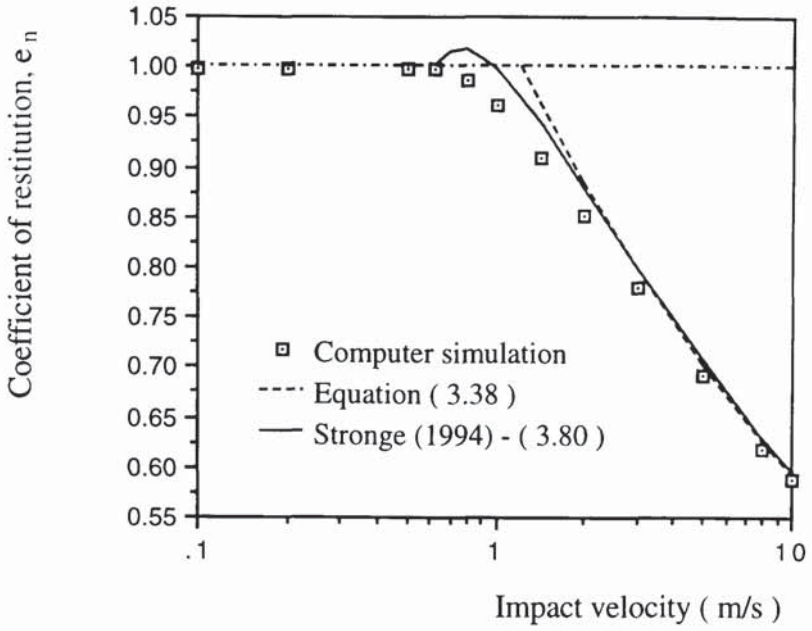

Fig. 3.7 Computer simulated coefficient of restitution compared with the predictions given by Stronge (1994b).

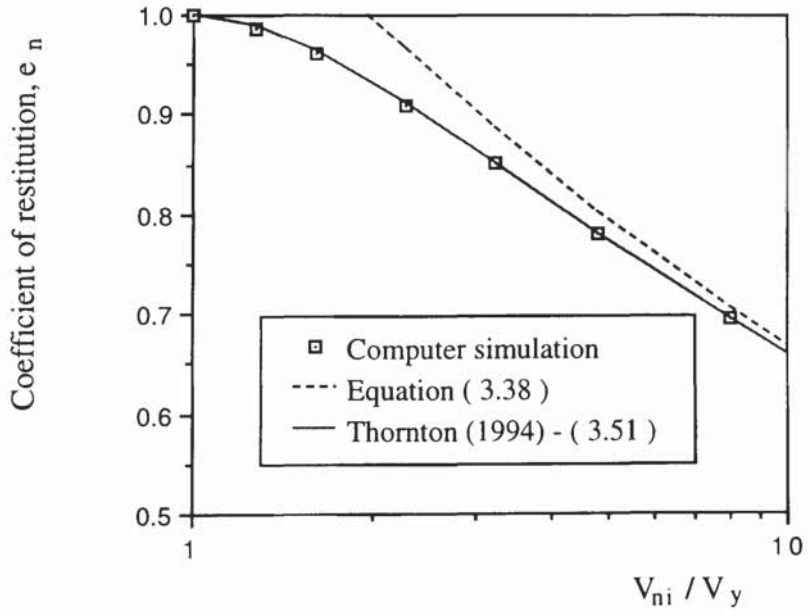

Fig. 3.8 Computer simulated coefficient of restitution compared with the predictions given by Thornton (1994).

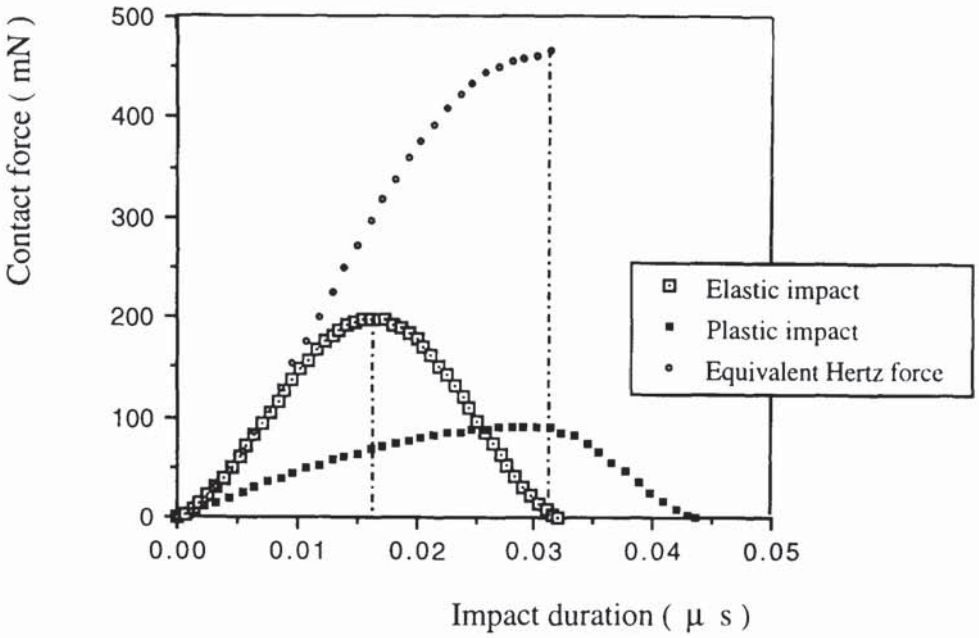

Fig. 3.9 Force-time curves of elastic and plastic impact at an impact velocity of 50.0 m/s.

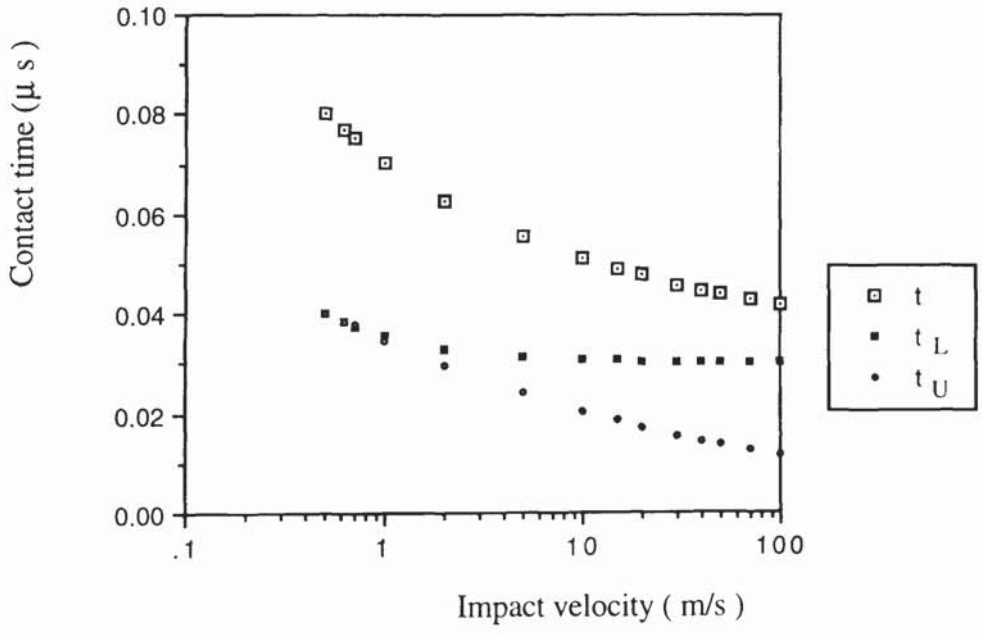

Fig. 3.10 Computer simulated contact duration of elastic-plastic impact

3.7 Summary and discussion

The compliance and force-time relationships based on the classical Hertzian theory have been extended to incorporate plastic deformation for orthogonal impacts. It has been demonstrated that the portion of the initial kinetic energy lost due to the elastic wave propagation during an elasto-plastic impact is not significant and can be neglected. The asymmetric evolution of the normal force during the contact period and the velocity independent plastic loading time obtained in the simulations are in agreement with the experimental observations by Andrews (1931). The computer simulation results match the theoretical predictions of the coefficient of restitution and contact duration very well.

The coefficient of restitution at high impact velocities, shown in Equation (3.38), is $1.185\ (V_y/V_{ni})^{1/4}$. Although the normal contact stiffness derived in this study is half that given by Johnson (1985) the power law relationship between the normal coefficient of restitution and impact velocity has the same exponent of -1/4 for both cases, a feature which is supported by experimental measurements. From the experimental point of view, the yield velocity V_y above which $e_n < 1$, is much easier to measure. Consequently, in order to verify the theory the impact model presented in this study can avoid the difficulties in measuring the yield stress.

In the literature, there exists an unsolved problem of the yield stress suitable for use in elasto-plastic impact models. It has been found (Timoshenko, 1934; referring Johnson, 1985) that for a particle indenting a free surface of semi-infinite solid the condition for plasticity is first reached when the maximum contact pressure $p_0 = 1.6Y$ or the mean pressure $p_m = 1.1Y$ is obtained, where Y is a uniaxial yield stress. Both experimental and numerical studies (Tabor 1951, Hardy et al 1971) suggest that the mean contact pressure increases with the severity of the indentation and under high loads rapidly approaches a value of $p_m = 3Y$, at which a fully plastic state is obtained. For the mean pressure in the range of $1.1Y < p_m < 3Y$, the indentation is called elasto-plastic. Johnson's (1985) model,

which is based on the assumption $p_m = 3Y$, overestimated the coefficient of restitution even for fully plastic impacts. In this study, it is assumed that the limiting normal pressure $\sigma_y = KY$ maintains constant during plastic loading, where the constant K, according to Hardy et al (1971), should be in the range of 2.3 - 2.5. For fully plastic impacts σ_y is approximately equal to the mean stress at the contact. For impact velocities which are close to the yield velocity, as indicated by Hardy et al (1971), the stress distribution is between the uniform distribution and the elliptic Hertzian distribution, but p_0 is larger than 1.6Y. The assumed distribution in this study, a Hertzian one with a cut-off of σ_y, may slightly increases the yield velocity but the distribution is close to the actual distribution and the difficulty caused by variations of p_m for use in the impact models can be avoided.

It is important to note that, since the contact force and the contact radius are in continuity at the transition from loading to unloading, an imbalance of the contact pressure distribution occurs at this transition during which the approximately uniform distribution is instantaneously changed to the elliptic Hertzian distribution. The same problem exists for the models by Johnson (1985) and Stronge (1994b).

Chapter 4 Oblique impact of elasto-plastic spheres

4.1 Introduction

Although the theory of particle impact for normal collisions has been relatively well established, at least for high velocities, there appear to be no published analytical solutions for oblique impact with plastic deformation. The problem of oblique rigid body collisions has been investigated by Brach (1981, 1984, 1988, 1989), Keller (1986) and Stronge (1990, 1991, 1992, 1994a). However, by ignoring the particle elasticity and plastic deformation at the contact, rigid body collision theory has limitations for process engineering applications.

In this chapter, results of computer simulated oblique impact will be presented. The normal contact interaction law was based on the theory presented in Chapter 3. For simplicity, it is assumed that Mindlin's (1949) partial-slip solution remains valid for all impact velocities and hence the tangential stiffness is given by (2.18). Therefore, it should be noted that for normal components of velocity higher than the yield velocity the contact radius is related to the effective Hertzian normal force P_e. The sliding criterion is controlled by the actual normal force, i.e. $|T| = \mu P$. Some of the work in this chapter has been reported by Thornton and Ning (1994).

4.2 Evolution of contact forces and energy components

For oblique elastic impacts the normal-tangential force and tangential force-displacement relationships were reported by Thornton and Yin (1991). In this section the effect of plastic deformation on these relationships is examined. Figures 4.1 and 4.3 show the evolution of

the normalised tangential force during the impact period for different impact angles at impact speeds of 5.0 m/s and 20.0 m/s respectively. Compared with Fig. 2.3, which was obtained by Maw et al (1976, 1981) for elastic impacts, it is seen from Fig. 4.1 that the tangential force-time curves are affected by plastic deformation at low impact angles, but for other impact angles the pattern of evolution is similar to that under elastic deformation. For example, at $\theta = 15°$, the tangential force undergoes three half cycles of oscillation, though the last one is very small. Contact sliding only occurs at the final stage of impact. As demonstrated in Section 3.4, the plastic loading time t_L is longer than the elastic unloading period t_U and the total contact time for an elastic-plastic impact, therefore, is longer than that for an equivalent elastic impact. Consequently, for small impact angles at which sliding only occurs over part of the impact duration, the tangential force has to undergo an extra half cycle to compensate for this. For an impact speed of 20.0 m/s, Fig. 4.3 shows that the last cycle becomes longer at $\theta = 15°$. Further computer simulation results indicate that for V_i = 100 m/s there is a third half cycle of tangential force even for $\theta = 30°$. It is also seen from Fig. 4.3 that contact sliding occurs at the beginning of the impact. The reason for this is that, since the contact force for a high velocity plastic impact is significantly less than the effective elastic force which determines the contact area, the limiting friction condition $|T| = \mu P$ is easier to obtain and therefore sliding occurs. It should be noted that, in Figs. 4.1 and 4.3, the total contact time varies with the normal component of impact speed which is dependent on the impact angle.

Figures 4.2 and 4.4 show the loading and unloading paths for different impact angles at two impact speeds. For an impact speed of 5.0 m/s, at low impact angles, e.g. $\theta = 15°$, contact sliding only occurs in the final stage of unloading and the direction of sliding is opposite to that for elastic impacts as reported by Yin (1992). If the impact angle is greater than a certain value sliding initiates at the start of loading and continues until the moment at which the tangential incremental force $\Delta T < \mu \Delta P$ is obtained. After passing the peak value the tangential force reduces, reverses in direction and finally contact sliding reoccurs. The ratio of sliding duration to the total contact time is dependent on the impact angle. At very

large impact angles, e.g. 75°, sliding occurs throughout the impact with no reversal of the tangential force direction. For an impact speed of 20.0 m/s, it is seen from Figure 4.4 that at $\theta = 15°$ contact sliding occurs at the start of the impact and finishes when the condition $\Delta T < \mu\Delta P$ is reached during loading. After the maximum negative value is obtained the tangential force increases and becomes positive again. When the friction condition is reached sliding reoccurs and continues until the end of the impact. The maximum normal force in Fig. 4.2 and Fig. 4.4 decreases with an increase of the impact angle since the simulations were performed for a constant impact speed.

It should be noted that, for elastic impacts, the condition governing initial sliding during loading, as reported by Maw et al (1976), is that the parameter $\psi_i \geq 1.0$ which corresponds to $\theta \geq 23°$. However, when plastic deformation is severe, e.g. $V_i = 20.0$ m/s, sliding initiates at the start of the impact with $\theta = 15°$. For elastic impacts, contact sliding occurs throughout the impact when $\psi_i \geq 4\chi - 1 = 4.77$, corresponding to the impact angle of $\theta \geq 63.7°$ for the material properties used in this study. It will be shown in Section 4.3.3 that plastic deformation affects this criterion.

The tangential force-displacement relationship is plotted in Fig. 4.5 and Fig. 4.6 for various impact angles at the two impact speeds. The energy loss during oblique impact in terms of shear deformation can be demonstrated by the force-displacement curves. It is seen from both figures that the tangential displacement prior to particle departure increases with an increase of impact angle since the tangential component of impact velocity increases. Finally for the impact angles at which sliding occurs throughout the impact process there is no reversal in the direction of tangential displacement. Figure 4.7 shows the normalised tangential force-displacement relationship at $\theta = 15°$ for impact speeds of 0.5 m/s and 20.0 m/s respectively. It can be seen that, as a result of plastic deformation, the second reversal in the tangential displacement leads to a positive tangential force prior to the end of the collision.

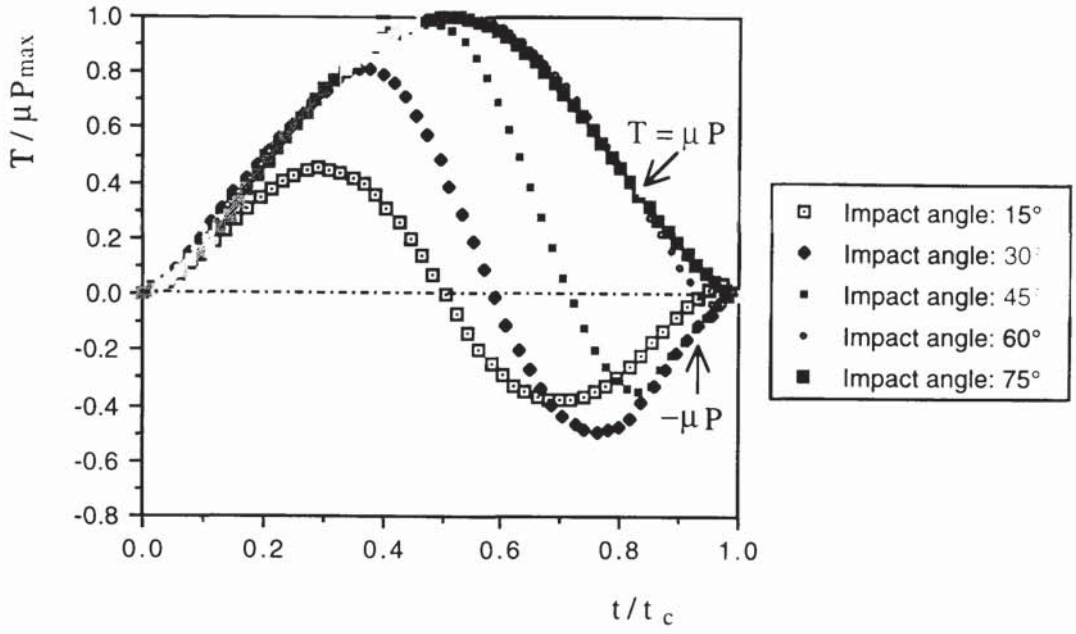

Fig. 4.1 Normalised tangential force plotted against normalised contact time for different impact angles at an impact speed of 5.0 m/s.

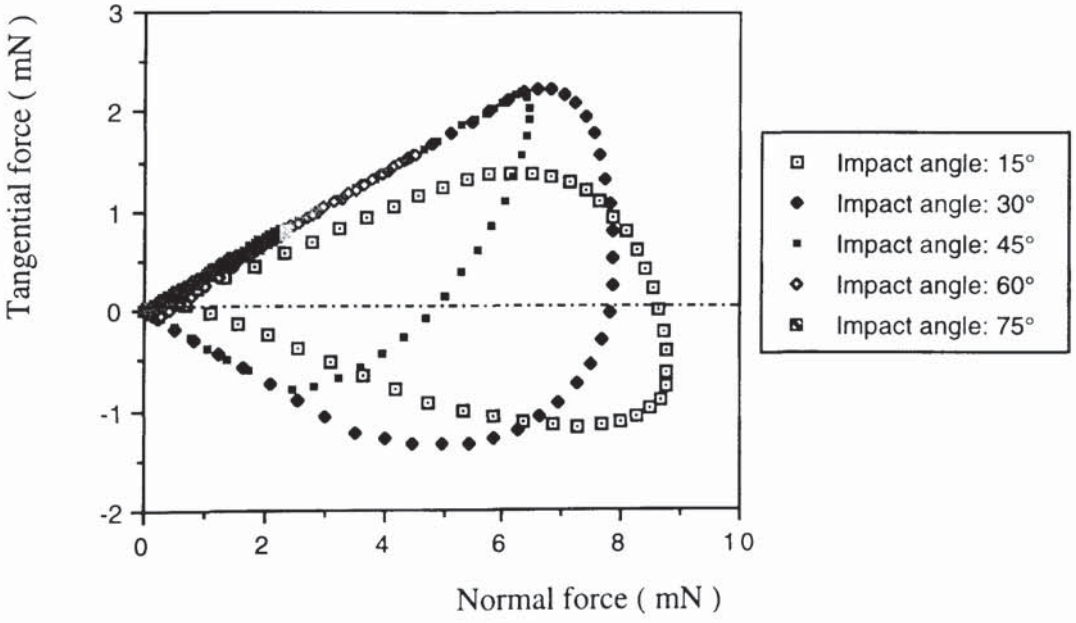

Fig. 4.2 Normal force-tangential force relationship at an impact speed of 5.0 m/s.

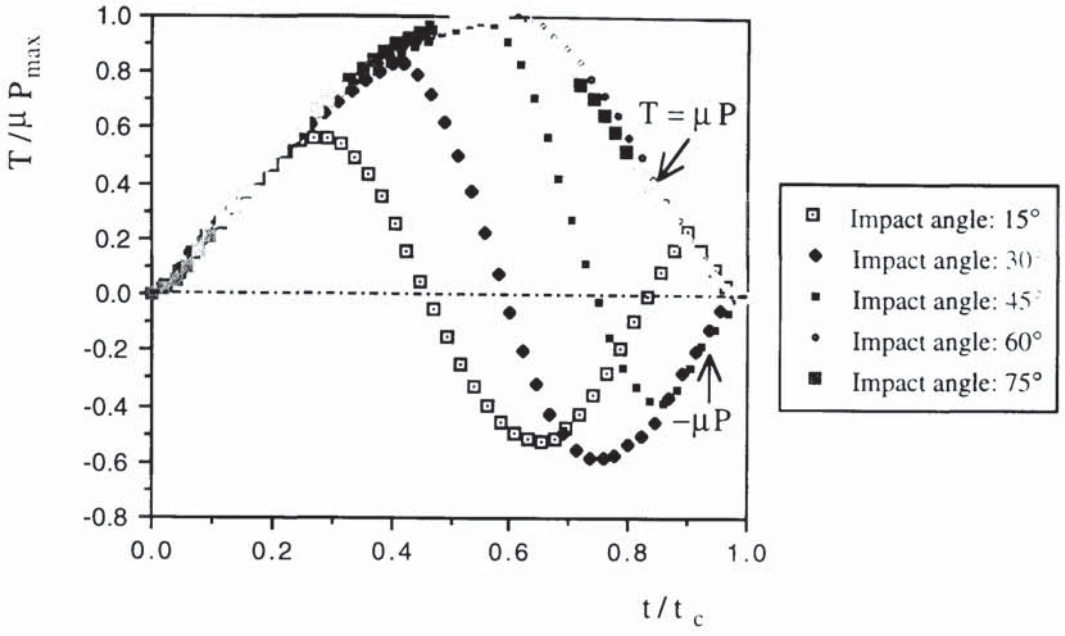

Fig. 4.3 Normalised tangential force plotted against normalised contact time at an impact speed of 20.0 m/s.

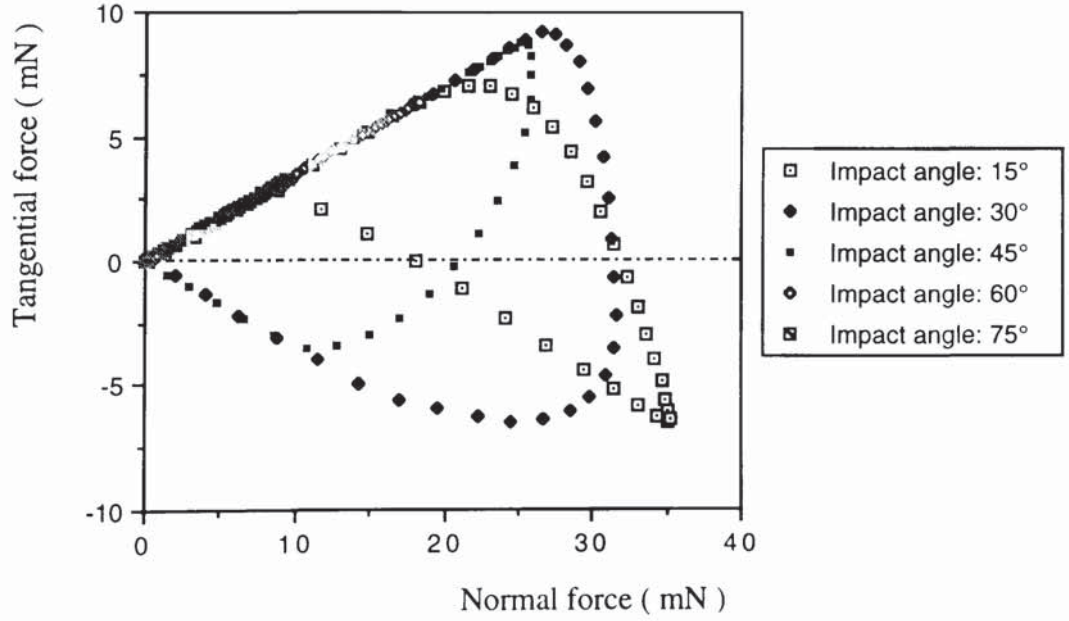

Fig. 4.4 Normal-tangential force relationship at impact speed of 20.0 m/s.

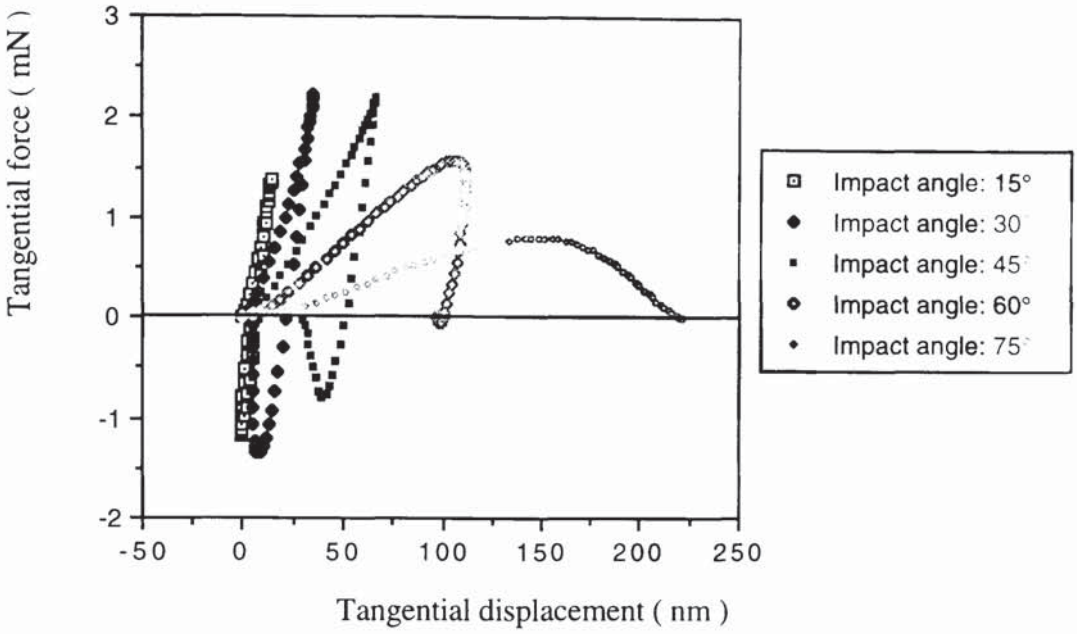

Fig. 4.5 Tangential force-displacement relationship at impact speed of 5.0 m/s.

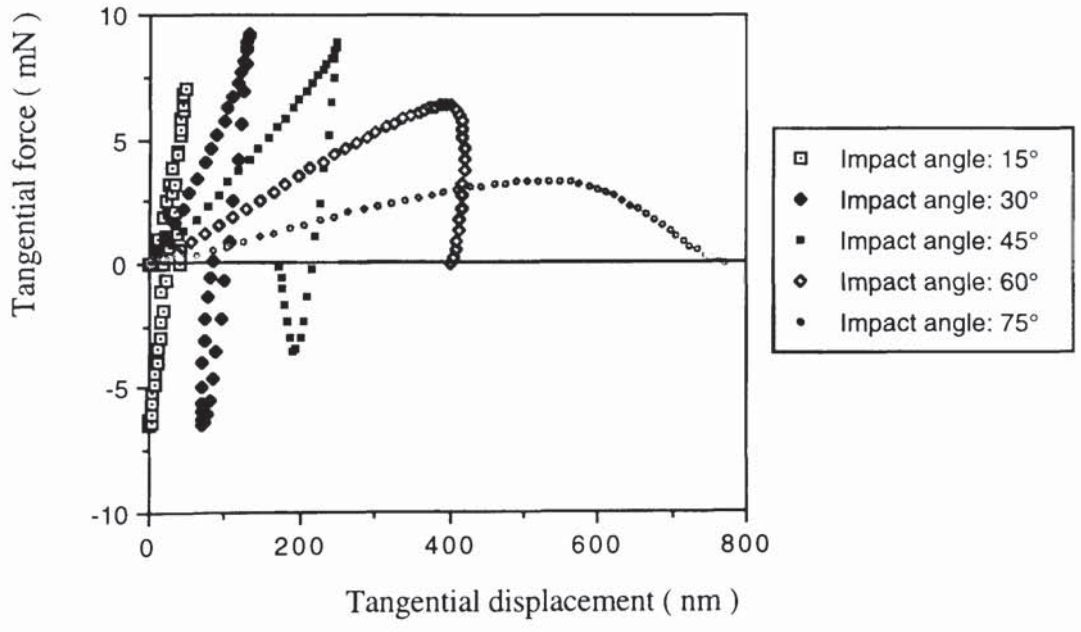

Fig. 4.6 Tangential force-displacement relationship at impact speed of 20.0 m/s.

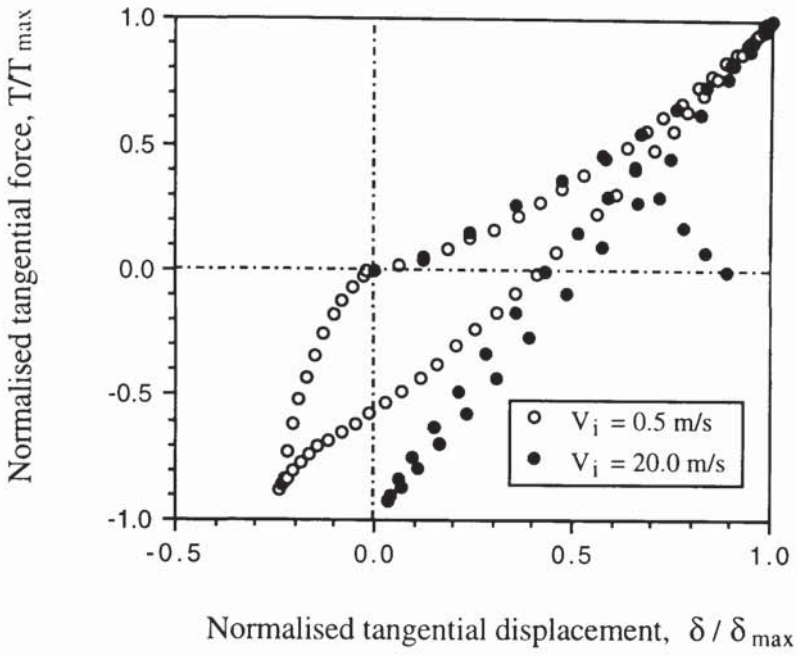

Fig. 4.7 Normalised tangential force-displacement relationship at an impact angle of 15° for impact speeds of 0.5 and 20.0 m/s.

In this study two types of energy loss mechanisms under consideration are friction and plastic deformation. Information about the distribution of energy and work done by the normal and tangential forces will allow us to understand the role each energy loss mechanism plays and investigate the impact process more precisely, for instance, by examining whether the energy terms violate the principle of energy conservation. The evolution of total (both linear and rotational) kinetic energy and types of work done during impact are shown in Fig. 4.8 and Fig. 4.9 for impact speeds of 5.0 m/s and 20.0 m/s respectively. For the case of normal impacts shown in Fig. 4.8 (a) and Fig. 4.9 (a) the kinetic energy decreases with a corresponding increase in the work done by the normal force during loading since the kinetic energy is gradually transformed into local elastic and plastic strain energy. When the normal force and normal work done simultaneously approach their maximum values the kinetic energy becomes zero because the particle is momentarily stationary. In the unloading process the stored elastic strain energy furnishes the kinetic energy of rebound. Due to the involvement of plastic deformation the collision process is not

reversible and a certain amount of energy, depending on the severity of plastic indentation, has been lost.

For oblique impacts the total kinetic energy never reduces to zero partly due to the rotational kinetic energy developed and partly due to the fact that the normal and tangential velocities reverse directions at different times. As for normal impacts, the normal work done is not reversible if the normal approach velocity is above the yield velocity. The work done by the tangential force is twofold: work done in shear at contacting surfaces and work done to furnish particle rotation. The way in which these two components of tangential work evolve during an impact is shown in Fig. 4.8 and Fig. 4.9. For impact angles less than the angle at which sliding occurs throughout the impact the tangential work exhibits two local maxima and one local minimum corresponding to the maximum and zero values of tangential force respectively. The rotational work done has a maximum value at zero tangential force after which there is some partial recovery. However, if sliding occurs throughout the impact both components of tangential work increase continuously.

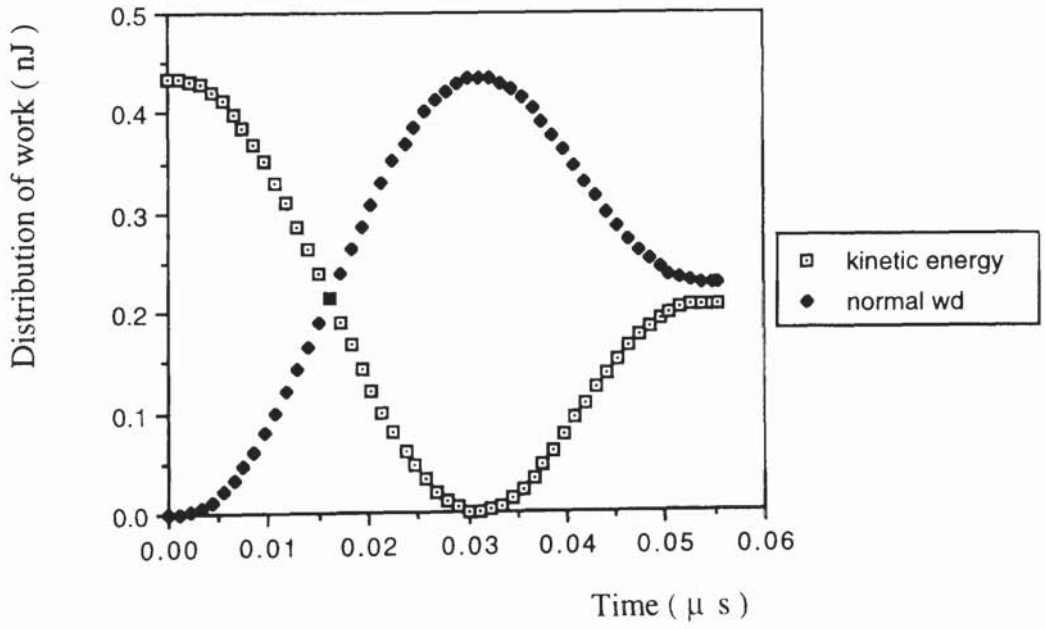

(a). Impact angle: 0°

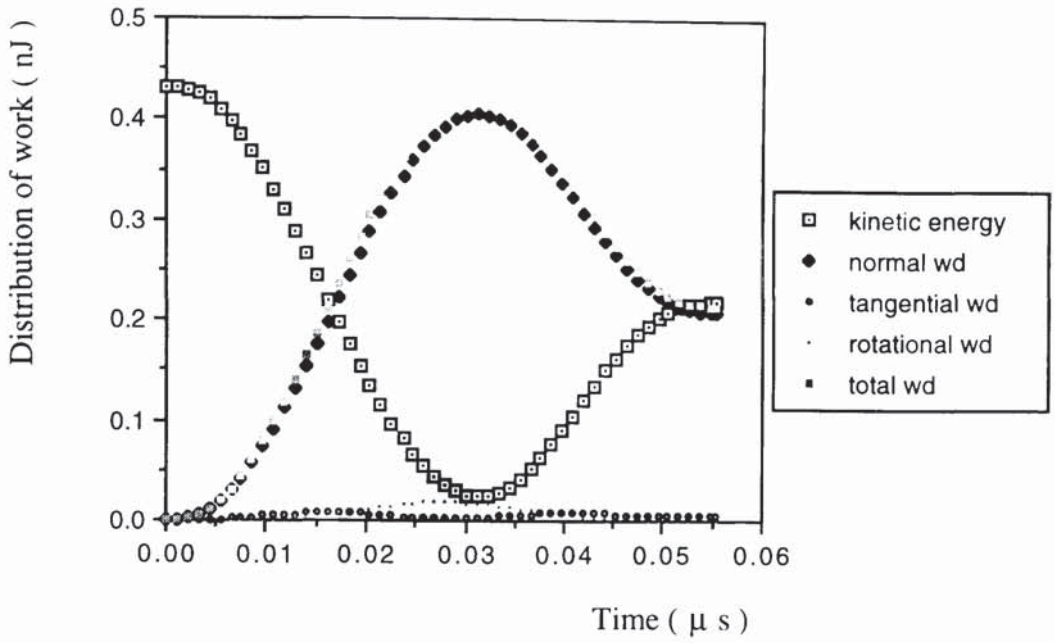

(b). Impact angle: 15°

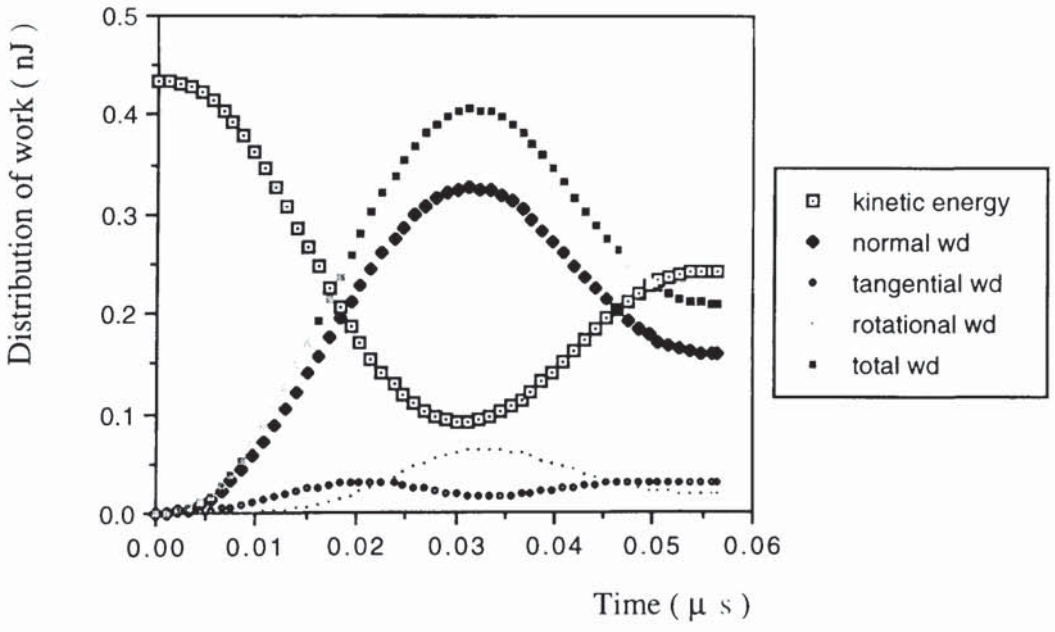

(c). Impact angle: 30°

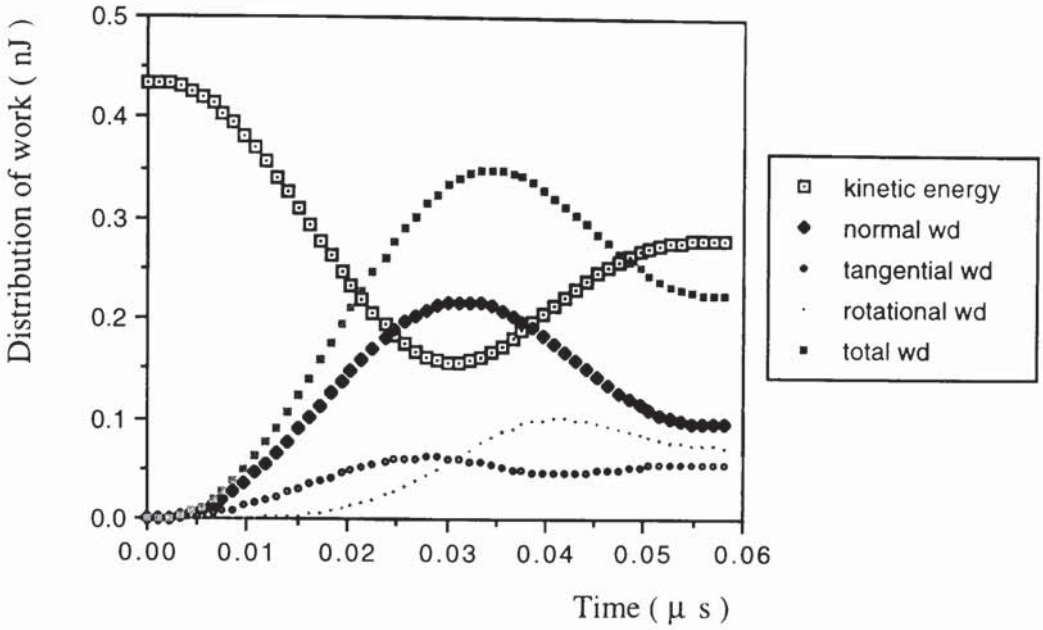

(d). Impact angle: 45°

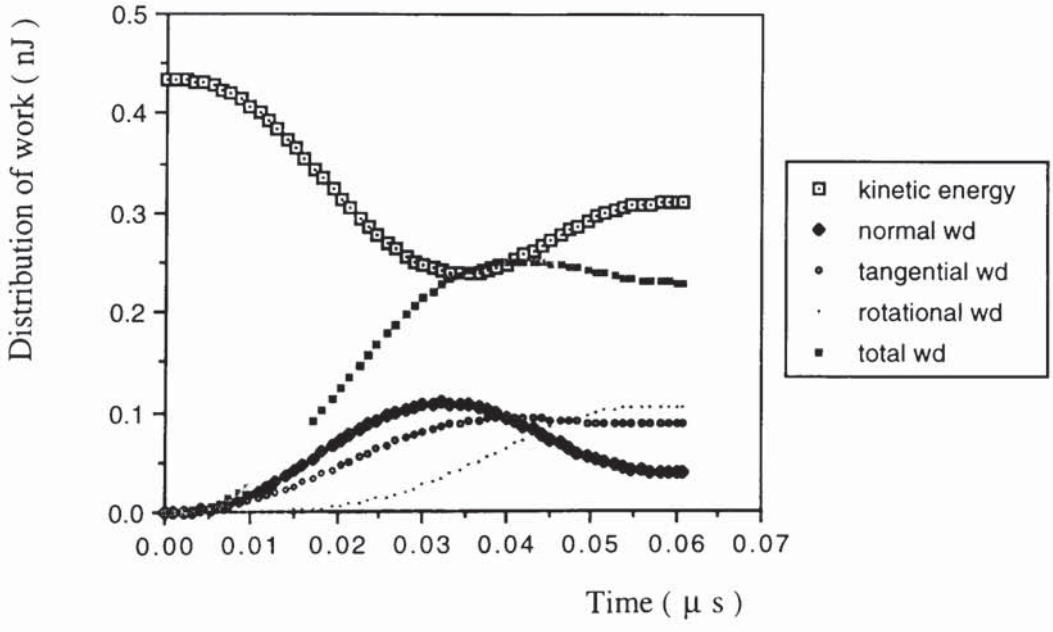

(e). Impact angle: 60°

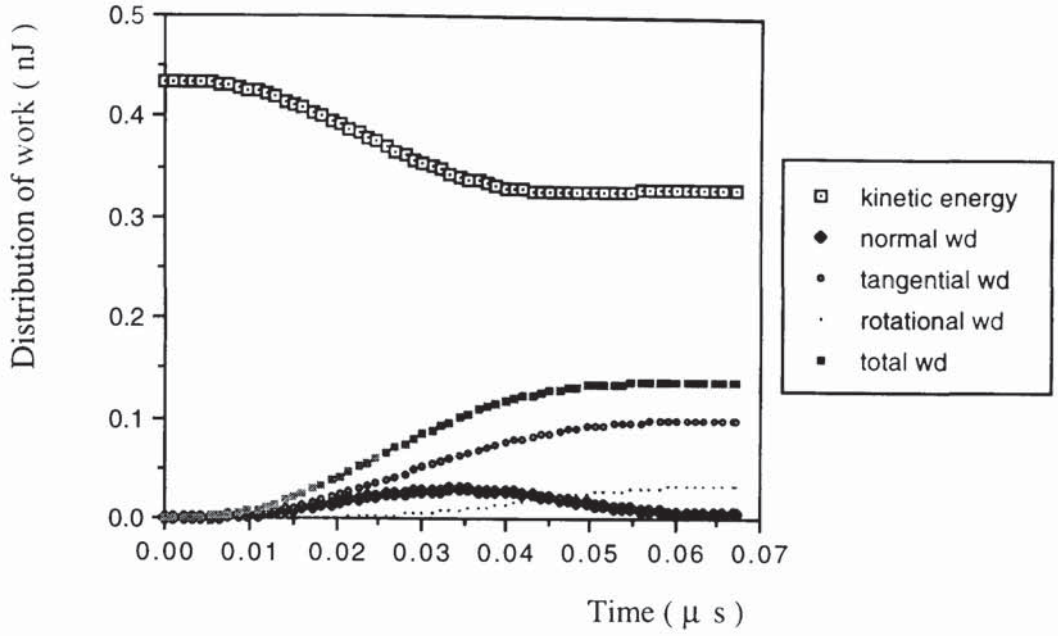

(f). Impact angle: 75°

Fig. 4.8 Distribution of energy and work done at an impact speed of 5.0 m/s for different impact angles.

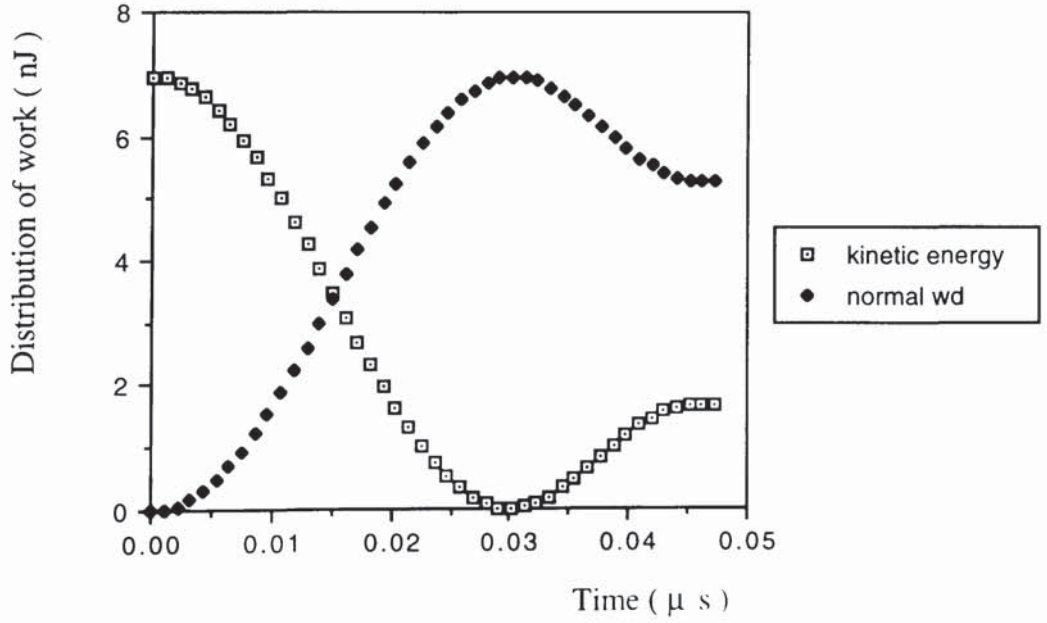

(a). Impact angle: 0° - normal impact

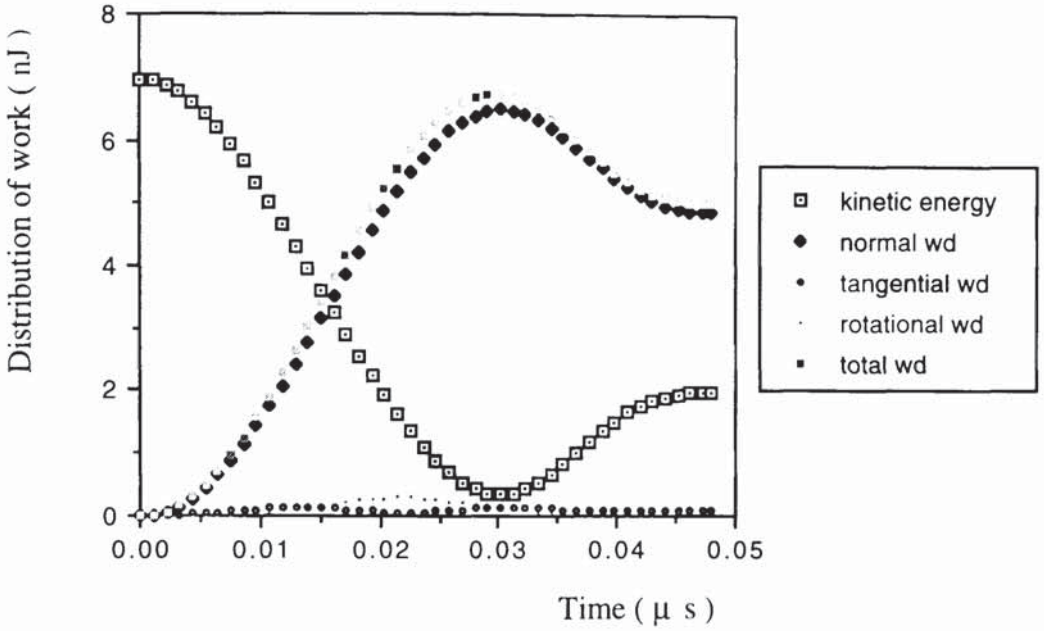

(b). Impact angle: 15°

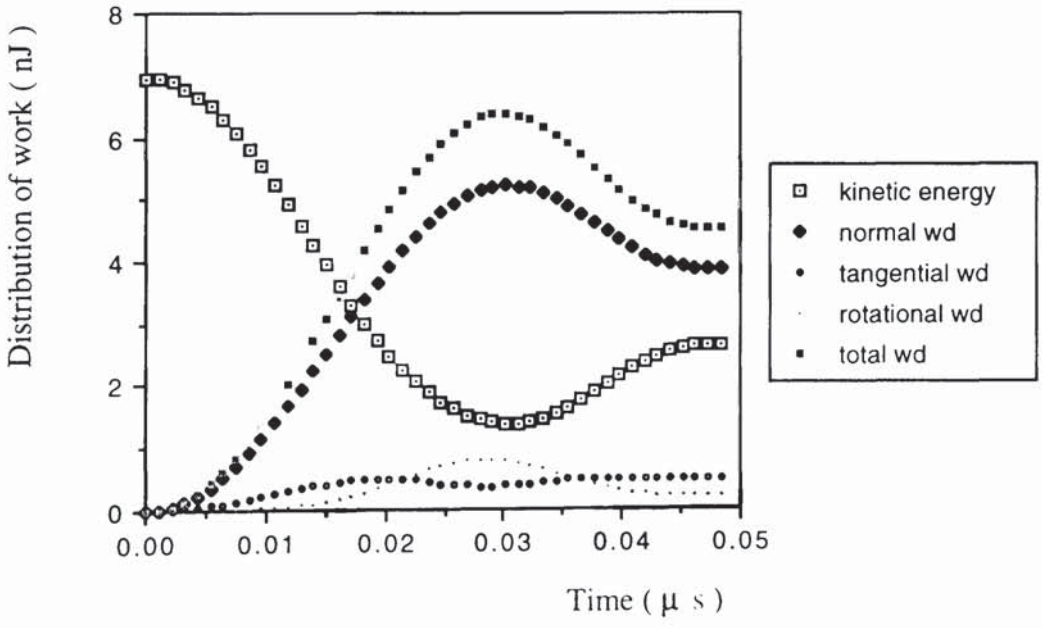

(c). Impact angle: 30°

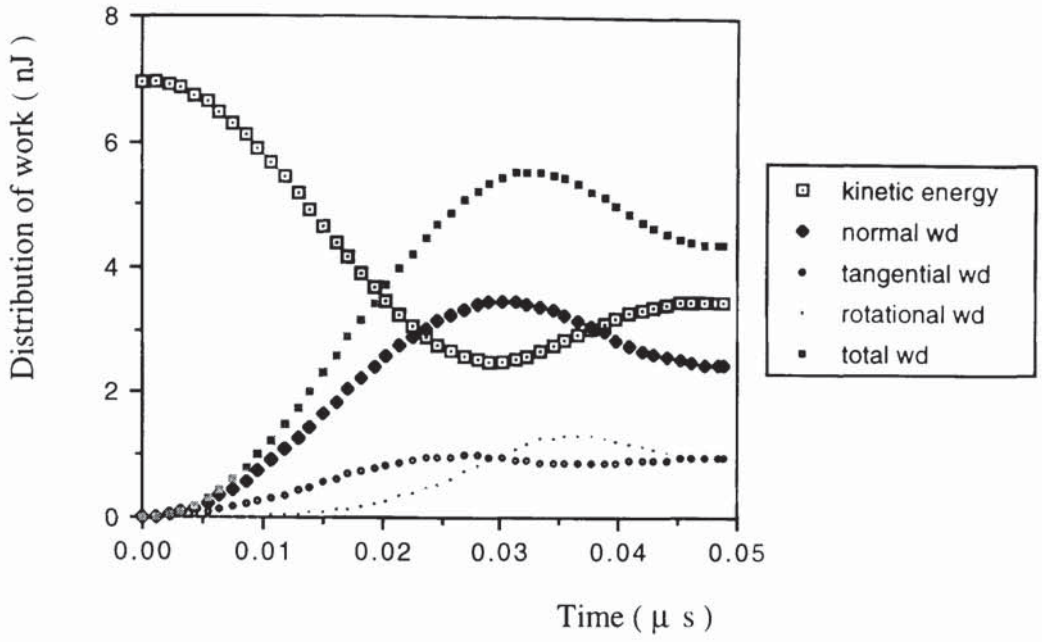

(d). Impact angle: 45°

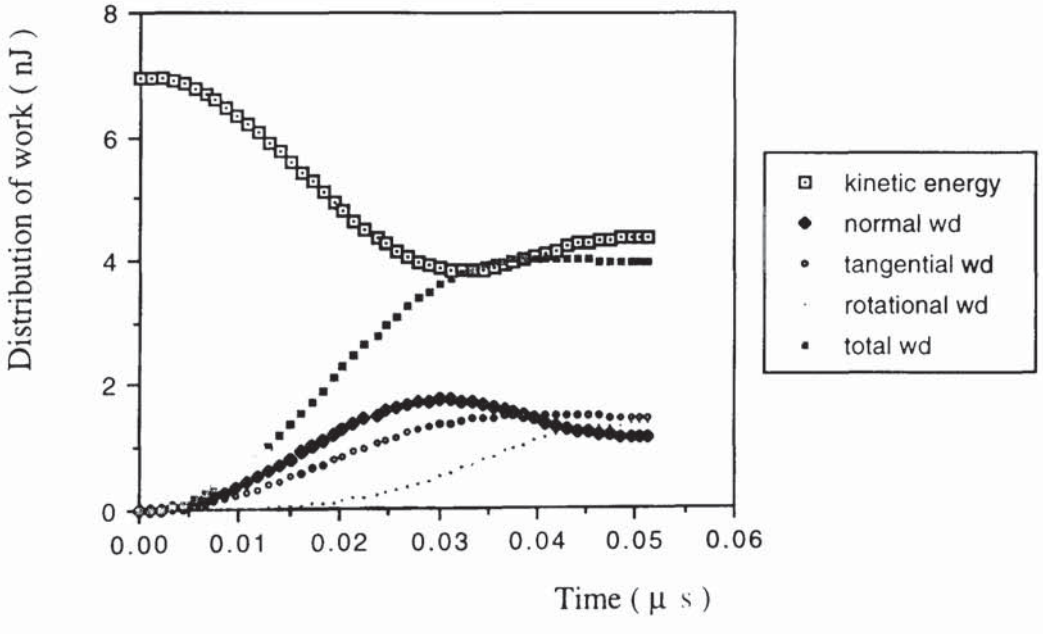

(e). Impact angle: 60°

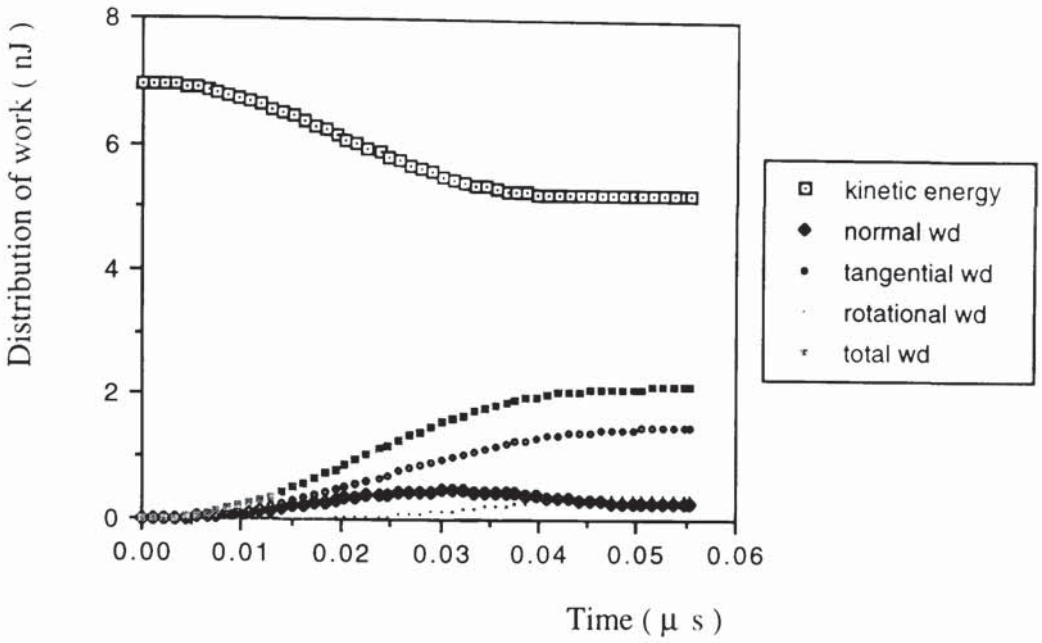

(f). Impact angle: 75°

Fig. 4.9 Distribution of energy and work done at an impact speed of 20.0 m/s for different impact angles.

As a result of an oblique impact there is a reduction in linear kinetic energy, a gain in rotational kinetic energy and energy is dissipated due to plastic deformation and friction. In Fig. 4.10 and 4.11 each of the three components of energy are expressed as a ratio of the initial kinetic energy and plotted against impact angle for collisions of a U_3O_8 particle to a steel wall with R = 10 μm, ν = 0.3 and μ = 0.35. Figure 4.10 shows the effect of impact angle for elastic collisions. The linear kinetic energy ratio reduces with impact angle until a minimum value of 0.53 is obtained at an impact angle θ = 60° and then increases to unity when θ = 90°. The rotational kinetic energy ratio increases with impact angle to a maximum of 0.28 at θ = 55° and then decreases to zero at θ = 90°. The ratio of energy dissipated also increases to a maximum value of 0.25 at θ = 70° and then reduces to zero at θ = 90°.

The effect of impact angle on the three energy ratios is shown in Fig. 4.11 for an impact speed of 5.0 m/s. For a normal impact the linear kinetic energy ratio is 0.48 since $V_m > V_y$

and, because there is no rotational kinetic energy developed, the ratio of energy dissipated is 0.52 and is entirely due to plastic deformation. As can be seen in the figure, the effect of impact angle on the rotational kinetic energy ratio is very similar to that obtained for the elastic impact, Fig. 4.10. The maximum occurs at the same impact angle, $\theta = 55°$, but is 0.25 which is slightly less than that for elastic impacts. The linear kinetic energy ratio increases slightly to a value of 0.52 at $\theta \approx 22°$ and then decreases to a minimum of 0.45 at $\theta = 55°$ before increasing to unity at $\theta = 90°$. The ratio of energy dissipated decreases to about 0.29 at $\theta = 55°$ and then is approximately constant in the range of $55° < \theta < 65°$ before reducing to zero at $\theta = 90°$. The shape of the dissipated energy ratio curve indicates a transition from plastic dissipation to frictional dissipation. It is important to note that, since the speed is constant for all simulations, there is a transition from elasto-plastic to elastic impact at $\theta = 83°$ and that in the range $0 < \theta < 83°$ the degree of plastic indentation reduces with an increase of impact angle.

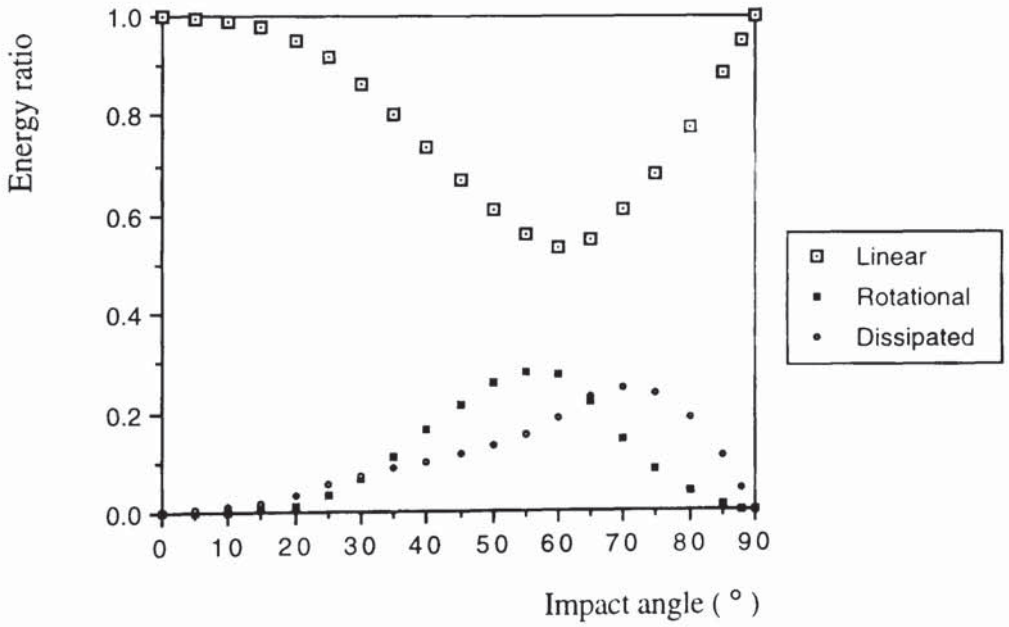

Fig. 4.10 Effect of impact angle on linear and rotational kinetic energies and energy dissipated at an impact speed of 0.5 m/s.

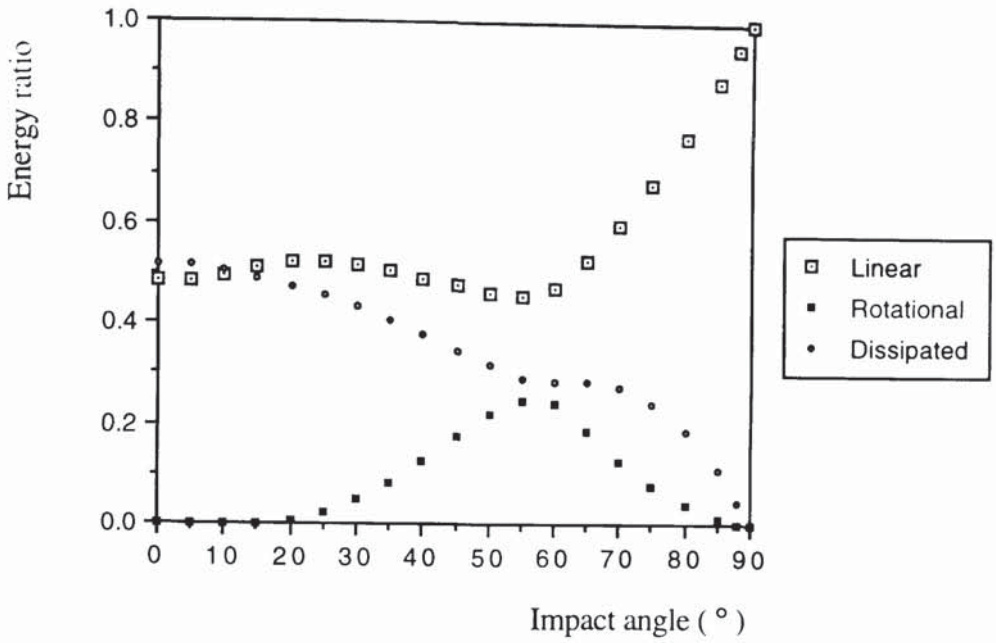

Fig. 4.11 Effect of impact angle on linear and rotational kinetic energies and energy dissipated at an impact speed of 5.0 m/s.

4.3 Coefficient of restitution and rebound angles

4.3.1 Theoretical considerations

According to Newton's laws of motion the normal and tangential impulses, F_n and F_t, developed at the contact patch are given by

$$F_n = m (V_{ni} - V_{nr}) \qquad (4.1)$$

$$F_t = m (V_{ti} - V_{tr}) \qquad (4.2)$$

and the rotational impulse is

$$F_\omega = mk^2 (\omega_i - \omega_r) \qquad (4.3)$$

where k is the radius of gyration of the solid; ω_i and ω_r are the initial and rebound rotational velocities respectively. If there is no initial particle rotation, $\omega_i = 0$, and

$$\omega_r = -\frac{F_t R}{mk^2} = -\frac{R\,(V_{ti} - V_{tr})}{k^2} \qquad (4.4)$$

In this case the normal approach and departure velocities of the local contact point are equal to the corresponding components of the particle centre. The tangential velocity of the contact point upon departure, v_{tr}, is given by

$$v_{tr} = V_{tr} + R\omega_r = V_{tr} - \frac{R^2\,(V_{ti} - V_{tr})}{k^2} \qquad (4.5)$$

For a solid sphere $R^2 / k^2 = 5/2$. Therefore, we have

$$v_{tr} = \frac{7}{2} V_{tr} - \frac{5}{2} V_{ti} = V_{ti}\left(\frac{7}{2}\frac{V_{tr}}{V_{ti}} - \frac{5}{2}\right) = V_{ti}\left(\frac{7}{2} e_t - \frac{5}{2}\right) \qquad (4.6)$$

where e_t is the tangential coefficient of restitution, defined as the ratio of the tangential departure velocity to the tangential approach velocity at the particle centre. Using the definition of the normal coefficient of restitution, $e_n = V_{nr} / V_{ni}$, we may rewrite (4.6) as

$$\frac{v_{tr}}{V_{nr}/e_n} = \frac{V_{ti}}{V_{ni}}\left(\frac{7}{2} e_t - \frac{5}{2}\right) \qquad (4.7)$$

from which

$$e_t = \frac{5}{7} + \frac{2}{7}\frac{e_n v_{tr}/V_{nr}}{V_{ti}/V_{ni}} = \frac{5}{7} + \frac{2}{7}\frac{e_n v_{tr}/v_{nr}}{V_{ti}/V_{ni}} = \frac{5}{7} + \frac{2}{7}\frac{e_n \tan\theta_{cr}}{\tan\theta} \qquad (4.8)$$

where $\theta_{cr} = \arctan\,(v_{tr} / v_{nr})$ is the reflection angle of the contact point which, as shown by Maw et al (1976, 1981), is dependent on the impact angle θ. The rebound rotational velocity is dependent on the initial tangential impact velocity as indicated by (4.4) which may be rewritten as

$$\frac{\omega_r}{V_{ti}} = -\frac{5\,(1 - e_t)}{2R} \qquad (4.9)$$

Finally the total coefficient of restitution, defined as the ratio of the rebound speed to the impact speed of the particle centre, is obtained from

$$e^2 = e_n^2 \cos^2\theta + e_t^2 \sin^2\theta \qquad (4.10)$$

and the rebound angle θ_r of the particle centre is given by

$$\frac{\tan\theta_r}{\tan\theta} = \frac{e_t}{e_n} \qquad (4.11)$$

Equations (4.8), (4.9), (4.10), (4.11) and (3.51) completely define the kinematics of the rebounding particle provided that e_t is known. To proceed further it is useful to introduce the two parameters suggested by Maw et al (1976, 1981)

$$\psi = \frac{\lambda}{\mu}\tan\theta \qquad (4.12)$$

$$\chi = \frac{\lambda}{2}\left(1 + \frac{R^2}{k^2}\right) \qquad (4.13)$$

where, for a sphere impacting a target of the same material,

$$\lambda = \frac{2(1-\nu)}{2-\nu} = \frac{4G^*}{E^*} \qquad (4.14)$$

and, since $R^2 / k^2 = 5/2$ for a solid sphere, we have

$$\chi = 7\lambda / 4 \qquad (4.15)$$

Consequently, we can rewrite (4.8) as

$$e_t = \frac{5}{7} + \frac{2}{7}\frac{e_n\psi_{cr}}{\psi_i} \qquad (4.16)$$

and rewrite (4.11) as

$$\psi_r = \frac{e_t}{e_n}\psi_i \qquad (4.17)$$

Therefore, it is necessary to understand how ψ_{cr} and ψ_r vary with ψ_i. Consider a special case, when contact sliding occurs throughout the whole impact process, we have $F_t = \mu F_n$. From (4.1) and (4.2) there results

$$V_{ti} - V_{tr} = \mu(V_{ni} - V_{nr}) \qquad (4.18)$$

or

$$e_t = 1 - \frac{\mu(V_{ni} - V_{nr})}{V_{ti}} = 1 - \frac{\mu(1 - V_{nr}/V_{ni})}{\tan\theta} \qquad (4.19)$$

The direction of V_{nr} is always opposite to that of V_{ni} and therefore we may rewrite (4.19) as

$$e_t = 1 - \frac{\mu(1 + e_n)}{\tan\theta} = 1 - \frac{(1 + e_n)}{\psi_i / \lambda} \qquad (4.20)$$

and for elastic impacts we have

$$e_t = 1 - \frac{2}{\psi_i / \lambda} \qquad (4.21)$$

which is only dependent on the coefficient of friction and impact angle.

4.3.2 Elastic impact

A series of simulations was performed to examine the effects of impact angle, coefficient of friction and Poisson's ratio on the particle rebound after collisions. In order to provide a comparison with the next section which deals with plastic deformation, the normal approach velocity was fixed for all angles of impact and to ensure elastic deformation during an impact a value of V_{ni} = 0.5 m/s was used. Figure 4.12 shows the effect of impact angle on the tangential coefficient of restitution for three values of friction coefficient μ. It is seen that there is a minimum coefficient of restitution which is independent of μ but the corresponding optimum angle increases with μ. Using the parameter ψ suggested by Maw et al (1976), e_t plotted against ψ_i is shown in Fig. 4.15. As can be clearly seen from the figure, the three curves merge into one in which the minimum tangential coefficient of restitution $e_{t,min}$ = 0.582 occurs at $\psi^*_i = 4\chi - 3 = 2.765$. With respect to (4.8), e_t is related to the local reflection angle θ_{cr} and the impact angle θ.

For μ = 0.35, ν = 0.3 and λ = 0.82353, computer simulation results suggest that $\theta_{cr} \approx$ 28.56° at an optimum impact angle θ^* = 49.6°. Using (4.8) this gives $e_{t,min}$ = 0.582, which is equal to that obtained by simulation. The relationship between the tangential coefficient of restitution and the impact angle may be approximated by

$$e_t = \begin{cases} 1 - (1 - e_{t,min}) \sin(\pi\theta / 2\theta^*) & \text{for} \quad 0 \le \theta \le \theta^* \\ 1 - (1 - e_{t,min}) \sin\left(\frac{\pi}{2}\left(\frac{\pi}{2} - \theta\right) / \left(\frac{\pi}{2} - \theta^*\right)\right) & \text{for} \quad \theta^* \le \theta \le \frac{\pi}{2} \end{cases} \qquad (4.22)$$

The comparison between the predictions given by (4.22) and the computer simulation results for $\mu = 0.35$ and $\nu = 0.3$ is shown in Fig. 4.19. It is seen that Equation (4.22) can provide a good fit to the computer simulated data for the parameters used. It should be noted that for low and high values of friction, for example, $\mu = 0.1$ and $\mu = 0.8$, the curve fitting is not satisfactory and that other mathematical functions need to be considered.

The rebound angle of the particle centre plotted against impact angle is shown in Fig. 4.13, which demonstrates that under all circumstances the rebound angle is equal or less than the impact angle. The normalised data using the parameter ψ is shown in Fig. 4.16. Variations of the reflection angle at the contact point with impact angle and friction are shown in Fig. 4.14. The unified data of ψ_{cr} against ψ_i is shown in Fig. 4.17, which is in agreement with Fig. 2.4 provided by Maw et al (1976, 1981). The condition governing initial contact sliding at the start of the impact is $\psi_i \ge 1.0$ according to Maw et al (1976). However, it is apparent from Fig. 4.17 that when $\psi_i \ge 1/\lambda$ contact sliding initiates at the start of the impact and this indicates that the corresponding initial sliding angle is larger than that suggested by Maw et al (1976) due to the effect of Poisson's ratio. It is clear that the parameter ψ normalises the data in terms of friction. The effect of Poisson's ratio on elastic impacts, which Maw et al (1976, 1981) did not take into account, needs further clarification.

Figure 4.20 shows the variations of reflection angle of the contact patch for different values of Poisson's ratio. It is seen that when the impact angle is larger than a critical value, at which contact sliding occurs throughout the impact process, there is no effect of Poisson's ratio. It is also seen that the impact angle corresponding to initial sliding at the start of the impact decreases with an increase of ν, which corresponds to a decrease in λ. The effect of ν

on the rebound angle of the particle centre is shown in Fig. 4.21. The tangential coefficient of restitution is plotted against impact angle for different values of ν in Fig. 4.22. If the impact angle is less than the angle which produces sliding throughout the impact, it can be seen that the tangential coefficient of restitution depends on the value of ν. The minimum value of e_t decreases with an increase in ν. The normalised reflection angle ψ_{cr}, ratio ψ_{cr}/ψ_i, and e_t plotted against the normalised impact angle ψ_i are shown in Figs. 4.23, 4.24, and 4.25 respectively. The proportional relationship between ψ_{cr}/ψ_i and e_t is clearly illustrated in the figures and is in agreement with (4.16). The trend of ψ_{cr} at small impact angles is emphasised in Fig. 4.26 by replotting Fig. 4.23. It is seen that for all values of Poisson's ratio, ψ_{cr} is approaching zero when ψ_i is reduced to zero. A numerical problem therefore arises since, according to (4.16), e_t is indeterminate due to the fact that the second term involves a zero divided by a zero. Further simulation results indicates that for any value of Poisson's ratio e_t and ψ_{cr}/ψ_i are approaching unity as $\psi_i \rightarrow 0$.

From Figs. 4.23, 4.24 and 4.25, it is also seen that by using ψ the data for high impact angles becomes scattered due to the change of ν. To unify the data, an alternative way according to (4.21) is to use ψ_i / λ rather than ψ_i. Figures 4.27, 4.28 and 4.29 show the variations of ψ_{cr} / λ, ψ_{cr} / ψ_i and e_t with ψ_i / λ respectively and all the data is unified if the sliding condition exists during the whole process of the impact. It is therefore concluded that, for elastic impacts, the tangential bouncing behaviour can be predicted when $\psi_i \geq 6\lambda$ at which contact sliding occurs throughout the impact, while the pattern of the tangential coefficient of restitution for other impact angles varies with the material properties and needs further investigation.

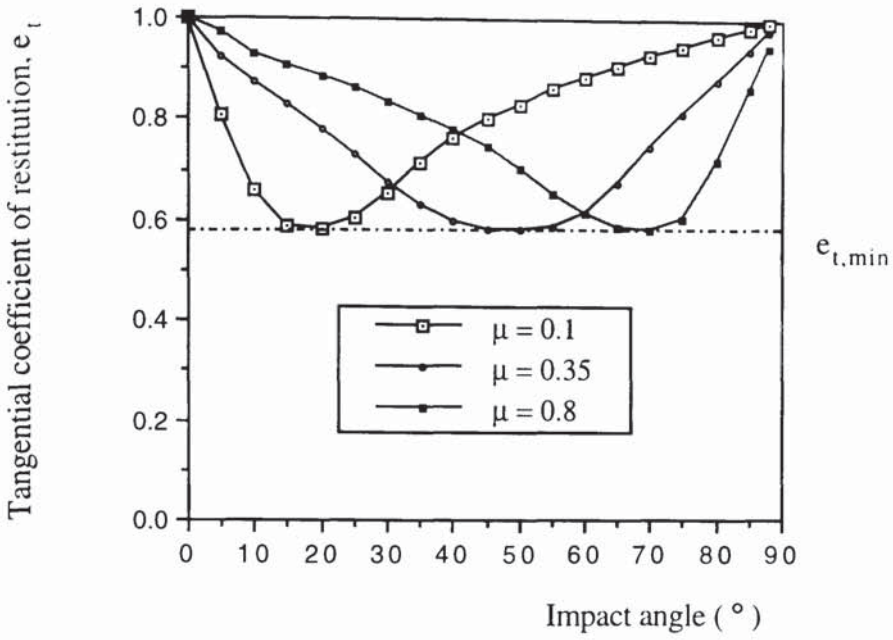

Fig. 4.12 Tangential coefficient of restitution against impact angle.

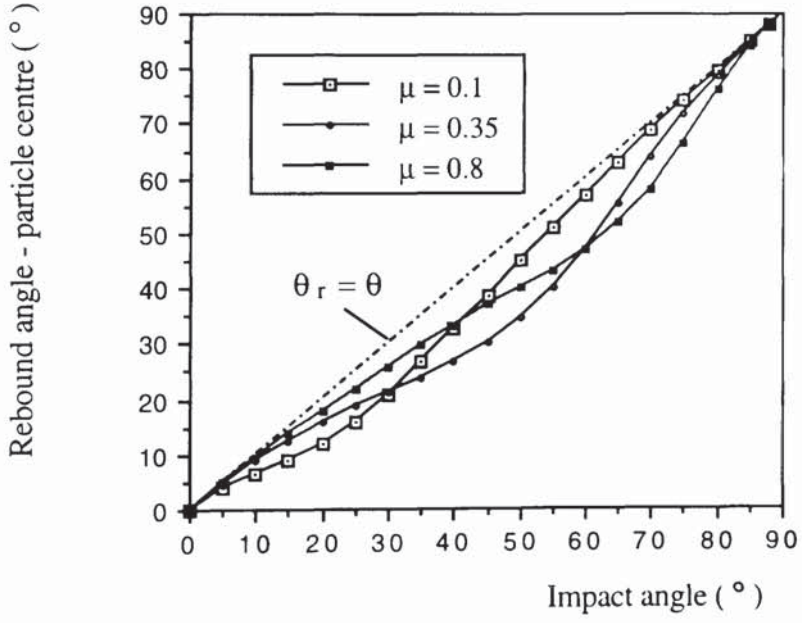

Fig. 4.13 Rebound angle of the particle centre against impact angle.

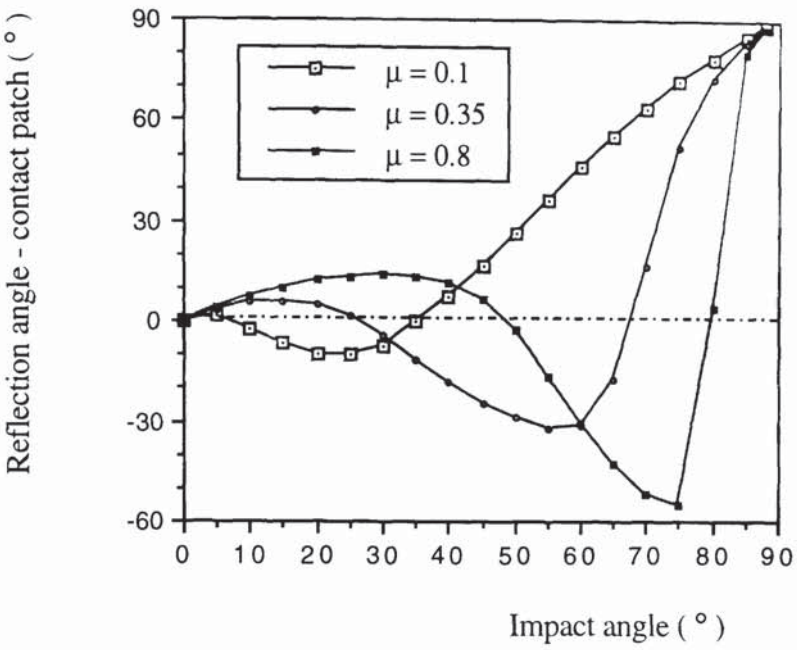

Fig. 4.14 Reflection angle of the contact patch against impact angle.

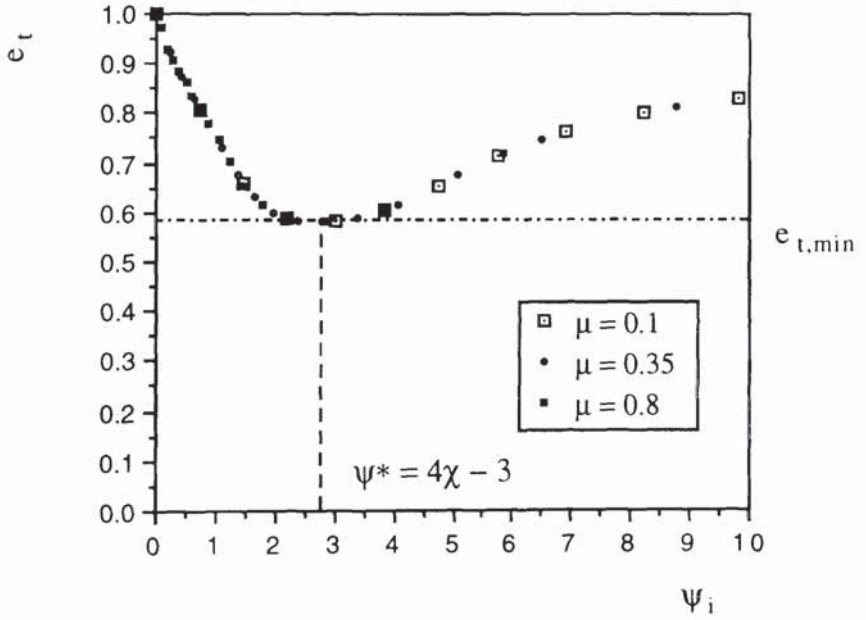

Fig. 4.15 Tangential coefficient of restitution against nondimensional impact angle.

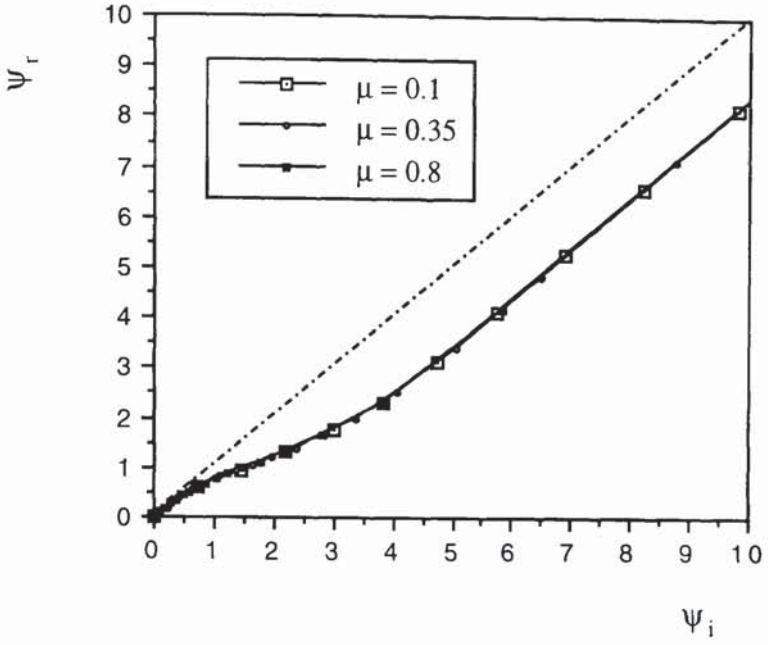

Fig. 4.16 Nondimensional rebound angle of the particle centre against nondimensional impact angle.

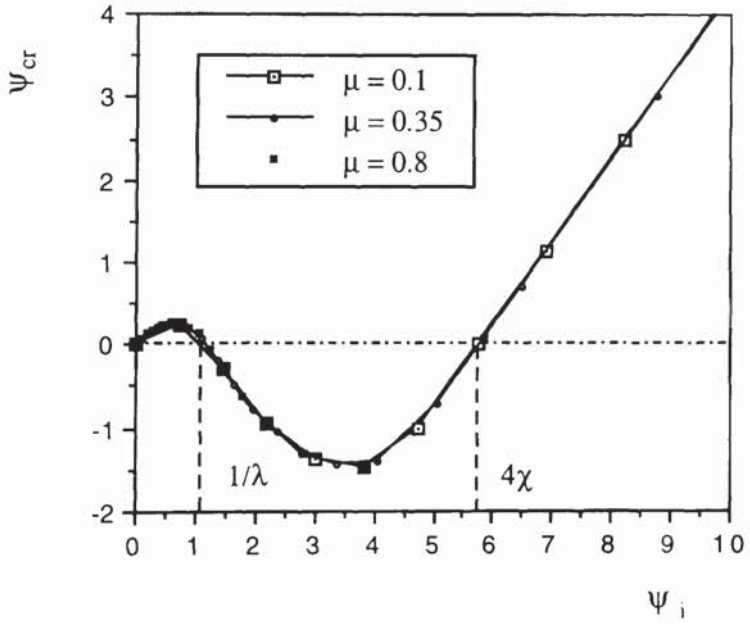

Fig. 4.17 Nondimensional reflection angle of the contact patch against nondimensional impact angle.

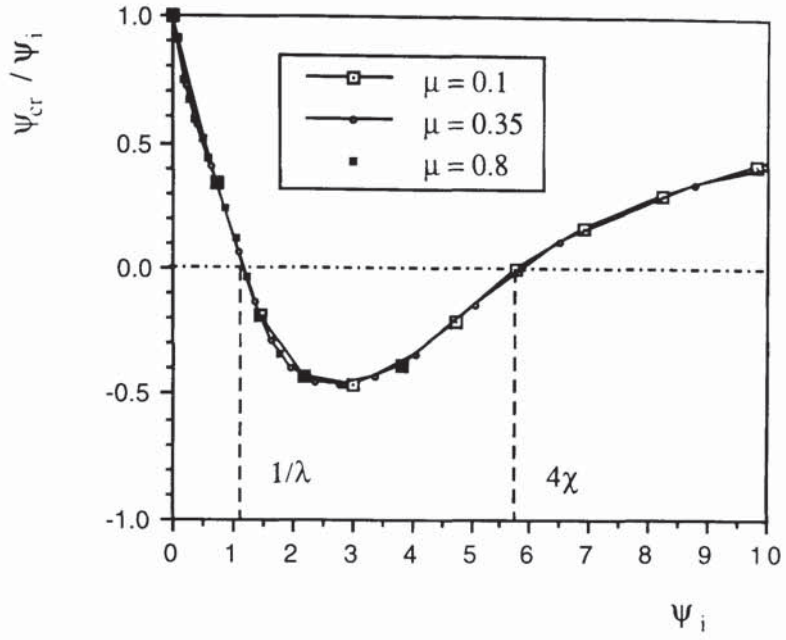

Fig. 4.18 Nondimensional reflection angle ratio against nondimensional impact angle.

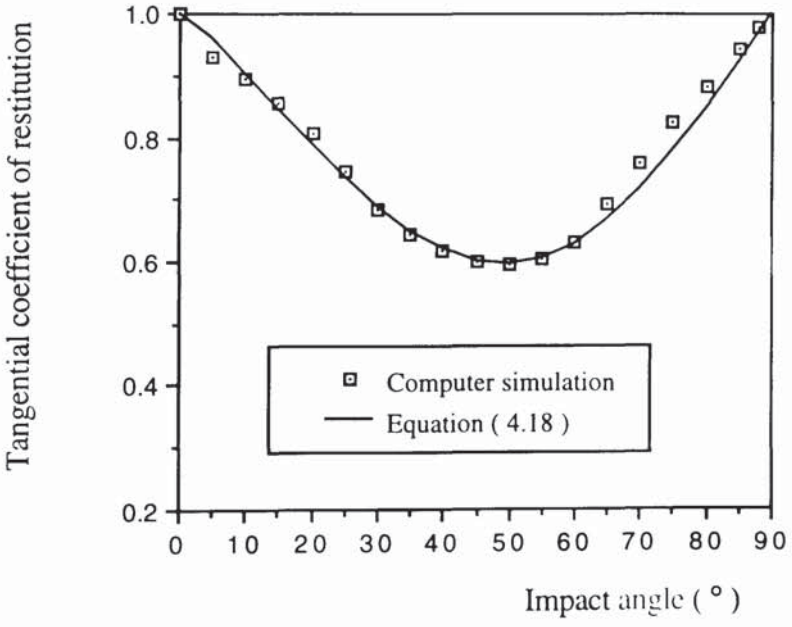

Fig. 4.19 Computer simulated tangential coefficient of restitution compared with the predictions by (4.22) with properties μ = 0.35 and ν = 0.3.

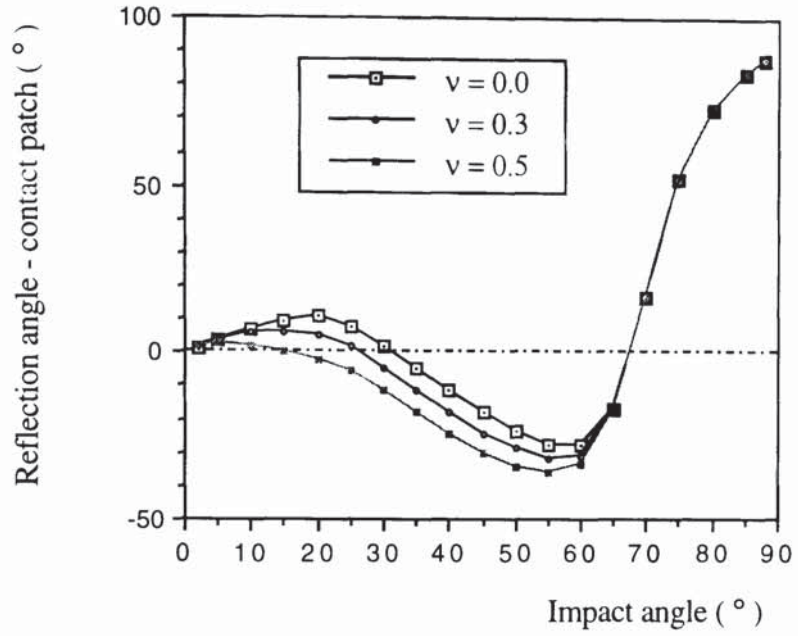

Fig. 4.20 Reflection angle of the contact patch against impact angle for different values of Poisson's ratio.

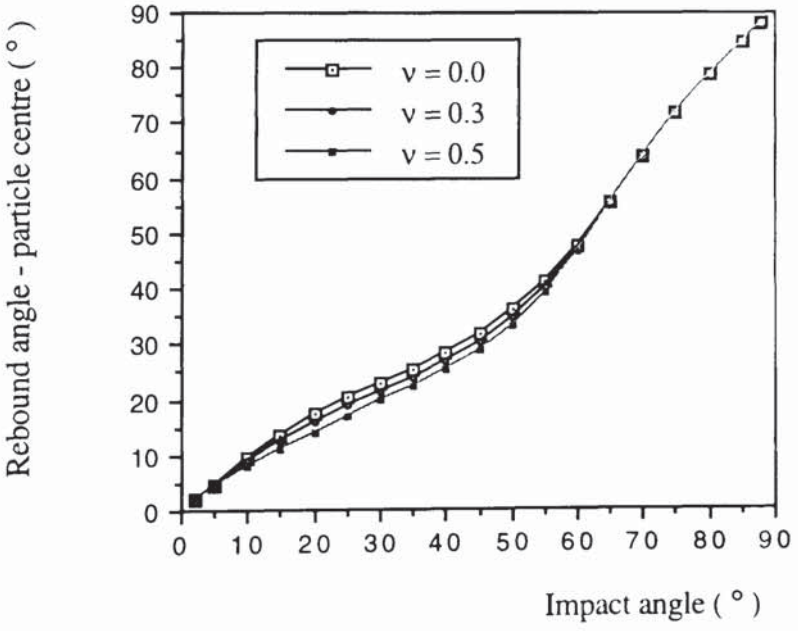

Fig. 4.21 Rebound angle of the particle centre against impact angle for different values of Poisson's ratio.

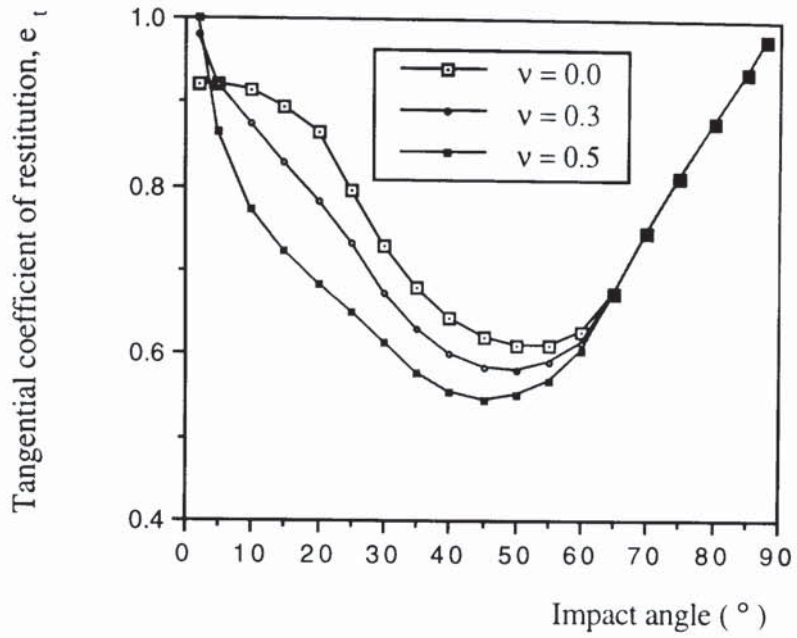

Fig. 4.22 Tangential coefficient of restitution against impact angle for different values of Poisson's ratio.

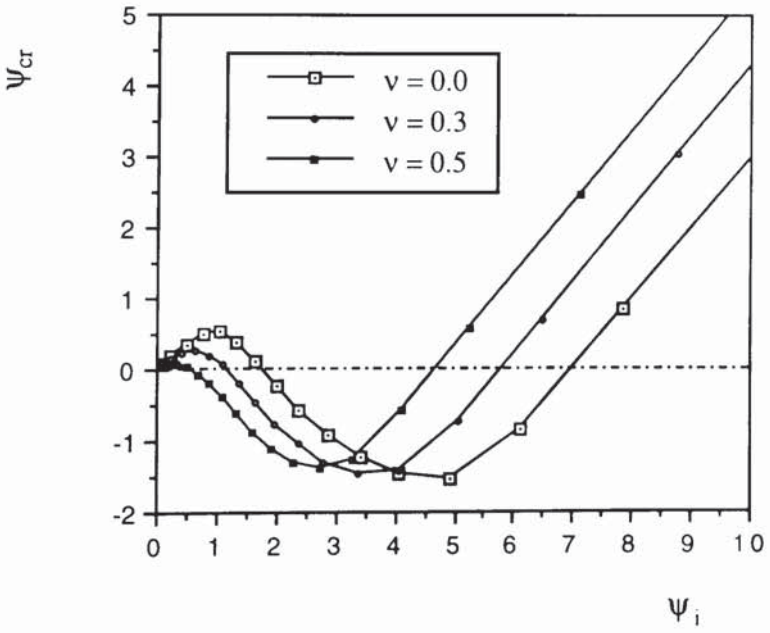

Fig. 4.23 Nondimensional reflection angle of the contact patch against nondimensional impact angle for different values of Poisson's ratio.

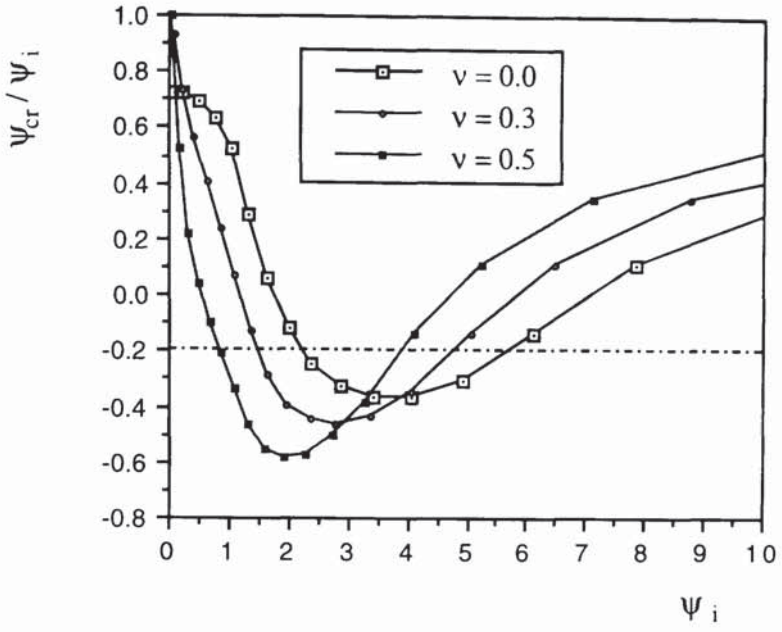

Fig. 4.24 Nondimensional reflection angle ratio against nondimensional impact angle for different values of Poisson's ratio.

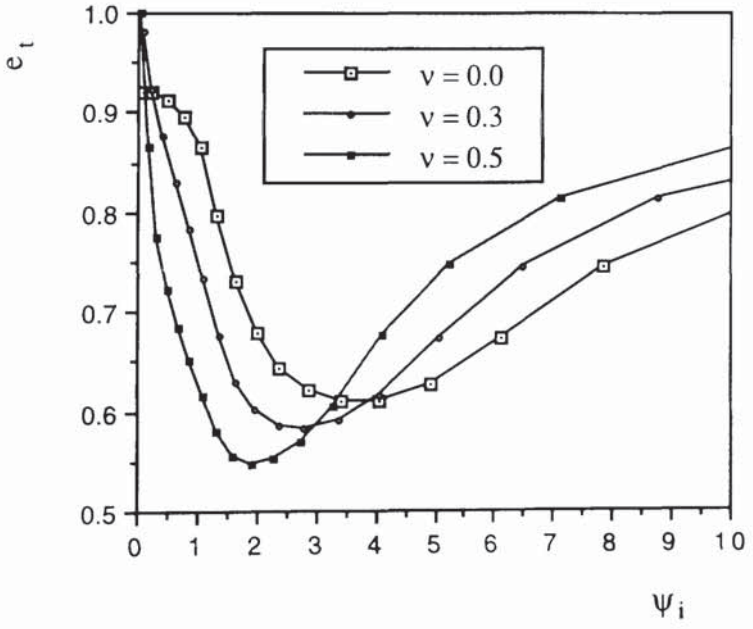

Fig. 4.25 Tangential coefficient of restitution against nondimensional impact angle for different values of Poisson's ratio.

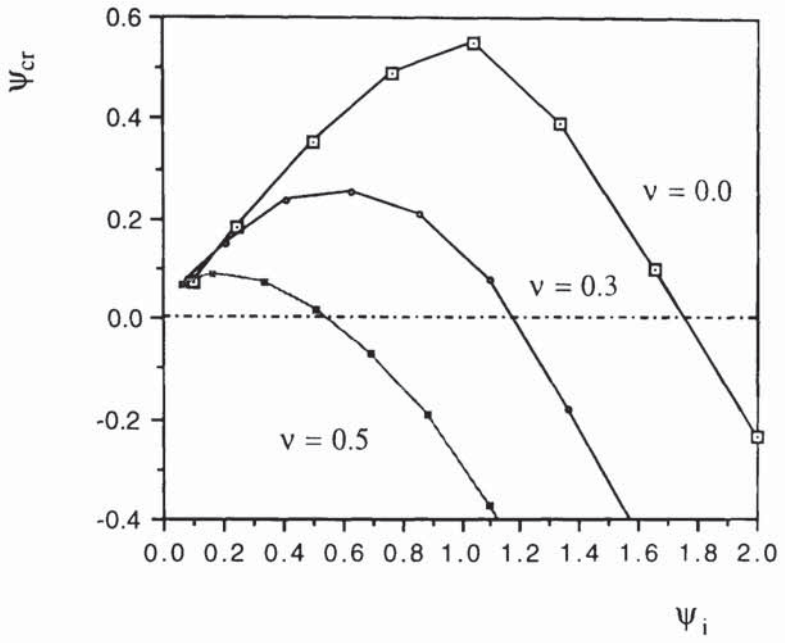

Fig. 4.26 Replot of Fig. 4.23 to emphasis the trend of ψ_{cr} at small impact angles.

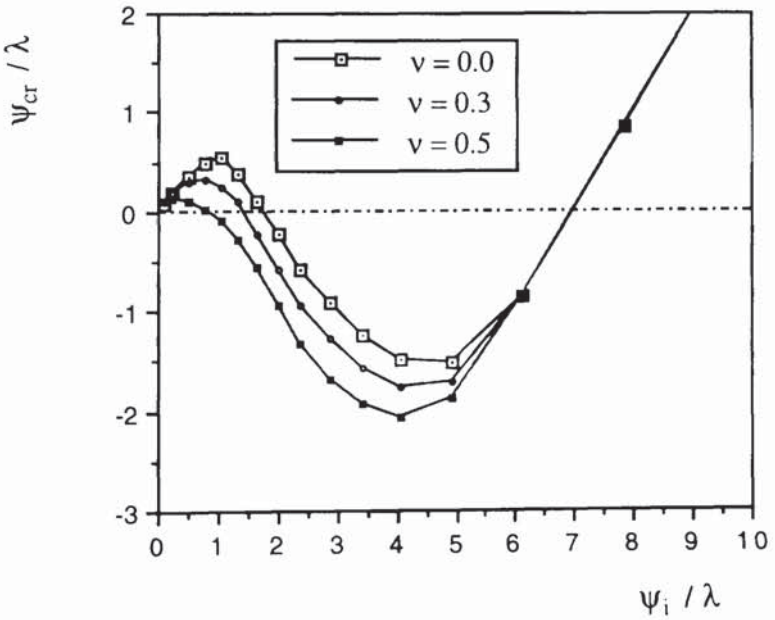

Fig. 4.27 Nondimensional reflection angle of the contact patch against nondimensional impact angle.

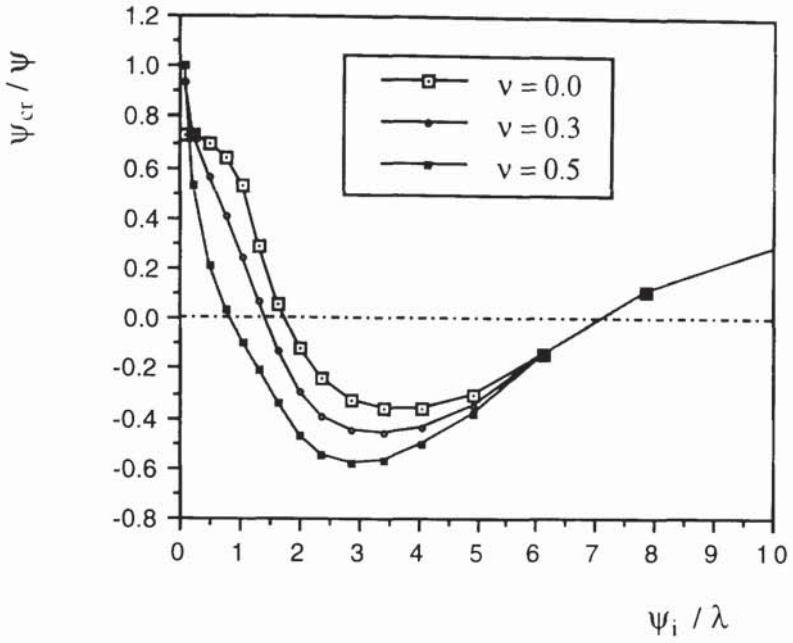

Fig. 4.28 Nondimensional reflection angle ratio against nondimensional impact angle for different values of Poisson's ratio.

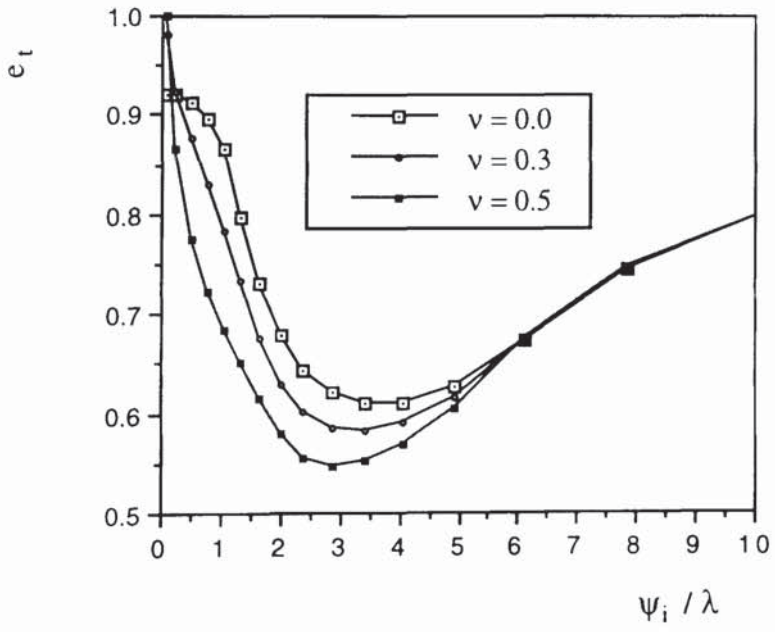

Fig. 4.29 Tangential coefficient of restitution against nondimensional impact angle for different values of Poisson's ratio.

4.3.3 Elasto-plastic impact

Computer simulations were performed to investigate oblique collisional behaviour for impact velocities above the yield velocity. From oblique impact simulations using constant impact speeds it was demonstrated that, as shown in Fig. 4.30, the impact angle has no effect on the normal interactions and the normal departure velocity is determined by the normal approach velocity. However, as indicated by (4.16), the tangential coefficient of restitution is dependent on the severity of plastic indentation. In order to exclude variations due to this effect, the normal approach velocity was kept constant for each set of simulation tests in which the impact angle was varied from zero to a value close to 90°. Four different normal approach velocities (V_{ni} = 5.0, 10.0, 20.0 and 100.0 m/s) were used corresponding to a range of values for the normal coefficient of restitution (e_n = 0.694, 0.588, 0.496 and 0.332). The results are compared with those of elastic impacts using a normal approach velocity of 0.5 m/s.

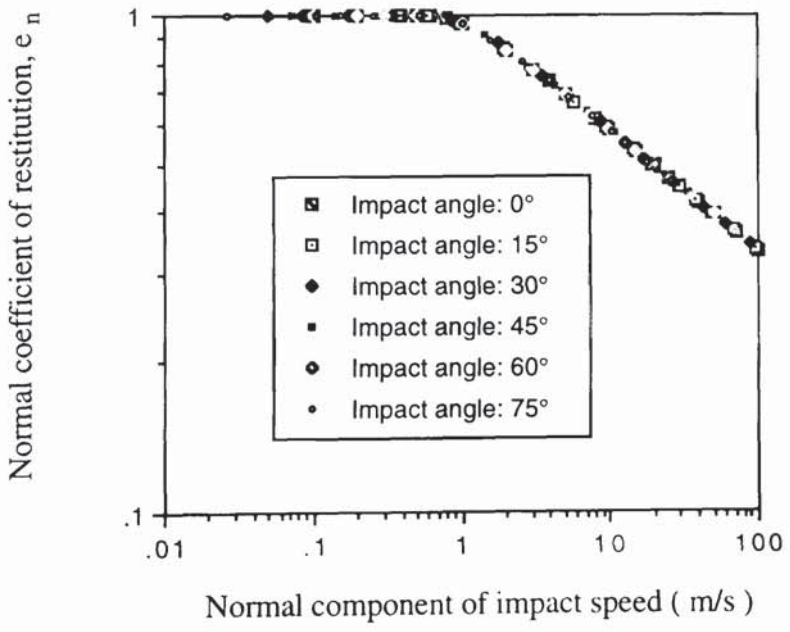

Fig. 4.30 Normal coefficient of restitution against normal approach velocity.

The effect of plastic deformation on the reflection angle of the contact patch is shown in Fig. 4.31. It is seen that, for the range $0.5 \leq V_{ni} \leq 20.0$ m/s ($e_n \geq 0.5$), the variation of

reflection angle with impact angle is similar to that obtained for elastic impacts but the transition from forward to backward motion occurs at a higher impact angle with an increase in plastic deformation. However, the results obtained from V_{ni} = 100 m/s show that at very high impact velocities and low impact angles the contact patch rebounds backwards. It is also seen from the figure that the reflection angle is equal to the impact angle when $\theta = 0°$ and 90° and there is a unique minimum value which does not depend on the normal approach velocity. Figure 4.32 shows the variations of the rebound angle of the particle centre with the impact angle. The results show that, due to plastic deformation, the rebound angle can be larger than the impact angle, a behaviour which is supported by the experimental results (Brauer, 1980).

The tangential coefficient of restitution plotted against impact angle is shown in Fig. 4.33 in which the minimum value of e_t increases with an increase of the impact velocity but the corresponding impact angle is not affected. The minimum value of e_t corresponds to the value of the reflection angle which is not affected by the normal approach velocity (see Fig. 4.31). For ν = 0.3, computer simulation suggests that θ_{cr} = -28.56° at θ^* = 49.6°. Therefore, using (4.8) we obtain

$$e_{t,min} = \frac{5}{7} - \frac{0.926\, e_n}{7} \qquad (4.23)$$

which confirms the trend shown in Fig. 4.33. The figure also shows that as $\theta \rightarrow 90°$, e_t = 1.0. However, an uncertainty exists for e_t at θ = 0 since both $\tan\theta_{cr}$ and $\tan\theta$ are approaching zero. Although further computer simulation results have clearly indicated that as $\theta \rightarrow 0$, e_t = 1.0, there is an abrupt change in the tangential coefficient of restitution at very small impact angles when plastic deformation occurs.

As discussed in Section 4.3.2, for elastic impacts the tangential coefficient of restitution is proportional to the ratio of ψ_{cr}/ψ_i since e_n = 1.0. When plastic deformation occurs, (4.16) indicates that the relevant parameter is $e_n\psi_{cr}/\psi_i$. Therefore, in agreement with Stronge (1994a), for oblique elasto-plastic impacts we examine the variation of

$$\frac{e_n \psi_{cr}}{\lambda} = \frac{e_n \tan\theta_{cr}}{\mu} = \frac{v_{tr}}{\mu V_{ni}} \qquad (4.24)$$

with

$$\frac{\psi_i}{\lambda} = \frac{\tan\theta}{\mu} = \frac{v_{ti}}{\mu V_{ni}} \qquad (4.25)$$

as shown in Fig. 4.34. The results may be compared with the predictions of Stronge (1994a) which are shown in Fig. 4.35. It can be seen that, if sliding occurs throughout the impact, there is an agreement between the two sets of predictions. However, if sliding only occurs over part of the impact duration the results of the computer simulated impacts are significantly different from the predictions of Stronge (1994a) who used linear compliance relationships for both normal and tangential interactions. The effect of the normal coefficient of restitution illustrated by the computer simulated results suggests that in the extreme case of $e_n = 0$, as shown in Fig. 4.34,

$$\frac{e_n \psi_{cr}}{\lambda} = 0 \qquad \text{for} \qquad 0 \le \frac{\psi_i}{\lambda} \le 3.5 \qquad (4.26)$$

$$\frac{e_n \psi_{cr}}{\lambda} = \frac{\psi_i}{\lambda} - 3.5 \qquad \text{for} \qquad \frac{\psi_i}{\lambda} \ge 3.5 \qquad (4.27)$$

and that sliding occurs throughout the whole impact process if $\psi_i/\lambda \ge 3.5$. Further examination of the data indicates that, for the general case, gross sliding occurs if

$$\frac{2\psi_i}{(1+e_n)\lambda} \ge 7 - e_n \qquad (4.28)$$

or

$$\tan\theta \ge \frac{\mu(1+e_n)}{2}(7-e_n) \qquad (4.29)$$

Therefore, if sliding occurs throughout the impact, the data shown in Fig. 4.34 is normalised by multiplying both axes by $2/(1+e_n)$, as illustrated in Fig. 4.36. Figure 4.37 shows the tangential coefficient of restitution plotted against the normalising parameter $2\psi_i/\lambda(1+e_n)$ and it can be seen that if (4.28) is not satisfied the data are significantly dependent on the normal coefficient of restitution.

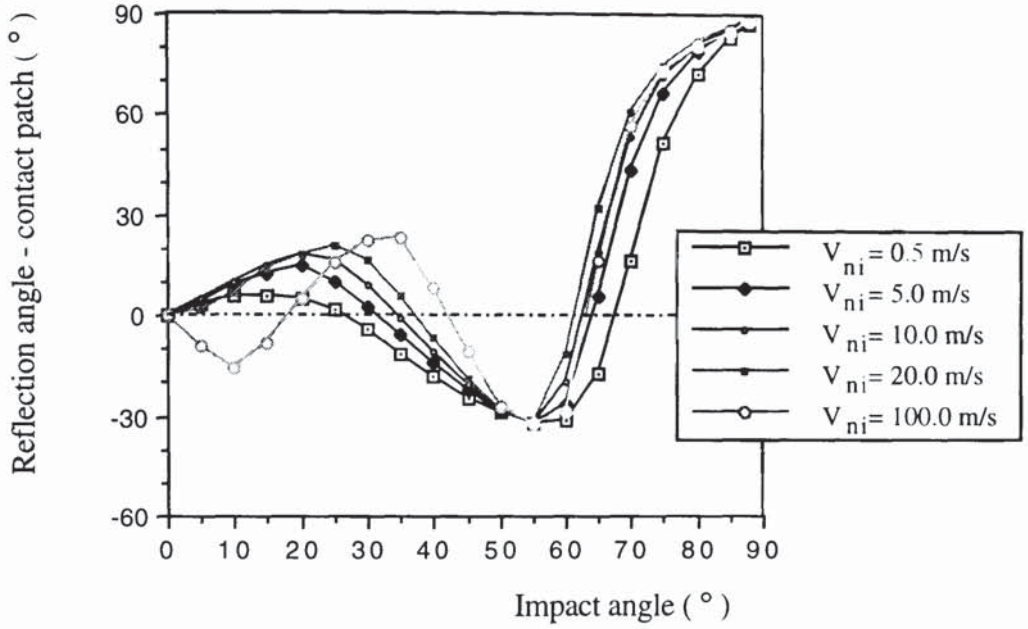

Fig. 4.31 Reflection angle of the contact patch against impact angle for different normal approach velocities.

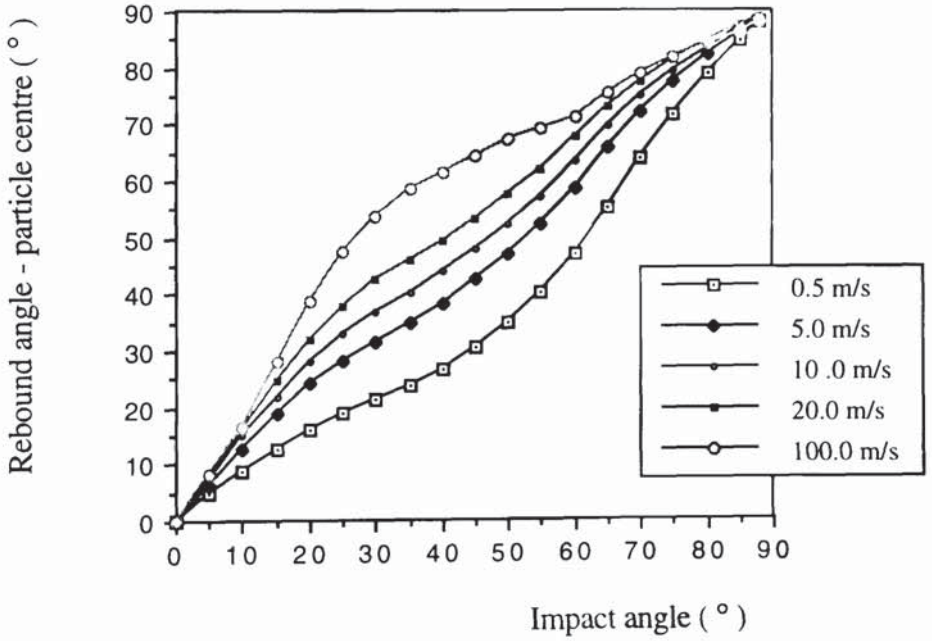

Fig. 4.32 Rebound angle of the particle centre against impact angle for different normal approach velocities.

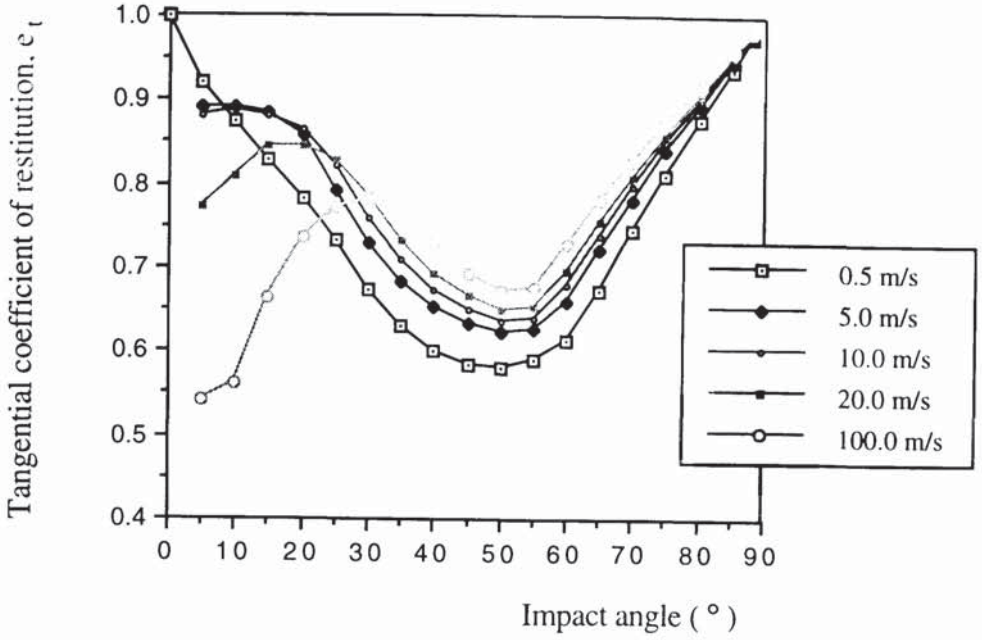

Fig. 4.33 Tangential coefficient of restitution against impact angle for different normal approach velocities.

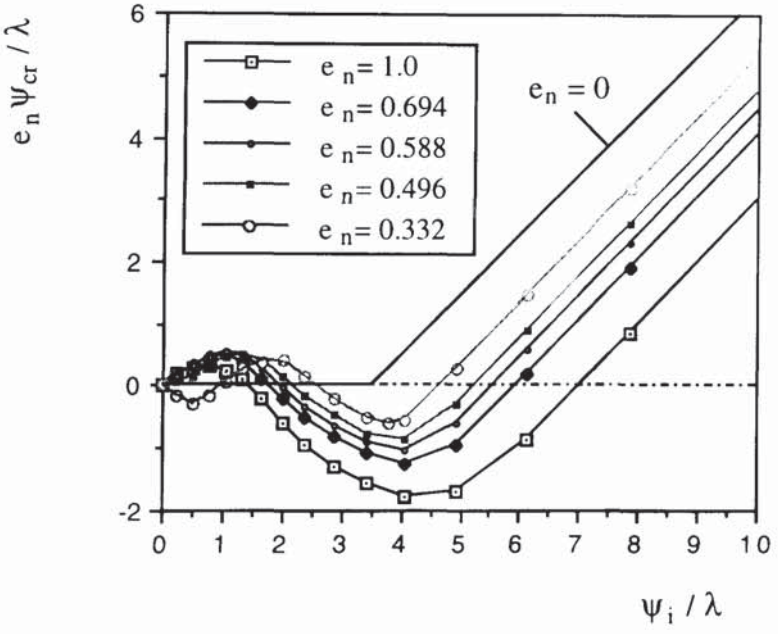

Fig. 4.34 Nondimensional reflection angle against nondimensional impact angle - effect of normal coefficient of restitution.

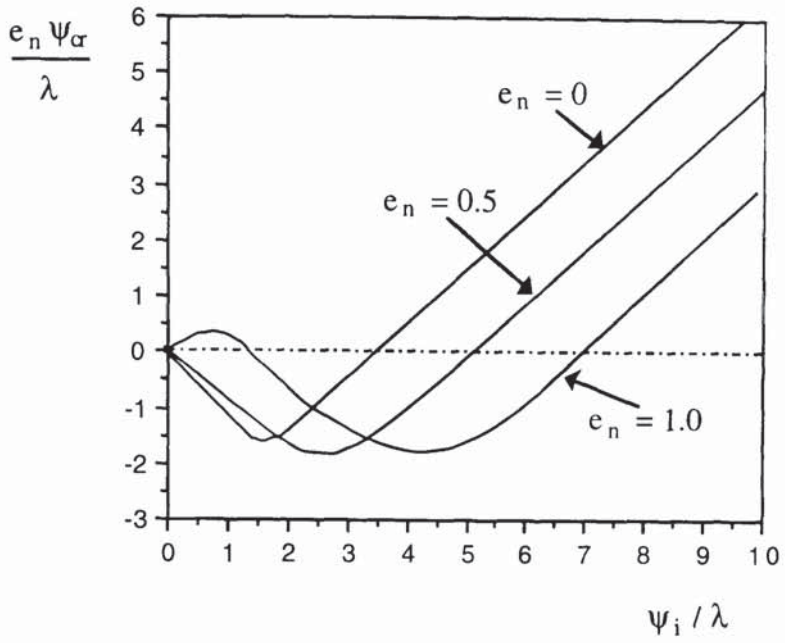

Fig. 4.35 Nondimensional reflection angle against nondimensional impact angle (Stronge, 1994a).

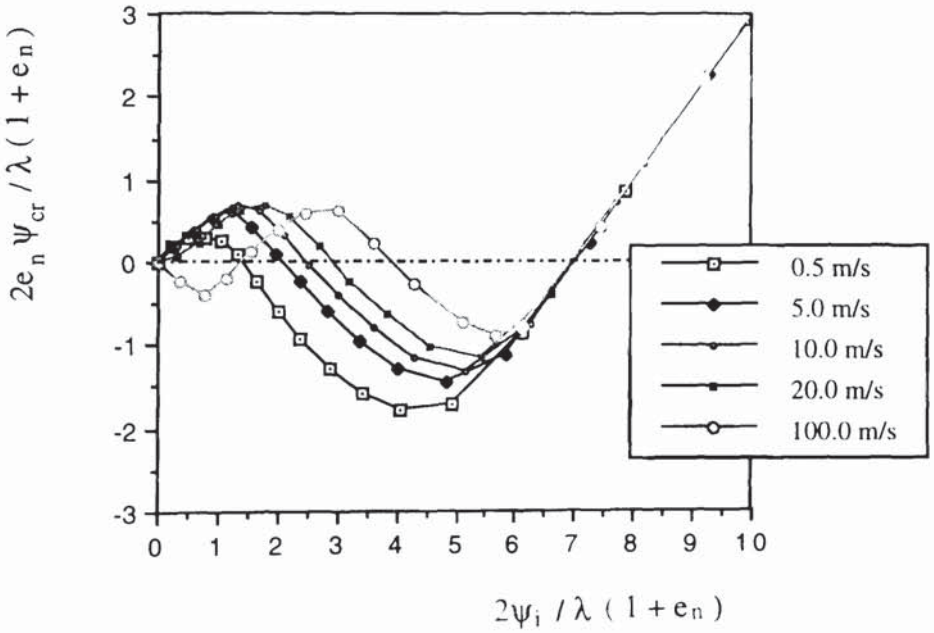

Fig. 4.36 Nondimensional reflection angle against nondimensional impact angle for different normal approach velocities.

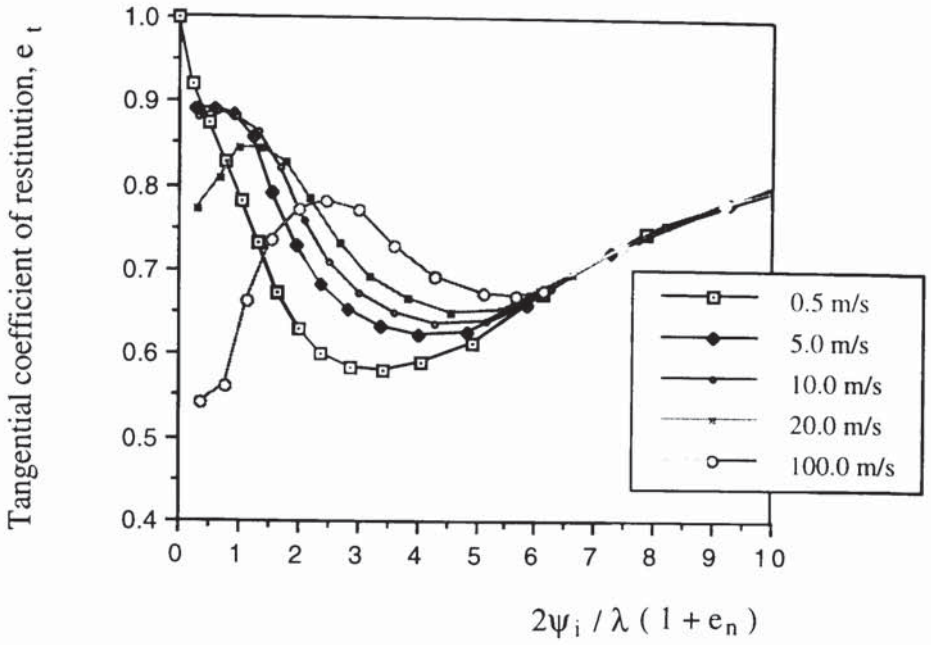

Fig. 4.37 Tangential coefficient of restitution against nondimensional impact angle for different normal approach velocities.

4.3.4 Oblique impacts at a constant impact speed

To measure the particle rebound from a target surface, constant impact speeds are normally used in real experiments rather than a constant normal approach velocity. Figures 4.38, 4.39 and 4.40 show the coefficients of restitution e_n, e_t, and e for different impact angles at impact speeds of 5, 10, and 20 m/s respectively. It is seen that the normal coefficient of restitution increases as the impact angle increases due to the reduction in the normal velocity component. The tangential coefficient of restitution exhibits a minimum value which increases with impact speed due to the decrease in e_n , in accordance with (4.23); and the optimum impact angle is independent of impact speed. As defined by (4.10), the total coefficient of restitution e is dominated by e_n at small impact angles but approaches the same value as e_t at very large angles of impact.

Figure 4.41 shows the experimental measurements of normal and tangential coefficients of restitution reported by Brauer (1980) who used steel spheres of 2R = 6 mm colliding on a PMMA target surface at an impact speed of 4.4 m/s. It is seen that the transition from elastic to plastic deformation is clearly illustrated. When $\theta = 0°$, it is observed that $e_n = 0.93$ and this means that plastic deformation occurs; for $\theta = 90°$, $e_n = 1.0$ and deformation is elastic. The evolution of the total coefficient of restitution with impact angle observed by Brauer (1980) is in agreement with the linear kinetic energy of the particle after the collision obtained by computer simulation shown in Fig. 4.11. It is also seen from the figure that for high impact angles, $e_t \rightarrow 1$ and the data for the tangential coefficient of restitution becomes scattered at very small impact angles. Based on the experimental measurements, Brauer (1980) suggested that the minimum tangential coefficient of restitution $e_{t,min} \approx 0.68$ occurred at $\theta \approx 25°$ and the total coefficient of restitution reached its minimum vale of $e \approx 0.875$ at $\theta \approx 35°$.

Since the experimental data become scattered at relatively low impact angles, Brauer's (1980) estimation of the impact angle, at which $e_{t,min}$ occurs, may not be reliable. According to the previous analysis, the corresponding impact angle for $e_{t,min}$ is determined by the friction between the two contacting surfaces. With respect to (4.8), the reflection angle θ_{cr} will be zero at a certain impact angle when gross sliding occurs and this gives $e_t = 5/7$. Using Brauer's (1980) data, we obtain $\theta = 32°$ when $e_t = 5/7$. Referring to (4.20), we have $\psi_i/\lambda = 7(1+e_n)/2$ or $\mu = 2\tan\theta/7(1+e_n) = 0.0925$. At this friction level and with $e_n = 0.93$, the minimum tangential coefficient of restitution will be less than Brauer's (1980) estimation and previous computer simulated results suggest that $e_{t,min} \approx 0.6$ at $\theta \approx 15°$. An alternative interpretation of Brauer's results, based on the above argument, is also shown in Fig. 4.41.

Computer simulated oblique impacts were also performed at a constant speed in order to attempt a comparison with the experimental data. Figure 4.42 shows the coefficients of restitution e_n, e_t, and e for different impact angles for a constant speed of 1.25 m/s, which

corresponds to a normal coefficient of restitution of 0.93 at $\theta = 0$. A friction value of 0.0925 was used according to the previous argument. Other material properties, such as Poisson's ratio and yield stress, etc. are the same as those of U_3O_8 particles. Although the particle and target materials used are different from those of Brauer (1980), Fig. 4.41 and Fig. 4.42 demonstrate that the trends are similar except for that of the normal coefficient of restitution. From Fig. 4.42, it is seen that the normal coefficient of restitution increases with the increase of impact angle due to the decrease of normal approach velocity. However, the normal coefficient of restitution in Fig. 4.41 remains approximately constant until $\theta \approx 60°$ and then increases with an increase of impact angle. The reason for this may be due to the experimental conditions and differences in the material properties used in the impact tests. It also should be noted that the impact speed of 1.25 m/s used in the computer simulations is less than that used by Brauer (1980) (V_i = 4.4 m/s). However, since the yield stress of PMMA is less than U_3O_8 but the particle radius of R = 3 mm is significantly larger than that of U_3O_8 particles (10 μm), the same value of the normal coefficient of restitution can still be achieved.

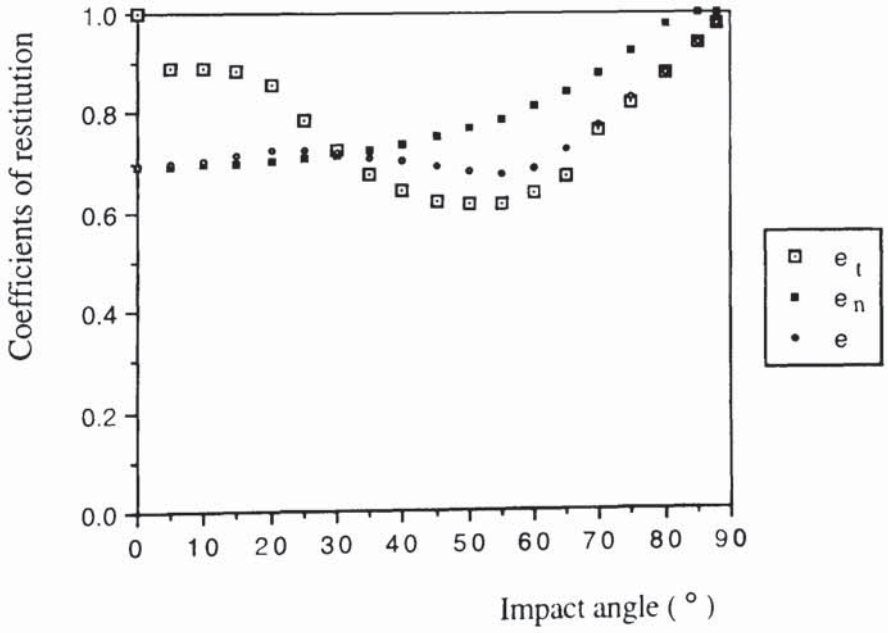

Fig. 4.38 Coefficients of restitution at a constant impact speed of 5.0 m/s.

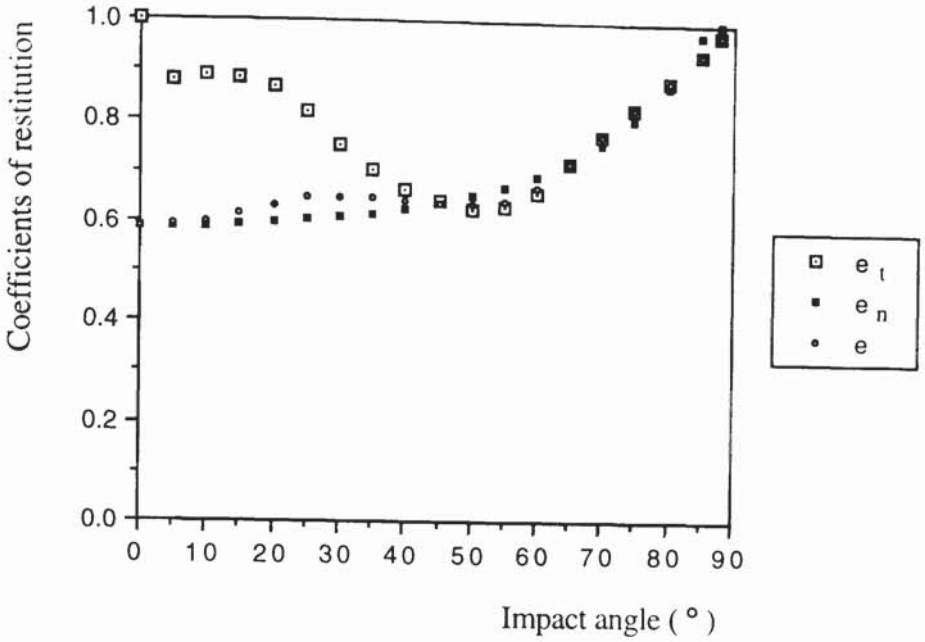

Fig. 4.39 Coefficients of restitution at a constant impact speed of 10.0 m/s.

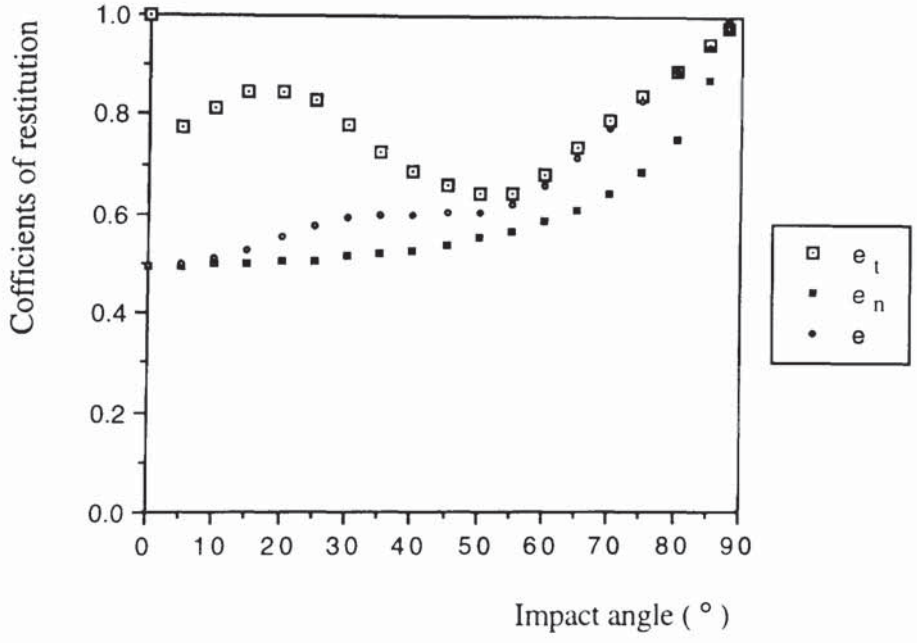

Fig. 4.40 Coefficients of restitution at a constant impact speed of 20.0 m/s.

Fig. 4.41 Experimental measurements of coefficients of restitution for steel spheres (2R = 6 mm) colliding on a PMMA target surface at an impact speed of 4.4 m/s (Brauer 1980).

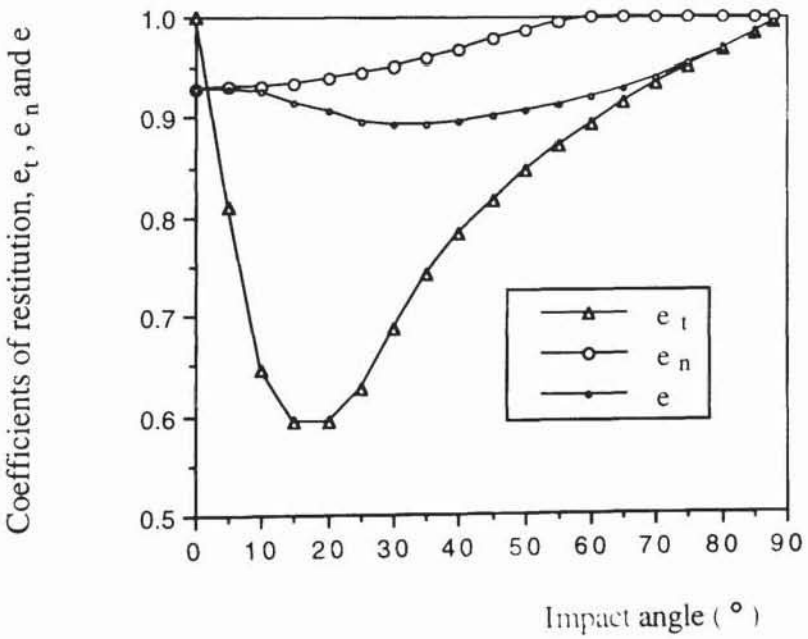

Fig. 4.42 Computer simulated coefficients of restitution of a U_3O_8 particle for an impact speed of V_i = 1.25 m/s (R = 10 μm, μ = 0.0925, ν = 0.3).

4.4 Computer simulated impacts with initial particle rotation

4.4.1 Theoretical considerations

The rotational motion of U_3O_8 particles in the transportation rig is a common occurrence. For instance, after an oblique collision there must exist an angular velocity for the particle upon departure no matter if the initial angular velocity was zero or not. In order to simplify the situation, only plane motion is considered in this study. As shown in Fig. 4.43, a particle with an initial angular velocity ω_i is moving towards the target surface in the n-t plane. The normal and tangential approach velocities are V_{ni} and V_{ti} respectively. Consider the case of a normal collision, where $V_{ti} = 0$. After a very small time step Δt there is a relative tangential movement, $\Delta\delta = \omega_i R\Delta t$, as well as the relative normal motion, $\Delta\alpha = V_{ni}\,\Delta t$, between the two contacting surfaces. The tangential displacement $\Delta\delta$ will result in a tangential incremental force ΔT according to (2.18). The rebound trajectory will therefore no longer be normal to the target plane but inclined at an angle to the n axis due to the effect of the tangential force caused by the initial particle rotation. In oblique collisions with initial particle rotation the tangential displacement at the contact therefore should include the tangential component of linear velocity of the particle as well as the displacement resulting from initial particle rotation.

With respect to (4.1), (4.2) and (4.3), when initial particle rotation exists we may rewrite (4.4) as

$$\omega_i - \omega_r = F_t R / mk^2 = R (V_{ti} - V_{tr}) / k^2 \qquad (4.30)$$

The tangential rebound velocity of the contact patch after the impact is given by

$$v_{tr} = V_{tr} + R\omega_r = V_{tr} + R\omega_i - R^2 (V_{ti} - V_{tr}) / k^2 \qquad (4.31)$$

Since $R^2 / k^2 = 5/2$ we have

$$v_{tr} = R\omega_i + \frac{7}{2} V_{tr} - \frac{5}{2} V_{ti} = R\omega_i + V_{ti} (\frac{7}{2} e_t - \frac{5}{2})$$

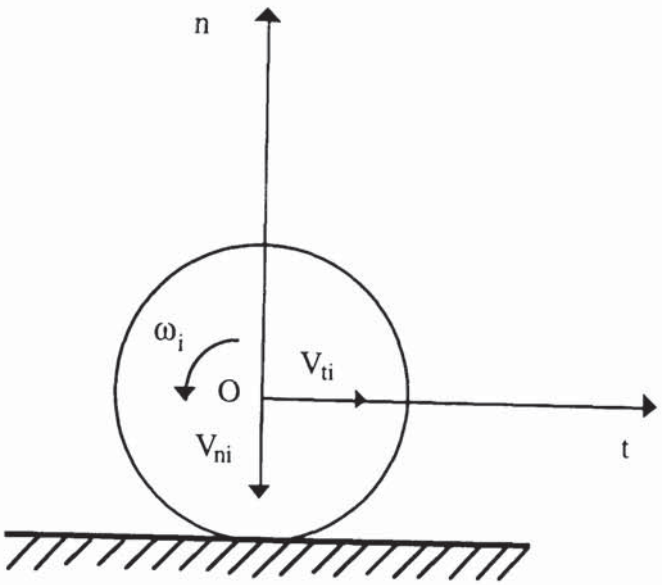

Fig. 4.43 Particle-wall impact with initial rotation (plane motion).

$$= V_{ti}\left(\frac{7}{2}e_t - \frac{5}{2} + \frac{R\omega_i}{V_{ti}}\right) \qquad (4.32)$$

In order to normalise the initial angular velocity ω_i, we here define a new parameter, ϕ_i, as

$$\phi_i = \frac{R\omega_i}{V_{ni}} \qquad (4.33)$$

and from (4.32) we obtain

$$\frac{e_n v_{tr}}{V_{nr}} = \frac{V_{ti}}{V_{ni}}\left(\frac{7}{2}e_t - \frac{5}{2} + \frac{\phi_i}{\tan\theta}\right) \qquad (4.34)$$

Therefore

$$e_t = \frac{5}{7} + \frac{2}{7}\left(\frac{e_n \tan\theta_{cr}}{\tan\theta} - \frac{\phi_i}{\tan\theta}\right) \qquad (4.35)$$

or

$$e_t = \frac{5}{7} + \frac{2\mu}{7\tan\theta}\left(\frac{v_{tr}}{\mu V_{ni}} - \frac{\phi_i}{\mu}\right) \qquad (4.36)$$

where μ is the coefficient of friction. When contact sliding occurs throughout the whole impact process, since (4.18) is still applicable, the tangential coefficient of restitution is given by (4.20). However, due to the effect of initial particle rotation, the corresponding

gross sliding impact angle varies with the initial angular velocity and it has to be determined by computer simulation.

4.4.2 Elastic impacts with initial rotation

The objective of this section is to examine the effect of initial rotation on the tangential coefficient of restitution, the rebound angle of the particle centre and the reflection angle of the contact patch. To ensure elastic deformation during the process of an impact a constant normal approach velocity of 0.5 m/s was used in the simulated tests. The effect of initial rotation on plastic impacts will be presented in the next section.

We, first of all, examine the departure angular velocity due to oblique collisions with no initial rotation in order to identify the possible range of angular velocities in a particle flow system. It was found (see Fig. 4.51) that for a U_3O_8 particle with R = 10 μm the maximum value of ϕ_r is in the range of $\phi_r < 2.0$, or in terms of the departure angular velocities $\omega_{r,max} < 10^5$ rad/s. The angular velocity resulting from an initial impact will affect the behaviour during further collisions and the angular velocity of the particle can continue to increase with the number of collisions that may occur. In this study, only the second collision will be considered. In reality, interactions of contacting micron-sized particles are significantly affected by surface energy effects and the surface forces will substantially reduce the departure angular velocity for oblique impacts.

In computer simulations the rotational direction is positive if the tangential motion of the contact point caused by the particle rotation is positive. In the case of normal impacts, a positive ω_i will lead to a negative rebound angle of the particle centre and vice versa. For oblique impacts, the rebound angle depends on the impact angle, initial angular velocity and the direction of the particle rotation. In the computer simulated tests, four different initial angular velocities (ω_i = 40000, 100000, -40000, and -100000 rad/s) were used,

corresponding to a range of values for the parameter ϕ_i (ϕ_i = 0.8, 2, -0.8 and -2 respectively).

Figure 4.44 shows the variations of the tangential coefficient of restitution with impact angle for the given initial angular velocities. It is seen that at low impact angles a positive value of ϕ_i leads to a negative tangential coefficient of restitution. When $\theta \rightarrow 0$, e_t will be approaching infinity at different directions according to the sign of ϕ_i. It is also seen that if the impact angle is approaching 90° the tangential coefficient of restitution is equal to unity, regardless of the value and direction of the initial angular velocity. The rebound angle plotted against impact angle is shown in Fig. 4.45. The normalised data of the rebound angle in Fig. 4.47 illustrates that, for elastic impacts under all circumstances, $|\psi_r/\lambda+\phi_i/\mu| \leq |\psi_i/\lambda+\phi_i/\mu|$. Figure 4.46 shows the reflection angle of the contact patch against impact angle. Since the magnitude and direction of the initial angular velocity influences contact sliding, it is seen from the figure that different ϕ_i correspond to different gross sliding angles. As can be expected, if the initial angular velocity is large enough, gross sliding occurs at a zero impact angle. The nondimensional reflection angle is plotted against nondimensional impact angle, shown in Fig. 4.48. Due to the effect of initial particle rotation, the data is not unified. In order to normalise the data, it is necessary to account for ϕ_i as shown in Fig. 4.49. It is seen that the unified data curve can be subdivided into two parts in the range $-\infty < \psi_i/\lambda+\phi_i/\mu \leq 0$ and $0 \leq \psi_i/\lambda+\phi_i/\mu < \infty$ respectively. Each part of the curve corresponds to the curve of Fig. 2.4, initially reported by Maw et al (1976, 1981). For the negative values of $\psi_i/\lambda+\phi_i/\mu$, when $\phi_i \rightarrow \infty$, θ_{cr} is approaching -90°. The condition which governs gross sliding during an impact is $|\psi_i/\lambda+\phi_i/\mu| \geq 6$. The normalised data of the tangential coefficient of restitution are shown in Fig. 4.50. It is seen that when gross sliding occurs the computer simulated results agree very well with the theoretical predictions given by (4.21). It can be concluded that Fig. 4.50 provides a unique curve which determines the tangential coefficient of restitution for elastic impacts under the circumstances of variations in friction, impact angle and initial angular velocity.

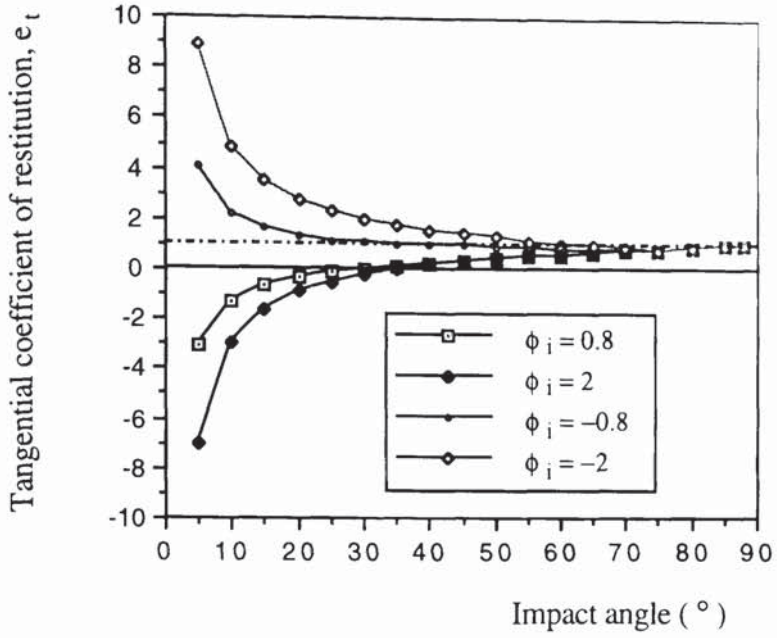

Fig. 4.44 Tangential coefficient of restitution against impact angle for different initial angular velocities (V_{ni} = 0.5 m/s).

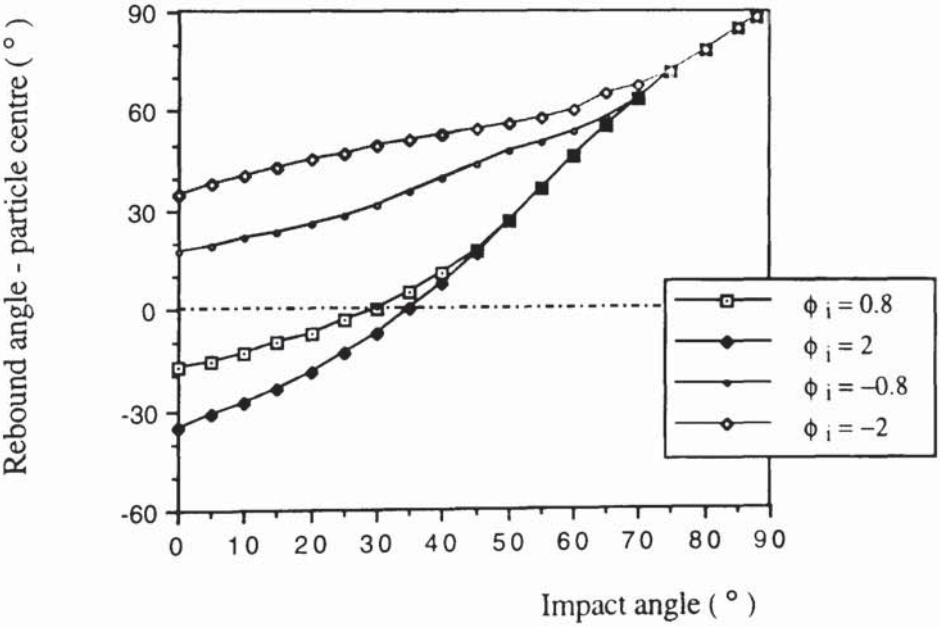

Fig. 4.45 Rebound angle of the particle centre against impact angle for different initial angular velocities (V_{ni} = 0.5 m/s).

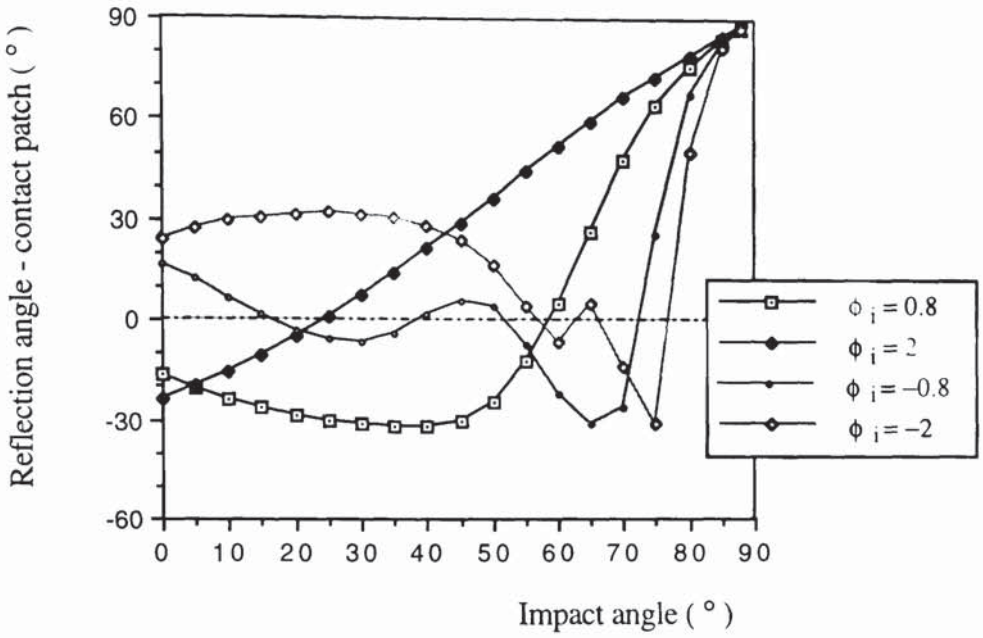

Fig. 4.46 Reflection angle of the particle centre against impact angle for different initial angular velocities ($V_{ni} = 0.5$ m/s).

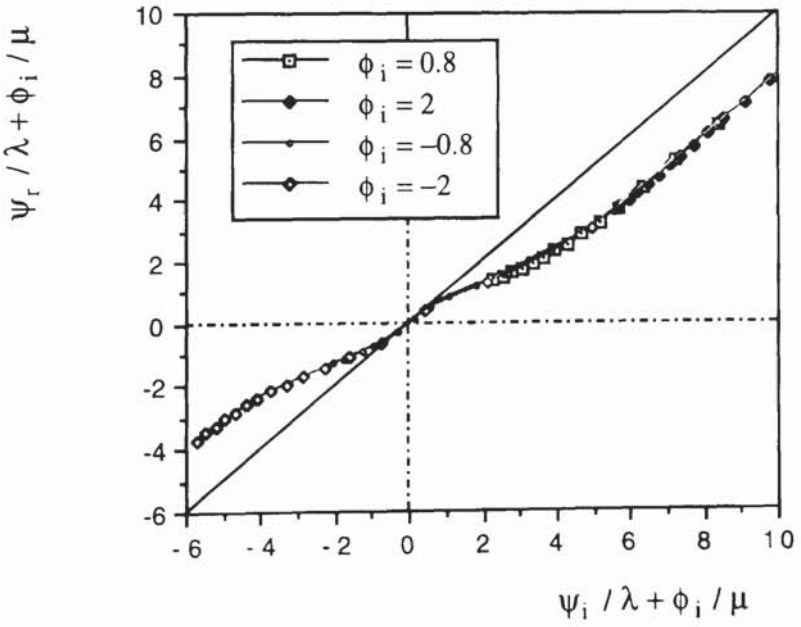

Fig. 4.47 Normalised rebound angle against the parameter $\psi_i/\lambda+\phi_i \mu$ for different initial angular velocities ($V_{ni} = 0.5$ m/s).

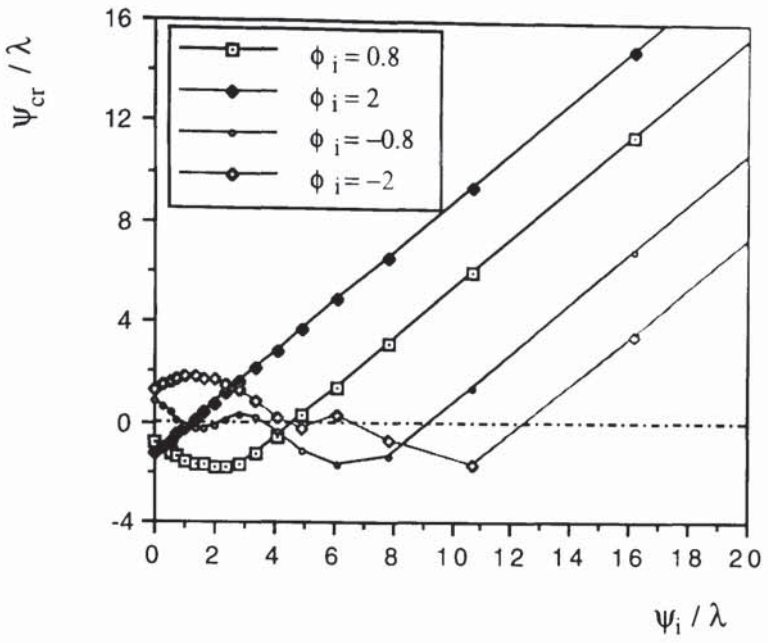

Fig. 4.48 Nondimensional reflection angle against nondimensional impact angle for different initial angular velocities (V_{ni} = 0.5 m/s).

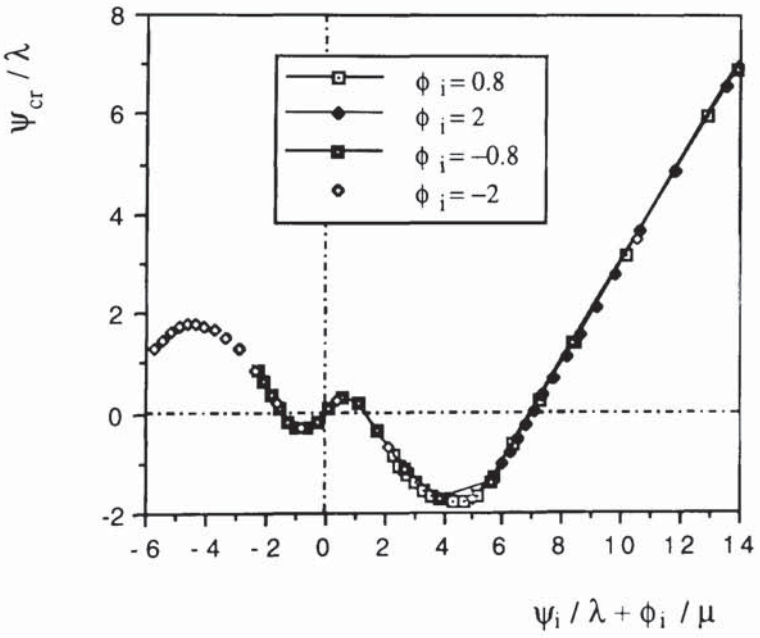

Fig. 4.49 Normalised reflection angle against the parameter $\psi_i/\lambda+\phi_i/\mu$ for different initial angular velocities (V_{ni} = 0.5 m/s).

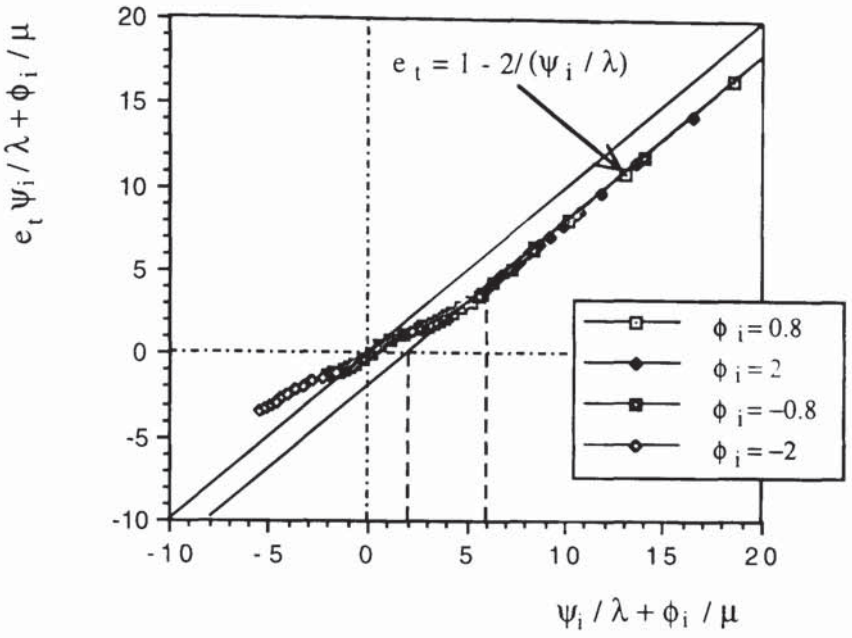

Fig. 4.50 Normalised tangential coefficient of restitution against the parameter $\psi_i/\lambda+\phi_i/\mu$ for different normal approach velocity (V_{ni} = 0.5 m/s).

4.4.3 Elasto-plastic impacts with initial particle rotation.

The effect of initial particle rotation on elasto-plastic collisions will be discussed in this section. A constant normal approach velocity of V_{ni} = 5.0 m/s was used in the simulated tests. Figure 4.51 shows the variations of the non-dimensional parameter ϕ_r with impact angle for oblique collisions with no initial particle rotation. The corresponding results obtained for elastic impacts (V_{ni} = 0.5 m/s) are also shown. It is seen that in both cases the maximum value of ϕ_r is less than 2.0 and the maximum value decreases with an increase in normal impact velocity when plastic deformation occurs. For the computer simulated elasto-plastic impacts the departure angular velocities are in the range of $\omega_r < 10^6$ rad/s.

The tangential coefficient of restitution, rebound angle and reflection angle of the contact patch are plotted against impact angle in Figs. 4.52, 4.53 and 4.54 respectively. It is clear that the trends are qualitatively similar to those for elastic impacts. However, it can be seen

that, when $\theta = 0$, due to the effect of plastic deformation, the absolute value of the rebound angle is larger than that for elastic impacts, but the reflection angle is less. When $\theta \rightarrow 90°$, it can be seen that both θ_r and θ_{cr} are approaching 90°, the same behaviour which is observed for elastic impacts. Normalisation of the reflection angle is achieved by using $2(\psi_i/\lambda+\phi_i/\mu)/(1+e_n)$, as shown in Fig. 4.55. It is evident that contact sliding occurs throughout the whole process of the impact when $|2(\psi_i/\lambda+\phi_i/\mu)/(1+e_n)| \geq 6$. The normalised data for the tangential coefficient of restitution is shown in Fig. 4.56. It should be noted that, although the tangential coefficient of restitution is predictable if gross sliding occurs according to (4.20), the unified data curve of e_t is dependent on the normal approach velocity, as was illustrated in Fig. 4.37.

Figure 4.57 provides the comparison of normalised reflection angle for elastic and plastic impacts. The effect of plastic deformation on the reflection angle in the range of $-6 < 2(\psi_i/\lambda+\phi_i/\mu)/(1+e_n) < 6$ is clearly seen. Finally, the comparison of the normalised tangential coefficient of restitution between the two normal approach velocities is shown in Fig. 4.58. Since plastic indentation is not very severe, the difference between the two curves is not large but this difference will increase with an increase of normal approach velocity.

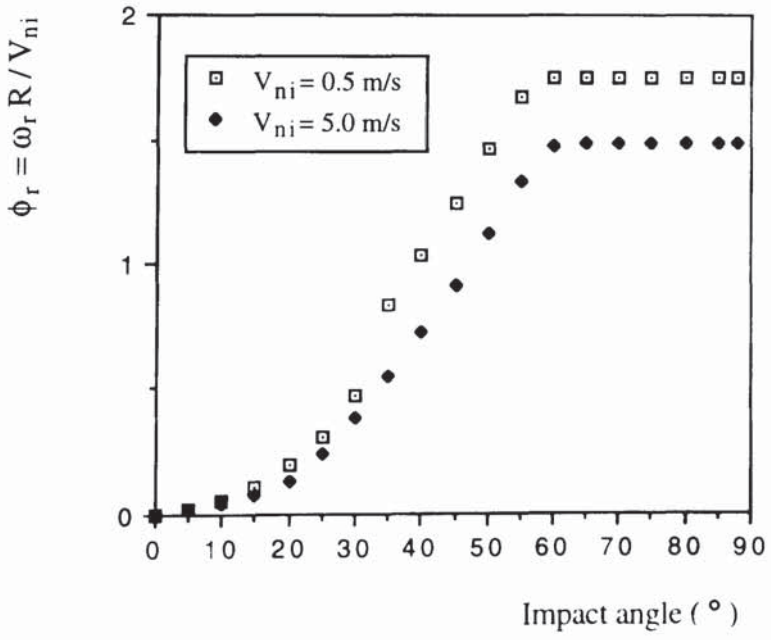

Fig. 4.51 The departure angular velocities resulting from oblique impacts (R = 10 μm).

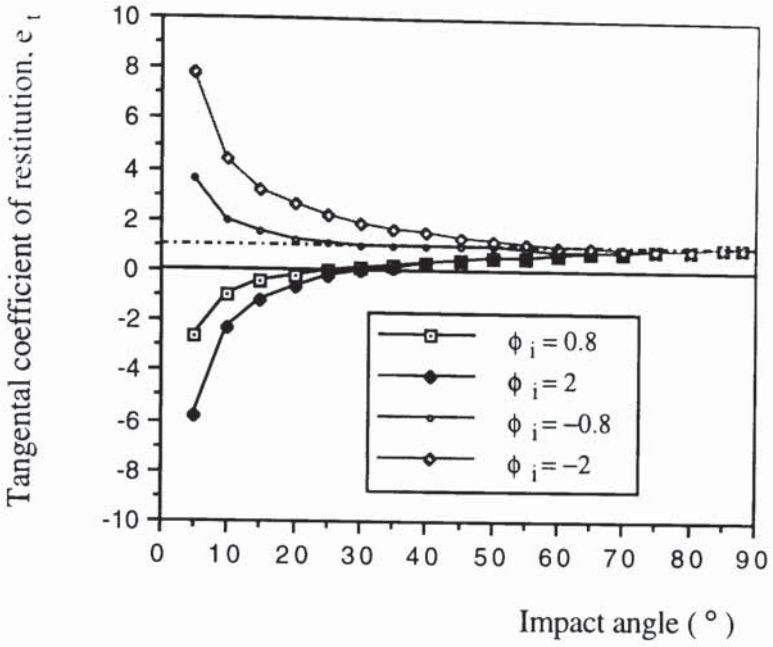

Fig. 4.52 Tangential coefficient of restitution against impact angle for different initial angular velocities (V_{ni} = 5.0 m/s).

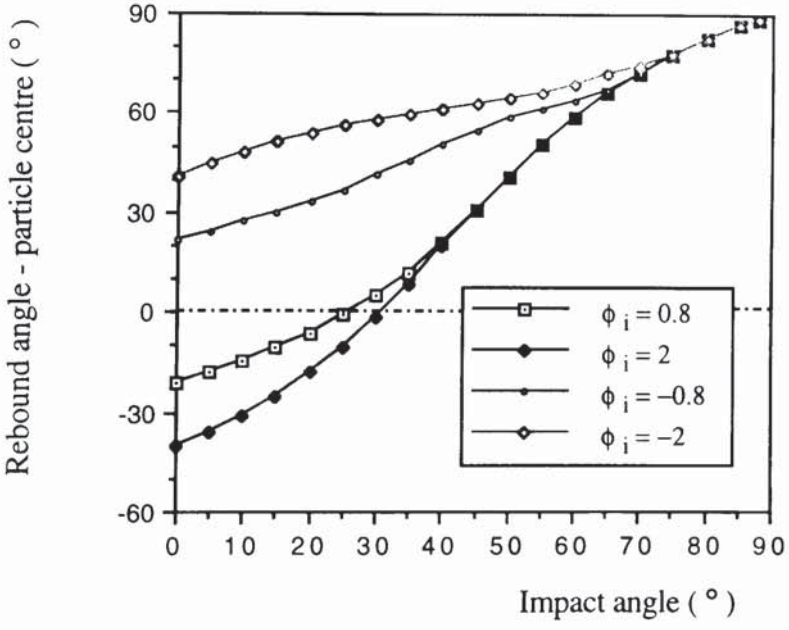

Fig. 4.53 Rebound angle of the particle centre against impact angle for different initial angular velocities (V_{ni} = 5.0 m/s).

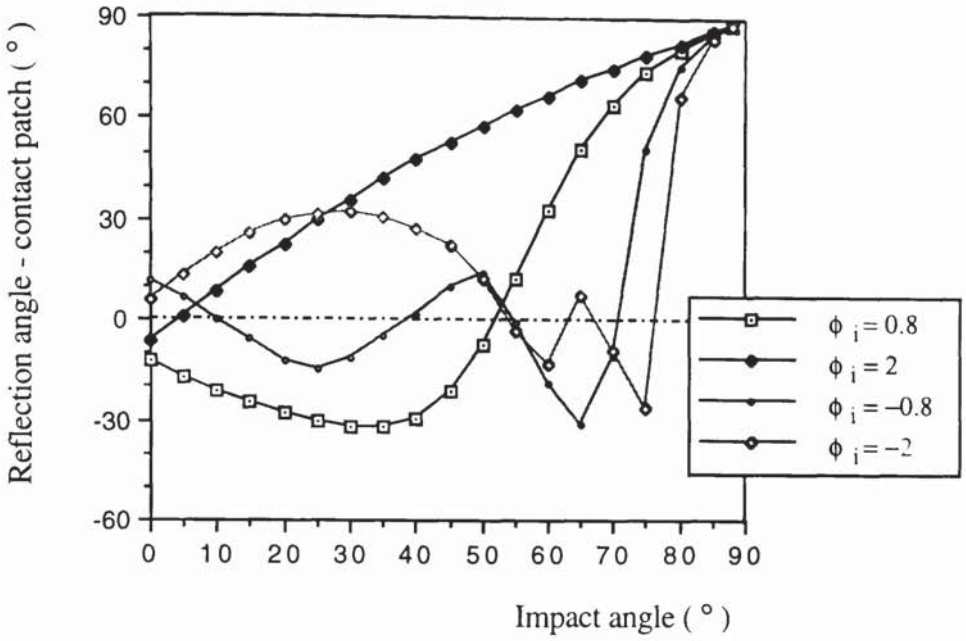

Fig. 4.54 Reflection angle of the contact patch against impact angle for different initial angular velocities (V_{ni} = 5.0 m/s).

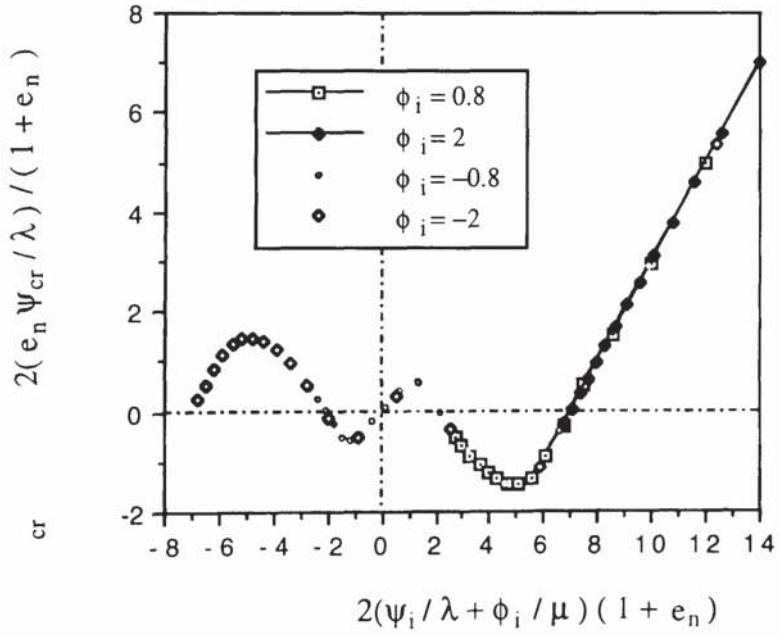

Fig. 4.55 Normalised contact rebound velocity for different initial angular velocities (V_{ni} = 5.0 m/s).

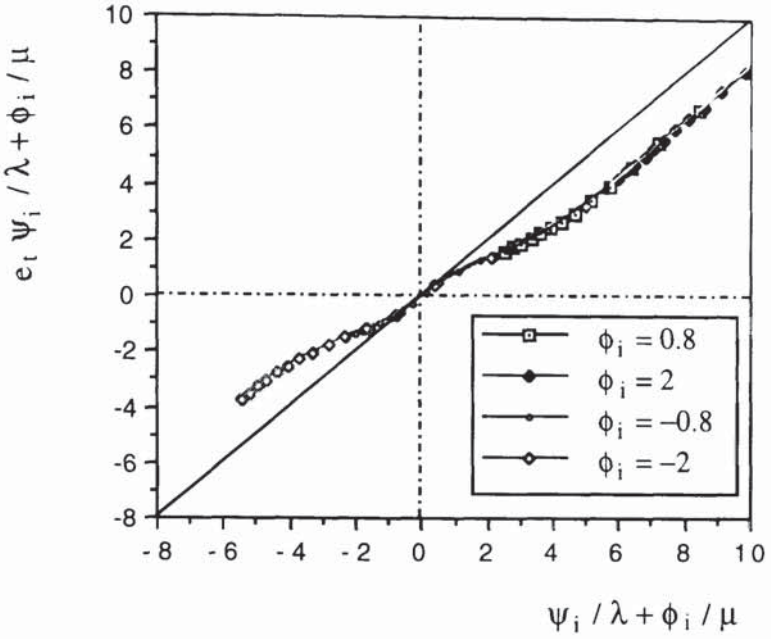

Fig. 4.56 Normalised tangential coefficient of restitution against the parameter $\psi_i/\lambda+\phi_i/\mu$ with different initial angular velocities (V_{ni} = 5.0 m/s).

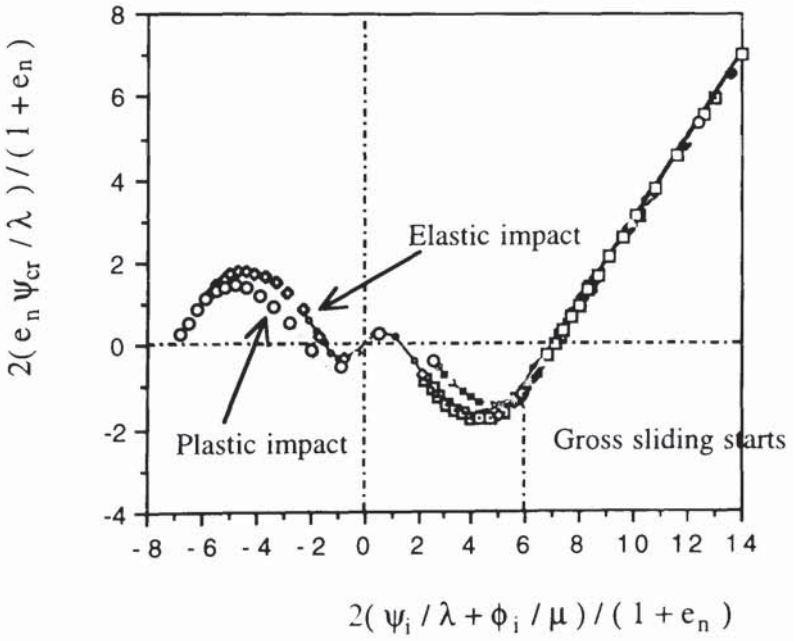

Fig. 4.57 Comparison of normalised contact rebound velocity between elastic and plastic impacts.

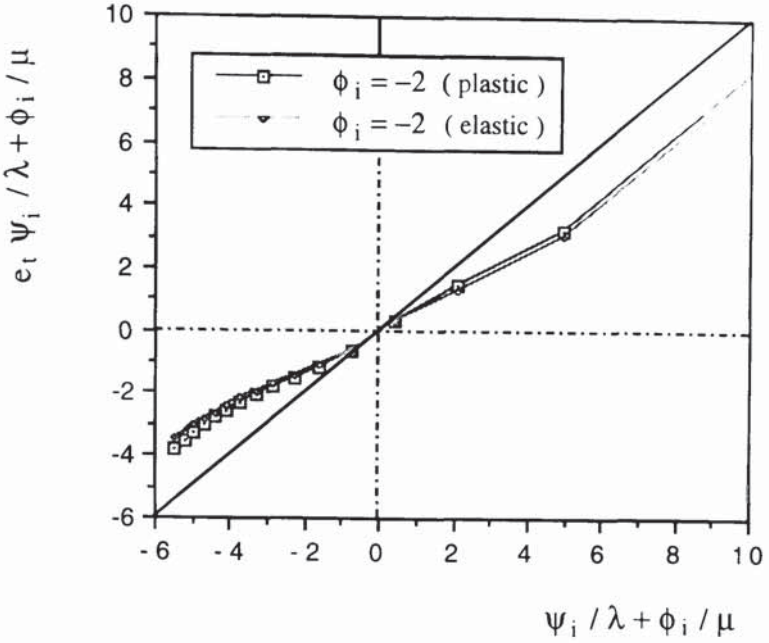

Fig. 4.58 Comparison of normalised tangential coefficient of restitution between elastic and plastic impacts.

4.5 Summary

Computer simulated tests have been performed to investigate oblique collisions of elasto-plastic spheres in this Chapter. Results have been presented to illustrate the tangential force-displacement relationships and the evolution of contact forces and energy components over the impact duration. The effects of two material properties, interfacial friction and Poisson's ratio, on particle bounce behaviour have been examined for variations of impact conditions (impact angle, impact velocity, initial particle rotation). The results obtained were then compared with experimental measurements and theoretical predictions provided by the impulse equations based on Newton's laws. Good agreement between the computer simulated results and experimental data reported by Maw et al (1976, 1981) was obtained for elastic impacts. Although different material properties were used, the results of elasto-plastic impacts presented in this study show an encouraging agreement with the real experimental results of Brauer (1980).

It has been demonstrated that if contact sliding occurs throughout the impact duration analytical solutions are available to define the complete post-impact conditions. For all cases investigated, the gross sliding condition applies if

$$\frac{2}{1+e_n}\left(\frac{\tan\theta+\phi_i}{\mu}\right)\geq 7-e_n \qquad (4.37)$$

or

$$\tan\theta \geq \frac{\mu(1+e_n)}{2}(7-e_n)-\phi_i \qquad (4.38)$$

If (4.38) is satisfied, then

$$e_t = 1-\frac{\mu(1+e_n)}{\tan\theta} \qquad (4.39)$$

$$\frac{R\omega_r}{V_{ni}} = \phi_r = \phi_i - \frac{5}{2}\mu(1+e_n) \qquad (4.40)$$

and the rebound angle of the particle centre, θ_r, is given by

$$\tan\theta_r = \frac{e_t}{e_n}\tan\theta \qquad (4.41)$$

where e_n is defined by (3.51).

It has been demonstrated that, for any impact angle, an additional initial angular velocity affects the collisional behaviour in a way that corresponds to an equivalent impact angle θ_{eq} where

$$\tan\theta_{eq} = \tan\theta + \phi_i \qquad (4.42)$$

If contact sliding does not occur throughout the impact process the particle rebound behaviour is more complex. It has been shown that the parameter $\psi = \lambda\tan\theta/\mu$, suggested by Maw et al (1976, 1981), provides the scaling rule for interparticle friction but not for the elastic properties of the particle/target interface characterised by $\lambda = 2(1-\nu)/(2-\nu)$. It has also been shown how the severity of plastic indentation, defined by the normal coefficient of restitution e_n, affects the rebound behaviour.

For impact angles which do not satisfy the criterion provided by (4.38) it is possible to apply curve fitting techniques to the computer simulated data to predict the rebound condition for specified values of ν and e_n. However, further work is required to examine the possibility that analytical solutions can be found for the cases when contact sliding does not occur throughout the whole process of the impact.

Chapter 5 Normal impact of adhesive spheres

5.1 Introduction

For micron-sized particles the impact behaviour is significantly affected by surface energy effects. When particles impact a surface there is a critical velocity above which the particles do not remain adhered to the surface but bounce off. Theoretical analysis and experimental observations indicate that the critical impact velocity is very sensitive to variations in the particle and target properties, such as particle size and density, surface energy and surface roughness, and elastic/plastic properties of both particle and target. The critical impact velocity of particles colliding with a wall is of great importance in process engineering since gas-borne particles present many operational and environmental problems. A criterion for determining whether particles bounce or adhere upon impact needs to be established for use in the numerical modelling of particle transport in turbulent flow fields. It is also necessary to be able to predict the rebound behaviour.

When the impact velocity is larger than the critical sticking velocity, the particle bounces off the target surface with a departure velocity which is always less the impact velocity, even for elastic collisions, because a certain amount of initial kinetic energy has to be dissipated in order to break the adhesive bound. If the impact velocity is larger than the yield velocity then energy dissipation will also occur due to plastic deformation at the contact patch. Although several elasto-plastic adhesion models have been developed, see Chapter 2, none of the existing theories has considered the effect of surface adhesion during both the loading and the unloading stages of the impact event.

This chapter discusses the normal impact of both elastic and elasto-plastic adhesive spheres. The JKR model of adhesion is extended to account for plastic deformation and theoretical solutions for the critical sticking velocity and the yield velocity are presented. The impact behaviour where particle bounce occurs is also investigated and some results of computer simulation are presented. Some of the work in this chapter has been reported by Ning and Thornton (1993).

5.2 Force-displacement relationships

For adhesive elastic spheres, Johnson (1976) provides relationships between the contact force, the contact radius and the relative approach; which may be written as

$$\frac{\alpha}{\alpha_f} = \frac{3(P/P_c) + 2 \pm 2(1 + P/P_c)^{1/2}}{3^{2/3}[P/P_c + 2 \pm 2(1 + P/P_c)^{1/2}]^{1/3}} \qquad (5.1)$$

and

$$\frac{\alpha}{\alpha_f} = 3^{1/3}\left(\frac{a}{a_c}\right)^2\left[1 - \frac{4}{3}\left(\frac{a}{a_c}\right)^{-3/2}\right] \qquad (5.2)$$

where

$$P_c = \frac{3}{2}\pi\Gamma R \qquad (5.3)$$

$$\alpha_f = \frac{3}{4}\left(\frac{\pi^2\Gamma^2 R}{E^{*2}}\right)^{1/3} = \left(\frac{3P_c^2}{16RE^{*2}}\right)^{1/3} \qquad (5.4)$$

$$a_c = \left(\frac{9\pi\Gamma R^2}{8E^*}\right)^{1/3} = \left(\frac{3RP_c}{4E^*}\right)^{1/3} \qquad (5.5)$$

and Γ is the interface energy. The contact radius is defined, Johnson et al (1971), by

$$a = \left(\frac{3RP_1}{4E^*}\right)^{1/3} \qquad (5.6)$$

where

$$P_1 = P + 2P_c \pm (4PP_c + 4P_c^2)^{1/2} \qquad (5.7)$$

is the effective Hertzian contact force. The relative approach and contact force may also be expressed, Johnson (1985), as

$$\alpha = \frac{a^2}{R} - \left(\frac{2\pi\Gamma a}{E^*} \right)^{1/2} \qquad (5.8)$$

$$P = \frac{4E^* a^3}{3R} - \left(8\pi\Gamma E^* a^3 \right)^{1/2} \qquad (5.9)$$

Fig. 5.1 Force-displacement relationship with adhesion (Johnson, 1976).

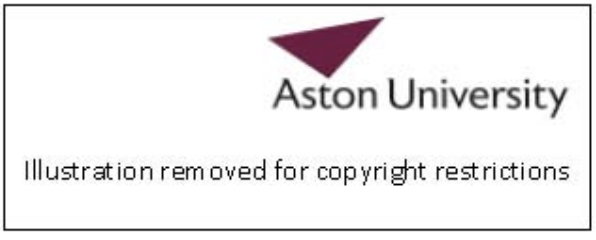

Fig. 5.2 Force-contact radius relationship with adhesion (Johnson, 1976).

Table 5.1 Key points on the curves of force-displacement and force-contact radius

	P	α	a
A	$-\frac{8}{9}P_c$	0	$(\frac{4}{3})^{2/3}a_c$
B	0	$(\frac{4}{3})^{2/3}\alpha_f$	$4^{1/3}a_c$
C	$-P_c$	$-(\frac{1}{3})^{2/3}\alpha_f$	a_c
F	$-\frac{5}{9}P_c$	$-\alpha_f$	$(\frac{1}{3})^{2/3}a_c$

It was shown by Thornton and Yin (1991) that, by differentiating both (5.8) and (5.9) with respect to a and then combining, the normal stiffness is given by

$$\frac{dP}{d\alpha} = 2E^*a \frac{3 - 3\,(a_c/a)^{3/2}}{3 - (a_c/a)^{3/2}} \qquad (5.10)$$

or using (5.5) and (5.6),

$$\frac{dP}{d\alpha} = 2E^*a \frac{3\sqrt{P_1} - 3\sqrt{P_c}}{3\sqrt{P_1} - \sqrt{P_c}} \qquad (5.11)$$

which degenerates to the Hertzian solution ($dP/d\alpha = 2E^*a$) when there is no adhesion ($P_c = 0$).

In Figs. 5.1 and 5.2 the force-displacement curve and the relationship between the contact radius and the contact force are plotted in terms of the dimensionless parameters P/P_c, α/α_f and a/a_c. For key points on the curves the corresponding expressions for P, α and a are provided in Table 5.1.

According to JKR theory, Johnson (1985), the pressure distribution over the contact area is given by

$$p(r) = \frac{2E^*a}{\pi R}[\,1-(r/a)^2\,]^{1/2} - \left(\frac{2\Gamma E^*}{\pi a}\right)^{1/2}[\,1-(r/a)^2\,]^{-1/2} \qquad (5.12)$$

Adopting a similar approach to that presented in Chapter 3 for the case of no adhesion, we assume that during plastic deformation there is a limiting compressive contact stress, σ_y, as shown in Fig. 5.3. It then follows that the normal contact force is given by

$$P = P_e - 2\pi\int_0^{a_p}[\,p(r)-\sigma_y\,]\,r\,dr \qquad (5.13)$$

where P_e is the elastic force according to JKR theory. Therefore

$$P = P_e - \frac{4E^*a^3}{3R}\left[\,1-\left(1-\frac{a_p^2}{a^2}\right)^{3/2}\right] + (8\Gamma\pi E^*a^3)^{1/2}\left[\,1-\left(1-\frac{a_p^2}{a^2}\right)^{1/2}\right] + \pi a_p^2\sigma_y \qquad (5.14)$$

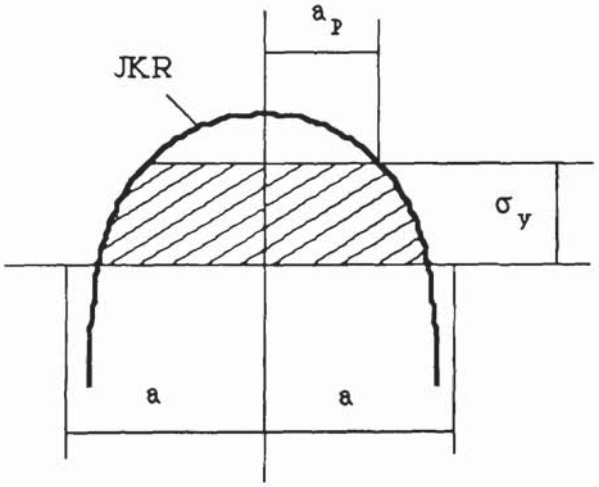

Fig. 5.3 Pressure distribution with adhesion.

As we demonstrated in Chapter 3, Bitter's (1963) assumption is analytically correct for the case of no adhesion. In the presence of adhesion, this assumption is no longer valid. However, in order to simplify (5.14) we shall assume Bitter's assumption

$$a^2 = a_p^2 + a_y^2 \qquad (5.15)$$

where the contact radius at initial yield is, according to (5.12), related to the limiting yield stress by

$$\sigma_y = \frac{2E^*a_y}{\pi R} - \left(\frac{2\Gamma E^*}{\pi a_y}\right)^{1/2} \qquad (5.16)$$

Substituting (5.15) into (5.14),

$$P = P_e - \frac{4E^*a^3}{3R}\left(1 - \frac{a_y^3}{a^3}\right) + \left(8\Gamma\pi E^*a^3\right)^{1/2}\left(1 - \frac{a_y}{a}\right) + \pi\sigma_y\left(a^2 - a_y^2\right) \qquad (5.17)$$

and using (5.9), we obtain

$$P = \frac{4E^*a_y^3}{3R} - \left(8\Gamma\pi E^*a\right)^{1/2}a_y + \pi\sigma_y\left(a^2 - a_y^2\right) \qquad (5.18)$$

Differentiating (5.18) and (5.8),

$$\frac{dP}{da} = 2\pi\sigma_y a - \left(\frac{2\Gamma\pi E^*a_y^2}{a}\right)^{1/2} \qquad (5.19)$$

$$\frac{d\alpha}{da} = \frac{2a}{R} - \left(\frac{\Gamma\pi}{2E^*a}\right)^{1/2} \qquad (5.20)$$

from which

$$\frac{dP}{da} \Big/ \frac{d\alpha}{da} = \frac{2\pi\sigma_y a - a_y\left(2\Gamma\pi E^*/a\right)^{1/2}}{2a/R - \left(\Gamma\pi/2E^*a\right)^{1/2}} \qquad (5.21)$$

Therefore

$$\frac{dP}{d\alpha} = \frac{\pi R\sigma_y - a_y\left(\Gamma\pi E^*R^2/2a^3\right)^{1/2}}{1 - \left(\Gamma\pi R^2/8E^*a^3\right)^{1/2}} \qquad (5.22)$$

However, from (5.5)

$$\pi\Gamma R^2 = 8E^*a_c^3/9 \qquad (5.23)$$

and, therefore, the contact stiffness during plastic indentation is defined as

$$\frac{dP}{d\alpha} = \frac{3\pi R\sigma_y - 2E^*a_y\left(a_c/a\right)^{3/2}}{3 - \left(a_c/a\right)^{3/2}} \qquad (5.24)$$

or

$$\frac{dP}{d\alpha} = \frac{3\pi R\sigma_y\sqrt{P_1} - 2E^*a_y\sqrt{P_c}}{3\sqrt{P_1} - \sqrt{P_c}} \qquad (5.25)$$

which degenerates to the solution for the non-adhesive case (3.18) when $\Gamma = 0$ since $P_c = 0$ and, from (5.5), $\pi R\sigma_y = 2E^*a_y$.

During unloading the force-displacement relationship is assumed to be elastic and is provided by the JKR theory but with a changed radius of contact curvature R_p due to flattening of the contact surfaces. The unloading process is equivalent to one in which a particle of radius R_p undergoes elastic deformation during which the stored elastic strain energy is gradually released. Due to the change in contact curvature the pull-off force is given as $P = -P_{cr}$ where

$$P_\alpha = \frac{3}{2}\pi\Gamma R_p \qquad (5.26)$$

which is greater than that for the case of elastic adhesive spheres given by (5.3). Consequently, modifying (5.10) and (5.11), the contact stiffness during unloading is given by

$$\frac{dP}{d\alpha} = 2E^*a\,\frac{3 - 3\,(a_\alpha/a)^{3/2}}{3 - (a_\alpha/a)^{3/2}} \qquad (5.27)$$

or

$$\frac{dP}{d\alpha} = 2E^*a\,\frac{3\sqrt{P_{lr}} - 3\sqrt{P_\alpha}}{3\sqrt{P_{lr}} - \sqrt{P_\alpha}} \qquad (5.28)$$

where

$$a^3 = \frac{3R_p}{4E^*}P_{lr} \qquad (5.29)$$

$$a_\alpha^3 = \frac{3R_p}{4E^*}P_\alpha \qquad (5.30)$$

and

$$P_{lr} = P + 2P_\alpha \pm \sqrt{4PP_\alpha + 4P_\alpha^2} \qquad (5.31)$$

It is necessary to define R_p in the above equation. In order to do this, we assume a smooth transition in the contact radius as the impact conditions change from plastic loading to elastic unloading. For continuity at the point of unloading

$$a^{*3} = \frac{3RP^*_1}{4E^*} = \frac{3R_pP^*_{1r}}{4E^*} \qquad (5.32)$$

Therefore

$$RP^*_1 = R_p P^*_{1r} = R_p (P^* + 2P_{cr} + \sqrt{4P^*P_{cr} + 4P_{cr}^2}) \qquad (5.33)$$

or

$$[P^*_1 R / R_p - (P^* + 2P_{cr})]^2 = 4P^*P_{cr} + 4P_{cr}^2 \qquad (5.34)$$

Expanding the left hand side of (5.34) leads to

$$(RP^*_1 - R_p P^*)^2 = 4RR_pP^*_1P_{cr} = 4R_p^2P^*_1P_c \qquad (5.35)$$

Since, using (5.3) and (5.26), we find $P_{cr}R = P_cR_p$. Therefore the required expression for R_p is given by

$$R_p = \frac{RP^*_1}{P^* + \sqrt{4P_cP^*_1}} \qquad (5.36)$$

The complete force-displacement curve for elasto-plastic loading and elastic unloading is diagrammatically illustrated in Fig. 5.4.

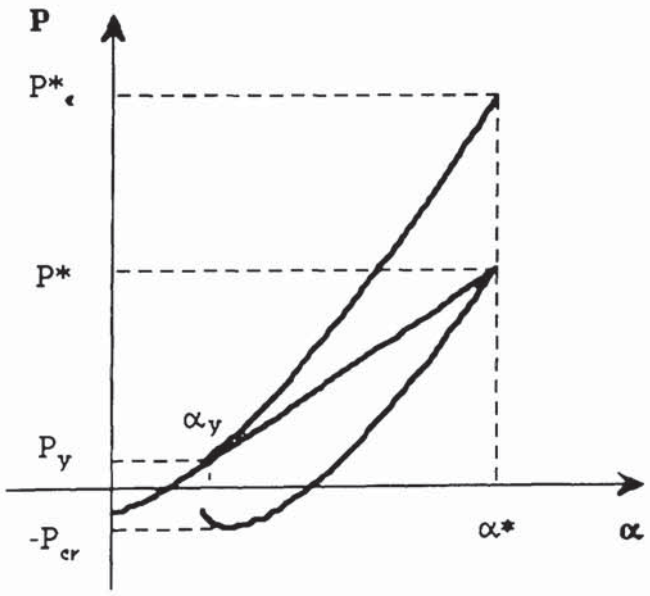

Fig. 5.4 Force-displacement relationship for elasto-plastic loading and elastic unloading.

5.3 Yield velocity

For fine particles, the impact velocity below which no plastic deformation occurs depends on both the limiting yield stress and the interface energy. The yield velocity increases with an increase in yield stress, as shown in Chapter 3, but decreases if the interface energy is increased.

Referring to Fig. 5.4, an expression for the yield velocity may be obtained from

$$\frac{1}{2} mV_y^2 = \int_0^{\alpha_y} P d\alpha \qquad (5.37)$$

using (5.9) and (5.20), (5.37) may be rewritten as

$$\frac{1}{2} mV_y^2 = \int_{a_0}^{a_y} [\frac{4E^*a^3}{3R} - (8\pi\Gamma E^* a^3)^{1/2}][\frac{2a}{R} - (\frac{\pi\Gamma}{2E^* a})^{1/2}] da \qquad (5.38)$$

where

$$a_0 = a|_{\alpha=0} = (\frac{4}{3})^{2/3} a_c = (\frac{2\pi\Gamma R^2}{2E^*})^{1/3} = (\frac{4RP_c}{3E^*})^{1/3} \qquad (5.39)$$

Rewriting (5.38) as

$$\frac{1}{2} mV_y^2 = \int_{a_0}^{a_y} [\frac{8E^*a^4}{3R^2} - \frac{14}{3R}(2\pi\Gamma E^*)^{1/2} a^{5/2} + 2\pi\Gamma a] da \qquad (5.40)$$

and integrating, leads to

$$\frac{1}{2} mV_y^2 = \frac{8E^*a_y^5}{15R^2} - \frac{4}{3R}(2\pi\Gamma E^*)^{1/2} a_y^{7/2} + \pi\Gamma a_y^2$$

$$- [\frac{8E^*a_0^5}{15R^2} - \frac{4}{3R}(2\pi\Gamma E^*)^{1/2} a_0^{7/2} + \pi\Gamma a_0^2] \qquad (5.41)$$

Substituting (5.39) and (5.3) into the above equation, it can be shown that

$$\frac{1}{2} mV_y^2 = \frac{8E^* a_y^5}{15R^2} - \frac{4}{3R} (2\pi\Gamma E^*)^{1/2} a_y^{7/2} + \pi\Gamma a_y^2 + 0.881\, \pi\Gamma a_c^2 \qquad (5.42)$$

which agrees with (3.1) when $\Gamma = 0$.

Combining (5.42) and (5.16) in order to obtain an analytical solution for the yield velocity in terms of the yield stress appears to be impracticable. However, it is possible to solve (5.16) numerically to find the contact radius which satisfies the equation and then this value can be substituted into (5.42) to obtain the yield velocity. Following this procedure for U_3O_8 particles (R = 10 μm) the effect of interface energy on the yield velocity and the contact radius at yield was examined. The results are shown in Fig. 5.5. It can be seen that an increase in interface energy leads to an increase in the contact radius at yield and a decrease in the yield velocity. There is only a small reduction in yield velocity for $\Gamma < 1$ but the yield velocity reduces significantly in the range $\Gamma > 1$.

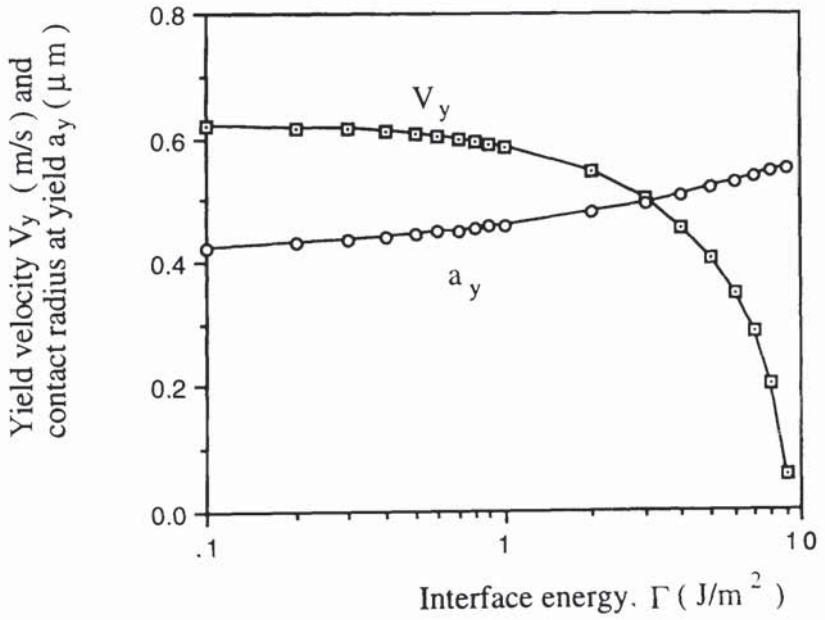

Fig. 5.5 Variations of yield velocity and contact radius at yield with interface energy

Equation (5.41) indicates that if $a_y = a_o$ then $V_y = 0$ and (5.16) may be written as

$$\sigma_y = \frac{2E^* a_0}{\pi R} - \left(\frac{2\Gamma E^*}{\pi a_0}\right)^{1/2} \qquad (5.43)$$

Substituting (5.39) into (5.43) leads to

$$\sigma_y = \left(\frac{2\Gamma E^{*2}}{\pi^2 R}\right)^{1/3} \qquad (5.44)$$

which demonstrates that if the yield stress is less that given by (5.44) plastic deformation occurs at the instant that the surfaces come together for all values of impact velocities.

5. 4 Stick/bounce conditions

5.4.1 Elastic spheres

The following explanation of the stick/bounce criterion was provided by Professor K.L. Johnson in an oral contribution to a meeting of the Institute of Physics (Tribology Group) on " Adhesive Forces in Powder Flows " at the University of Surrey in September 1985.

According to JKR theory, when two colliding surfaces come into contact the normal force between the two bodies will immediately drop to a certain value, $P = -8P_c/9$ (point A in Fig. 5.1), due to van der Waals attractive forces. The velocity of the sphere is then reduced gradually and part of the initial kinetic energy is radiated into the substrate as elastic waves. When the contact force reaches a maximum value the particle velocity has been reduced to zero and the incoming stage is complete.

In the recovery stage the stored elastic energy is released and converted into kinetic energy and the particle moves in the opposite direction. All the work done during the loading stage has been recovered when point A is reached during the recovery stage. However, at this point, when $\alpha = 0$, the sphere remains adhered to the target and further work is required to separate the surface. As shown in Fig. 5.1, separation occurs at point F and hence the

work required to break the contact is given by the shaded area U_s. It was suggested by Professor Johnson that a sufficiently accurate expression for U_s was

$$U_s = P_c \alpha_f \qquad (5.45)$$

and by substituting (5.3) and (5.4) this leads to

$$U_s = \frac{9}{8}\left(\frac{\pi^5 \Gamma^5 R^4}{E^{*2}}\right)^{1/3} = 7.58\left(\frac{\Gamma^5 R^4}{E^{*2}}\right)^{1/3} \qquad (5.46)$$

Thornton (1991) integrated the equation

$$U_s = \int_0^{-\alpha_f} P d\alpha \qquad (5.47)$$

to obtain

$$U_s = 0.9355\, P_c \alpha_f = 7.09\left(\frac{\Gamma^5 R^4}{E^{*2}}\right)^{1/3} \qquad (5.48)$$

which was also obtained by Johnson and Pollock (1993).

Neglecting energy losses due to elastic wave propagation, the only work dissipated during the collision is the work done in separating the surfaces, U_s. Therefore we may write

$$\frac{1}{2} m V_{ni}^2 - \frac{1}{2} m V_{nr}^2 = U_s \qquad (5.49)$$

The critical velocity V_s, below which sticking occurs, is given by

$$V_s = \left(\frac{2}{m} U_s\right)^{1/2} \qquad (5.50)$$

Therefore, substituting (5.48) we have

$$V_s = 1.84\left(\frac{1}{\rho_1}\right)^{1/2}\left(\frac{1}{E^*}\right)^{1/3}\left(\frac{\Gamma}{R}\right)^{5/6} \qquad (5.51)$$

For $V_{ni} > V_s$ bounce occurs and (5.49) may be written in the form of

$$1 - \left(\frac{V_{nr}}{V_{ni}}\right)^2 = \frac{2U_s}{m V_{ni}^2} \qquad (5.52)$$

and, combining (5.50) and (5.52), the coefficient of restitution is given by

$$e_n = [\, 1 - (\frac{V_s}{V_{ni}})^2 \,]^{1/2} \qquad (5.53)$$

Figure 5.6 illustrates the particle size dependence of the critical sticking velocity, given by (5.51), for U_3O_8 particles impacting a stainless steel target and the analytical predictions are also compared with those obtained by computer simulations. Particle and target properties used in the calculations and computer simulations are listed in Table 1.1. Plastic deformation affects the onset of particle bounce since the work done during the impact includes the irreversible work deforming the surface in the contact region. However, as shown in Fig. 5.5, for U_3O_8 particles of R = 10 μm the limiting elastic velocity is about 0.62 m/s which is larger than the critical impact velocity of $V_s \approx 0.016$ m/s for the parameters used. It is also true that plastic deformation will not occur for the particle size range of R = 1 - 20 μm. We are, therefore, justified to use the JKR elastic adhesion theory to predict the onset of bounce for U_3O_8 particle transport in turbulent flows.

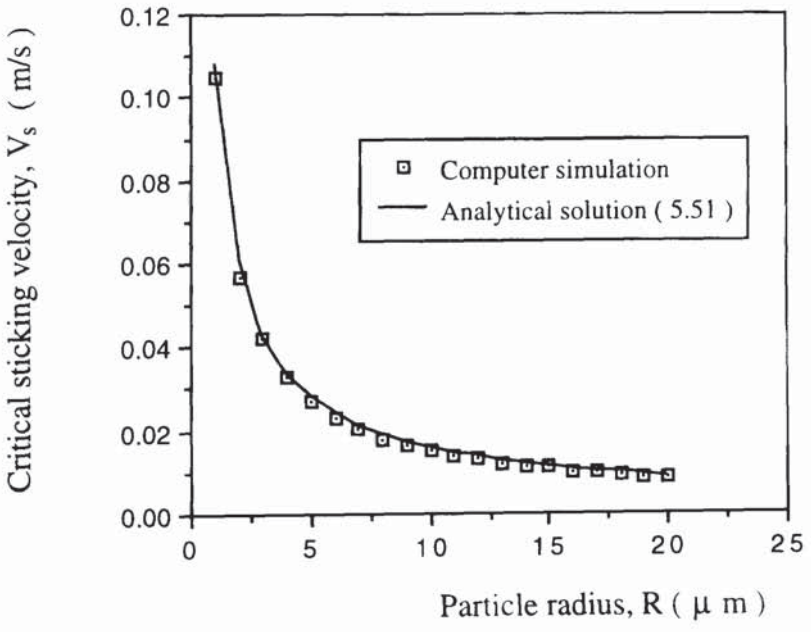

Fig. 5.6 Critical impact velocities of U_3O_8 particles with different particle sizes.

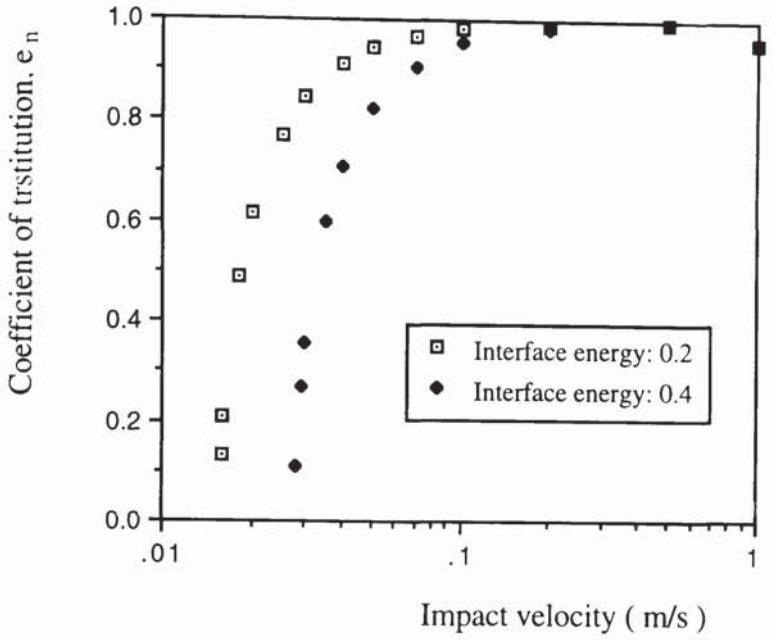

Fig. 5.7 Coefficient of restitution plotted against impact velocity for interface energies of $\Gamma = 0.2$ and 0.4 J/m^2.

The relationship (5.53) between the coefficient of restitution and impact velocity is shown in Fig. 5.7 for U_3O_8 particles of radius R = 10 μm with surface energy $\Gamma = 0.2$ and 0.4 J/m^2 respectively. It is seen that after the critical sticking velocity is reached the coefficient of restitution increases sharply with an increase of impact velocity. As the impact velocity is increased further the coefficient of restitution gradually increases towards unity, where the energy required to break the contact, U_s, is far less than the initial kinetic energy of the particle. The critical sticking velocity increases with an increase of surface energy, in agreement with (5.51). It should be noted that with a further increase in impact velocity, the coefficient of restitution will decrease if plastic deformation occurs.

5.4.2 Elasto-plastic spheres

In the previous section simple equations were obtained for the critical sticking velocity and the coefficient of restitution for the case of adhesive elastic spheres. For adhesive elasto-

plastic spheres the force-displacement behaviour during the complete loading-unloading cycle is more complicated, as shown in Fig. 5.4.

During elastic recovery the behaviour is equivalent to the unloading of an elastic sphere of radius R_p. Therefore, we may define the rebound kinetic energy as

$$\frac{1}{2} mV_{nr}^2 = \frac{8E^*a^{*5}}{15R_p^2} - \frac{4}{3R_p} (2\pi\Gamma E^*)^{1/2} a^{*7/2} + \pi\Gamma a^{*2} + 0.881\, \pi\Gamma a_{cr}^2 - 0.973\, \pi\Gamma a_{cr}^2 \qquad (5.54)$$

where

$$a_{cr} = (\frac{9\pi\Gamma R_p^2}{8E^*})^{1/3} = (\frac{3R_pP_{cr}}{4E^*})^{1/3} \qquad (5.55)$$

and a* is the maximum contact radius during the impact. The initial kinetic energy may be written as

$$\frac{1}{2} mV_{ni}^2 = \frac{1}{2} mV_y^2 + \int_{\alpha_y}^{\alpha^*} P d\alpha \qquad (5.56)$$

Using (5.18) and (5.20),

$$\int_{\alpha_y}^{\alpha^*} P d\alpha = \int_{a_y}^{a^*} [\frac{4E^*a_y^3}{3R} - 2 (2\Gamma\pi E^*)^{1/2} a_y a^{1/2} + \pi\sigma_y(a^2 - a_y^2)]$$

$$[\frac{2a}{R} - (\frac{\pi\Gamma}{2E^*})^{1/2} a^{-1/2}] da \qquad (5.57)$$

which, it can be shown, leads to

$$\int_{\alpha_y}^{\alpha^*} P d\alpha = \frac{4E^*a_y^3}{3R^2} (a^{*2} - a_y^2) + \frac{\pi\sigma_y}{2R} (a^{*2} - a_y^2)^2 + 2\pi\Gamma a_y(a^* - a_y)$$

$$- \frac{4}{15R} (2\Gamma\pi E^*)^{1/2} a_y (6\, a^{*5/2} + 5\, a_y^2 a^{*1/2} - 11 a_y^{5/2})$$

$$- \frac{2\pi\sigma_y}{5} (\frac{\Gamma\pi}{2E^*})^{1/2} (a^{*5/2} - 5\, a_y^2 a^{*1/2} + 8 a_y^{5/2}) \qquad (5.58)$$

The coefficient of restitution $e_n = V_{nr} / V_{ni}$ can, in principle, be obtained from (5.54),

(5.42) and (5.58) but it is clear that the resulting equation will be extremely complicated and solutions are more easily obtained by performing computer simulated impacts.

5.5 Dynamic yield stress

It has been shown that, for both adhesive and non-adhesive spheres, the coefficient of restitution is dependent on the contact yield stress σ_y which has been assumed to be independent of impact velocity. However, in material science it is generally recognised that, for most metals, alloys, and many non-metallic materials, the mechanical response is dependent on the rate of straining. Consequently, for some impact situations, it may be necessary to introduce the concept of a dynamic yield stress which is strain rate dependent.

The following logarithmic law was proposed by Deutler (1932) (see Goldsmith, 1960) to describe the observed dependence of yield stress on the plastic strain-rate

$$\overset{d}{\sigma_y} = \sigma_y (1 + A \ln (\dot{\varepsilon}_p / B)) \qquad (5.59)$$

where A and B are constants, $\sigma_y^{\,d}$ is the dynamic yield stress and σ_y is normally taken as the static yield stress corresponding to $\dot{\varepsilon}_y = B$. The dynamic plastic strain-rate $\dot{\varepsilon}_p$ can be determined from the maximum relative approach α^* and the duration of plastic loading t_p. Assuming that the effect of surface adhesion is not significant when impact velocities are well above the yield velocity, we may use (3.64) and (3.70) to define

$$\alpha^* = 2RV_{ni} \left(\frac{\rho}{3\sigma_y} \right)^{1/2} \qquad (5.60)$$

$$t_p = \pi R \left(\frac{\rho}{3\sigma_y} \right)^{1/2} \qquad (5.61)$$

and the plastic strain rate is

$$\dot{\varepsilon}_p = \frac{\alpha^*}{2Rt_p} = \frac{V_{ni}}{\pi R} \qquad (5.62)$$

It also follows from (3.2) and (3.71) that

$$B = \dot{\varepsilon}_y = \frac{\alpha_y}{2Rt_y} = \frac{1}{2R^2}\left(\frac{15R^2 m V_y^2}{16E^*}\right)^{2/5} \frac{2}{2.87}\left(\frac{RE^{*2}V_y}{m^2}\right)^{1/5} \qquad (5.63)$$

or

$$B = 0.34\,\frac{V_y}{R} \qquad (5.64)$$

Therefore

$$\frac{\dot{\varepsilon}_p}{B} = 0.938\,\frac{V_{ni}}{V_y} \qquad (5.65)$$

and, without any significant loss in accuracy, the dynamic yield stress may be expressed as

$$\sigma_y^d = \sigma_y\,(1 + A \ln (V_{ni}/V_y)) \qquad (5.66)$$

It was demonstrated in Section 5.3 that plastic yield can occur at $V_{ni} = 0$ when $V_y < V_s$. In this case, it is more convenient to define σ_y^s as the contact yield stress corresponding to the critical sticking velocity V_s and rewrite (5.66) as

$$\sigma_y^d = \sigma_y^s\,(1 + A \ln (V_{ni}/V_s)) \qquad (5.67)$$

5.6 Computer simulated experiments

Figure 5.8 shows the results of computer simulated impacts of a U_3O_8 particle of radius R = 10 μm with a stainless steel wall. The properties of both sphere and wall are given in Table 1.1. Figure 5.9 illustrates the effect of surface energy on the coefficient of restitution obtained. It can be seen that, for the range of $V_s < V_{ni} < V_y$, the coefficient of restitution increases with an increase in impact velocity. For impact velocities $V_{ni} > V_y$, the coefficient of restitution decreases as the impact velocity is increased and, as shown in Fig. 5.9, is not significantly affected by surface energy. Consequently, if $V_y >> V_s$, we may define the critical sticking velocity V_s by (5.51) and use (5.53) to predict the coefficient of restitution for $V_s < V_{ni} < V_y$; for $V_{ni} > V_y$, (3.51) is used to predict the coefficient of restitution with

yield velocity V_y defined by (3.5). Using these procedures, the analytical solution and the computer simulation results are in very good agreement, as shown in Fig. 5.8.

Further simulations have been performed to examine the effects of yield stress on the coefficient of restitution. The results are plotted for three values of yield stress in Fig. 5.10. Except for the value of the yield stress used, all the properties corresponded to a U_3O_8 particle impacting a stainless steel target, as given in Table 1.1, For comparison, the normal case (σ_y = 3.04 GPa) gives V_y = 0.62 m/s, V_s = 0.016 m/s and the maximum value of e_n $\approx$ 1.0. If the yield stress is reduced to σ_y = 1.2 GPa the critical sticking velocity is not affected but the yield velocity is reduced to V_y = 0.048 m/s and the maximum coefficient of restitution is reduced to $e_n \approx 0.95$. When the yield stress is further reduced to σ_y = 0.5 GPa, the yield velocity is less than the sticking velocity which is increased to V_s = 0.032. For this case of $V_y < V_s$ the maximum coefficient of restitution is approximately 0.5. It should be noted that at high impact velocities, $V_{ni} >> V_y$, all the data sets approximate to a power law relationship with an exponent of -1/4.

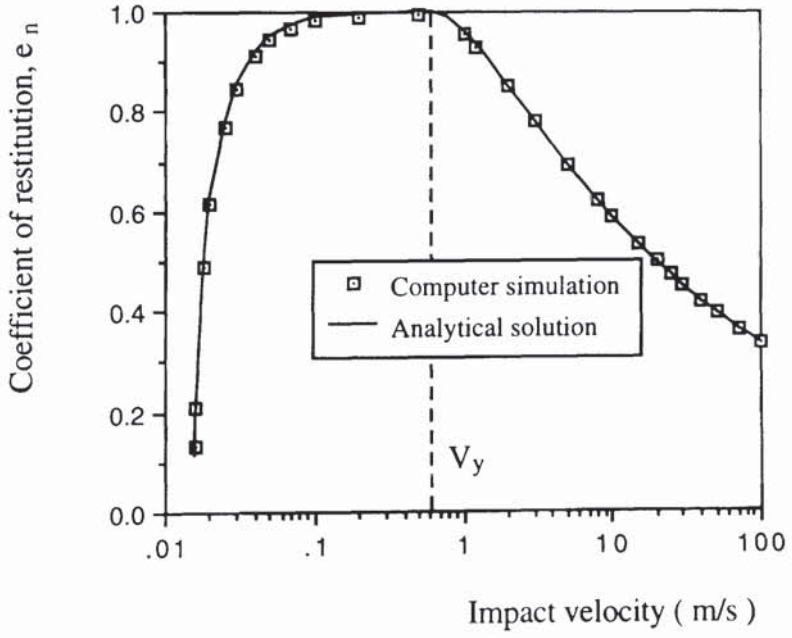

Fig. 5.8 Comparison of the coefficient of restitution between computer simulated results and analytical predictions based on (5.52) and (3.51).

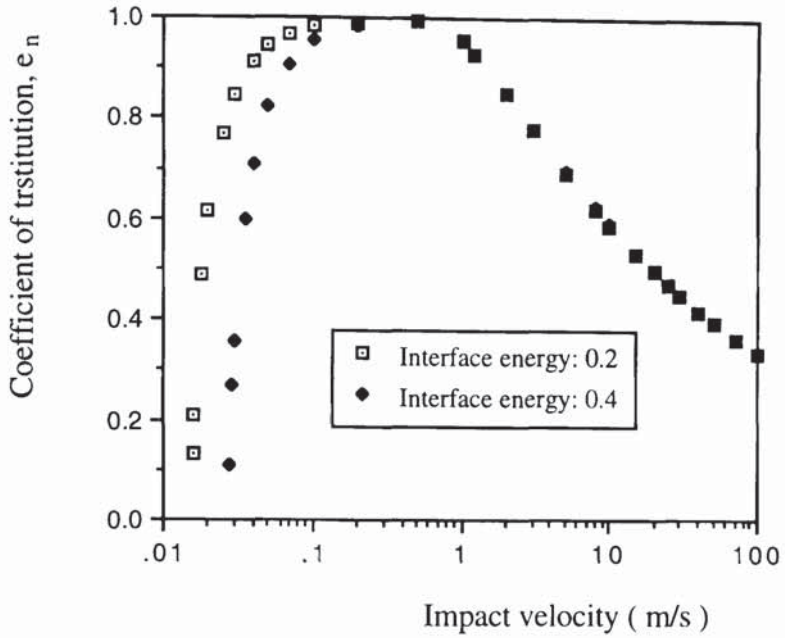

Fig. 5.9 Effect of interface energy on the coefficient of restitution.

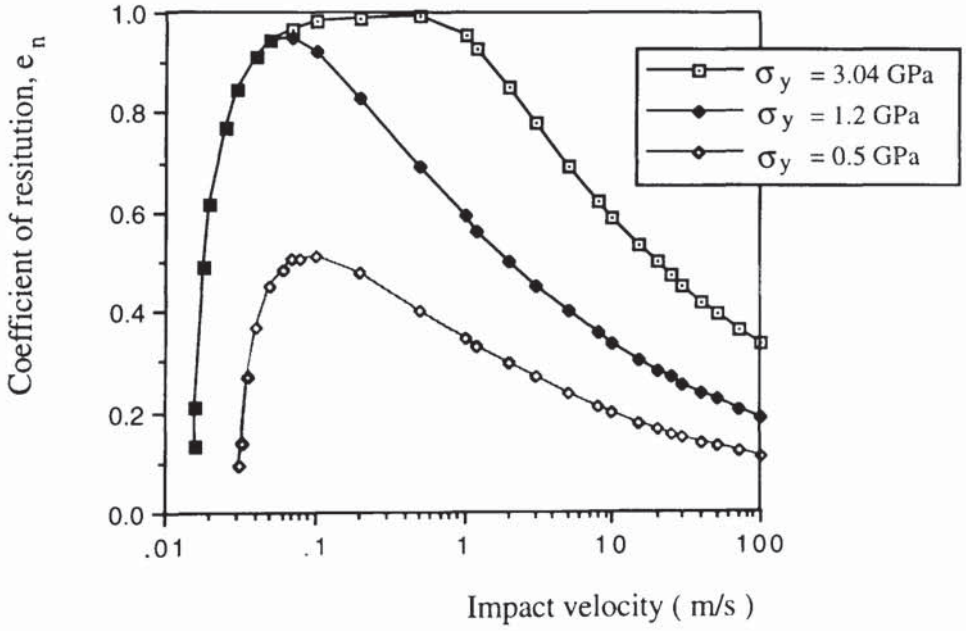

Fig. 5.10 Effect of yield stress on the coefficient of restitution.

Wall et al (1989,1990) reported some experimental results of ammonium fluorescein particles impacting a silicon target. It was decided to investigate whether agreement with their results could be achieved using the modified version of TRUBAL. Simulations have been performed for a range of impact velocities up to 100 m/s using the following properties given by Wall et al for the particle: R = 2.45 μm, ρ = 1.35 Mg/m^3, E = 1.2 GPa, ν = 0.3, μ = 0.35; and for the wall: ρ = 1.35 Mg/m^3, E = 182 GPa, ν = 0.3, μ = 0.35.

Using theories which did not account for surface energy effects during the loading stage, Wall et al (1989) found that a reasonable fit to the experimental data was obtained using the fitting parameters σ_y = 74 MPa and Γ = 0.38 J/m^2. However, they recognised that the value for the interface energy was higher than expected. It was suggested that the surface energy of ammonium fluorescein should be in the range 0.04-0.05 J/m^2 and for silicon the surface energy should be between 0.10 and 0.14 J/m^2. In the simulated impacts we have used Γ = 0.2 J/m^2. With these values the critical sticking velocity V_s = 0.567m/s according to (5.51) and is significantly less than the experimentally implied value of V_s ~ 2 m/s. Impact simulations were, therefore, carried out to match the experimental data for the lowest velocity reported by Wall et al (1989), i.e. V_{ni} = 2.0 m/s with e_n = 0.38, and it was found that a contact yield stress of σ_y = 35.3 MPa was required. With this value of σ_y the velocity required to initiate plastic yield V_y is less than the critical velocity for sticking V_s = 1.9 m/s. In fact, it was found that plastic yield occurs, in the centre of the contact area, even for zero load.

For a given set of impact velocities, Fig. 5.11 shows the typical force-displacement curves obtained. The slope of the loading curve is the same for all three different velocities. It is evident that, in the elastic recovery process, the maximum negative normal force, or pull-off force, increases with an increase of impact velocity: a clear indication that plastic indentation leads to an increase in the radius of contact curvature. With σ_y = 35.3 MPa, Γ = 0.2 J/m^2 and other properties as defined above, Fig. 5.12 shows the coefficients of restitution obtained for different velocities and the comparison with the experimental results

of Wall et al (1989). It can be seen that, for $V_{ni} > V_s$, the simulated results underpredict the coefficient of restitution by a significant amount. However, at high impact velocities the computer simulated results are parallel to the experimental data when plotted on a log-log plot. Consequently, in order to explain the difference between the computer simulated impacts and the experimental results a further series of impact simulations was performed to determine what values of σ_y were required to fit the experimental data. The results are shown in Fig. 5.13.

It can be seen that, in order to obtain agreement with the experimental data, it is necessary to assume a yield stress which increases with impact velocity. At velocities above 40 m/s the results imply a decrease in yield stress with increasing velocity. This may be explained by shear heating effects at high strain-rates in the experiments, Johnson (1985). However, since the experimental data was obtained by scaling the figure provided by Wall et al (1989), this is not certain. In addition, the coefficient of restitution is quite sensitive to the value of yield stress used, especially for an impact velocity which is just slightly above the sticking velocity.

Ignoring the possible decrease in yield stress due to shear heating at high velocities, the fitted values of yield stress are approximated by (5.67) with A = 1.429, V_s = 2.02 m/s and a limiting value of σ_y= 150 MPa, as shown in Fig. 5.13. We therefore introduce a dynamic yield stress which is defined as

$$\sigma_y^{\,d} = \begin{cases} 30\,(\,1 + 1.429 \ln(\,V_{ni} / 2.02\,)\,) & V_{ni} \le 30 \quad \text{m/s} \\ 150 & V_{ni} > 30 \quad \text{m/s} \end{cases} \qquad (5.68)$$

The computer code was then modified to incorporate a dynamic yield stress in this way and a final series of simulations was performed. The results, illustrated in Fig. 5.14, show good agreement with the experimental data over the complete velocity range.

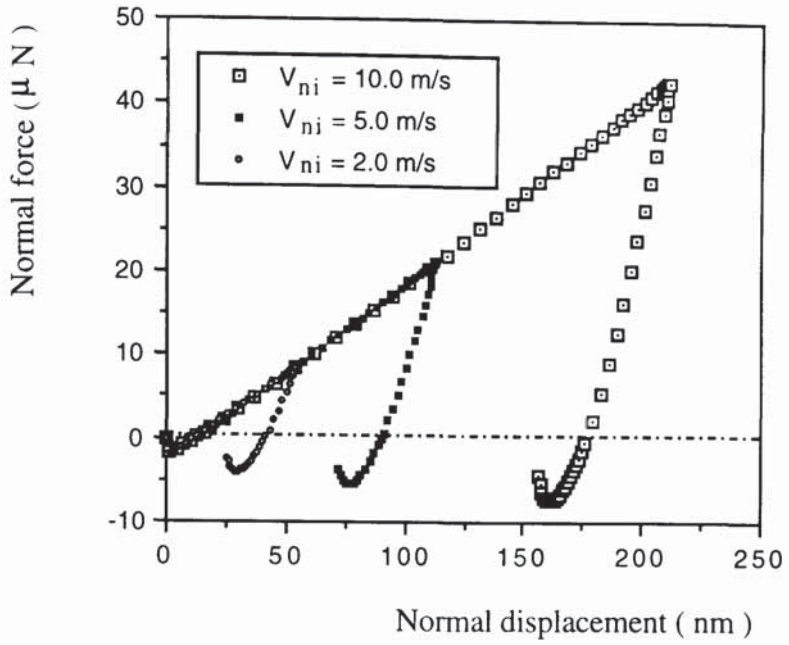

Fig. 5.11 Normal force-displacement relationships of soft particles at different impact velocities.

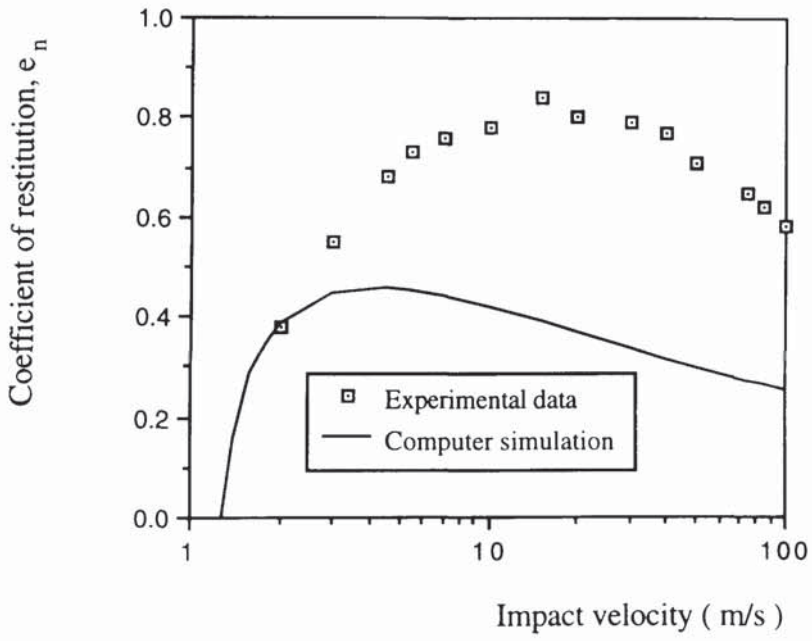

Fig. 5.12 Comparison of computer simulated impacts (σ_y = 35.3 MPa. Γ = 0.2 J/m^2) with results of Wall et al (1989) for ammonium fluorescein particle impacting a silicon target surface.

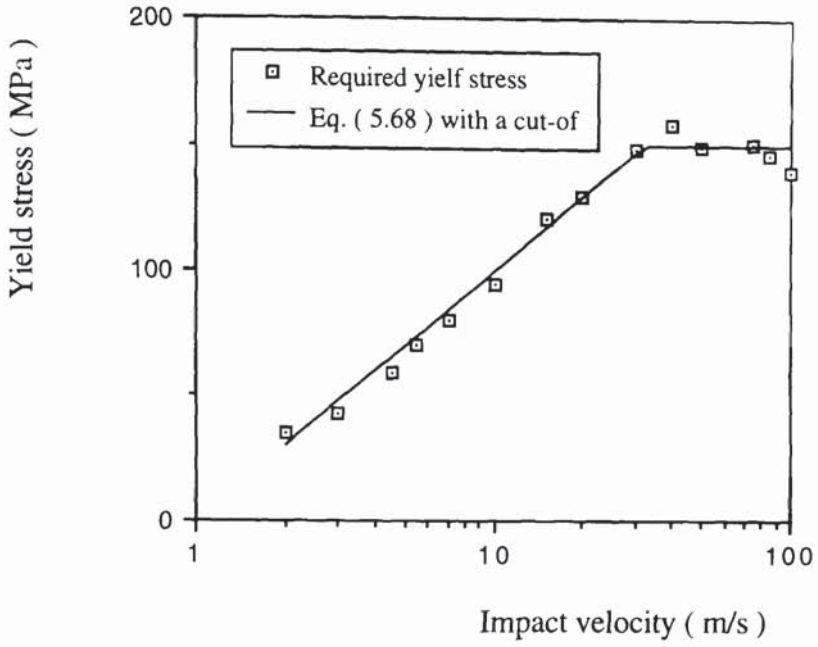

Fig. 5.13 Effect of impact velocity on the yield stress required to fit the experimental data of Wall et al (1989).

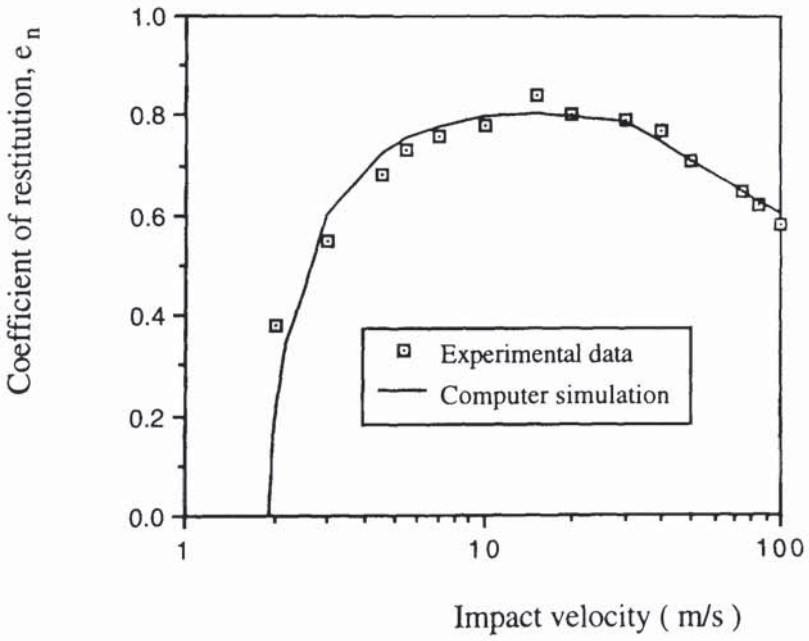

Fig. 5.14 Comparison of experimental results with computer simulated impacts incorporating a dynamic yield stress.

5.7 Summary

In the presence of adhesion the normal impact behaviour is analysed in this chapter. For elastic spheres a criterion which determines whether the particle bounces or adheres with the target surface has been established for the investigated materials. The computer simulation results show a very good agreement with the analytical solution. The impact velocity which initiates plastic deformation is examined and a criterion governing the onset of plastic yield has been obtained. It has been found that the yield velocity decreases with an increase of surface energy as well as yield stress. Consequently, the yield velocity obtained in this study is less than that in the case of no adhesion estimated by Davies (1949).

For adhesive elasto-plastic spheres a new mathematical model, which is an extension to the JKR model of adhesion, has been developed to deal with the capture and rebound of small particles from surfaces. The normal coefficient of restitution is based on the normal force-displacement relationship during loading and unloading with consideration of the flatting of the contact surfaces due to plastic deformation. The effects of interface energy and yield stress on particle bouncing are investigated. It has been analytically and numerically demonstrated that, at relatively high impact velocities, the effect of surface adhesion is not significant and the impact behaviour can therefore be described by the equations without adhesion. Computer simulated impacts of hard spheres of U_3O_8 have been shown to provide sensible results in terms of the effect of velocity on the coefficient of restitution. For soft, micron-sized particles of ammonium fluorescein impacting a silicon target it is found that it is necessary to introduce the concept of a velocity dependent dynamic yield stress in order to obtain computer simulated results which are in agreement with real experimental data of Wall et al (1989, 1990).

Chapter 6 Oblique impact of adhesive spheres

6.1 Introduction

There appears to be no published detailed investigation of oblique impacts of micron-sized particles for which the effect of surface adhesion may be important. In general, however, most impacts will be oblique. Therefore, in this project, oblique impacts of adhesive spheres have been simulated and are reported in this chapter.

6.2 Theoretical considerations

The theoretical basis for the normal contact force-displacement behaviour was described in Chapter 5. It is assumed that the theories of Savkoor and Briggs (1977) and Thornton (1991), see Section 2.3.2, are still applicable after plastic yield and that the tangential interaction only affects the normal interaction rules by the way in which the initial tangential peeling process suggested by Savkoor and Briggs (1977) reduces the contact radius. This affects the magnitude of the normal contact stiffness, defining by (5.11), (5.25) and (5.28), and the calculation of the modified contact curvature, R_p, as explained below.

Savkoor and Briggs (1977) incorporated the tangential work done into the JKR energy balance model and obtained the following equation for the contact radius

$$a^3 = \frac{3R}{4E^*}\left(P + 2P_c \pm \sqrt{4PP_c + 4P_c^2 - T^2E^*/4G^*} \right) \qquad (6.1)$$

Consequently, to define R_p, it is necessary to modify (5.32) to (5.36). Assuming a smooth transition in the magnitude of the contact radius at the change from plastic loading to elastic unloading we may rewrite (5.32) as

$$a^{*3} = \frac{3RP^*_1}{4E^*} = \frac{3R_pP^*_{1r}}{4E^*} \qquad (6.2)$$

but with the substitutions

$$P^*_1 = P^*_e + 2P_c \pm \sqrt{4P^*_eP_c + 4P_c^2 - T^2E^*/4G^*} \qquad (6.3)$$

$$P^*_{1r} = P^* + 2P_{cr} \pm \sqrt{4P^*P_{cr} + 4P_{cr}^2 - T^2E^*/4G^*} \qquad (6.4)$$

where P^*_1 and P^*_{1r} are the equivalent Hertzian forces at the end of loading and at the beginning of unloading respectively. Therefore

$$RP^*_1 = R_pP^*_{1r} = R_p\left(P^* + 2P_{cr} \pm \sqrt{4P^*P_{cr} + 4P_{cr}^2 - T^2E^*/4G^*}\right) \qquad (6.5)$$

which leads to

$$R_p = \frac{RP^*_1}{P^* + \sqrt{4P_cP^*_1 - T^2E^*/4G^*}} \qquad (6.6)$$

rather than (5.36). A problem arises with (6.6) if $T^2E^*/4G^* > 4P_cP_1^*$. In this case R_p is calculated as

$$R_p = \frac{RP^*_1}{P^*} \qquad (6.7)$$

During elastic unloading the contact stiffness is provided by (5.28) with the equivalent Hertzian force defined as

$$P_{1r} = P + 2P_{cr} \pm \sqrt{4PP_{cr} + 4P_{cr}^2 - T^2E^*/4G^*} \qquad (6.8)$$

where P is the actual contact force.

6.3 High speed oblique impacts ($V_{ni} > V_y$)

Using the properties given in Table 1.1, with σ_y = 3.04 GPa, computer simulations of U_3O_8 particles (R = 10 μm) impacting a stainless steel target have been performed to examine the effect of impact velocity and impact angle on the rebound behaviour. For impact speeds up to 100 m/s, Fig. 6.1 shows the variations of the normal coefficient of restitution with normal

approach velocity. The figure clearly demonstrates that the effect of impact angle on the normal coefficient of restitution is not significant for high speed impacts. At impact velocities close to the sticking velocity there are minor variations of e_n with impact angle.

For oblique collisions at high impact speeds, or more relevantly high normal approach velocities, the effect of surface adhesion is not significant since the interactions between the two contacting surfaces are dominated by the effect of plastic deformation. This is demonstrated in Fig. 6.2, 6.3 and 6.4 which are typical of all the simulated high speed impacts of adhesive spheres. Figures 6.2, 6.3 and 6.4 show the effect of impact angle on the reflection angle of the contact patch, the rebound angle of the particle centroid and the tangential coefficient of restitution respectively. The results shown are for a series of simulations in which a constant normal approach velocity of 5.0 m/s was used, which is higher than the yield velocity $V_y \approx 0.62$ m/s. In the figures, the results are also compared with the corresponding series of simulation tests of non-adhesive elasto-plastic spheres reported in Figs. 4.31, 4.32 and 4.33. Except for the tangential coefficient of restitution obtained for a 5° angle of impact the data from both series of simulations are almost identical.

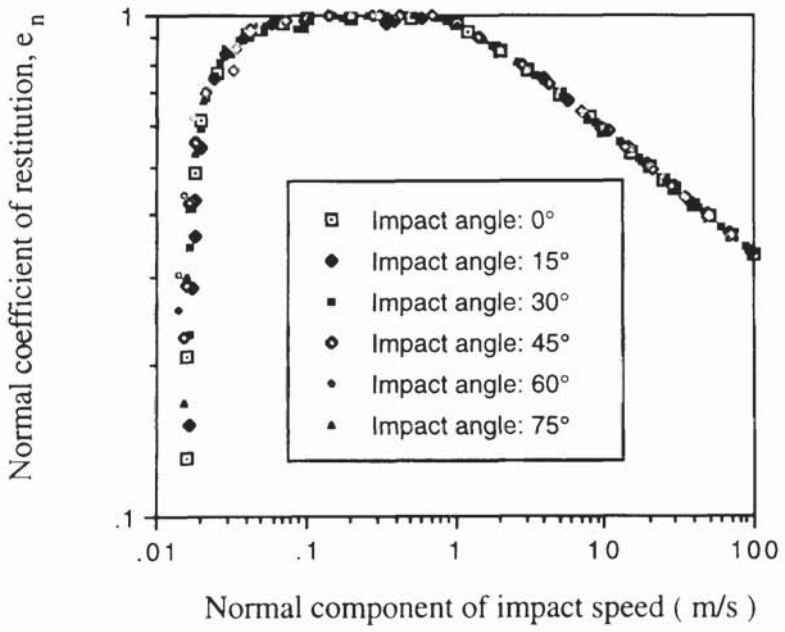

Fig. 6.1 Effect of impact angle on the normal coefficient of restitution.

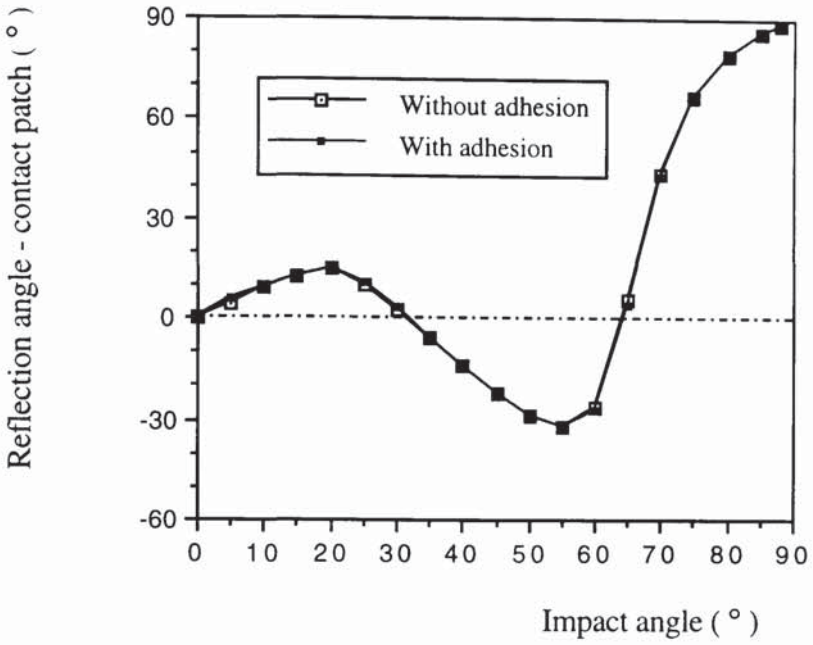

Fig. 6.2 Comparison of reflection angle at the contact patch with and without adhesion at V_{ni} = 5.0 m/s.

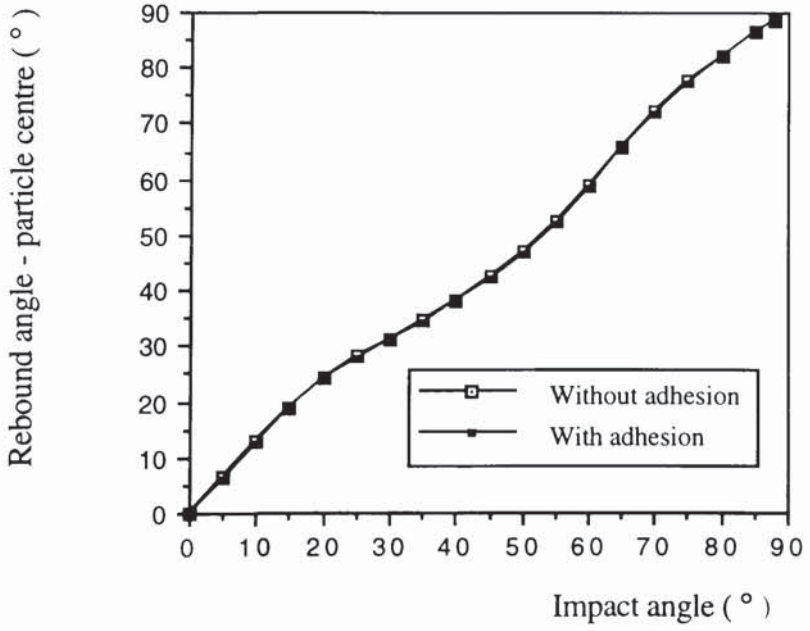

Fig. 6.3 Comparison of rebound angle of the particle centre with and without adhesion at V_{ni} = 5.0 m/s.

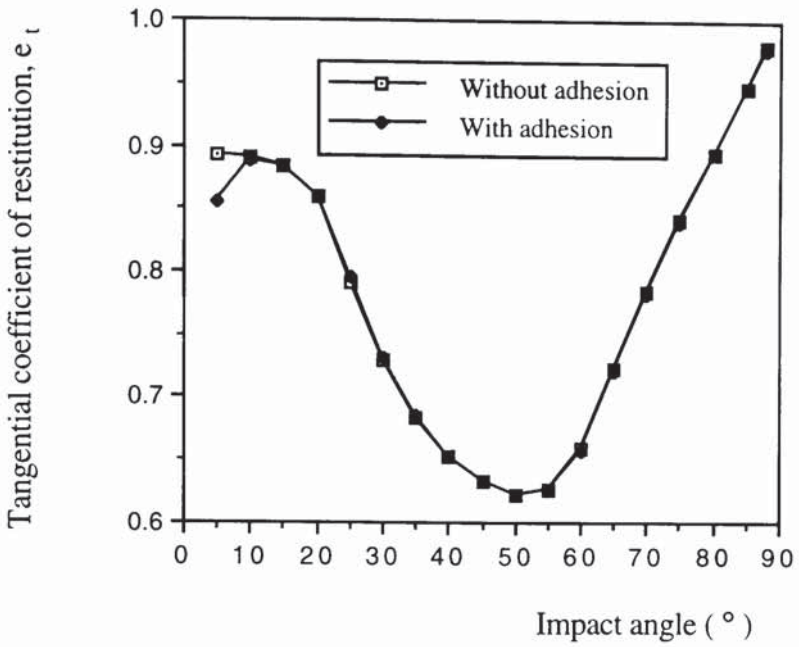

Fig. 6.4 Comparison of tangential coefficient of restitution with and without adhesion at V_{ni} = 5.0 m/s.

6.4 Critical sticking velocity

Computer simulations have been performed in order to examine the effect of impact angle on the critical sticking velocity. From (5.51) we may write

$$V_s / A = 1.84 \qquad (6.9)$$

where

$$A = \left(\frac{\Gamma^5}{\rho_1^3 E^{*2} R^5} \right)^{1/6} \qquad (6.10)$$

Figure 6.5 shows how V_s/A varies with impact angle. It can been seen that as the impact angle is increased the critical sticking velocity (speed) increases at an increasing rate. Superimposed on the figure is the curve $V_s/A = 1.84 \sec \theta$ which fits the simulation data points very well. This suggests that the critical parameter is the normal component of the impact velocity. The normal component of the critical impact velocity, as obtained from the

computer simulations, has been plotted against impact angle for different particle sizes in Fig. 6.6. The figure shows that, although there is some observed variation with impact angle, the normal component of the critical impact velocity is approximately constant. Simulations were repeated for different coefficients of friction. Typical results are shown in Fig. 6.7 which illustrate that, although small differences were observed for zero friction, the critical sticking velocity is not affected by friction. Computer simulations have also been conducted to examine the effects of other factors, such as surface adhesion energy, Young's modulus, and particle density. The value of the critical velocity changes with particle and target material properties, but the variation of the critical velocity with impact angle remains the same. This, of course, confirms the validity of Fig. 6.5 for the normalised critical velocity. Therefore, we may conclude that the critical sticking velocity (speed) below which particles will remain adhered to the target surface is given by

$$V_s = \frac{1.84}{\cos\theta}\left(\frac{\Gamma^5}{\rho_1^3 E^{*2} R^5}\right)^{1/6} \qquad (6.11)$$

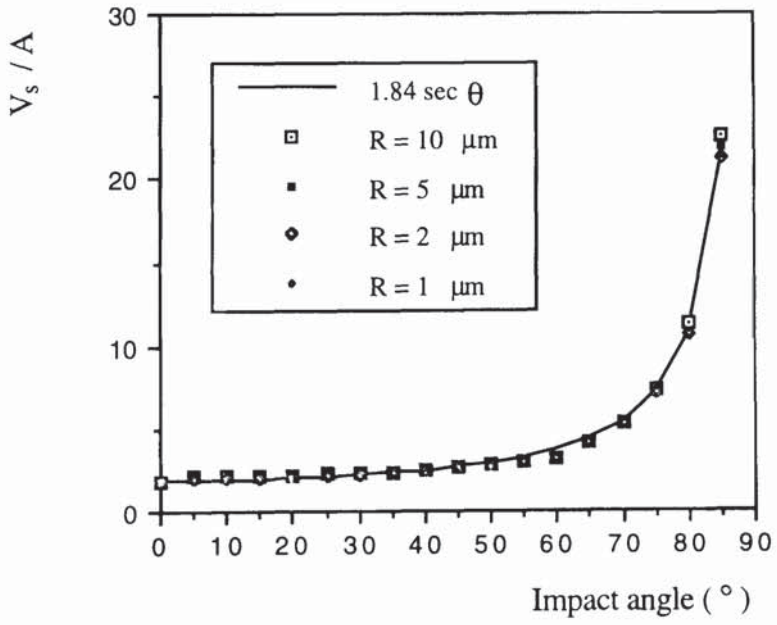

Fig. 6.5 Normalised critical impact velocity.

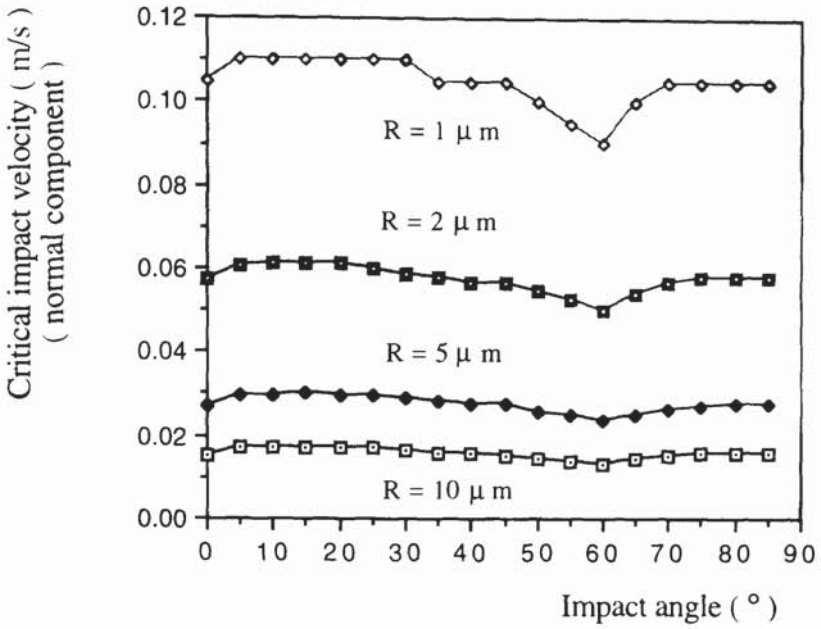

Fig. 6.6 Normal component of the critical sticking velocity.

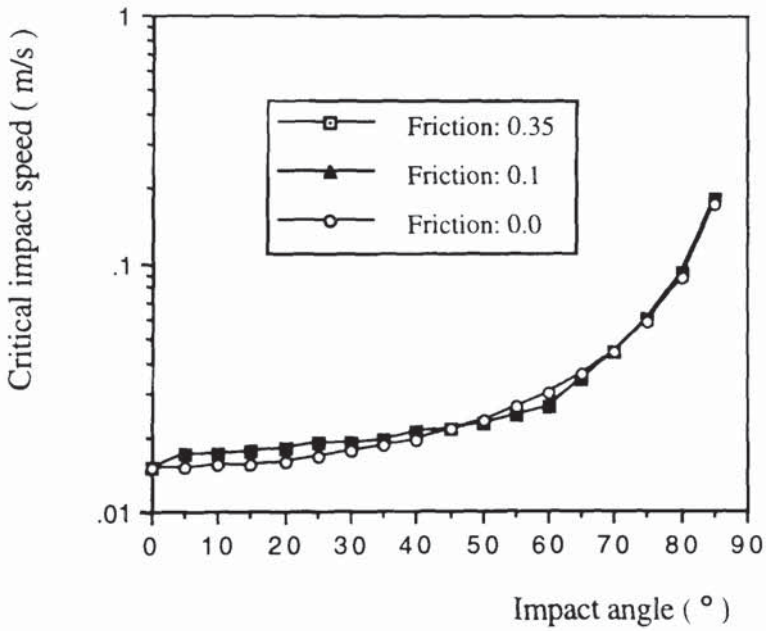

Fig. 6.7 Effect of friction on the onset of bounce: particle radius R = 10 μm.

In the analysis of particle impact behaviour the energy lost due to elastic wave propagation, as demonstrated in Chapter 4, is not significant and therefore is ignored. However, in computer simulated impacts, if the particle sticks to the wall and this energy loss mechanism is not considered the contact forces will continue to oscillate indefinitely and an equilibrium state will never be attained. Furthermore, in the computer simulated experiments of particle systems in which energy is transferred through the solid bodies the energy loss has to be considered in order to reach a quasi-static equilibrium state. To account for this type of energy dissipation, " contact damping " is used. More details about the so-called damping forces are provided in Chapter 7. The significance of normal and tangential contact damping is demonstrated in Fig. 6.8, which shows the evolution of the normal and tangential forces with time when the impact speed is less than the critical sticking value. It can be seen that the amplitude of both the normal and tangential forces decreases with time and finally zero values are approached when the state of equilibrium is obtained. The corresponding relationship between normal force and tangential force is shown in Fig. 6.9.

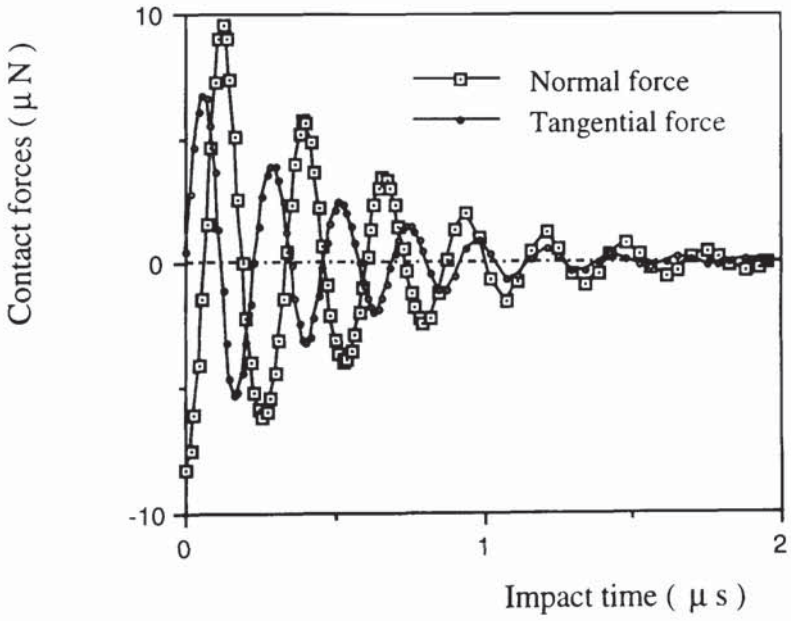

Fig. 6.8 Variations of normal and tangential forces with impact time for an impact speed of 0.01 and impact angle of 60°.

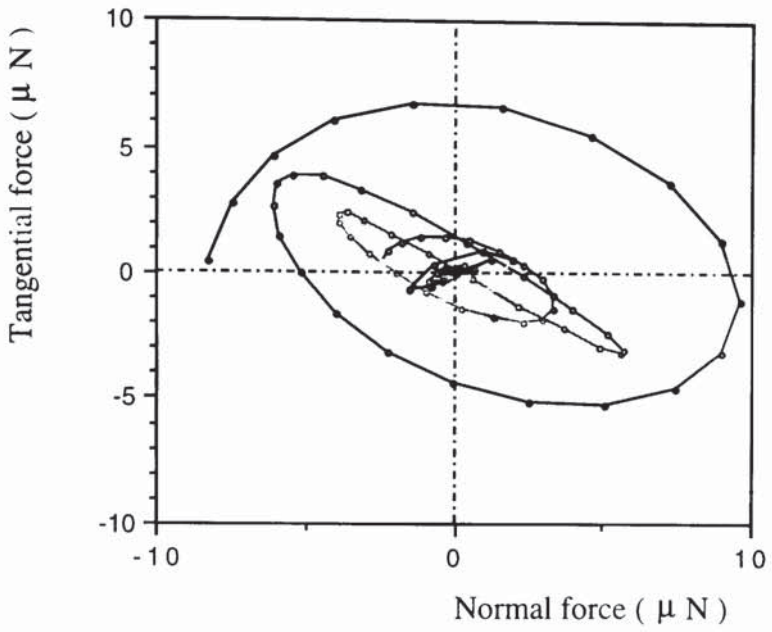

Fig. 6.9 Oscillation of normal and tangential forces when the particle sticks with the target wall at an impact speed of 0.01 m/s and impact angle of 60°.

6.5 Bounce behaviour of elastic spheres

Since it was shown in Section 6.3 that high speed impacts are not significantly affected by surface adhesion, this section will focus on normal approach velocities in the range $V_s < V_{ni} < V_y$.

6.5.1 Effect of initial particle rotation

It was shown in Fig. 4.51 that the normalised angular velocity at rebound, $\phi_r = \omega_r R/V_{ni}$, resulting from oblique impacts of non-adhesive elastic spheres with no initial rotation increased with impact angle to a maximum value of 1.75 when sliding occurred throughout the impact. It was also shown that the maximum value of ϕ_r decreased as the normal approach velocity increased, for $V_{ni} > V_y$. Figure 6.10 shows ϕ_r plotted against impact angle

for three different constant normal approach velocities in the range of $V_s < V_{ni} < V_y$. It can be seen that, for a normal approach velocity of 0.5 m/s, the maximum value of $\phi_r \approx 1.75$ in close agreement with the non-adhesive case. As the normal approach velocity decreases the maximum value of ϕ_r increases. For $V_{ni} = 0.02$ m/s the maximum normalised rebound angle velocity $\phi_r \approx 5.15$. However, this corresponds to a tangential rebound velocity of the contact patch of 0.103 m/s which is less than the value of 0.875 m/s corresponding to $V_{ni} =$ 0.5 m/s.

Simulations have been performed in order to examine the effect of initial particle rotation, defined by the normalised initial angular velocity ϕ_i, on the rebound condition following oblique impacts. The results obtained for a constant normal approach velocity of 0.1 m/s are used to illustrate the typical behaviour. Figure 6.11 shows the effect of initial rotation on the rebound angle of the particle centroid, for both positive and negative values of initial angular velocity. The corresponding reflection angle of the contact patch is shown in Fig. 6.12. It can be seen that, for the case of no initial particle rotation, the behaviour is similar to that reported in Section 4.3.2 for non-adhesive elastic spheres (see Figs. 4.13 and 4.14) except at small impact angles. Figures 6.11 and 6.12 show that both the particle centroid and the contact patch rebound back along the initial approach trajectory if the impact angle $\theta \leq 25°$. This phenomenon was also observed by Thornton and Yin (1991). By examining the detailed contact force evolution during the simulated impacts, it was identified that the initial peeling process of Savkoor and Briggs (1977) was completed during the loading stage for $\theta > 25°$. For the impacts with $\theta \leq 25°$, when the " bounce back " phenomenon was observed, tangential peeling was only completed as the end of the unloading stage was approached.

The effect of initial rotation, as illustrated in Figs. 6.11 and 6.12, suggests that the data may be normalised by the same procedures as described in Section 4.4.2. Therefore, the data shown in Fig. 6.12 is also shown in Fig. 6.13 in terms of ($e_n\psi_i/\lambda$) plotted against ($\psi_i/\lambda+\phi_i/\mu$). It can be seen that the pattern of behaviour is similar to that obtained for non-

adhesive elastic spheres, as shown in Fig. 4.49, except for two features. First, for adhesive elastic spheres there is the bounce back phenomenon at small angles, as described above. The second difference is that the remainder of the curve is displaced by an amount $\pm \Delta$ in comparison with the non-adhesive case. It would appear, from the results shown, that $\Delta \approx (\tan \theta_c) / \mu$, where θ_c is the maximum impact angle at which bounce back occurs when there is no initial particle rotation.

Figure 6.14 shows the effect of initial particle rotation on the tangential coefficient of restitution. Using the same normalisation procedures as in Section 4.4.2, the data has been reported in Fig. 6.15. Comparing Fig. 6.15 with Fig. 4.50 the same differences are observed as found in the comparison of the contact patch behaviour for adhesive and non-adhesive particles. This is as would be expected due to the theoretical relationship presented in Section 4.3.1.

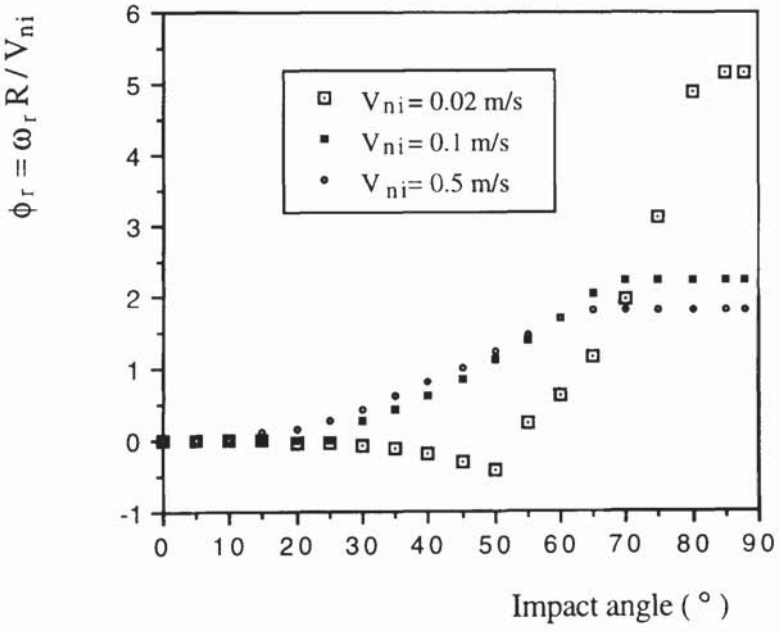

Fig. 6.10 The normalised departure angular velocities caused by oblique impacts with no initial particle rotation (interface energy $\Gamma = 0.2$ J/m^2).

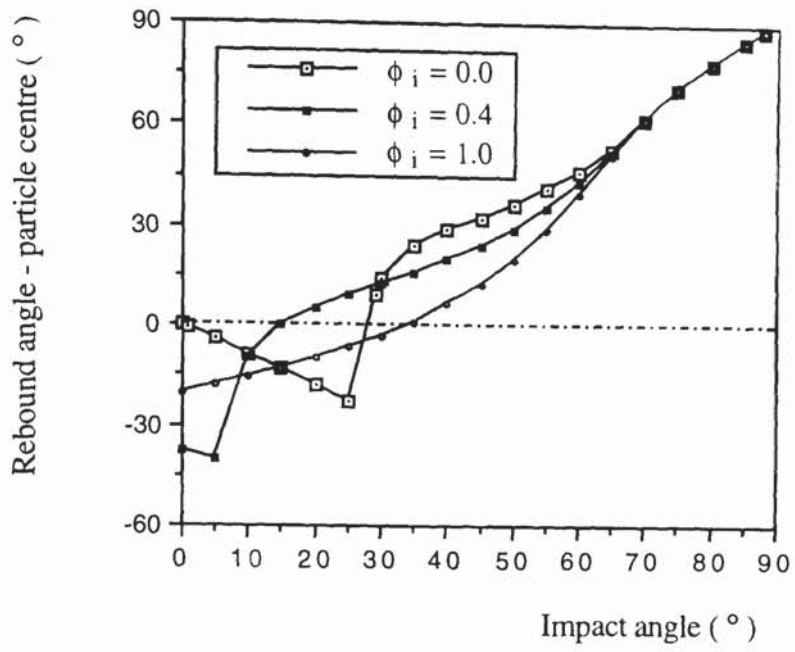

(a)

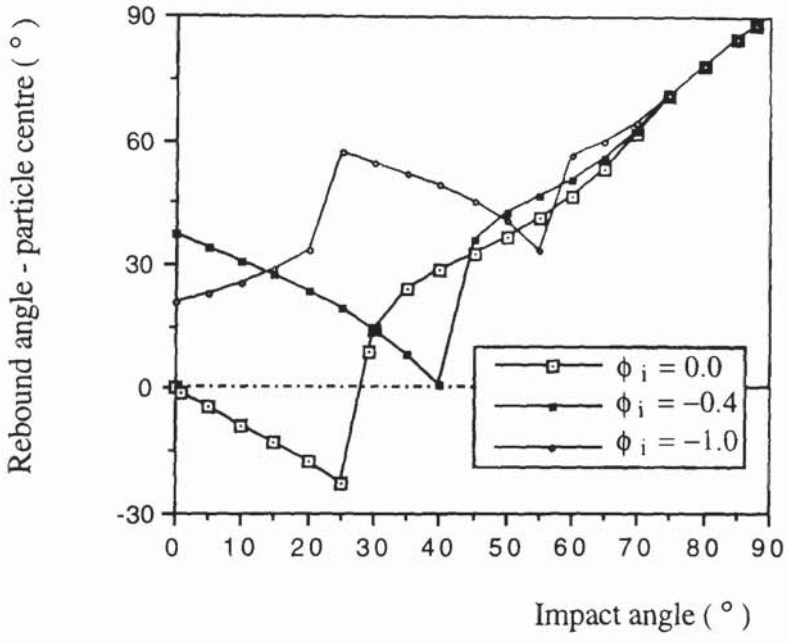

(b)

Fig. 6.11 Effect of initial rotation on the rebound angle of particle centre at a constant normal approach velocity of 0.1 m/s with positive (a) and negative (b) initial angular velocities.

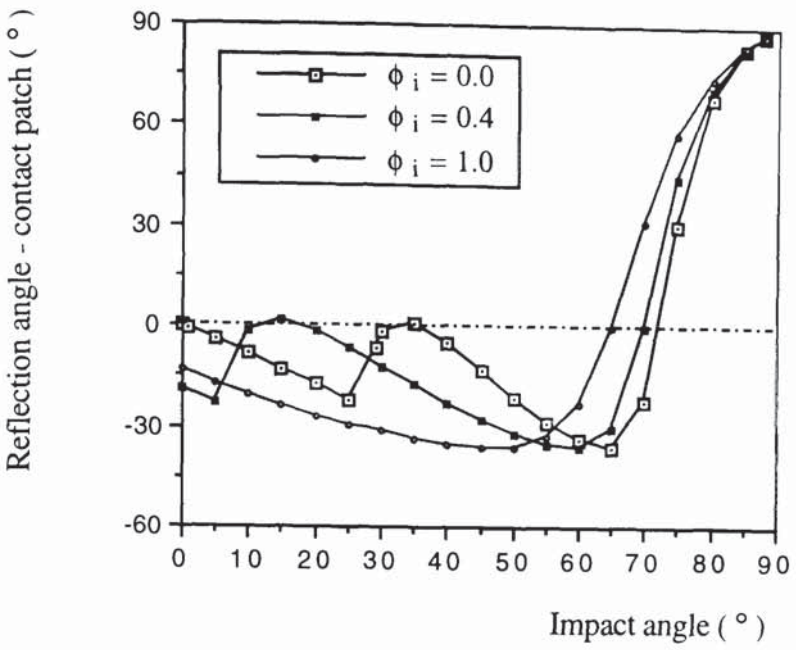

(a)

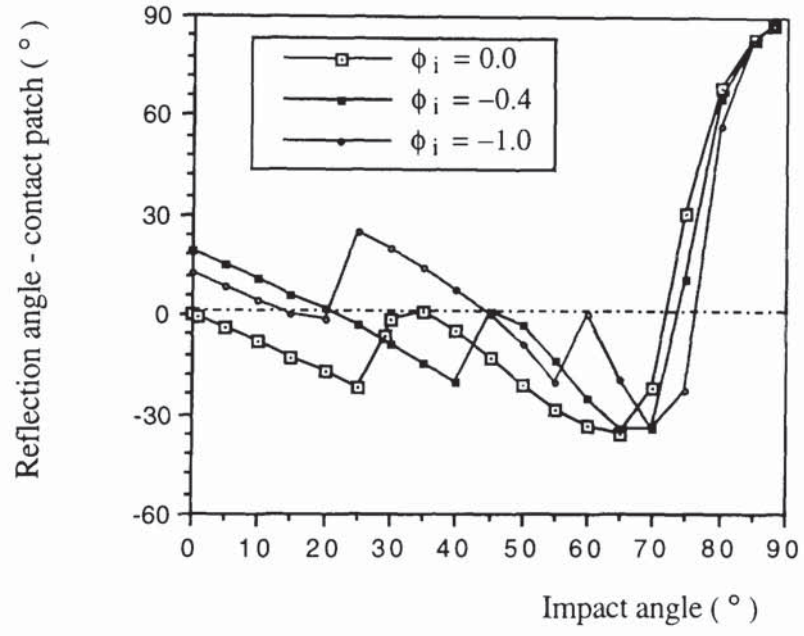

(b)

Fig .6.12 Effect of initial rotation on the reflection angle of contact patch at a constant normal approach velocity of 0.1 m/s with positive (a) and negative (b) initial angular velocities.

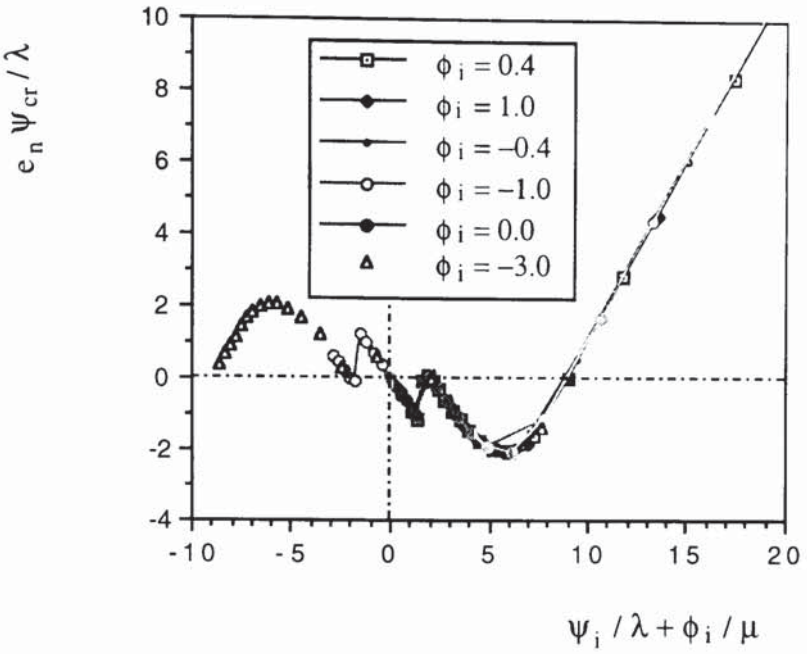

Fig. 6.13 Normalised reflection angle against the parameter $\psi_i/\lambda+\phi_i/\mu$ for different initial angular velocities (V_{ni} = 0.1 m/s).

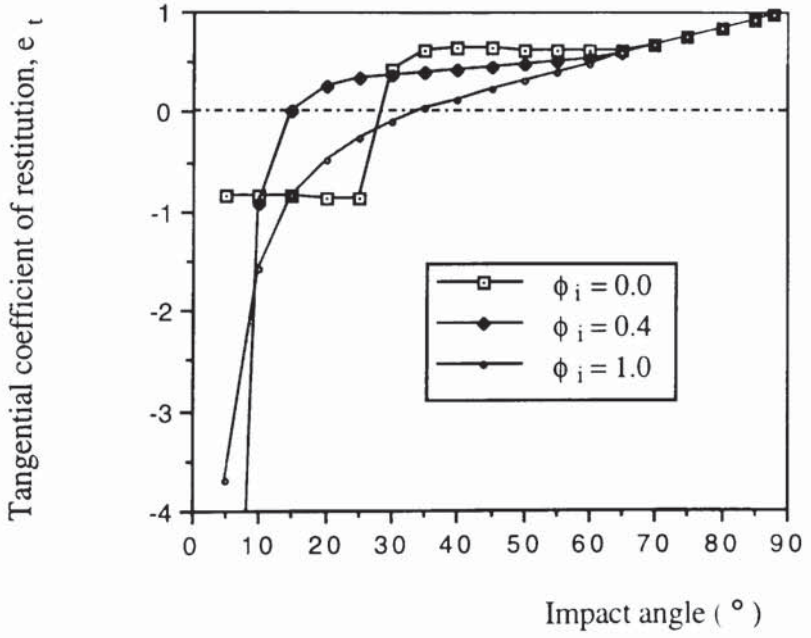

(a)

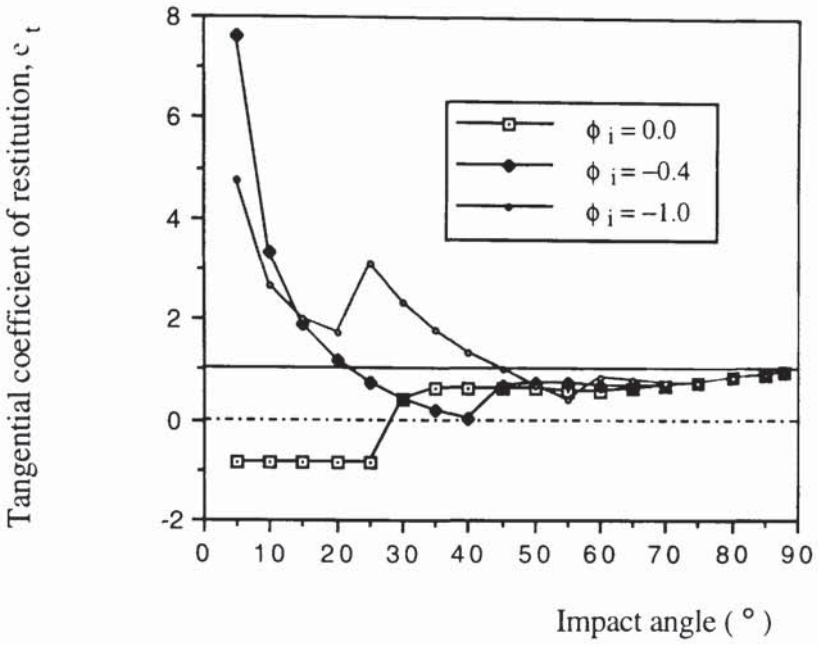

(b)

Fig. 6.14 Tangential coefficient of restitution against impact angle with positive (a) and negative (b) initial angular velocities (V_{ni} = 0.1 m/s).

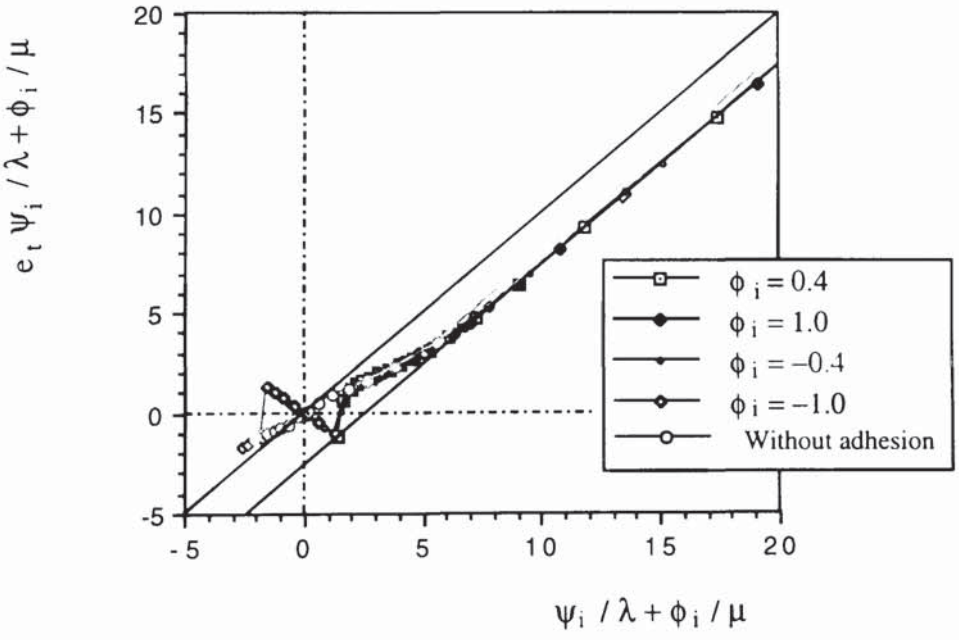

Fig. 6.15 Normalised tangential coefficient of restitution against the parameter $\psi_i/\lambda+\phi_i/\mu$ for different initial angular velocities (V_{ni} = 0.1 m/s).

6.5.2 Effect of impact velocity

The effect of impact velocity on the bounce behaviour of adhesive elastic spheres is illustrated by results of oblique impact simulations using three normal approach velocities V_{ni} = 0.02, 0.1 and 0.5 m/s, which correspond to normal coefficients of restitution e_n = 0.617, 0.982 and 0.993 respectively. In Figs. 6.16, 6.17 and 6.18, the tangential coefficient of restitution, the rebound angle of the particle centroid and the reflection angle of the contact patch are plotted against impact angle for the three normal approach velocities.

The three figures show that, for the case of V_{ni} = 0.5 m/s when impacted at angles of 5° and 10°, the particle rebounds back along the initial approach trajectory without any particle rotation having been generated by the impact. For $\theta \geq 25°$ the tangential coefficient of restitution, as shown in Fig. 6.16, are almost identical to the values obtained for the non-adhesive case, which is superimposed on the figure. When V_{ni} = 0.1 m/s, the particle rebounds backwards for $\theta \leq 25°$ but the rebound angle is not equal to the impact angle because $e_t \approx -0.85$. When $\theta \geq 35°$ the variation of e_t with impact angle is similar to that of the non-adhesive case but the values are significantly different.

If the impact velocity is only slightly higher than the critical sticking velocity, e.g. V_{ni} = 0.02 m/s, then it is clear from Figs. 6.16, 6.17 and 6.18 that the surface energy has a significant effect on the rebound conditions. Even at large impact angles the tangential coefficients of restitution are very different from the values obtained with no adhesion. Figures 6.16 and 6.17 show that the particle bounces forward for $\theta \leq 35°$ and that the bounce back behaviour is only observed in the range $40° \leq \theta \leq 50°$. Figure 6.18 shows that, for $\theta \leq 50°$, the contact patch moves forward at the end of the collision and a comparison of the rebound angles and reflection angles over this range of the impact angles indicates that particle rotation occurs as a result of the impact.

The data shown in Fig. 6.18 has been replotted in Fig. 6.19 in terms of $(e_n \psi_{cr} / \lambda)$

against (ψ_i/λ) with the non-adhesive case superimposed. It can be seen that, when sliding occurs throughout the impact, parallel linear relationships are obtained. In Chapter 4 it was shown that, for the continuous sliding condition, the data sets could be normalised by using the parameters ($2e_n\psi_{cr}/\lambda(1+e_n)$) and ($2\psi_i/\lambda(1+e_n)$). However, it is clear from Fig. 6.19 that this procedure will not work but separates the data sets even more. A method of normalising the data shown in Fig. 6.19 for the effect of adhesion has not been found and this aspect of the work requires further investigations.

6.5.3 Effect of friction

For small impact angles the tangential peeling process is only completed as the end of the unloading stage is approached. Consequently, it is not expected that friction will affect the bounce behaviour for these impact angles and Fig. 6.20 confirms this expectation. When peeling is completed during loading, the figure also indicates that, as found for non-adhesive elastic spheres, the minimum tangential coefficient of restitution is independent of friction. In Fig. 6.21 the nondimensional reflection angle of the contact patch ψ_{cr}/λ is plotted against the nondimensional impact angle ψ_i/λ. If peeling is completed during the loading stage then

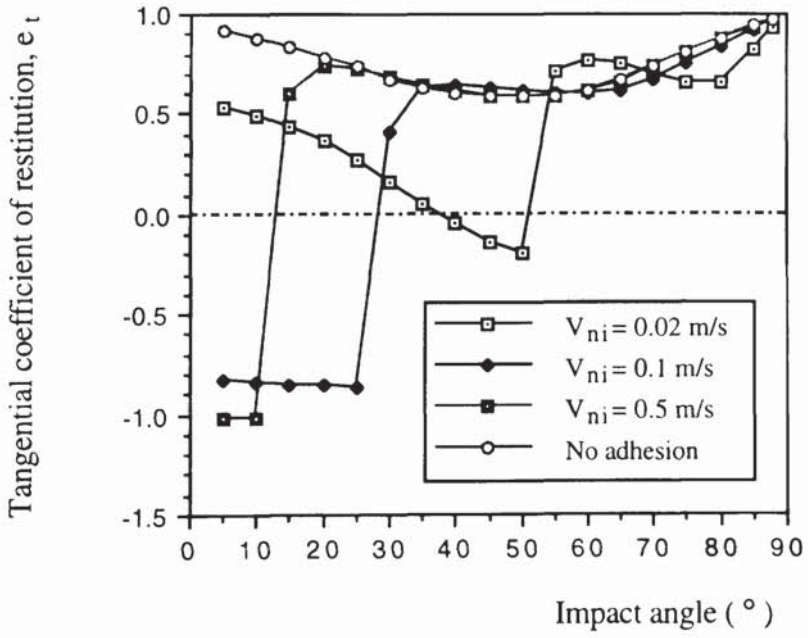

Fig. 6.16 Tangential coefficient of restitution against impact angle.

the data is satisfactorily normalised for the effect of friction, as was shown in Chapter 4 for non-adhesive elastic spheres. Therefore, as shown in Fig. 6.22, the relationship between the tangential coefficient of restitution and the impact angle may be normalised by using the parameter ψ_i/λ, provided that the peeling process is completed during loading.

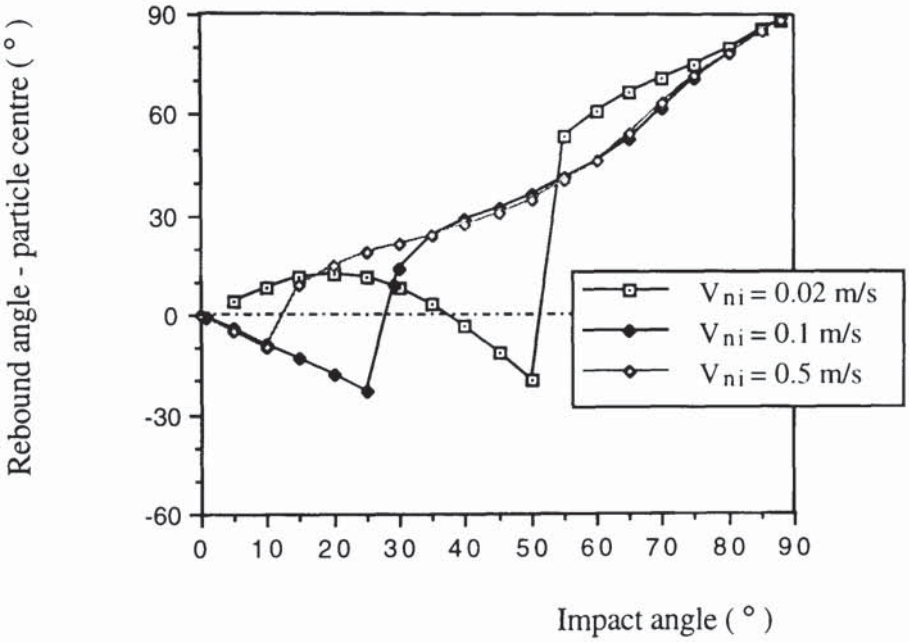

Fig. 6.17 Rebound angle of the particle centre against impact angle.

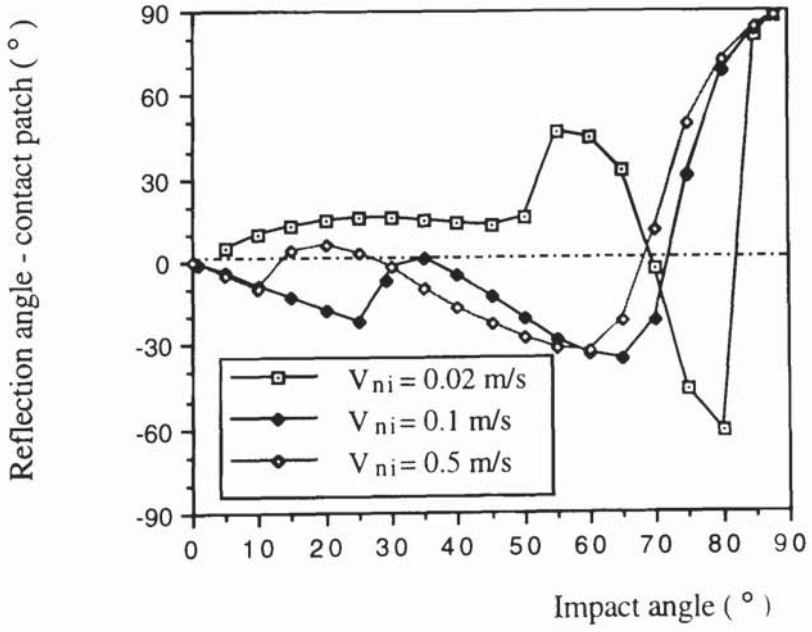

Fig. 6.18 Reflection angle of the contact patch against impact angle.

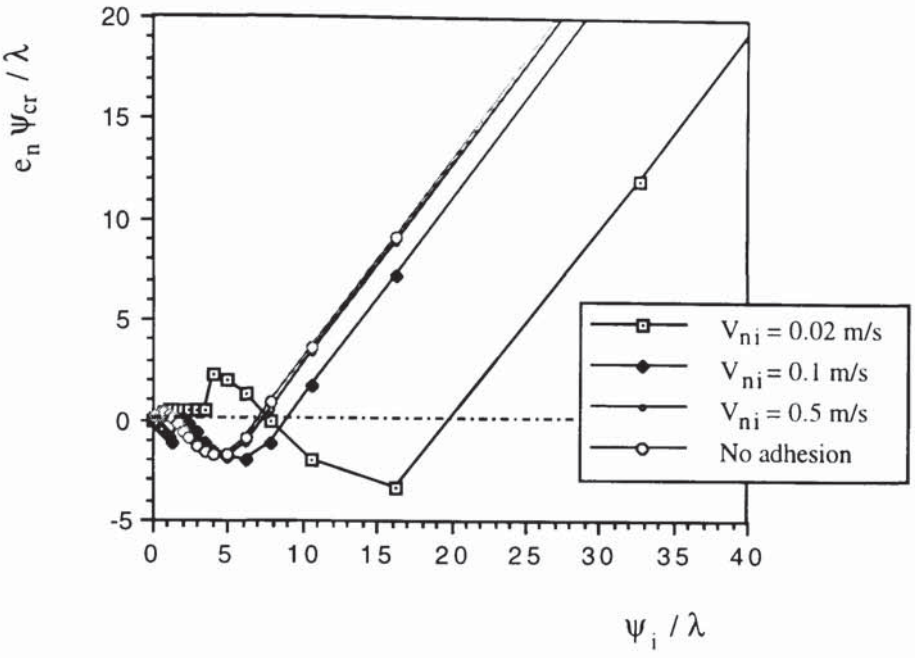

Fig. 6.19 Nondimensional reflection angle of the contact patch against non-dimensional impact angle for different normal approach velocities.

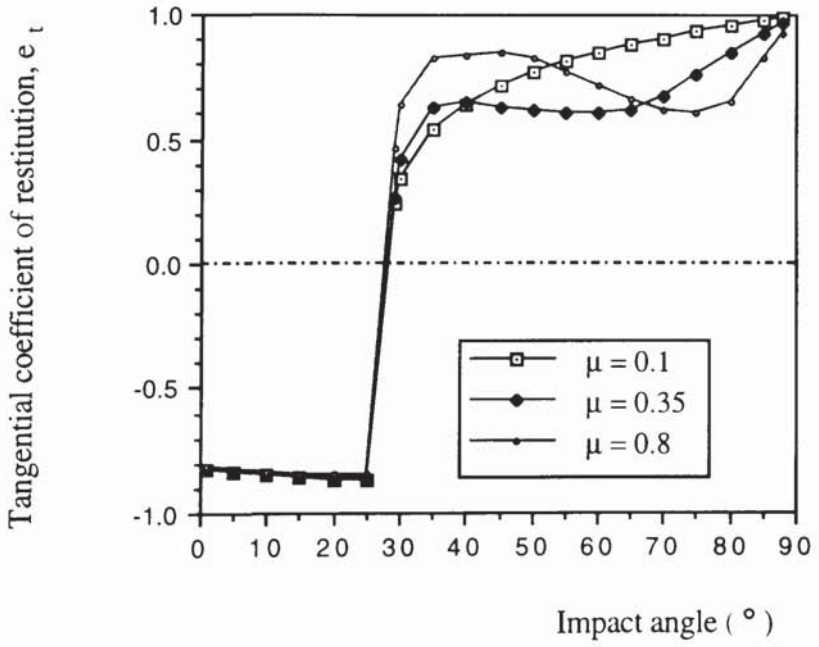

Fig. 6.20 Tangential coefficient of restitution against impact angle for different values of friction at V_{ni} = 0.1 m/s.

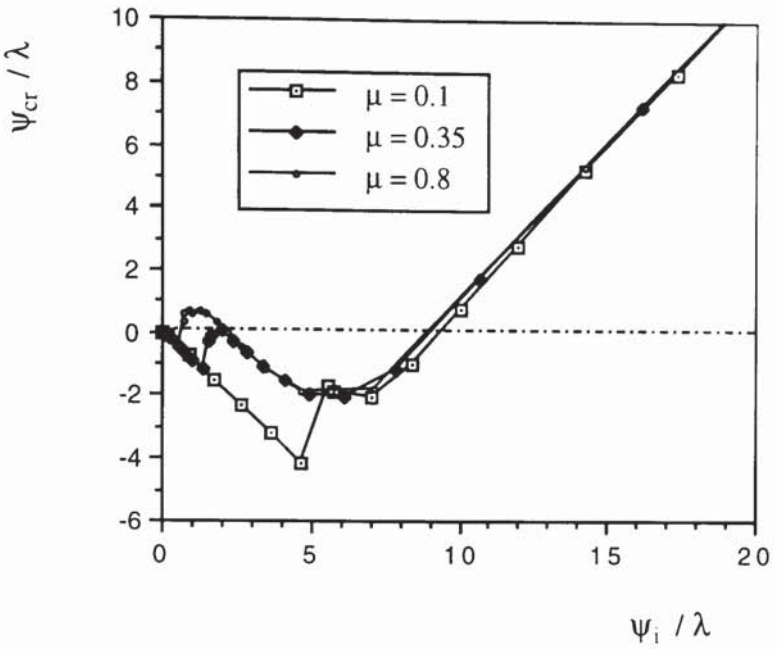

Fig. 6.21 Nondimensional reflection angle against nondimensional impact angle for different values of friction at V_{ni} = 0.1 m/s.

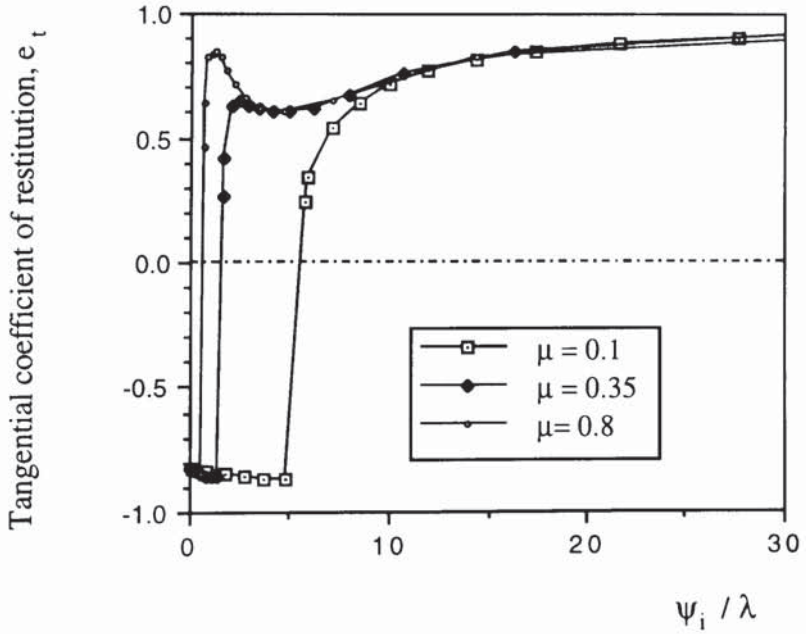

Fig. 6.22 Tangential coefficient of restitution against nondimensional impact angle for different values of friction at V_{ni} = 0.1 m/s.

6.6 Summary

Computer simulations have been performed to examine the capture and rebound of adhesive particles upon oblique collisions. At high impact speeds, the effect of surface adhesion on the bounce conditions has been found to be insignificant since plastic deformation dominates the process of the impact. The results obtained for the case of no adhesion, presented in Chapter 4, can therefore be used for the impacts of adhesive spheres.

Variations in particle and target properties can lead to a change for the value of critical impact velocity but the curve pattern of velocity with impact angle always remains the same. It has been found that the normal component of the particle initial velocity is the dominant factor determining whether the particle bounces off or sticks to the surface. The computer simulation results also show that the effect of friction on the onset of bounce is not significant due to the adhesion between two contacting surfaces. Nevertheless, there is a need for detailed experimental observations to confirm the prediction of computer simulated results.

For the rebound behaviour of elastic adhesive spheres, the effects of initial particle rotation, friction and impact velocity on particle bounce are examined. It has been found that the surface adhesive peeling is one of the most influential factors affecting the bounce behaviour and the transition of the peeling failure from unloading to loading leads to a significant change in the magnitude of the bouncing parameters. It has been demonstrated that, using the same normalisation techniques as for non-adhesive particles, scaling rules are available in order to account for the variations in initial particle rotation and friction. However, for the effect of impact velocity, further investigation is needed.

Chapter 7 Computer program TRUBAL

7.1 Introduction

TRUBAL is a computer program for the modelling of three-dimensional particle systems. Using the Distinct Element Method (DEM) the structure of TRUBAL resembles that of the two-dimensional program BALL. At Aston, the adapted program from Cundall's 1988 version of TRUBAL has been modified and enhanced extensively by incorporating particle-particle interaction laws based on theoretical contact mechanics. Also, a number of facilities such as simultaneous screen monitoring, three-dimensional graphics output, assembly generation of random and regular packings, and the introduction of planar walls have been included in the program. Current computer simulations at Aston are being applied to quasi-static shear deformation of dense granular media, ensemble properties of mixtures of hard and soft spheres, hopper flow, particle crushing and agglomerate impact fracture / fragmentation.

There are two versions of TRUBAL at Aston. The basic version is used to simulate dry particle assemblies while the other one is newly developed from the basic version in order to model pendular liquid bridges in moist particle systems. In the basic version, for the case of no adhesion, the normal and tangential contact forces are based on Hertzian theory and Mindlin and Deresiewicz (1953) respectively. In the presence of adhesion the JKR model is used for the normal contact stiffness while the tangential behaviour is governed according to Savkoor and Briggs (1977) and Thornton (1991).

In this Chapter a short introduction to the simulation procedures and program structure is

first presented with a focus on the storage of ball data, wall data, and contact links in the main memory array. Based on the basic version of TRUBAL, incorporation of plastic deformation without adhesion according to the theory described in Chapter 3 is then discussed. For adhesive elasto-plastic particles, the implementation of the modified JKR model presented in Chapter 6 is described. Finally a brief description about the use of the program is given with an emphasis on the simulation of single particle impacts with a wall and agglomerate-wall collisions.

7.2 Main structure of TRUBAL

7.2.1 Simulation procedure and program structure

A granular medium is composed of distinct particles which displace independently from one to another and interact only at the contact points. The discrete character of the medium results in a complex behaviour under conditions of loading and unloading. The process of simulation in TRUBAL consists of assembly generation, cyclic calculation of contact forces and particle movements, data processing for various purposes, and output of numerical data and graphic plotting. The basic structure of TRUBAL developed by Cundall and Strack (1979) remains in the present version of the program although a number of modifications, especially in the interaction laws, have been made and more options have been provided in order to deal with a wide range of practical engineering problems.

Figure 7.1 shows the main structure of TRUBAL. At the beginning of a simulation an "input command file", which contains the operative commands and the particle parameters is connected to the main executive program. Particles and boundaries such as walls are then generated randomly or created in positions specified by the user. For a restart run the assembly and boundaries are retrieved based on the previously saved file. Using the Distinct Element Method the evolution of contact forces and particle movements is achieved through

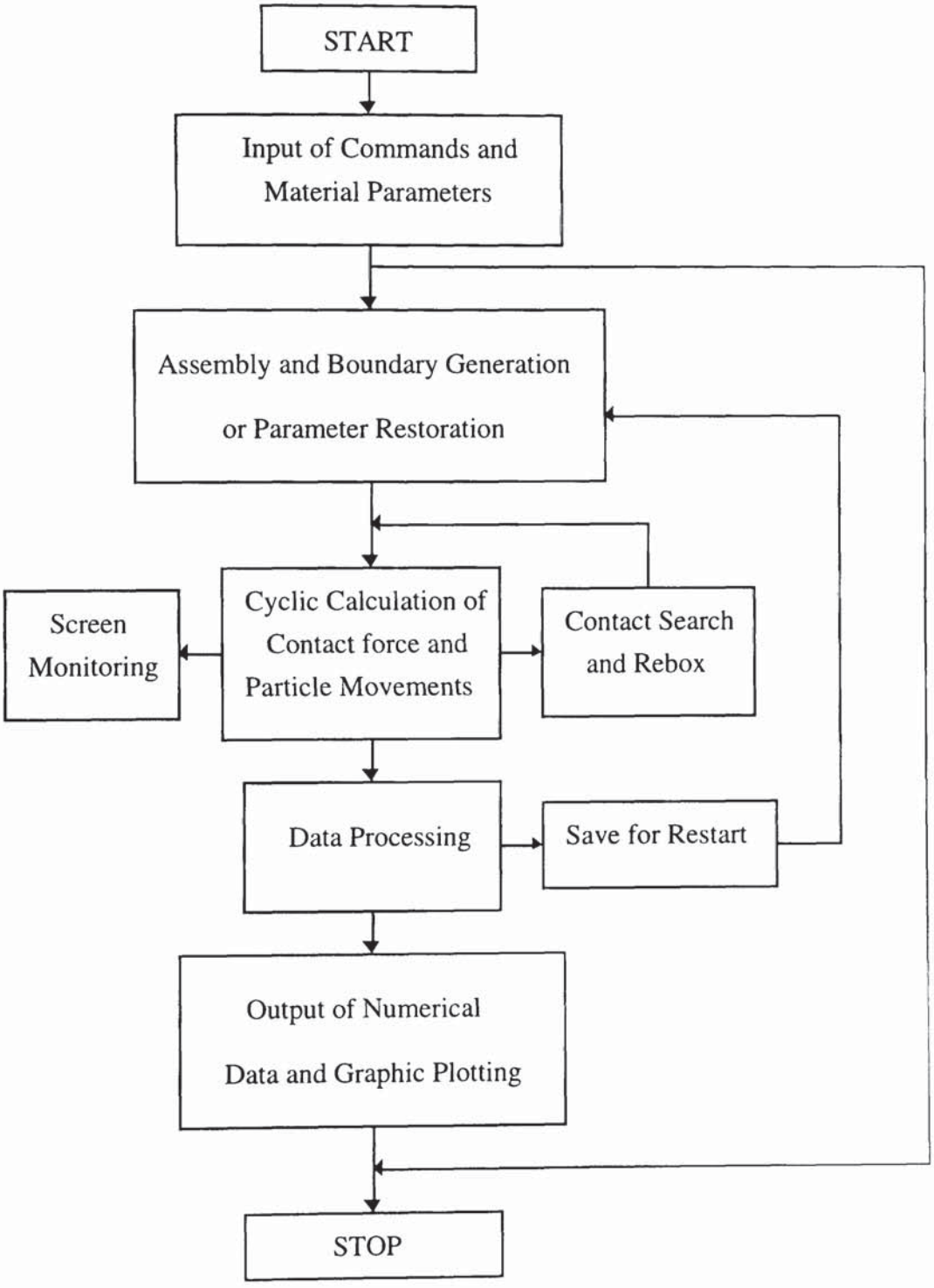

Fig. 7.1 Diagram of the program structure of TRUBAL.

a series of calculation cycles in which contact forces and particle positions are updated over each small time step. The number of cycles is set by the user.

The program identifies a cubic " workspace " which is divided up by a grid to form a series of boxes. Particles are mapped into their respective boxes according to the corners of a circumscribing cube. The maximum number of boxes in which a particle has entries is eight. When it is necessary to determine those particles that are neighbours or contacted to a given particle, only the local boxes which the particle has entered need to be searched rather than the whole defined space. The resulting contacts are stored in a linked list memory structure which allows fast re-allocation of memory when contacts are created or deleted. When a particle is mapped into a box the particles which were mapped previously into the same box are searched and their distance to the newly mapped particle is calculated. If the accumulated component of the translational displacement for a boxed particle exceeds a specified value a check is made to test if the particle then needs to be remapped into different boxes.

When executing the program, the facility of screen graphic monitoring incorporated in the current Aston version of TRUBAL simultaneously provides information such as the relationships of normal force-displacement, normal-tangential force, and tangential force-displacement for single particle collisions; energy partitions and contact number for agglomerate impact. This facility is particularly useful when the user does not know how many cycles are needed to reach a particular state of the particle system.

Computer simulation using the Distinct Element Method was originally performed by Cundall and Strack (1979) to examine the quasi-static shear deformation of compact assembles of particles. However, the computational technique lends itself more readily to many other areas of scientific and industrial interests. A variety of capabilities for data processing has been developed and enhanced in TRUBAL, enabling the users easily to access the computational results and vision images according to their own problems. The subroutines in the original version of TRUBAL, which provide contact histograms and

calculate maximum, minimum, and average contact forces and particle velocities, stress and energy partitions, are retained. The Aston version of TRUBAL provides additional facilities such as identifying clusters from a contact list of particles in contact with each other, drawing connection diagrams for the assembly and other data processing facilities related to the simulation of agglomerate impact fracture / fragmentation.

In the process of simulation the control mode, boundary conditions, and material properties may need to be changed. The results obtained at one stage can be saved for further use. With the desired parameters changed further simulation is then based on the previous stage rather than starting at the very beginning. Finally the output facilities in TRUBAL provides both printed numerical data and graphic plottings. With the printout options the results include sphere data, wall data, contact data, energy terms, stress tensor. Using the graphic plotting options the user can obtain 2-D and 3-D colour pictures of spheres, walls, contact forces, contact connection diagram, particle velocities and clusters of connected particles. The graphic package of the current version of the program is written in FORTRAN using graPHIGS API for IBM RS6000 workstations.

7.2.2 Memory partition

A single array A(I) used in TRUBAL contains all the information on particles, walls, boxes, and contacts and is continuously updated during the process of simulation. The array A(I) is equivalenced to an integer array IA(I) so that integers may also be stored. The main array can be subdivided into three parts for storing the ball data, wall data, and contact data. The dimension of each part is determined by the number of boxes and the maximum number of particles and walls set by the user. Figure 7.2 shows the main memory map.

The memory limit of I = M5 in A(I) is set in the program and can be adjusted by the user when it is necessary. If the capacity of the main memory is exceeded an error message will be given and the program stops. The addresses of M2, M3, and M3A indicate the upper

limits of the array of ball data, wall data, and box data respectively. Free memory units should always be allowed between each array. For the maximum number of balls and walls, denoted by M_{ball} and M_{wall} respectively, we have

$$M2 = M1 + M_{ball} * N_{varb} \quad (7.1)$$

$$M3 = M2 + M_{wall} * N_{varw} \quad (7.2)$$

$$M3A = M3 + 2 * N_{box} \quad (7.3)$$

where N_{varb} is the number of variables stored in each ball data array; N_{varw} is the number of variables stored in each wall data array; and N_{box} is the number of boxes. The actual storage units occupied by the arrays of ball data, wall data, and box data are less than the partitional memory because the number of particles and walls in the simulation system is less than the number defined initially. If a number of particles N_{ball} and walls N_{varb} are generated we have the upper addresses of the actual storage

$$M1A = N_{ball} * N_{varb} \quad (7.4)$$

$$M2A = M2 + N_{wall} * N_{varw} \quad (7.5)$$

$$M4 = M3A + 2 * N_{link} + N_{cont} * N_{varc} \quad (7.6)$$

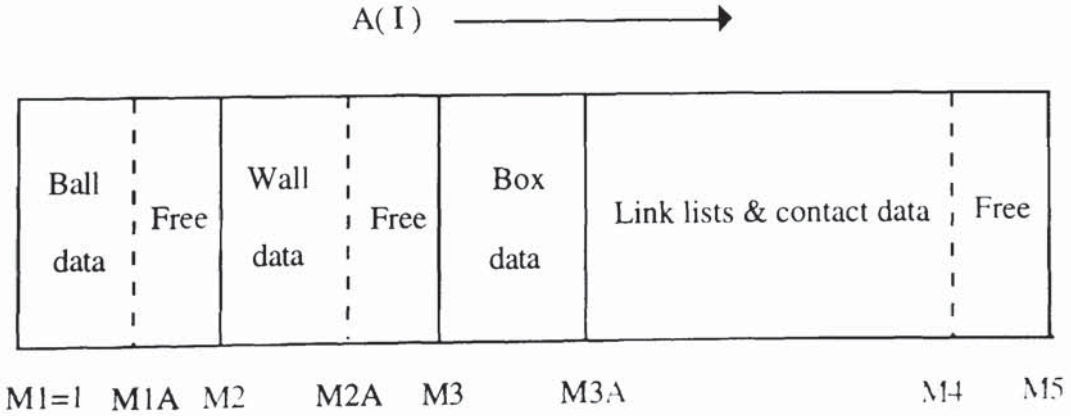

Fig. 7.2 The memory map of the main array A(I).

where N_{varc} is the number of variables stored in each contact data array; N_{link} and N_{cont} are the number of links and contacts created during the process of simulation. All of the addresses of M1A, M2, ···, M5 except M4 are fixed during each session of simulation for a given input file. However, the upper address of link lists and contact data, M4, is dynamically located depending on the number of links and contacts, which changes from time to time. The storage scheme for link lists and contact arrays is shown in Fig. 7.3.

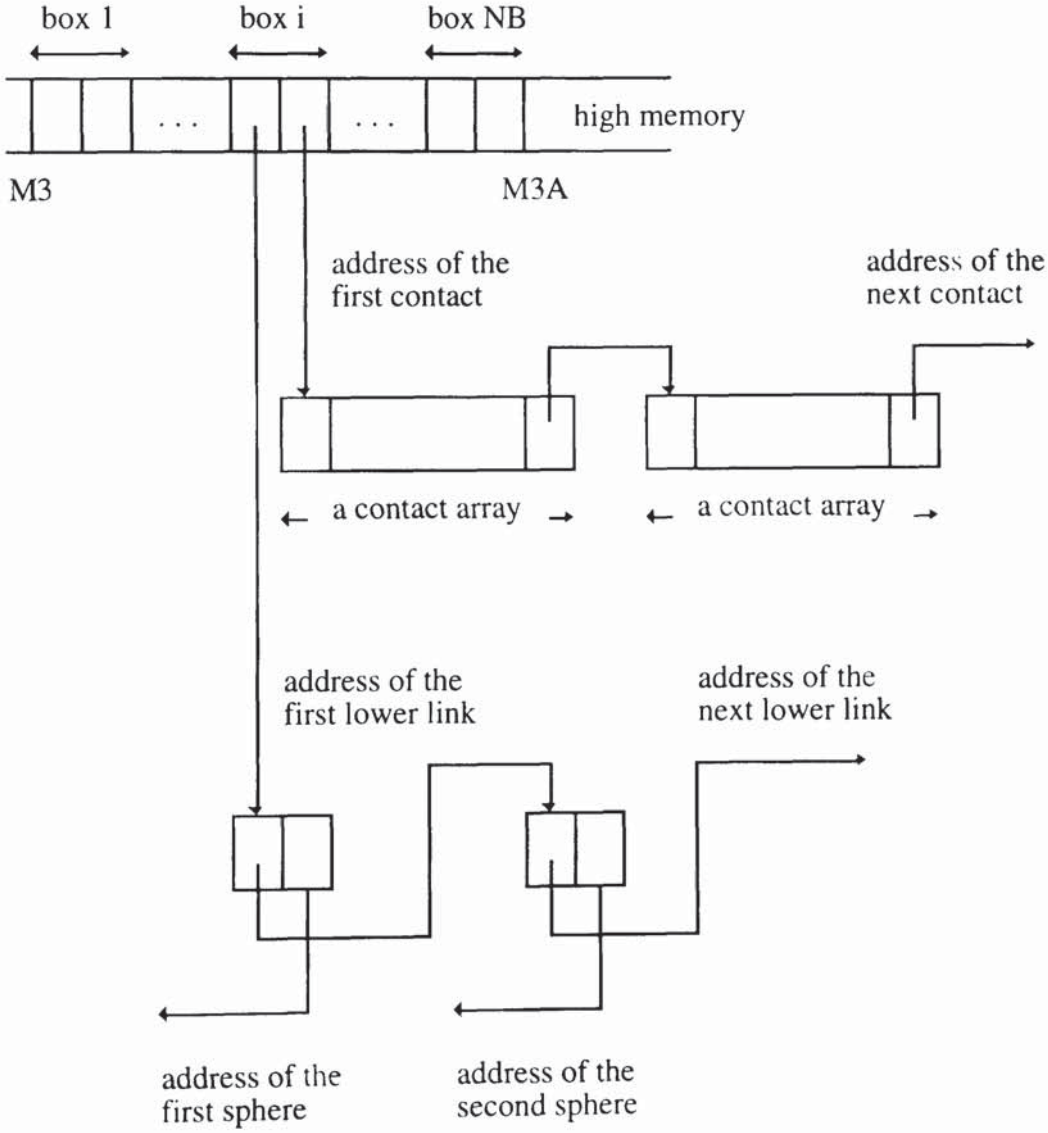

Fig. 7.3 The storage scheme for link lists and contact arrays.

7.2.3 Data array of balls, walls, and contacts

In the current version of TRUBAL the dimension size of one ball data array is set to N_{varb} = 31 and the size for the wall data array is set to N_{varw} = 41. The variables allocated into the 31 elements of a ball data array B(N_{varb}) are

B(1) to B(3): Co-ordinates of the ball centre x, y, z;

B(4) to B(6): Accumulated displacement increments Δx, Δy, Δz;

B(7) to B(9): Components of the translation velocity V_x, V_y, V_z;

B(10) to B(12): Angular displacements ϕ_x, ϕ_y, ϕ_z about x, y, and z axis respectively;

B(13) to B(15): Accumulated angular displacement increments $\Delta\phi_x$, $\Delta\phi_y$, $\Delta\phi_z$;

B(16) to B(18): Components of angular velocity ω_x, ω_y, ω_z;

B(19) to B(21): Components of out-of-balance force F_x, F_y, F_z;

B(22) to B(24): Components of out-of-balance moment M_x, M_y, M_z;

B(25): Code made up of two variables ITYPS and ITYPM, indicating the particle size type and material type respectively;

B(26) to B(29): Free;

B(30): Code identifying which agglomerate the ball belongs to (1 or 2):

B(31): Free.

The information stored in the 41 elements of a wall data array W (N_{varw}) are

W(1) to W(4): Parameters d, a, b, c which define a planar wall as the form of $d = ax + by + cz$;

W(5) to W(7): Components of wall translational velocity V_{wx}, V_{wy}, V_{wz};

W(15) to W(17): Accumulated displacement increments of the wall Δx_w, Δy_w, Δz_w;

W(19) to W(21): Components of out-of-balance wall force F_{wx}, F_{wy}, F_{wz};

W(25): Code indicating the material type ITYPM;

Others: Free.

The variables allocated in the contact data array C(N_{varc}) have always been changed from time to time. Even for the Aston version of TRUBAL the allocation of the variables varies from different research projects. For instance, based on the basic version of TRUBAL which is used to simulate dry particle assemblies ($N_{varc} = 23$). Lian (1994) extended each contact array from 23 to 31 elements to add liquid bridge forces for the simulation of moist particle systems. In this study when implementing plastic deformation into the computer code the number of variables in each contact array is set to $N_{varc} = 27$ and the allocations in the contact array are as follows

C(1) to C(3): Components of the tangential force at the contact point T_x, T_y, T_z;

C(4): Normal contact force (Hertz, or JKR, or plastic contact force), P;

C(5) to C(6): Addresses of the two bodies in contact (ball-ball or wall-ball);

C(7) to C(9): Components of the relative tangential displacement δ_x, δ_y, δ_z;

C(10): Resultant tangential displacement, δ;

C(11): Resultant tangential force at the contact point, T;

C(12): Tangential force from which unloading commenced, T* ;

C(13): Tangential force from which reloading commenced, T** ;

C(14): Accumulated distance that the tangential force falls short of its equivalent curve of constant normal force, DD;

C(15): Tangential peeling force in the presence of adhesion, T_c;

C(16): Interfacial surface energy, $\gamma = \Gamma/2$;

C(17): Radius of the contact area, a;

C(18): Code indicating the direction of the tangential force, CDF(1 or -1);

C(19): Free;

C(20): Code to indicate if the work done in breaking contact is to be calculated (0 or -10);

C(21): Normal plastic contact force at the transition point from loading to unloading, P*;

C(22): Equivalent particle radius, R_p;

C(23): Equivalent elastic contact force determining contact radius. P_e without adhesion and P_1 with adhesion;

C(24): Contact radius at initial yield. a_y;

C(25): Normal displacement at recontact point. α_p;

C(26): Code indicating the direction of loading in the JKR curve (1 or -1);

C(27): Link to the address of next contact.

An explanation of the variables partitioned in C(21) to C(26) will be given in the next section.

7.3 Incorporation of plastic deformation using DEM

7.3.1 System evolution

Newton's equations are applied in TRUBAL to govern the motion and displacement of particles in the simulated assembly, where the related parameters such as displacements ($\alpha(t)$, $\delta(t)$), velocities ($V(t)$, $\omega(t)$), and contact forces ($P(t)$, $T(t)$) are time dependent. Using the Distinct Element Method the evolution of a dynamic process consists of a series of calculation cycles in which the state of the particle system is advanced over a small increment of time Δt. For the finite difference method the out-of-balance force and acceleration of the particle are assumed to be constant during the given interval of time.

According to Newton's second law we have

$$F_i(t) + mg_i - \beta_g \frac{V_i(t+\Delta t) + V_i(t)}{2} = m \frac{V_i(t+\Delta t) - V_i(t)}{\Delta t} \qquad (7.7)$$

$$M_i(t) - \beta_g \frac{\omega_i(t+\Delta t) + \omega_i(t)}{2} = I \frac{\omega_i(t+\Delta t) - \omega_i(t)}{\Delta t} \qquad (7.8)$$

from which the new velocity components of the particle are obtained

$$V_i(t+\Delta t)=\frac{m/\Delta t-\beta_g/2}{m/\Delta t+\beta_g/2}V_i(t)+\frac{F_i+mg_i}{m/\Delta t+\beta_g/2} \tag{7.9}$$

$$\omega_i(t+\Delta t)=\frac{I/\Delta t-\beta_g/2}{I/\Delta t+\beta_g/2}\omega_i(t)+\frac{M_i}{I/\Delta t+\beta_g/2} \tag{7.10}$$

where Δt is the time step; I is the moment of inertia of the sphere; β_g is the coefficient of global damping; i = 1,2,3 indicates the three directions in x, y, z coordinate system respectively; F_i and M_i are the components of the out-of-balance force and momentum respectively while g_i are the components of gravity.

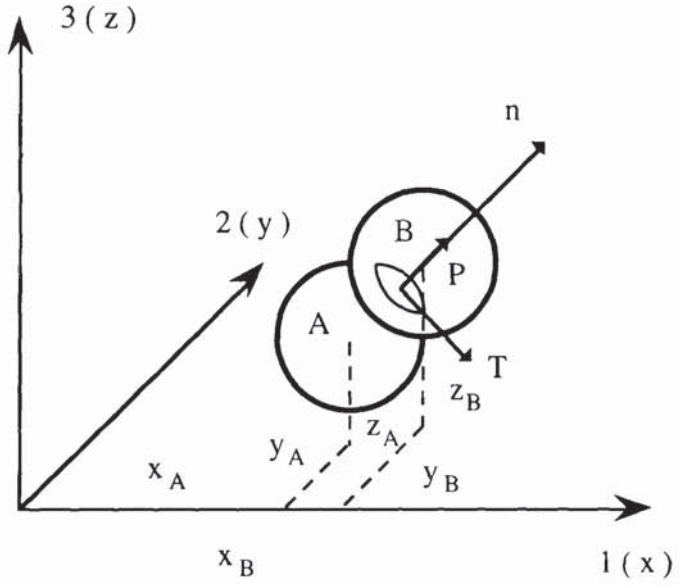

Fig. 7.4 Two contacting spheres in a 3-D Cartesian coordinate system.

If a pair of spheres A and B are in contact, as shown in Fig. 7.4, the relative normal displacement increment at the contact during a small time step is given by

$$\Delta\alpha = (V_i^B - V_i^A)\, n_i\, \Delta t \tag{7.11}$$

where V_i^B and V_i^A are the linear velocities of sphere A and B respectively; n_i are the direction cosines of the unit vector normal to the contact plane and with a direction from sphere A to sphere B. For elastic spheres with adhesion (the no adhesion case corresponds to $\Gamma = 0$, $P_c = 0$), the normal force increment is given by

$$\Delta P = k_n^e \Delta\alpha \qquad (7.12)$$

where

$$k_n^e = 2E^*a\,\frac{3 - 3\sqrt{a_c/a}}{3 - \sqrt{a_c/a}} = 2E^*a\,\frac{3\sqrt{P_1} - 3\sqrt{P_c}}{3\sqrt{P_1} - \sqrt{P_c}} \qquad (7.13)$$

and

$$P_1 = P + 2P_c \pm \sqrt{4PP_c + 4P_c^2 - T^2E^*/4G^*} \qquad (7.14)$$

which is the effective Hertzian force. In the case of no adhesion both the pull-off force P_c and the contents in the square root in (7.14) are set to zero although the tangential force T is not zero during oblique loading. The new normal contact force is therefore given by

$$P(t + \Delta t) = P(t) + \Delta P = P(t) + k_n^e \Delta\alpha \qquad (7.15)$$

and the contact radius is updated using

$$a(t + \Delta t) = \sqrt[3]{\frac{3R^*P_1(t + \Delta t)}{4E^*}} \qquad (7.16)$$

In a three dimensional space the tangential displacement components are calculated from

$$\Delta\delta_i = (V_i^B - V_i^A)\Delta t - \Delta\alpha n_i - (\overset{A}{\omega}_{i+1} n_{i+2} - \overset{A}{\omega}_{i+2} n_{i+1}) R_A \Delta t$$
$$- (\overset{B}{\omega}_{i+1} n_{i+2} - \overset{B}{\omega}_{i+2} n_{i+1}) R_B \Delta t \qquad (7.17)$$

where R_A and R_B are the radii of the two contacting spheres. The updated tangential displacement components are

$$\delta_i(t + \Delta t) = \delta_i(t) + \Delta\delta_i \qquad (7.18)$$

and the resultant tangential displacement is given as

$$\delta(t + \Delta t) = \text{sign}[\delta(t + \Delta t)]\,\text{sign}[\delta_i(t + \Delta t)\Delta\delta_i]\sqrt{\delta_i(t + \Delta t)^2} \qquad (7.19)$$

However, the Mindlin and Deresiewicz (1953) tangential force-displacement relationship is non-linear and loading history dependent. Consequently the new tangential force can not be obtained by updating the tangential force components. Therefore, having obtaining the new tangential displacement (7.19) the resultant displacement increment is obtained from

$$\Delta\delta = \delta (t + \Delta t) - \delta (t) \qquad (7.20)$$

and the resultant tangential force increment is given by

$$\Delta T = k_t \Delta\delta \qquad (7.21)$$

where, using the updated normal contact force and contact radius. the tangential contact stiffness is

$$k_t = 8G^* a\Theta \pm \mu\Delta P (1 - \Theta) / \Delta\delta \qquad (7.22)$$

with

$$\Theta_L = [1 - (T + \mu \Delta P) / (\mu P)]^{1/3} \qquad (7.23)$$

$$\Theta_U = [1 - (T^* - T + 2 \mu \Delta P) / (2 \mu P)]^{1/3} \qquad (7.24)$$

$$\Theta_R = [1 - (T - T^{**} + 2 \mu \Delta P) / (2 \mu P)]^{1/3} \qquad (7.25)$$

The subscripts L, U and R in (7.23) to (7.25) refer to loading, unloading and reloading respectively. The negative sign in (7.22) is only invoked during unloading. The parameters T* and T** define the load reversal points and need to be continuously updated ($T^* = T^* + \mu \Delta P$ and $T^{**} = T^{**} - \mu \Delta P$) to allow for the effect of varying the normal force. It should be noted that P and ΔP are the actual contact force and force increment respectively rather than their effective elastic counterparts P_e and ΔP_e.

The resultant updated tangential force is calculated using

$$T (t + \Delta t) = T (t) + \Delta T \qquad (7.26)$$

and the new tangential force components are obtained from

$$T_i (t + \Delta t) = T (t + \Delta t) \frac{\delta_i (t + \Delta t)}{\left| \delta (t + \Delta t) \right|} \qquad (7.27)$$

In the presence of adhesion the initial tangential stiffness is obtained by setting $\Theta = 1$ in (7.22) until the tangential force obtains the critical value

$$T_c (t + \Delta t) = \sqrt{\frac{16G^* [P (t + \Delta t) P_c + P_c^2]}{E^*}} \qquad (7.28)$$

When the peeling process is complete, at which point the content of the square root in (7.14) is set to zero. A flag is then set to indicate that the initial contact peeling is complete and subsequent tangential force increments are calculated using (7.22) to (7.25). Finally, a check is made if the tangential force at the end of peeling is greater than that necessary for sliding. The normal contact force is compared with the value defined in (2.35) to determine whether or not the sliding criterion of (2.35) should be used.

7.3.2 Plastic deformation without adhesion

If the elastic yield limit is exceeded then, according to the theory presented in Chapter 3, the initial yield force and the normal contact stiffness during plastic loading are calculated from

$$P_y = \frac{\pi^3 R^{*2} \sigma_y^3}{6E^*} \qquad (7.29)$$

$$k_n^p = \pi R^* \sigma_y \qquad (7.30)$$

Therefore, during a time step the new plastic contact force P is obtained from

$$P(t+\Delta t) = P(t) + \Delta P = P(t) + \pi R^* \sigma_y \Delta\alpha \qquad (7.31)$$

and the contact radius is updated using

$$a(t+\Delta t) = \sqrt{\frac{2P(t+\Delta t) + P_y}{2\pi\sigma_y}} \qquad (7.32)$$

Unloading in the normal direction is assumed to be elastic but it is necessary to allow for the reduced contact curvature resulting from plastic deformation of the contact patch. Therefore, at the transition point from loading to unloading it is necessary to store the maximum normal force P* and to calculate the " effective radius " R_p using

$$R_p = \frac{4E^*}{3R^*}\left(\frac{2P^* + P_y}{2\pi\sigma_y}\right)^{3/2} \qquad (7.33)$$

During unloading the normal contact force is obtained from (7.15) and the new contact radius is calculated according to (7.16) but with R_p substituted for R*. If reloading occurs before the contact breaks then the contact force and contact radius are updated using (7.15) and (7.16) but with $R^* = R_p$ until $P \geq P^*$. When $P \geq P^*$ further plastic deformation occurs and (7.31) and (7.32) are used.

When contact force reduces to zero the contact is considered to be broken although there is a residual apparent overlap α_p (see Fig. 3.3) which is stored in the contact data array for use in possible reloading. The other contents of the contact data array are set to zero except for P*, a_y and the links C(5), C(6) and C(27). When $\alpha < 0$ all the parameters in the contact data array are set to zero and the contact is deleted from the link list.

As explained in Chapter 4, it is assumed that the Mindlin and Deresiewicz (1953) tangential force-displacement relationship is applicable to both elastic and plastic behaviour. Consequently, having updated the normal contact force and contact radius using (7.31) and (7.32), the tangential contact force is updated using (7.21) to (7.27).

7.3.3 Plastic deformation with adhesion

Before initial yield occurs, the normal contact force and contact radius are updated using (7.12) and (7.16). Using the updated contact radius, the initial yield state is identified by testing the validity of the equation

$$\sigma_y = \frac{2E^* a_y}{\pi R^*} - \left(\frac{2\Gamma E^*}{\pi a_y} \right)^{1/2} \qquad (7.34)$$

Having determined a_y in this way, the normal contact stiffness is calculated. see (5.24), from

$$k_p^n = \frac{\Delta P}{\Delta \alpha} = \frac{3\pi R \sigma_y - 2E^* a_y \left(a_c / a \right)^{3/2}}{3 - \left(a_c / a \right)^{3/2}} \qquad (7.35)$$

During plastic indentation, both the plastic contact force and the equivalent elastic force are updated using

$$P(t+\Delta t) = P(t) + \Delta P = P(t) + k_p^n \Delta\alpha \qquad (7.36)$$

and

$$P_e(t+\Delta t) = P_e(t) + \Delta P_e = P_e(t) + k_e^n \Delta\alpha \qquad (7.37)$$

where the elastic contact stiffness k_e^n is defined by (7.13). The updated contact radius is calculated using

$$a^3(t+\Delta t) = \frac{3R^*P_1(t+\Delta t)}{4E^*} \qquad (7.38)$$

where

$$P_1(t+\Delta t) = P_e(t+\Delta t) + 2P_c + \sqrt{4P_e(t+\Delta t)P_c + 4P_c^2 - T^2(t)E^*/4G^*} \qquad (7.39)$$

is the effective Hertzian force. If, however, the following condition is true

$$T_c(t) \geq 4\sqrt{[P_cP_e(t+\Delta t) + P_c^2]\,G^*/E^*} \qquad (7.40)$$

then the effective Hertzian force is calculated from

$$P_1(t+\Delta t) = P_e(t+\Delta t) + 2P_c \qquad (7.41)$$

Having updated the normal contact force, the equivalent elastic normal force, the effective Hertzian force and the contact radius, the tangential contact force is updated using (7.21) to (7.27).

During elastic unloading the modified radius of contact curvature is calculated from

$$R_p = \frac{R^*P^*_1}{P^* + \sqrt{4P_cP^*_1 - T^2E^*/4G^*}} \qquad (7.42)$$

where

$$P^*_1 = P^*_e + 2P_c \pm \sqrt{4P^*_eP_c + 4P_c^2 - T^2E^*/4G^*} \qquad (7.43)$$

is the effective Hertzian force and P^* is the plastic contact force at the point of unloading. However, as can be seen from inspection of (7.42), a problem exits if

$$T_{cr}(t) \geq \sqrt{\frac{16G^*P_c P_1(t)}{E^*}} \qquad (7.44)$$

in which case the radius of contact curvature is calculated using

$$R_p = \frac{R^*P^*_1}{P^*} \qquad (7.45)$$

Having calculated R_p, the normal contact stiffness is obtained from

$$k_e^n = 2E^*a\,\frac{3 - 3(a_\alpha/a)^{3/2}}{3 - (a_\alpha/a)^{3/2}} \qquad (7.46)$$

The updated contact force is given by

$$P(t+\Delta t) = P(t) + \Delta P = P(t) + k_e^n \Delta\alpha \qquad (7.47)$$

and the contact radius is updated using

$$a^3(t+\Delta t) = \frac{3R_p P_{1r}(t+\Delta t)}{4E^*} \qquad (7.48)$$

In the above equation

$$P_{1r}(t+\Delta t) = P(t+\Delta t) + 2P_c + ABC\sqrt{4P(t+\Delta t)P_c + 4P_c^2 - T^2E^*/4G^*} \qquad (7.49)$$

and

$$P_\alpha = \frac{3}{2}\pi\Gamma R_p \qquad (7.50)$$

which is the pull-off force under a changed radius of contact curvature. According to the JKR theory, as shown in Fig. 7.7, when the contact force P reaches its lowest value at $-P_{cr}$ we have $\alpha = \alpha_l$; the contact breaks at $-5/9P_{cr}$ when $\alpha = \alpha_p$. If the contact is re-established this will occur at $\alpha = \alpha_d$ with an initial value of $P = -8/9P_{cr}$. It is necessary, therefore, to store α_d in the contact array for use in possible reloading. If the contact is broken it is necessary to continue to calculate α. If $-\alpha_c < \alpha < \alpha_p$, the contact force and contact radius are set to zero so that the program recognises that there is no contact although an overlap is identified. Other parameters such as P^*, R_p, α_d and a_y are retained in the memory array for use if the contact is re-established. If $\alpha < \alpha_c$, then all the contact data, including the links,

are deleted. The parameter ABC in (7.49) indicates the sign of the normal stiffness. During loading ABC = 1. During unloading ABC = 1 if $\alpha > \alpha_l$. but ABC = -1 if $\alpha \leq \alpha_l$. If reloading occurs before contact is broken then (7.47) and (7.48) are used to update the normal contact force and contact radius until $P \geq P^*$ after which (7.35) to (7.38) are used.

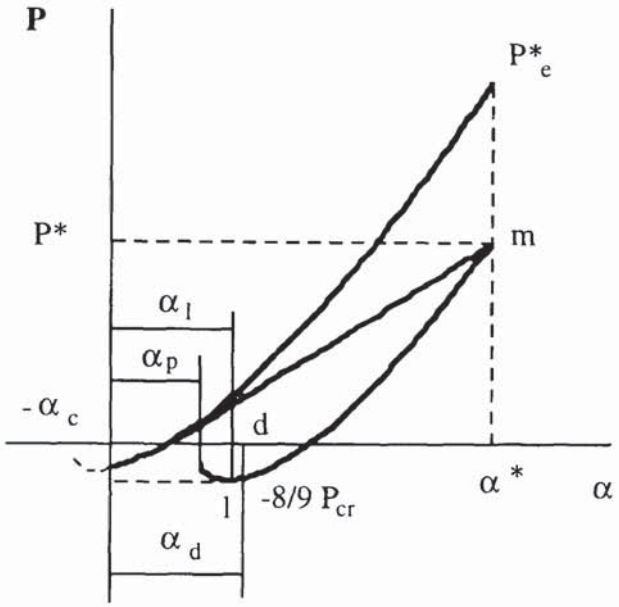

Fig. 7.7 Force-displacement curve of plastic deformation with adhesion.

7.4 Application of TRUBAL to single particle impacts and agglomerate/ wall collisions

7.4.1 Time step

In an assembly of granular material the majority of the energy transmission between individual particles is carried by Rayleigh waves which travel along the surface of the solids. For one single particle there is a time during which a force is transmitted from one contact point to another point along the particle surface. The criterion for specifying the time step in computer simulations of granular media using DEM is that the time step for calculating the

incremental forces and displacements is less than the time it takes for the wave to transverse the minimum sized particle in the assembly.

On application of a force to an elastic body the Rayleigh surface waves are propagated with a velocity

$$V_R = \eta \sqrt{\frac{G}{\rho}} \qquad (7.51)$$

where G and ρ are the shear modulus and density of the particle material; η is a parameter dependent on Poisson's ratio and can be approximately given as

$$\eta = 0.1631\nu + 0.876605 \qquad (7.52)$$

The critical time step is therefore given by

$$\Delta t_c = \frac{\pi R_{min}}{V_R} = \frac{\pi R_{min}}{\eta} \sqrt{\frac{\rho}{G}} \qquad (7.53)$$

where R_{min} is the radius of the smallest particle in the assembly. It is here assumed that the properties of all constituent particles are the same. For an assembly consisting of different material types the critical time step should be the lowest among those determined by different material properties.

The actual time step used in TRUBAL is a specified fraction of the Rayleigh critical time step given in (7.53). By using a smaller time step a greater degree of accuracy is obtained but more computational cycles are needed to achieve desired particle movements. The time step is also related to numerical stability, especially for the dynamic process of agglomerate collisions. Because the relative movements between spheres are not considered in the propagation of Rayleigh waves the time step may not be small enough to guarantee numerical stability. Since the relative velocities between individual particles may be very high the critical time step of real Rayleigh wave transmission is much smaller. During simulation of dynamic particle systems if numerical instability occurs the time step should be reduced further.

7.4.2 Damping

In the TRUBAL program, the granular assembly is treated as a system in which two energy dissipation mechanisms, plastic deformation and frictional dissipation through interfacial sliding, are incorporated in the theoretical contact interaction laws. Two additional energy dissipation mechanisms are available in the program by incorporating viscous dash-pots. The first type of viscous damping is referred to as contact damping in which the damping force is proportional to the normal and tangential contact velocities or strain rates. After updating the contact forces the damping forces are calculated and added to the contact forces to provide damping contributions to the out-of-balance forces and moments of each individual particle. This form of damping is essential and its importance has been demonstrated by considering an elastic oblique impact with surface adhesion (see Figs. 6.8 and 6.9). If the impact velocity is below the critical sticking velocity and there is no contact damping then the contact forces oscillate indefinitely and a state of equilibrium can never be achieved.

The second type of viscous damping is described as global damping or mass proportional damping. The global damping can be envisaged as dash-pots that connect all the individual particles to the reference axes of the simulated system. The damping effect is to add a resistance force to the out-of-balance force and moment of each particle, which govern the motion of the particle. Unlike the contact damping which is related to the contact velocities or strain rates, the magnitude of the global damping force is proportional to the absolute (both transitional and angular) velocity of the particle, but with a direction which is opposite to the velocity vector. The mechanism of the mass proportional damping is like immersing the system of particles in a viscous liquid, for instance, simulation of particle flow in a viscous medium. Although global damping is not normally used for the simulated tests of agglomerate impact fracture / fragmentation and quasi-static shear deformation of granular media it is useful to dissipate kinetic energy during the preparation of an assembly.

7.4.3 Input commands

TRUBAL uses operative commands which have various functions such as file handling, program execution and control, defining material properties and constants, etc. The format of all input commands is a word followed, in most cases, by a number of parameters, some of which may be words themselves. Although the computer program only detects the first three letters of the first word of a given optional command the user may sometimes find it useful to write out the full word for the understanding of its physical meaning. The parameters may be separated by any number of spaces or commas since multiple separators are treated as one. Integers may be entered as real numbers, but not vice versa. The advantage of introducing operative commands is that the user can apply TRUBAL to handle different problems without modifying the program. New commands can be added when new problems arise; at the same time the function of old commands is still retained.

The complete command list used in the current version of TRUBAL is given by Lian et al (1993). The first command on entering TRUBAL must be **STArt** or **REStart**. The next input command line can consist of any message. In the modified version of TRUBAL with plastic deformation a command **YIEld** has been added into the program. For two material types of particles in contact with elastic yield stress σ_{y1} and σ_{y2} respectively we can input a pair of commands into the program

YIEld σ_{y1} ITYP(1)

YIEld σ_{y2} ITYP(2)

The smaller value of σ_{y1} and σ_{y2} will be automatically chosen by the program as the elastic yield stress for plastic deformation calculation. If either of the two commands is omitted a very large yield stress will be set for that material type; if both commands are omitted the contact is treated as purely elastic.

When performing a simulation test the user can input all the command lines required by

the test one by one or compile them as an input command file. Due to its efficiency and flexibility the input file is commonly used in the computer simulated experiments. The sample input files used this study for single particle impacts and agglomerate/wall collisions are provided in Appendix B.

Chapter 8 Impact fracture / fragmentation of small agglomerates

8.1 Introduction

The understanding of the degradation of particulate material during handling and processing is of interest in many fields of engineering and technology. In the nuclear industry the gas-born U_3O_8 agglomerates degrade into fragments either by turbulent shear or upon impact with a surface. The process of fragmentation and the resulting size distribution, therefore, need to be examined in order to predict the flowability of fractured fragments, of which the primary particles may become resuspended in the flow field. By incorporating the information of agglomerate fragmentation and suitable criteria for bounce into numerical simulations of particle transport in turbulent flows comparisons then can be made of theoretical predictions for deposition with the measurements of particle suspension and deposition in straight pipes and bends of the transport rig.

The impact test is one of the most simple and direct methods to quantify and measure the agglomerate strength, which is related to attrition and breakage of the primary particles within the agglomerate. However, in real experiments, it is difficult to obtain the internal parameters describing the packing structure of the agglomerates, especially the interparticle contact forces. Computer simulation based on the Distinct Element Method (DEM) developed by Cundall (1971) can provide a detailed examination of the micromechanics of the particle system. The computer program adapted from the 2D program BALL, Cundall and Strack (1979), and 3D program TRUBAL, Cundall (1988) models the particle interactions as a dynamic process which involves energy dissipation due to interparticle

sliding. In all Aston versions of BALL and TRUBAL, incorporation of surface adhesion makes the simulation of agglomerate impact become possible. Two-dimensional simulations of a monodisperse 1000 particle agglomerate against a wall were carried out by Yin (1992) in order to clearly illustrate the internal agglomerate damage processes. Recently Thornton and Kafui (1992), Kafui and Thornton (1993, 1994) presented a series of 3D simulations in which a monodisperse spherical agglomerate consisting of 7912 primary particles in face-centred cubic arrangement was impacted against a wall. The effects of impact velocity, bond strength and primary particle size on the fracture / fragmentation were examined.

In this Chapter computer simulations of two randomly generated agglomerates, (one monodisperse and one polydisperse) each consisting of 50 primary particles impacting with a wall are presented. The fragmentation behaviour is first illustrated by the computer graphics in which the primary particles are colour coded according to the size of the cluster that they belong to. Impact damage behaviour and the effects of impact angle, impact velocity, the local structural arrangements close to the impact point, and plastic deformation at the contacts on agglomerate fragmentation are then discussed.

8.2 Sample preparation

The creation of all types of granules and lumps consisting of smaller primary particles can, in general, be termed as agglomeration. The possible bonding mechanisms between the primary particles include solid bridges, interfacial forces and capillary pressure in mobile liquid bridges, adhesion and other forces of attraction between the solid particles. These mechanisms together with the material properties and particle size distribution may contribute to variations in agglomerate behaviour.

In computer simulated experiments of agglomeration a number of primary particles are randomly generated within a spherical region and the agglomerate is formed by imposing a

centripetal gravity field to bring the particles together. In order to achieve a dense agglomerate an artificially high particle density ($\sim 10^7$) can be used. This method also can lead to a significant reduction in computing time. When a compact assembly of particles has been formed and the number of established contacts has reached a constant value, surface energy is introduced and the particle density is then reduced in very small increments to the normal level.

In reality the attraction force between the solid particles is very small and the centripetal gravity field needs to be transformed to a one dimensional gravity field. If the impact is to be simulated in the x-direction, for instance, the x-component of gravity should be -9.81 m/s^2, while the other two components, y and z, are then zeroed. The wall of an agglomerate-wall collision system is first created and then moved to a new location within a very small distance from the agglomerate. The gap between the wall and the agglomerate is so small that the effect of velocity increase due to the gravity can be ignored. Before the impact velocity is specified sufficient computational cycles must be carried out so that the kinetic energy of primary particles is gradually dissipated by introducing global damping, allowing the agglomerate to reach a static equilibrium state. However, it is impossible to reach an absolutely equilibrium state at which all the particles have uniform or zero velocities. Within the randomly generated agglomerate the individual particle always have different velocities, though very small.

Two agglomerates consisting of 50 U_3O_8 primary particles have been generated in the way described above. The particle properties ρ = 8.3 Mg/m^3, E = 215 GPa, ν = 0.3, μ = 0.35, and γ = 0.1 J/m^2 were used in both cases. It should be noted that for contact between two surfaces with surface energies γ_1, γ_2 and interface energy γ_{12}, the Dupre energy of adhesion is $\Gamma = \gamma_1 + \gamma_2 + \gamma_{12}$. In this study, due to $\gamma_1 = \gamma_2 = \gamma$ and $\gamma_{12} = 0$ we therefore have $\Gamma = 2\gamma$. The monodisperse agglomerate with particle radius R = 10 μm had 111 contacts initially and a porosity of 0.5291. The size distribution in the polydisperse sample is approximately Gaussian with a mean particle radius of 7 μm as shown in Table 8.1. The

wall properties are the same as those for particles except ρ = 7.8 Mg/m^3 was used. The initial number of contacts before collision was 131 and the porosity was 0.4162, which is significantly lower than the value for the monodisperse agglomerate. The coordination number, which represents the average number of contacts within the assembly, was 4.44 and 5.23 for the monodisperse and polydisperse agglomerate respectively. The values of both coordination number and porosity are affected by the final size of an agglomerate and are significantly affected when the agglomerate is small.

Particle radius (μm)	Particle number
R = 10	7
R = 8	11
R = 7	14
R = 6	11
R = 4	7

Table 8.1 Particle size distribution for the polydisperse agglomerate

8.3 Visual observation

A series of 3D simulations of agglomerate-wall collisions has been conducted at impact velocities of 0.2, 0.5, 1.0, and 3.0 m/s. Both the randomly generated monodisperse and polydisperse agglomerates were used to examine the contacts broken and fragmentation during the impact processes. Using computer graphics the fragmentation was observed by colour coding the primary particles according to the size of the cluster that they belonged to. For normal collisions, the fragmentation behaviour for both cases is illustrated in Fig. 8.1 and Fig. 8.2 respectively. At an impact velocity of 3.0 m/s the monodisperse agglomerate

was fractured into singlets and all the contacts were broken; but for the polydisperse assembly two doublets survived after the impact. At a low impact velocity of 0.2 m/s for both assemblies only a few singlets and doublets were broken off although a substantial number of broken contacts was observed. Comparing these two assemblies the agglomerate strength of the polydisperse sample, in terms of contacts broken, is stronger than that for the monodisperse one. The reason for this is that, considering the density dependent agglomerate strength, the lower value of porosity for the polydisperse agglomerate indicates higher density of the assembly. The smaller particles provide more interlocking within the assembly which will also increase the agglomerate strength.

(a)

Impact velocity: 0.2 m/s

Contacts broken: 57

Time: 0.645 μs

(b)

Impact velocity: 0.5 m/s

Contacts broken: 91

Time: 0.43 μs

(c)

Impact velocity: 1.0 m/s

Contacts broken: 114

Time: 0.43 μs

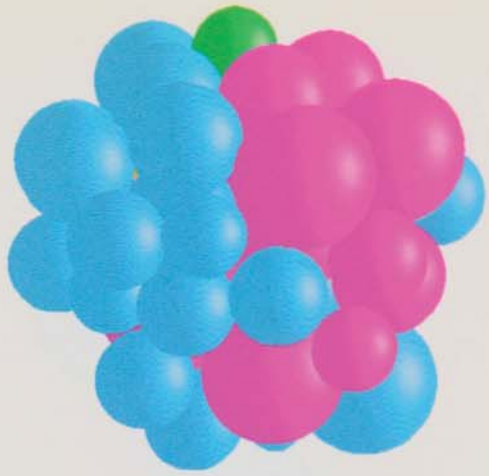

(d)

Impact velocity: 3.0 m/s

Contacts broken: 129

Time: 0.323 μs

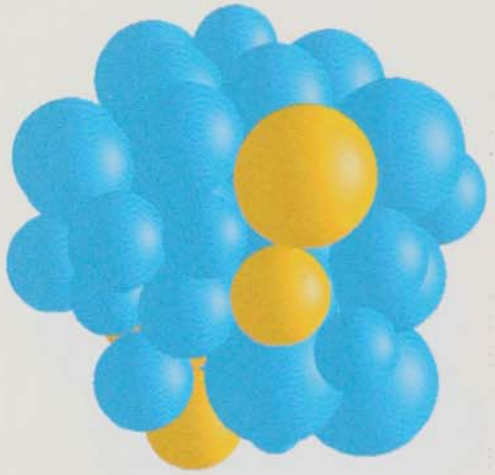

Fig. 8.1 Visual observation of fragmentation for the polydisperse agglomerate: blue - singlets; yellow - doublets; green - clusters contain 3-5 particles; pink - cluster of 11-20 particles; purple - cluster of 21-30 particles; red - cluster of 31-50 particles.

(a)

Impact velocity: 0.2 m/s

Contacts broken: 59

Time: 1.075 μs

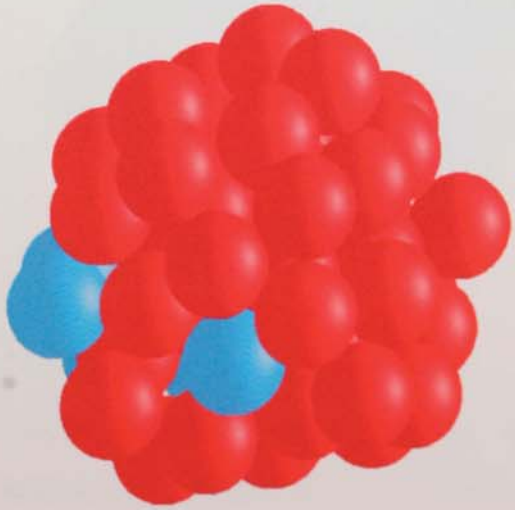

(b)

Impact velocity: 0.5 m/s

Contacts broken: 81

Time: 0.753 μs

(c)

Impact velocity: 1.0 m/s

Contacts broken: 99

Time: 0.591 μs

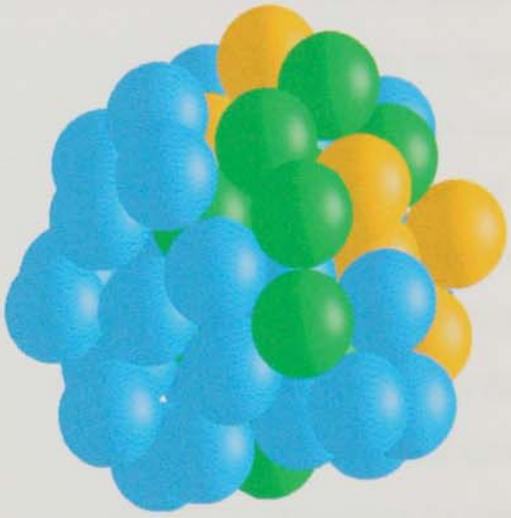

(d)

Impact velocity: 3.0 m/s

Contacts broken: 111

Time: 0.43 μs

Fig. 8.2 Visual observation of fragmentation for the monodisperse agglomerate: blue - singlets; yellow - doublets; green - clusters contain 3-5 particles; white - cluster of 6-10 particles; pink - cluster of 11-20 particles; red - cluster of 31-50 particles.

8.4 Damage assessment

To examine the change of microscopic structure of particulate material resulting from agglomerate collisions a damage ratio D is defined as the ratio of the number of contacts broken to the total number of contacts existing prior to the impact. Before investigating the impact velocity dependent damage ratio we first examine variations of the wall force, kinetic energy, and the contact breakage during the process of an agglomerate impact. At an impact velocity of 0.5 m/s for the polydisperse agglomerate, Fig. 8.3 (a), (b) and (c) show the evolution of the force on the target wall, the total kinetic energy of the particle system and the damage sustained by the agglomerate respectively. The trends illustrated in the figures are typical of all the simulated impacts, 2D or 3D, large agglomerates or small ones, according to the previous work carried out at Aston. It is seen that there is an initial period during which the wall force rises quickly to about 50 % of the maximum value, the kinetic energy starts to fall slowly but little damage of the agglomerate is observed. The same behaviour was reported by Yin (1992) and Kafui and Thornton (1994). The evolution of the force on the wall is approximately symmetric. It is seen from Fig. 8.3 (a) and (b) that the kinetic energy reaches a minimum value when the force on the wall is approaching its maximum value. During unloading only part of the initial kinetic energy is recovered. Although each individual particle undergoes loading and unloading at different times Fig. 8.3 (b) statistically represents the evolution of kinetic energy for the whole particle system. The unrecovered energy has been dissipated through interparticle sliding, contact breaking and contact damping. Once the wall force reaches near-zero the kinetic energy is approaching a steady state but, due to the effect of gravity, the kinetic energy decreases again with a very slow pace.

From Fig. 8.3 (c), it is seen that after the initial no damage period the damage ratio increases monotonically with impact duration until a constant value is reached. It is clear that the process of contact breaking continues after the force on the wall reaches zero. When a constant value of damage ratio is obtained, a new equilibrium state of the particle system is

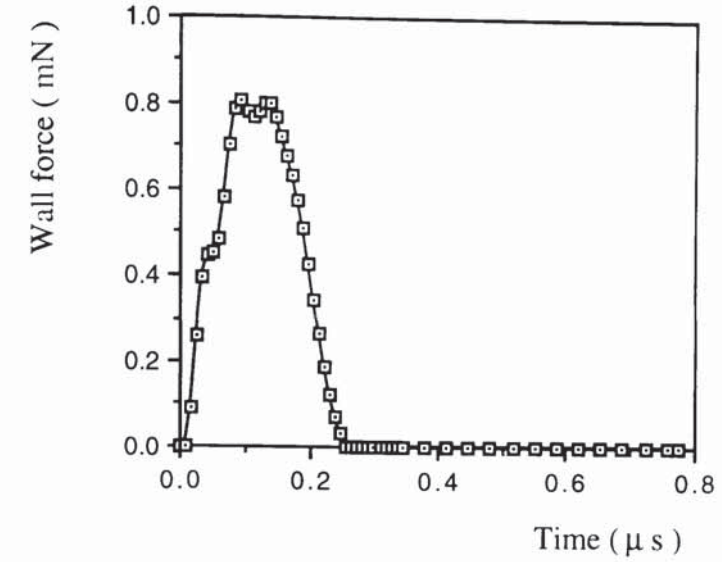

(a)

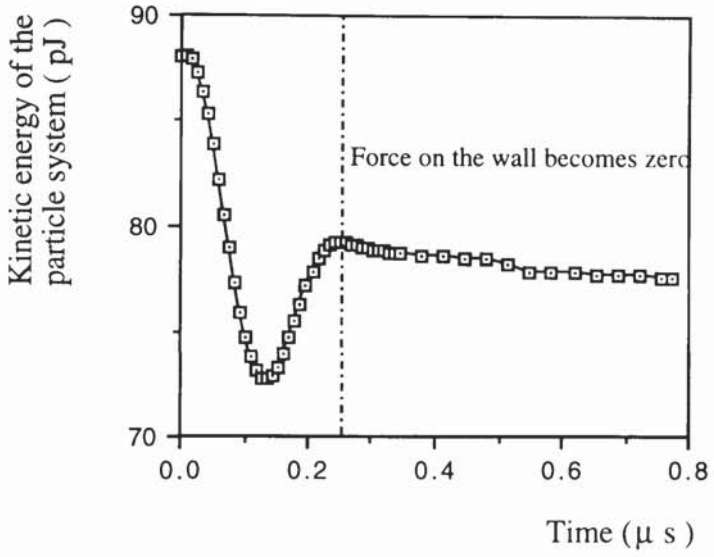

(b)

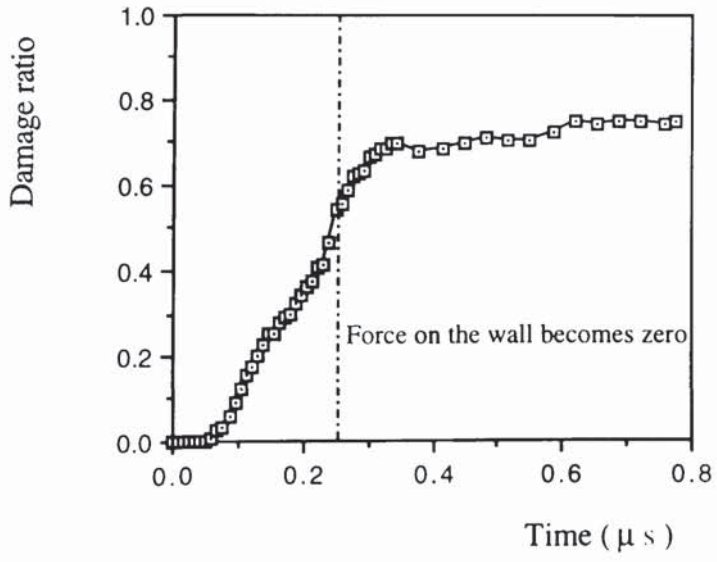

(c)

Fig. 8.3 Evolution of wall force (a); kinetic energy (b); and damage ratio (c).

temporarily reached. The constant value shown in Fig. 8.3 (c) is considered to be the damage caused by the initial impact and can be used to quantify the damage corresponding to the impact velocity. The effect of further collisions on the agglomerate impact damage is ignored in this study.

It was reported by Yin (1992) the relationship between the damage ratio and the impact velocity can be approximated by the simple equation

$$D = \alpha \ln (V / V_0) \qquad (8.1)$$

where α is a constant and V_0 is the threshold velocity below which no significant damage occurs. However, as recognised by Yin (1992), deviations from the simple relationship occur: a) at high damage ratios because even very high impact velocities are unlikely to produce singlets only, and b) at low impact velocities a few primary particles can be broken off over a range of velocities. Results presented by Kafui and Thornton (1993) for a large 3D agglomerate confirm that the relationship is more complex than that suggested by (8.1).

The actual damage and fragmentation resulting from an agglomerate impact, especially for the small assemblies, may depend on which part of the agglomerate makes contact with the target wall and the local structural arrangement close to the wall. In order to investigate this, the agglomerate was surrounded by six walls arranged to form a cube and the agglomerate was impacted orthogonally with each wall in turn. The results are shown in Figs. 8.4 (a) and (b) for the monodisperse and polydisperse systems respectively. In the figures, for a 3D coordinate system, the notation x-z wall (-) indicates that the target surface is located on the x-z plane below the agglomerate, x-z wall (+) indicates that the wall is above the agglomerate. For each set of simulations the gravity field is rotated to coincide with the initial impact velocity direction. It is observed from Fig. 8.4 (a) and (b) that the results for the six sets of impacts are reasonably consistent for both agglomerates. It is, therefore, concluded that the damage ratio is not significantly affected by the local structural arrangement close to the point of impact for small agglomerates.

From Fig. 8.4 it can be seen that, for the polydisperse agglomerate, the simple relationship of (8.1) gives a good fit to the data for $0.1 < D < 0.9$. However, for the monodisperse agglomerate the data only satisfies the simple relationship in the range of $0.4 < D < 0.9$. It is of interest to note that, as shown in Fig. 8.4 (c), the damage ratio resulting from the agglomerate impact for the polydisperse assembly is always lower than that for the monodisperse one. This means a higher agglomerate strength for the polydisperse assembly and the same behaviour has been illustrated in the previous section. For the monodisperse agglomerate there is a very distinct threshold velocity below which no damage is sustained by the agglomerate. For impact velocities only slightly above this value there is a significant number of contacts which have been broken within the assembly. The significant difference in the damage ratio between the two agglomerates at low impact velocities is perhaps due to the difference in the contact density and structural arrangement. However, further work is needed to clarify this. When the damage ratio reaches 0.9 which corresponds to the impact velocity of 1.0 m/s the simple relationship is not applicable for both cases, since a few contacts still remain unbroken even at very high impact velocities.

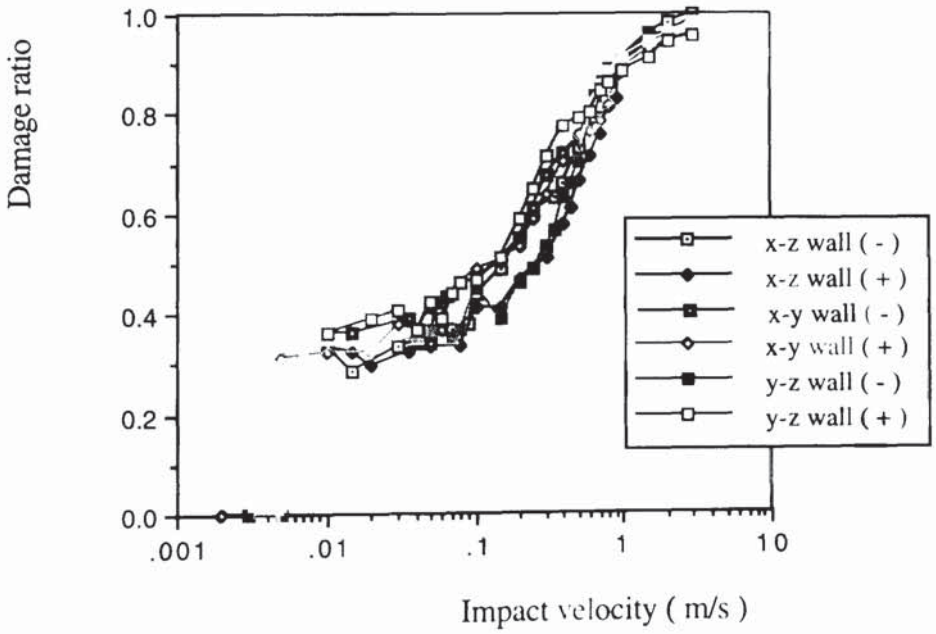

(a)

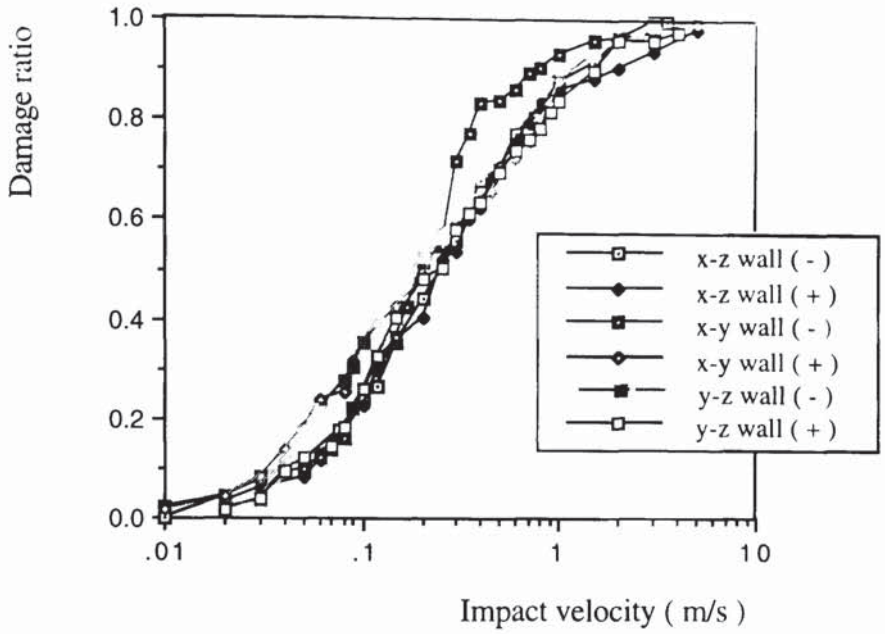

(b)

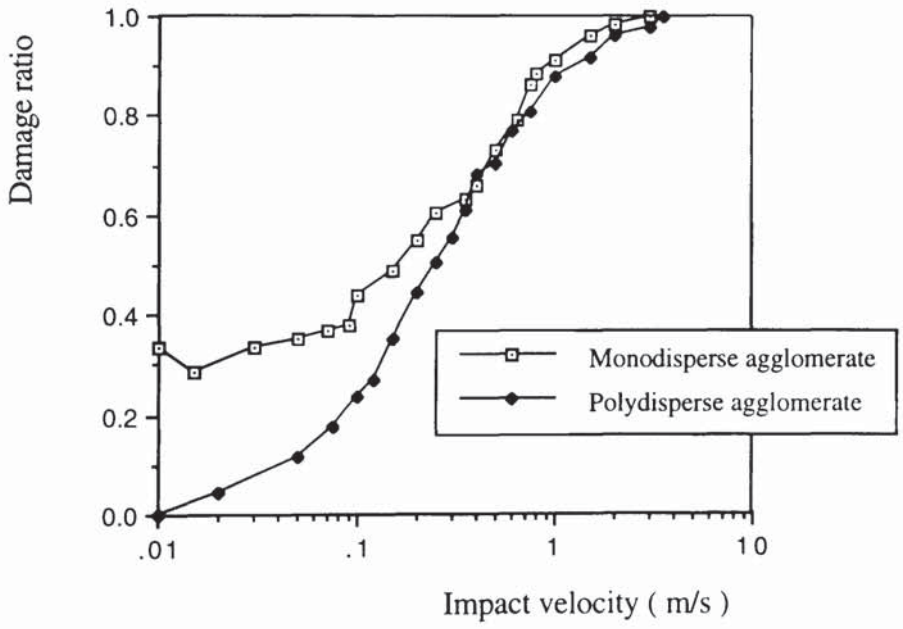

(c)

Fig. 8.4 Relationship between impact velocity and damage ratio for normal impacts:

(a) monodisperse agglomerate; (b) polydisperse agglomerate;

(c) comparison between the two assemblies with a x-z wall (-).

Oblique impact simulations were also performed on the polydisperse agglomerate for one wall. In order to check the effect of the local structural arrangement four directions of impact were employed, as shown in Fig. 8.5, where the target surface is located on the x-z plane. Direction x-y (+) is the direction in which the colliding agglomerate is moving in a x-y plane with a positive component of impact speed in the x direction; direction x-y (-) indicates that the velocity component in the x direction is negative. For a constant impact speed of 0.5 m/s, Fig. 8.6 shows the variations of damage ratio with impact angle. It is seen that the simulated data is reasonably consistent irrespective of impact direction. With the increase of impact angle the damage monotonically decreases and is approaching zero when the limiting angle of 90° is reached. The explanation for this is that the normal component of impact speed decreases with an increase of impact angle. In Fig. 8.7 the average damage ratio obtained for each angle of impact is compared with the damage ratio resulting from a normal impact at a velocity corresponding to the normal component of impact speed for the oblique collision. From the close agreement between the two sets of data it is evident that the normal component of impact speed is the dominant factor in determining the degree of damage resulting from an agglomerate impact.

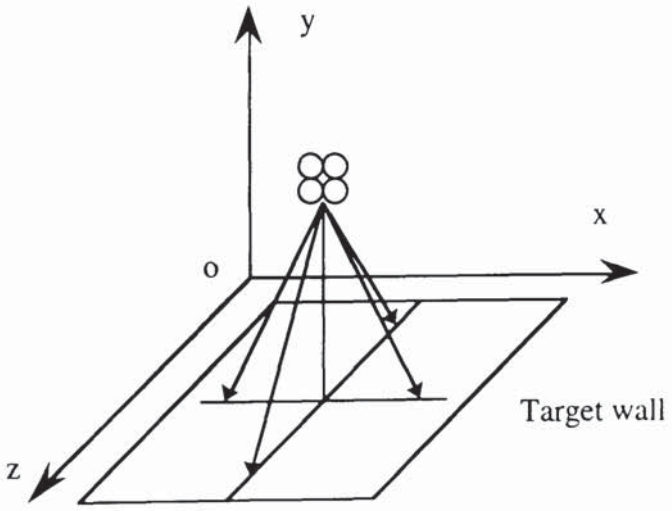

Fig. 8.5 Diagram for oblique impacts.

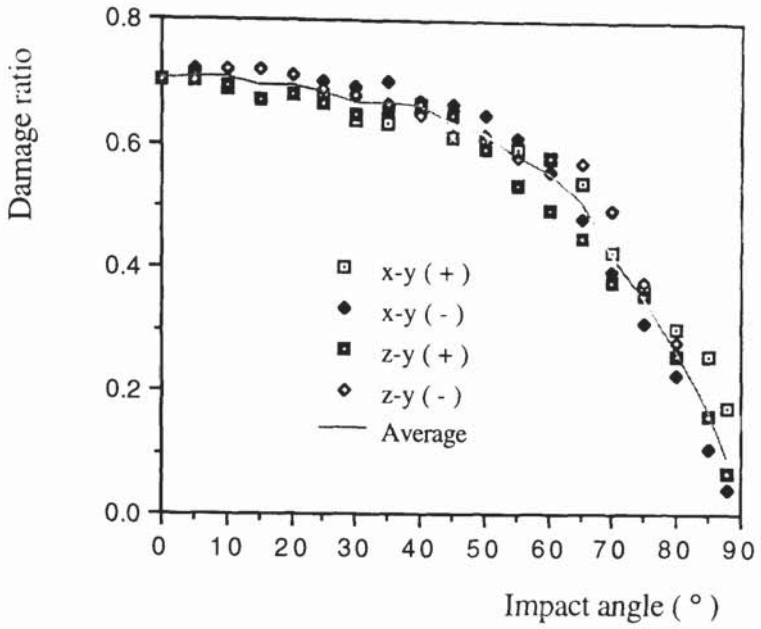

Fig. 8.6 Effects of impact angle and local structural arrangements close to the impact point on damage ratio for an impact speed of 0.5 m/s colliding on a x-z wall.

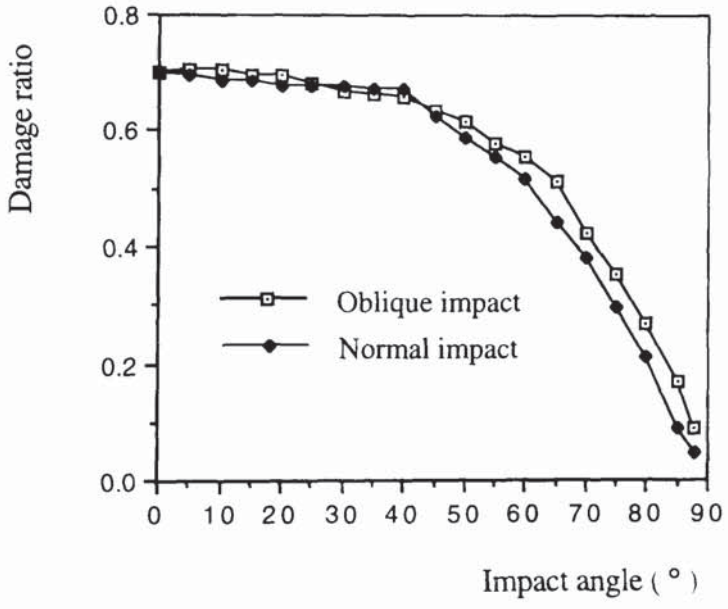

Fig. 8.7 Comparison of oblique impacts at a constant speed of 0.5 m/s with normal impacts carried out at the corresponding normal impact velocities.

8.5 Fragmentation

The damage ratio presented by computer simulation provides an absolute quantification of agglomerate breakage. However, it is not possible, in real experiments, to accurately measure the number of bonds broken within the particle system since the total number includes the internal bonds within the fragmentation clusters. In the cooling system of a transport rig at a nuclear plant the gas-born U_3O_8 agglomerates may be broken up into fragments either by turbulent shear or upon impact with the rig surface. This fragmentation will result a size distribution of smaller particles or agglomerates and the flow behaviour is therefore significantly affected. Although the final damage and fragmentation would be dependent on the initial impact and further collisions, for the convenience of analysis, the effects of further collisions were ignored in this study.

As reported by Arbiter et al (1969) the fragments resulting from an impact can be classified into three categories: the coarse fragments (residue), the fine fragments (complement) and the " dust ". In a double logarithmic plot of the cumulative percentage (by weight) of undersize fragments against fragment size, each category of fragments is represented by one of three straight lines for a given impact velocity. In computer simulated experiments the same behaviour was observed by Thornton and Kafui (1992), who used a monodisperse agglomerate consisting of approximately 8000 primary particles in a face-centred cubic packing. The cluster size was normalised by the ratio of the number of particles in a cluster to the number of particles in the initial agglomerate. There are alternative ways to characterise the fragment size, for instance, by the radius of the smallest sphere which circumscribes the cluster or by the radius of an equivalent sphere which has the same solid volume as the cluster. The use of circumscribing sphere radius was reported by Thornton and Kafui (1993), who observed that the power law relationship between the cumulative percentage mass of material undersize and the normalised cluster size has an exponent between 0.22 to 0.47. Considering the flowability of U_3O_8 agglomerates in the transport rig the circumscribing sphere radius seems to be a reasonable choice. However,

due to the significant effect of cluster shape, especially for the clusters consisting of only 2 - 4 primary particles, the fragment size defined in this way may not be appropriate for an agglomerate with only 50 primary particles.

In order to characterise the computer simulated data it was decided to define the size of a fragment by the particle number and then normalise it by the number in the initial agglomerate. For the two randomly generated agglomerates the normalised fragment size is plotted against the fraction undersize in Fig. 8.8 (a) and (b) for a range of impact velocities. Although the structure of the agglomerates were different, it is seen that the fragmentation pattern is similar for both assemblies and for each impact velocity the grading curve may be approximated by a straight line. The figure also shows that the power law exponent decreases with increase in impact velocity. At an impact velocity of 0.1 m/s, for the polydisperse agglomerate, 31 contacts were broken but there was no fragmentation resulting from the collision; for the monodisperse assembly, the number of broken contacts was 64 and there was one singlet produced. In this study we have only examined the impact fracture / fragmentation behaviour for small U_3O_8 agglomerates. The effect of surface energy has been investigated by Thornton and Kafui (1993).

Figure 8.9 shows the variations of the fraction of singlets produced after impact with impact velocity. It is seen that, for both assemblies, the fraction of singlets increases with an increases in impact velocity. Although the data curve for the monodisperse agglomerate is more scattered, it is observed that, for each impact velocity, the fraction of singlets produced for the monodisperse sample is higher than its counterpart. The normalised cluster size for the largest cluster resulting from an impact is plotted against impact velocity in Fig. 8.10. It is generally true that the particle number of the biggest cluster for the polydisperse one is larger than that for the monodisperse assembly, further evidence which demonstrates the difference in strength between these two types of agglomerates. The fragmentation behaviour obtained by computer simulation may be used for numerical modelling of particle and agglomerate transport in the cooling system.

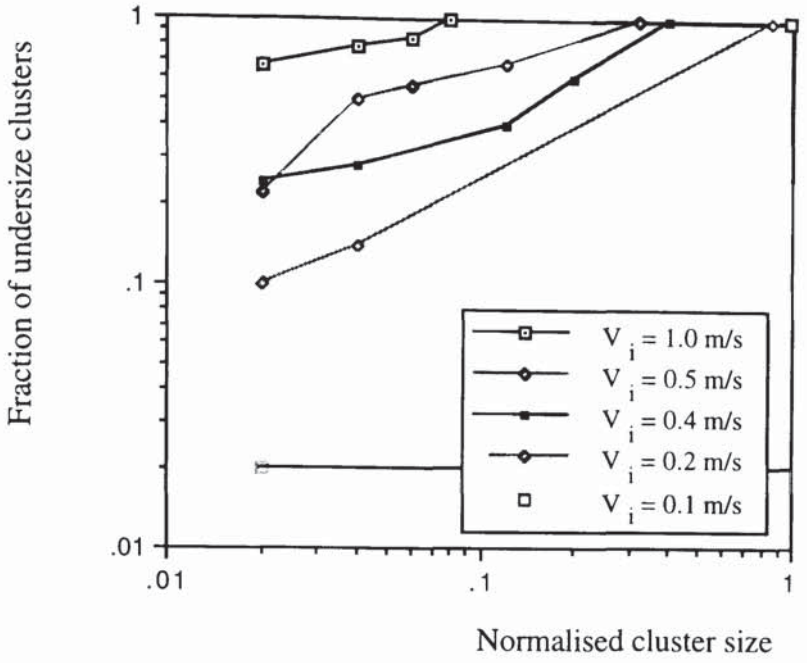

(a)

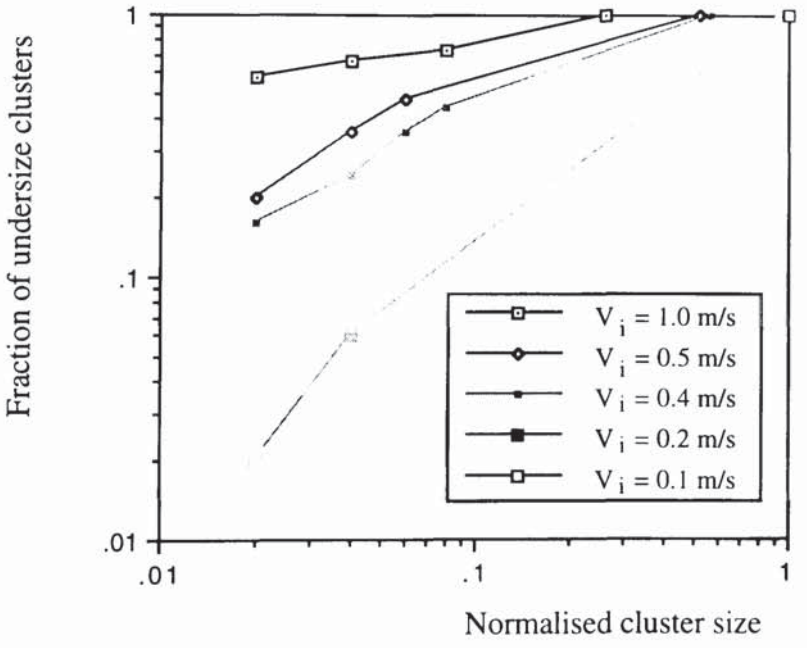

(b)

Fig. 8.8 Grading curves: (a) - monodisperse agglomerate;

(b) - polydisperse sample.

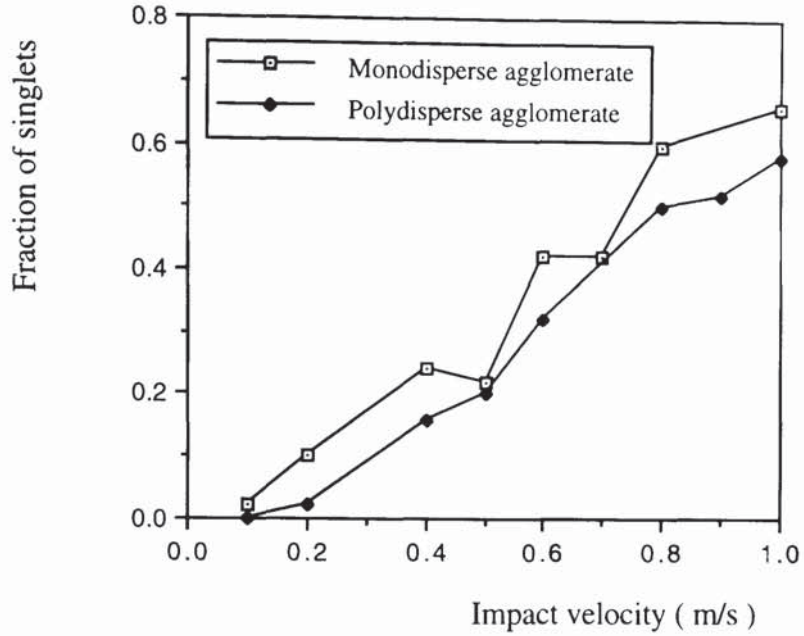

Fig. 8.9 Fraction of singlets produced after impact against impact velocity for both assemblies.

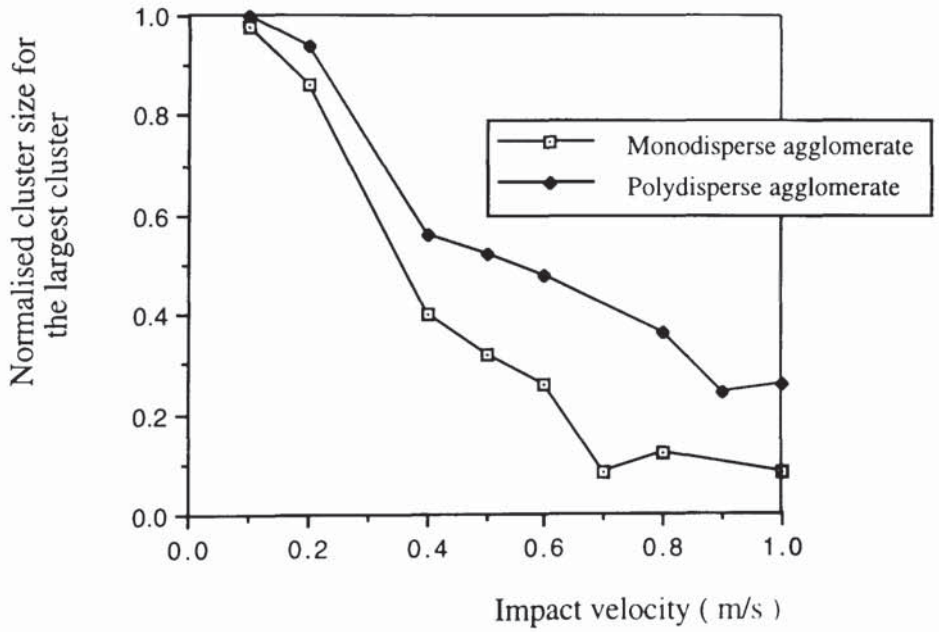

Fig. 8.10 Normalised cluster size for the largest cluster against impact velocity for both assemblies.

8.6 Effect of plastic deformation on agglomerate impact

During the process of an agglomerate collision with a target surface the initial kinetic energy of the particle system is responsible for breaking the contacting bonds within the agglomerate. It is expected that the level of damage and fragmentation resulting from an impact will be reduced if plastic deformation occurs between the individual particles. Part of the initial kinetic energy of the particle system goes into irreversible work deforming the surfaces in the contact region and finally this lost energy is transformed into heat or other forms of energy.

The previous computer simulated experiments were carried out using the old version of TRUBAL, which only deals with elastic deformation at the contact. Because the contact data array C(N_{varc}), see Chapter 7, has been extended in order to incorporate plastic deformation into the code the originally generated two assemblies could not be used for simulations using the new code. Due to the randomly generated particle connections within the assemblies, it is impossible to obtain exactly the same agglomerate as achieved before. Fortunately for a small agglomerate consisting of only 50 primary particles we can use the **CREATE** command to form a new agglomerate with the same coordinates of the primary particles as the original agglomerate. For the new polydisperse agglomerate the initial contact number of 131 has been achieved by generating each primary particle according to its previous initial location. It should be noted that the strength of the newly formed agglomerate and the damage ratio may differ from the old sample because a) for each particle position the coordinates are not absolutely the same as those for the previous assembly and b) all the particle velocities within the new agglomerate are zero, but for the old assembly they are not.

For the newly generated polydisperse agglomerate the effect of plastic deformation on the damage ratio is shown in Fig. 8.11, where the number of broken contacts increases with

increase of impact velocity. The results for elastic primary particles were obtained by using a very large yield stress to assure that no plastic deformation occurred at the contacts. For the yield stress of U_3O_8 material, 3.04 GPa suggested by Nuclear Electric, the corresponding yield velocity in the presence of surface adhesion is 0.615. It is seen that for an U_3O_8 agglomerate there is no significant difference in the damage ratio between elastic and plastic impacts. At an impact velocity of 1.0 m/s, which causes shattering of the agglomerate, the normal coefficient of restitution for a single particle is about 0.962 and only 7.46 % of initial kinetic energy will be lost in terms of plastic deformation. The small difference between the two curves justifies our simulations of U_3O_8 agglomerates using the old version of TRUBAL which neglects plastic deformation at the contacts. It is also seen from Fig. 8.11 that the difference in contact breakage increases when the yield stress is reduced because more initial kinetic energy is lost during impact.

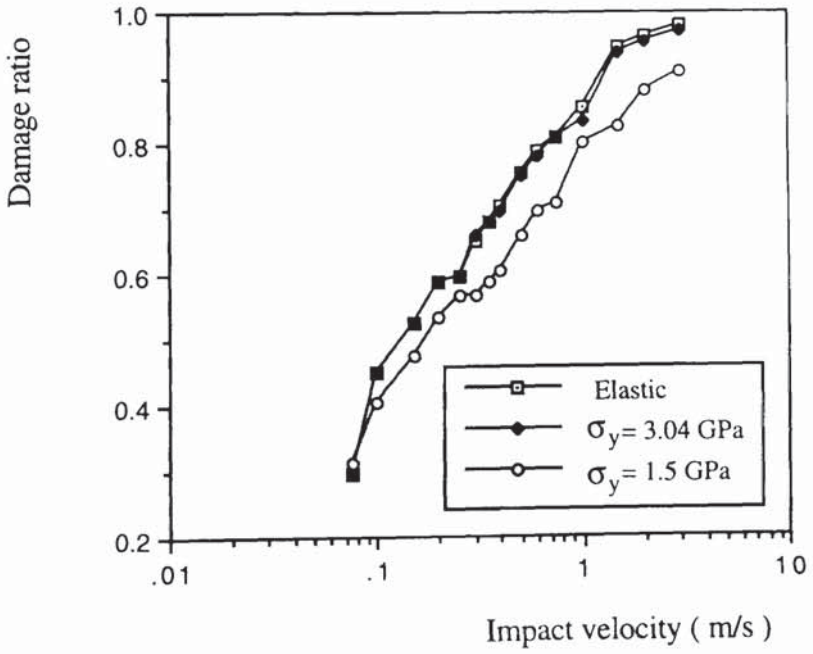

Fig. 8.11 Effect of plastic deformation on the damage ratio resulting from an polydisperse agglomerate collision with a wall.

8.7 Summary

Computer simulations of agglomerate-wall collisions have been carried out, in which a randomly generated monodisperse agglomerate and a polydisperse agglomerate both consisting of 50 primary particles were used. Concerning the evolution of the wall force, kinetic energy of the particle system, and the damage ratio during the process of an agglomerate-wall collision the trends observed in this study are in good agreement with previous simulations of 2D and 3D, large and small agglomerates carried out at Aston. The simulated data generally agrees with the simple relationship between the damage ratio and the impact velocity reported by Yin (1992), except for very high and low impact velocities. It has been demonstrated that the polydisperse agglomerate is stronger than the monodisperse one, due to the difference in contact density and structural arrangement between the two assemblies.

It has been shown in this study that agglomerate damage resulting from an oblique impact is determined by the normal velocity component rather than the impact speed. The damage caused by shearing during collision can be reasonably ignored. This observation, of course, was based on a very small agglomerate sample and more investigations of shear induced damage and fragmentation should be conducted for large agglomerates to confirm this behaviour. In order to check the effect of the local structural arrangement close to the impact point, six different wall positions for normal impacts and four directions of the agglomerate impacting to the target surface for oblique collisions were employed. The computer simulated data were found to be consistent irrespective of the impact directions and wall positions. Therefore, it is concluded that, for small agglomerates, the effect of the local structural arrangement on the damage ratio is not significant and the randomly generated agglomerates can be approximately regarded as isotropic solids.

For an agglomerate consisting of only 50 primary particles it is difficult to define, in an unambiguous way, the size distribution of the clusters resulting from the agglomerate-wall

impact. Defining the size of a fragment by the particle number and then normalising it by the number in the initial agglomerate, it is observed that the grading curve is similar for both assemblies and, for each impact velocity, approximately corresponds to a straight line. For practical use in the numerical modelling of particle and agglomerate transport in turbulent flow fields the fracture / fragmentation behaviour illustrated by the computer graphics should be consulted. Finally the effect of plastic deformation at the contacts on the damage ratio was examined. For small U_3O_8 agglomerates there is no significant difference in the damage ratio between elastic and plastic impacts. By reducing the elastic yield stress, however, it has been shown that the number of contacts broken is significantly reduced because of the additional energy dissipated.

Chapter 9 Conclusions

Since the establishment of classical elastic contact mechanics by Hertz (1882) considerable advances have been achieved in the theoretical understanding of the impact mechanisms and the experimental observations of the behaviour of particle-particle or particle-wall collisions. However, none of the current theoretical models can fully answer the question of capture and rebound of single particles colliding with a target surface, especially with variations of impact obliquity. The research project, supported by Nuclear Electric plc, Berkeley Laboratories, is related to surface deposition of aerosol particles which is a major concern for the maintenance, safety assessment and efficiency of the plant. This thesis presents theoretical investigations and computer simulations of single gas-born U_3O_8 particles impacting with the in-reactor surface and fragmentation of small agglomerates.

The major discoveries and achievements of this research project together with some suggestions for possible future study are described in this chapter.

9.1 Impact of non-adhesive spheres

A theoretical model for elasto-plastic spheres has been developed. The initial, pre-yield, behaviour is described by Hertzian classical theory. Assuming the absence of strain hardening or strain rate effects, the post-yield behaviour is described by modifying the Hertzian pressure distribution to account for the limiting normal pressure, σ_y, due to plastic deformation at the contact. The modified Hertzian theory was then used to obtain analytical

expressions for the coefficient of restitution, the contact force evolution and the contact duration. The relationship between impact velocity and the normal coefficient of restitution was obtained as

$$e_n = \left[\frac{108}{25} \frac{V_y / V_{ni}}{(V_y / V_{ni}) + 2\sqrt{\frac{6}{5} - \frac{1}{5}(V_y / V_{ni})^2}} \right]^{1/4} \left[1 - \frac{1}{6}\left(\frac{V_y}{V_{ni}}\right)^2 \right]^{1/2} \qquad (9.1)$$

or for $V_y << V_{ni}$,

$$e_n = 1.185 \left(\frac{V_y}{V_{ni}}\right)^{1/4} \qquad (9.2)$$

which indicates that the coefficient of restitution is not a material property, but depends upon the severity of impact indentation. The power law relationship of -1/4 is in agreement with previous models reported by Johnson (1985) and Stronge (1994b), a feature which is supported by experimental measurements. From the experimental point of view, (9.1) contains the form of the yield velocity V_y rather than the yield stress which is difficult to measure. Consequently, in order to verify the theory the impact model presented in this study can avoid the difficulties in measuring the yield stress.

Based on the theory, the total contact time including plastic loading time t_L and elastic recovery or unloading duration t_U is given as

$$t = t_L + t_U = \pi R \left(1 + \sqrt{5/4}\, e_n \right) \left(\frac{\rho_1}{3\sigma_y} \right)^{1/2} \qquad (9.3)$$

The force-time relationship qualitatively agrees with the experimental measurements by Andrews (1930, 1931). The fraction of the initial kinetic energy lost is

$$W^* = \frac{W}{\frac{1}{2} m V_{ni}^2} = \frac{\zeta(\nu_2)}{\rho_2 C_0^3} \pi \left(\frac{3\sigma_y^3}{4\rho_1} \right)^{1/2} \left(1 + \sqrt{\frac{4}{5}} \frac{1}{e_n} \right) \qquad (9.4)$$

For U_3O_8 particles striking a steel plate, at impact velocities of V_{ni} = 1.0, 10 and 100 m/s, the percentage energy loss W* is 0.818, 1.07 and 1.564 % respectively. It is therefore

concluded that the energy lost in terms of elastic wave propagation during elastic and elasto-plastic impacts can be reasonably ignored.

In order to investigate collisions of elasto-plastic spheres, the new theory has been incorporated into the computer code TRUBAL which uses the Distinct Element Method to numerically simulate experiments. For normal impacts, the computer simulated results match the theoretical predictions of the coefficient of restitution and contact duration very well. For oblique collisions, results have been presented to illustrate the tangential force-displacement relationships and the evolution of contact forces and energy components over the impact duration. The effects of two material properties, interfacial friction and Poisson's ratio, on particle bounce behaviour have been examined for variations of impact conditions (impact angle, impact velocity, initial particle rotation). The results obtained were then compared with experimental measurements and theoretical predictions provided by the impulse equations based on Newton's laws. Good agreement between the computer simulated results and experimental data reported by Maw et al (1976, 1981) was obtained for elastic impacts. Although different material properties were used, the results of elasto-plastic impacts presented in this study show an encouraging agreement with the real experimental results of Brauer (1980).

It has been demonstrated that if contact sliding occurs throughout the impact duration analytical solutions are available to define the complete post-impact conditions. It also has been found that, for any impact angle, an additional initial angular velocity affects the collisional behaviour in a way that corresponds to an equivalent impact angle. If contact sliding does not occur throughout the impact process the particle rebound behaviour is more complex. It has been shown that the parameter $\psi = \lambda\tan\theta/\mu$, suggested by Maw et al (1976, 1981), provides the scaling rule for interparticle friction but not for the elastic properties of the particle/target interface characterised by $\lambda = 2(1-\nu)/(2-\nu)$. It has also been shown how the severity of plastic indentation, defined by the normal coefficient of restitution e_n, affects the rebound behaviour. However, for impact angles which do not

satisfy the criterion of gross sliding, curve fitting techniques have to be used to predict the rebound condition for specified values of ν and e_n, according to the computer simulated data obtained.

9.2 Impact of adhesive spheres

For adhesive elastic spheres, using the JKR theory, a criterion which determines whether the particle bounces or adheres with the target surface has been established. The critical sticking velocity and the normal coefficient of restitution are obtained as

$$V_s = \frac{1.84}{\cos\theta}\left(\frac{\Gamma^5}{\rho_1^3 E^{*2} R^5}\right)^{1/6} \qquad (9.5)$$

$$e_n = \left[1 - \left(\frac{V_s}{V_{ni}}\right)^2\right]^{1/2} \qquad (9.6)$$

where θ is the impact angle. Computer simulation results show a very good agreement with the analytical solution. It has been demonstrated that the critical parameter is the normal component of the impact velocity. The impact velocity which initiates plastic deformation is examined and a criterion governing the onset of plastic yield has been obtained. It has been found that the yield velocity decreases with an increase of surface energy as well as yield stress. Consequently, the yield velocity obtained in this study is less than that in the case of no adhesion estimated by Davies (1949).

For adhesive elasto-plastic spheres a new mathematical model, which is an extension to the JKR model of adhesion, has been developed to deal with the capture and rebound of small particles from surfaces. The normal coefficient of restitution is based on the normal force-displacement relationship during loading and unloading with consideration of the flatting of the contact surfaces due to plastic deformation. The effects of interface energy and yield stress on particle bouncing have been investigated. It has been analytically and numerically demonstrated that, at relatively high impact velocities, the effect of surface

adhesion is not significant and the impact behaviour can therefore be described by the equations without adhesion. Computer simulated impacts of hard spheres of U_3O_8 have been shown to provide sensible results in terms of the effect of velocity on the coefficient of restitution. For soft, micron-sized particles of ammonium fluorescein impacting a silicon target it was found that it was necessary to introduce the concept of a velocity dependent dynamic yield stress in order to obtain computer simulated results which are in agreement with the real experimental data of Wall et al (1989, 1990).

For oblique impact of elastic adhesive spheres, the effects of initial particle rotation, friction and impact velocity on particle bounce were examined. It was found that the surface adhesive peeling process is one of the most influential factors affecting the bounce behaviour and the transition of the peeling failure from unloading to loading leads to a significant change in the magnitude of the bouncing parameters. It has been demonstrated that, using the same normalisation techniques as for non-adhesive particles, scaling rules are available in order to account for the variations in initial particle rotation and friction. However, for the effect of impact velocity, further investigation is needed.

9.3 Fracture / fragmentation of small agglomerates

The process of fragmentation and the resulting size distribution needs to be examined in order to predict the flowability of fractured fragments which may become resuspended in the flow field. Computer simulations of agglomerate-wall collisions have been carried out, in which a randomly generated monodisperse agglomerate and a polydisperse agglomerate both consisting of 50 primary particles were used. Concerning the evolution of the wall force, kinetic energy of the particle system, and the damage ratio during the process of an agglomerate-wall collision the trends observed in this study are in good agreement with previous simulations of 2D and 3D, large and small agglomerates carried out at Aston. The simulated data generally agree with the simple relationship between the damage ratio and the impact velocity reported by Yin (1992), except for very high and low impact velocities. It

has been demonstrated that the polydisperse agglomerate is stronger than the monodisperse one, due to the difference in contact density and structural arrangement between the two assemblies.

It has been shown in this study that agglomerate damage resulting from an oblique impact is determined by the normal velocity component rather than the impact speed. The damage caused by shearing during collision can be reasonably ignored. In order to check the effect of the local structural arrangement close to the impact point, six different wall positions for normal impacts and four directions of the agglomerate impacting to the target surface for oblique collisions were employed. The computer simulated data were found to be consistent irrespective of the impact directions and wall positions. Therefore, it is concluded that, for small agglomerates, the effect of the local structural arrangement on the damage ratio is not significant and the randomly generated agglomerates, in terms of impact damage, can be approximately regarded as isotropic solids.

Defining the size of a fragment by the particle number and then normalising it by the number in the initial agglomerate, it was observed that the grading curve is similar for both assemblies and, for each impact velocity, approximately corresponds to a straight line. The effect of plastic deformation at the contacts on the damage ratio was examined. For small U_3O_8 agglomerates there is no significant difference in the damage ratio between elastic and plastic impacts. By reducing the elastic yield stress, however, it has been shown that the number of contacts broken is significantly reduced because of the additional energy dissipated.

9.4 Limitations and future work

In this study, it is assumed that initial yield condition is only determined by the normal impact indentation. However, as shown by Brauer (1980) (Fig. 4.41), the normal coefficient of restitution remains approximately constant until $\theta = 60^\circ$ and then increases

with an increase of impact angle before unity is approached. This means that the initial yield condition could also depend on the tangential force at the contact. Our simplified theoretical model can not explain this behaviour. In the literature, there seems to be no publications about the effect of tangential force on plastic yield. Possible future investigations of collisions should take into account this effect.

It is also assumed in this study that Mindlin and Deresiewicz's (1953) partial-slip solution is still valid when plastic deformation occurs. After initial yield is exceeded the actual pressure distribution within the contact area is a Hertzian distribution with a cut-off, corresponding to the contact yield stress σ_y. However, a change in normal pressure distribution after plastic yield will undoubtedly lead to a change in the tangential pressure distribution and eventually affect tangential loading, unloading and reloading. Future work should effectively include this effect.

For non-adhesive spheres, when the gross sliding criterion is satisfied, the complete post-impact behaviour is described by the available analytical equations. Further work is required to examine the possibility that analytical solutions can be found for the cases when contact sliding does not occur throughout the whole process of the impact. In the presence of adhesion, in order to provide scaling rules or possible analytical solutions for impact velocity, further investigation is needed, for example, to re-examine the impulse equations by taking into account the effect of surface adhesion.

References

[1] Andrews, J.P. 1930. Theory of collision of spheres of soft metals. Philosophical Magazine, Vol. 9; 593-610.

[2] Andrews, J.P. 1931. A simple approximate theory of the pressure between two bodies in contact. Proceedings of the Physical Society, Vol. 43; 1-17.

[3] Arbiter, N., Harris, C.C. and Stamboltzis, G.A. 1969. Single fracture of brittle spheres. Trans. AIME, Vol. 244; 118-133.

[4] Bitter, J.G.A. 1963. A study of erosion phenomena. Wear, Vol. 6; 5-22.

[5] Borzone, L.A., Klinzing, G.E. and Yang, W.C. 1990. Energy losses and particle-wall interactions on rough surfaces. Powder Technology, Vol. 62; 277-290.

[6] Bowden, F.P. and Tabor, D. 1954. Friction and Lubrication of Solids, Methuen, London.

[7] Brauer, H. 1980. Report on investigations on particle movement in straight horizontal tubes, particle/wall collision and erosion of tubes and tube bends. Journal of Power & Bulk Solids Technology, Vol. 4; 3-12.

[8] Brach, R.M. 1984. Friction restitution and energy loss in planar collisions. Trans. ASME: Journal of Applied Mechanics, Vol. 51; 164-170.

[9] Brach, R.M. 1988. Impact dynamics with applications to solid particle erosion. International Journal of Impact Engineering, Vol. 7, No. 1; 37-53.

[10] Brach, R.M. 1989. Rigid body collisions. Trans. ASME: Journal of Applied Mechanics, Vol. 56; 133-138.

[11] Bradley, R.S. 1932. Cohesion between solid surfaces, and surface energy of solids. Philosophical Magazine, Vol. 13; 853-862.

[12] Brenner, S.S., Wrient, H.A. and Oriani, R.A. 1981. Impact adhesion of iron at elevated temperatures. Wear, Vol. 68; 169-190.

[13] Bulantsev, G.M., Korneer, A.I. and Nikolaev, A.P. 1985. Ricochet upon impact. Mech. Solids, Vol. 20, No. 2; 134-138.

[14] Bush, A.W., Gibson, R.D. and Thomas, T.R. 1975. Wear, Vol. 35; 87-111.

[15] Cheng, W.R., Etsion, I. and Bogy, D.B. 1987. An elastic-plastic model for the contact of rough surfaces. Trans. ASME: Journal of Tribology, Vol. 109; 231-257.

[16] Cundall. P.A. 1971. A computer model for simulating progressive, large scale movements in blocky rock systems. Proceedings of the Symposium International Soc. Rock Mech., Nancy, Article 8.

[17] Cundall, P.A. 1978. BALL – a program to model granular media using the distinct element method. Tech. Note TN-LN-B, Dames and Moor Advanced Technology Group, London.

[18] Cundall, P.A. 1988. Computer simulations of dense sphere assemblies. Micro-mechanics of Granular Materials (Eds. M. Satake and J.T. Jenkins), Elsevier, Amsterdam, pp 113-123.

[19] Cundall, P.A. and Strack, O.D.L. 1979a. A discrete numerical model for granular assemblies. Geotechnique, Vol. 29, No. 1; 47-65.

[20] Cundall, P.A. and Strack, O.D.L. 1979b. A distinct element method as a tool for research in granular media . Part II. Department of Civil and Mining Engineering, University of Minnesota.

[21] Dahneke, B. 1971. The capture of aerosol particles by surfaces. Journal of Colloid and Interface Science, Vol. 37, No. 2; 342-353.

[22] Dahneke, B. 1972. The influence of flattening on the adhesion of particles. Journal of Colloid and Interface Science, Vol. 40, No. 1; 1-13.

[23] Dahneke, B. 1973. Measurements of bouncing of small latex spheres. Journal of Colloid and Interface Science, Vol. 45, No. 3; 584-590.

[24] Dahneke, B. 1974. Further measurements of the bouncing of small latex spheres. Journal of Colloid and Interface Science, Vol. 51, No. 1; 58-65.

[25] Davies, R.M. 1949. The determination of static and dynamic yield stresses using a steel ball. Proceedings of the Royal Society of London A 197; 416-432

[26] de Boer, J.H. 1936. Trans. Faraday Soc., Vol. 32, pp 10.

[27] Deresiewicz, H. 1968. A note on Hertz impact. Acta Mechanica, Vol. 6; 110-112.

[28] Derjaguin, B.V., Muller, V.M. and Toporov, Y.U.P. 1975. Effect of contact deformation on the adhesion of particles. Journal of Colloid and Interface Science, Vol. 53, No. 2; 314-326.

[29] Fichman, M. and Pnueli, D. 1985. Sufficient conditions for small particles to hold together because of adhesion forces. Trans. ASME: Journal of Applied Mechanics , Vol. 52; 105-108.

[30] Follansbee, P.S. and Sinclair, G.B. 1984. Quasi-static normal indentation of an elastic-plastic half-space by a rigid sphere. International Journal of Solids and Structures, Vol. 20; 81-91.

[31] Fuller, K.N.G. and Tabor, D. 1975. The effect of surface roughness on the adhesion of elastic solids. Proceedings of the Royal Society of London A. 345; 327-342.

[32] Goldsmith, W. 1960. Impact, Edward Arnold (Publishers) Ltd.

[33] Graham, G.A.C. 1973. A contribution to Hertz's theory of elastic impact. International Journal of Engineering Science, Vol. 11; 409-313.

[34] Greenwood, J.A. and Tripp, J.H. 1967. The elastic contact of rough surfaces. Trans. ASME: Journal of Applied Mechanics, Vol. 34E; 153-159.

[35] Greenwood, J.A. and Tripp, J.H. 1970-71. The contact of two nominally flat rough surfaces. Proceedings of the Institution of Mechanical Engineers, Vol. 185; 625-633.

[36] Greenwood, J.A. and Williamson, J.B.P. 1966. Contact of nominally flat surfaces. Proceedings of the Royal Society of London A. 295; 300-319.

[37] Hamaker, H.C. 1937. The London-van der Waals attraction between spherical particles. Physica, Vol. 4; 1058-1078.

[38] Hardy, C., Baronet, C.N. and Tordion, G.V. 1971. The elasto-plastic indentation of a half-space by a rigid sphere. International J. for numerical methods in Engineering, Vol. 3; 451-462.

[39] Hisakado, T. 1974. Effects of surface roughness on contact between solid surfaces. Wear, Vol. 28, pp 217-234.

[40] Hunter, S.C. 1957. Energy absorbed by elastic waves during impact. Journal of Mechanics and Physics of Solids, Vol. 5; 162-171.

[41] Hutchings, I.M. 1979. Energy loss in elastic wave propagation during an elastic-plastic impact. J. Phys. D: Appl. Phys., Vol. 12; 1819-1824.

[42] Hutchings, I.M., Winter, R.E. and Field, J.E. 1976. Solid particle erosion of metals: the removal of surface material by spherical projectiles. Proceedings of the Royal Society of London A 348; 379-392.

[43] Hutchings, I.M., Macmillan, N.H. and Rickerby, D.G. 1981. International Journal of Mechanical Science, Vol. 23, pp 639-646.

[44] Johnson, K.L. 1976. Adhesion at the contact of solids. Theoretical and Applied Mechanics (Eds. W.T. Koiter), North-Holland Publishing Company: 133-143.

[45] Johnson, K.L. 1985. Contact Mechanics, Cambridge University Press.

[46] Johnson, K.L. 1986. Private communication.

[47] Johnson, K.L., Kendall, K. and Roberts, A.D. 1971. Surface energy and the contact of elastic solids. Proceedings of the Royal Society of London A 324: 301-313.

[48] Johnson, K.L. and Pollock, H.M. 1993. The role of adhesion in the impact of elastic spheres. Submitted to Journal of Adhesion Science and Technology.

[49] Kafui, D. and Thornton, C. 1993. Computer simulated impact of agglomerate. Powders & Grains 93, the Proceedings of the 2nd International Conference on Micromechanics of Granular Media, A.A. Balkema, pp 401-406.

[50] Kafui, D. and Thornton, C. 1994. Agglomerate fracture/fragmentation. Proceedings of the 1st International Particle Technology Forum, Denver, USA.

[51] Keller, J.B. 1986. Impact with friction. Trans. ASME: Journal of Applied Mechanics, Vol. 53; 1-4.

[52] Lian, G. 1994. Computer simulation of moist agglomerate collision. PhD Thesis. The University of Aston in Birmingham.

[53] Lifshitz, J.M. and Kolsky, H. 1964. Some experiments on anelastic rebound. Journal of Mechanics and Physics of Solids, Vol. 12; 35-43.

[54] Lo, C.C. 1969. Elastic contact of rough cylinders. International Journal of Mechanical Science, Vol. 11: 105-115.

[55] Longuet-Higgins, M.S. 1957. The statistical properties of an isotropic random surface. Phil. Trans. Roy. Soc. A 249; 321-387.

[56] Malvern, L.E. 1951. The propagation of longitudinal waves of plastic deformation in a bar of material exhibiting a strain-rate effect. Trans. ASME: J. Appl. Mech., Vol. 18; 203-208.

[57] Maw, N., Baeber, J.R. and Fawcett, J.N. 1976. The oblique impact of elastic spheres. Wear, Vol. 38, No. 1; 639-646.

[58] Maw, N., Barber, J.R. and Fawcett, J.N. 1981. The role of tangential compliance in oblique impact. Trans. ASME: Journal of Lubrication Technology , Vol. 103; 74-80.

[59] McEwen, E. 1949. Stresses in elastic cylinders in contact along a generatrix. Philosophical Magazine, Vol. 40; 454.

[60] Mikic, B.B. 1974. Thermal contact conductance: theoretical considerations. International Journal of Heat Mass Transfer, Vol. 17; 205-214.

[61] Miller, G.F. and Pursey, H. 1954. The field and radiation impedance of mechanical radiators on the free surface of a semi-infinite isotropic solid. Proceedings of the Royal Society of London A. 223; 521-541.

[62] Miller, G.F. and Pursey, H. 1955. On the partition of energy between elastic waves in a semi-infinite solid. Proceedings of the Royal Society of London A. 224; 55-69.

[63] Mindlin, R.D. 1949. Compliance of elastic bodies in contact. Trans. ASME: Journal of Applied Mechanics , Vol. 16; 259-269.

[64] Mindlin, R.D. and Deresiewicz, H. 1953. Elastic spheres in contact under varying oblique forces. Trans. ASME: Journal of Applied Mechanics , Vol. 20; 327-344.

[65] Nayak, P.R. 1971. Random process model of rough surfaces. Trans. ASME: Journal of Lubrication Technology , Vol. 93F; 398-407.

[66] Ning, Z. and Thornton, C. 1993. Elastic-plastic impact of small particles with a surface. Powders & Grains 93, the Proceedings of the 2nd International Conference on Micromechanics of Granular Media, A.A. Balkema, pp 33-38.

[67] Onions, R.A. and Archard, J.F. 1973. The contact of surfaces having a random structure. J. Phys. D: Appl. Phys., Vol. 6; 289-304.

[68] Payne, J.F.B. and Butterworth, B. 1986 CEGB Report, TPRD/B/0828/R86.

[69] Raman, C.V. 1920. On some applications of Hertz's theory of impact. Physical Review, Vol. 15; 277.

[70] Randall, C.W. 1989. The application of contact mechanics to the numerical simulation of particulate material. PhD Thesis, The University of Aston in Birmingham..

[71] Reed, J. 1985a. Energy losses due to elastic wave propagation during an elastic impact. J. Phys. D: Appl. Phys., Vol. 18; 2329-2337.

[72] Reed, J. 1985b. The impact-adhesion behaviour of U_3O_8 particles striking steel surfaces. CEGB Report No. TPRD/B/0724/N85 (Unr).

[73] Reed, J. 1987. Impact adhesion of particles. Tribology in Particulate Technology (Eds. B.J. Brisco and M.J. Adams), Adam Hilger, Bristol and Philadelphia, pp 123-134.

[74] Rickerby, D.G. and Macmillan, N.H. 1980. On the oblique impact of a rigid sphere against a rigid-plastic solid. International Journal of Mechanical Science, Vol. 22; 491-494.

[75] Rogers, L.N. and Reed, J. 1984. The adhesion of particles undergoing an elastic-plastic impact with a surface. J. Phys. D: Appl. Phys., Vol. 17;677-689.

[76] Savkoor, A.R. and Briggs, G.A.D. 1977. The effect of tangential force on the contact of elastic solids in adhesion. Proceedings of the Royal Society of London A 359; 103-114.

[77] Sears, J.E. 1908. On the longitudinal impact of metal rods with rounded ends. Proceedings of the Camb. Phil. Soc., Vol. 14; 257.

[78] Smith, J.O. and Liu, G.K. 1953. Stresses due to tangential and normal loads on an elastic solid. Trans. ASME: Journal of Applied Mechanics, Vol. 21; 371-378.

[79] Sondergaad, R., Cheney, K. and Brennen, C.E. 1990. Measurements of solid spheres bouncing off flat plates. Trans. ASME: Journal of Applied Mechanics, Vol. 57; 694-699.

[80] Stronge, W.J. 1990. Rigid body collisions with friction. Proceedings of the Royal Society of London A. 431; 169-181.

[81] Stronge, W.J. 1991. Unravelling paradoxical theories for rigid body collisions. Trans. ASME: Journal of Applied Mechanics, Vol. 58; 1049-165.

[82] Stronge, W.J. 1992. Energy dissipated in planar collisions. Trans. ASME: Journal of Applied Mechanics, Vol. 59; 681-682.

[83] Stronge, W.J. 1994a. Planar impact of rough compliant bodies. International Journal of Impact Engineering, Vol. 15; 435-450.

[84] Stronge, W.J. 1994b. Coupling of friction and internal dissipation in planar collision of compliant bodies. Proceedings of the 2nd International Symposium on Contact Mechanics, September 19-23, Carry-Le-Rouet, France.

[85] Sundararajan, G. and Shewmon, P.G. 1987. The oblique impact of a hard ball against ductile, semi-infinite target materials - experiment and analysis. International Journal of Impact Engineering, Vol. 6; 3-22.

[86] Tabor, D. 1951. The Hardness of Metals. Oxford University Press.

[87] Tabor, D. 1977. Surface forces and surface interactions. Journal of Colloid and Interface Science, Vol. 40, No. 1; 1-13.

[88] Thomas, T.R. 1982. Rough Surfaces, Longman.

[89] Thornton, C. 1990. Normal indentation of adhesive particles. Departmental Working Report, Department of Civil Engineering, The University of Aston in Birmingham.

[90] Thornton, C. 1991. Interparticle sliding in the presence of adhesion. J. Phys. D: Appl. Phys., Vol. 24; 1942-1946.

[91] Thornton, C. 1994. Coefficient of restitution of the particle upon normal impacts. Departmental Working Report, Department of Civil Engineering, The University of Aston in Birmingham.

[92] Thornton, C. and Kafui, D. 1992. Computer simulated agglomerate fracture / fragmentation. Proceedings of the Symposium Attrition and Wear in Powder Technology, Utrecht, the Netherlands, pp 19-28.

[93] Thornton, C. and Ning, Z. 1994. Oblique impact of elasto-plastic sphere. Proceedings of the 1st International Particle Technology Forum, Denver, USA.

[94] Thornton, C. and Randall, C.W. 1988. Applications of theoretical contact mechanics to solid particle system simulation. Micromechanics of Granular Materials, (eds. M. Satake and J.T. Jenkins) Elsevier, Amsterdam, pp 133-142.

[95] Thornton, C. and Yin, K.K. 1991. Impact of elastic spheres with and without adhesion. Powder Technology, Vol. 65; 153-166.

[96] Tiliett, J.P.A. 1954. A study of the impact on spheres of plates. Proceedings of the Phys. Sco. B 67; 677-688.

[97] Tsai, Y.M. 1968. A note on the surface waves produced by Hertzian impact. Journal of Mechanics and Physics of Solids, Vol. 16; 133-136.

[98] Wall, S., John, W. and Georen, S.L. 1989. Application of impact adhesion theory to particle kinetic energy loss measurements. Particles on Surfaces (Eds. K.L. Mittal). Plenum Publishing Corporation; 19-34.

[99] Wall, S., John, W. and Georen, S.L. 1990. Measurements of kinetic energy loss for particles impacting surfaces. Aerosol Science and Technology, Vol. 12; 926-946.

[100] Wempener, G. and Hwang, C.M. 1984. A simple model of elastic-plastic plates. International Journal of Solids Structures, Vol. 20; 77-80.

[101] Whitehouse, D.J. and Archard, J.F. 1970. The properties of random surfaces of significance in their contact. Proceedings of the Royal Society of London A. 316; 97-121.

[102] Yin, K.K. 1992. Numerical modelling of agglomerate degradation. PhD Thesis, The University of Aston in Birmingham.

[103] Zener, C. 1941. The intrinsic inelasticity of large plates. Physical Review, Vol. 59; 669-673.

Appendix A Energy dissipation in elastic waves during an elasto-plastic impact

The problem of the response of an isotropic elastic semi-infinite medium to time dependent surface forces was initially considered by Lamb (1904) and then by Miller & Pursey (1954, 1956). Based on the results given by Miller & Pursey (1954) for the normal displacement of the free surface of a semi-infinite body Hunter (1957) analysed the energy dissipated in terms of elastic wave propagation under a uniform periodic surface pressure acting over a circular area. The Hertzian theory of impact was then used to predict the fraction of initial kinetic energy loss during a purely elastic impact. The force-time relationship during plastic impact was proposed by Hutchings (1979) and a calculation of the fraction of initial kinetic energy loss was also reported. By using the previous interaction laws for elastic-plastic impact the force-time relationship during elastic-plastic loading and elastic recovery was analysed.

According to Hunter (1957) the total energy loss in elastic wave motion under transient force of f(t) is given by

$$W = \frac{8\beta(1 + \nu_2)}{\rho_2 C_0^3} \left(\frac{1 - \nu_2^2}{1 - 2\nu_2} \right)^{1/2} \int_0^{\infty} \omega | f(\varpi) |^2 \, d\varpi \qquad (A1)$$

where β is the imaginary of

$$\int_0^{\infty} [(\xi (\xi^{1/2} - 1) / F_0(\xi)] d\xi$$

where

$$F(\xi) = (2\xi^2 - \gamma^2)^2 - 4\xi^2 [(\xi^2 - 1) (\xi^2 - \gamma^2)]^{1/2}$$

$$\gamma = [\, 2(1 - \nu_2) / (1 - 2\nu_2) \,]^{1/2}$$

where ρ_2 and ν_2 are the density and the Poisson's ratio of the semi-infinite body; $f(\varpi)$ is the Fourier component of the time dependent force f(t). For $\nu_2 = 1/4$, the value of β given by Hunter (1957) is 0.537 and for $\nu_2 = 1/3$, $\beta = 0.415$. Based on Hunter's estimation we have $\beta = 0.488$ for $\nu_2 = 0.3$.

From Saint-Venant's principle the elastic strain field in regions remote from the area of contact will not be dependent on whether the local deformation around the indenter is elastic or plastic, but only on the magnitude and the pulse shape of the contact force. We therefore can still use (A1) for the present case of elastic-plastic impact. We may also find in 3.5 that the contact force in both cases of elastic and plastic deformation has the same pulse form of $f(t) = P^* \sin \varpi t$ with variations of the maximum force P^* and the response frequency ϖ.

If the transient contact force has the following pulse shape

$$f(t) = \begin{cases} P^* \cos \varpi_0 t & |t| \le \pi / 2\varpi_0 \\ 0 & |t| \ge \pi / 2\varpi_0 \end{cases} \qquad (A2)$$

where

$$f(\varpi) = \frac{1}{2\pi} \int_{-\infty}^{\infty} f(t) e^{-i\varpi t} dt = \frac{P^*}{2\pi} \int_{-\pi/2\varpi_0}^{\pi/2\varpi_0} \cos \varpi_0 t \, e^{-i\varpi t} dt$$

$$= \frac{P^* \varpi_0 \cos (\varpi\pi / 2\varpi_0)}{\pi (\varpi_0^2 - \varpi^2)} \qquad (A3)$$

and (A1) becomes

$$W = \frac{8\beta(1 + \nu_2)}{\rho_2 C_0^3} \left(\frac{1 - \nu_2^2}{1 - 2\nu_2} \right)^{1/2} \frac{P^{*2} \varpi_0^2}{\pi^2} \int_0^{\infty} \frac{\varpi^2 \cos^2 (\varpi\pi / 2\varpi_0)}{(\varpi_0^2 - \varpi^2)^2} d\varpi \qquad (A4)$$

Let $\varpi / \varpi_0 = z$ and

$$W = \frac{8\beta(1+\nu_2)}{\rho_2 C_0^3}\left(\frac{1-\nu_2^2}{1-2\nu_2}\right)^{1/2}\frac{P^{*2}\varpi_0^2}{\pi^2}\int_0^{\infty}\frac{z^2\cos^2(z\pi/2)}{(z^2-1)^2}dz \qquad (A5)$$

Because of

$$\int_0^{\infty}\frac{z^2\cos^2(z\pi/2)}{(z^2-1)^2}dz = \frac{\pi^2}{8} \qquad (A6)$$

there results

$$W = \frac{\beta(1+\nu_2)}{\rho_2 C_0^3}\left(\frac{1-\nu_2^2}{1-2\nu_2}\right)^{1/2}P^{*2}\varpi_0 = \frac{\zeta(\nu_2)}{\rho_2 C_0^3}P^{*2}\varpi_0 \qquad (A7)$$

where

$$\zeta(\nu_2) = \beta(1+\nu_2)\left(\frac{1-\nu_2^2}{1-2\nu_2}\right)^{1/2} \qquad (A8)$$

which is only related to the density of the substrate.

Referring to Fig. A1 the total energy loss can be subdivided into two parts: the energy loss in the plastic loading process W_p and the energy loss during elastic recovery W_e. The time dependent contact force during plastic loading is

$$f(t) = \begin{cases} P^*\sin\varpi_p t & 0 < t < \pi/2\varpi_p \\ 0 & t < 0 \text{ and } t > \pi/2\varpi_p \end{cases} \qquad (A9)$$

where the maximum force P^* and the respond frequency ϖ_p are

$$P^* = \pi R^2\left(\frac{4\rho_1\sigma_y}{3}\right)^{1/2}V_{ni} \qquad (A10)$$

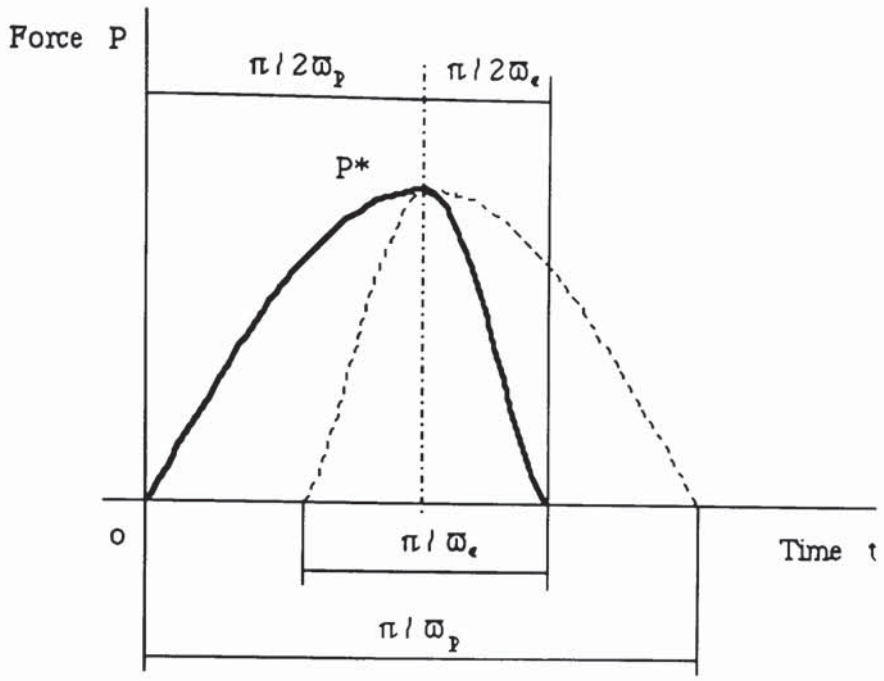

Fig. A1 The force-time relationship for an elastic-plastic impact.

$$\varpi_p = \left(\frac{3\sigma_y}{4\rho_1 R^2} \right)^{1/2} \qquad (A11)$$

where ρ_1 is the density of the particle and V_{ni} is the normal approach velocity. By extending the right time limit from $\pi/2\varpi_p$ to π/ϖ_p and moving the origin of time forward through $\pi/2\varpi_p$, (A9) may be rewritten

$$f(t) = \begin{cases} P^* \cos \varpi_p t & |t| \le \pi / 2\varpi_p \\ 0 & |t| \ge \pi / 2\varpi_p \end{cases} \qquad (A12)$$

which has the same form of (A2). The energy dissipated in elastic waves under surface force of (A12) should be twice the energy actually lost during plastic loading. Substituting (A10) and (A11) into (A7) we may have

$$W_p = \frac{W}{2} = \frac{\zeta(\nu_2)}{2\rho_2 C_0^3} \pi^2 R^4 \frac{4\rho_1 \sigma_y}{3} V_{ni}^2 \left(\frac{3\sigma_y}{4\rho_1 R^2} \right)^{1/2}$$

$$= \frac{\zeta(\nu_2)}{\rho_2 C_0^3} \pi^2 R^3 \left(\frac{\rho_1 \sigma_y}{3} \right)^{3/2} V_{ni}^2 \qquad (A13)$$

The contact force during elastic recovery is

$$f(t) = \begin{cases} P^* \cos \varpi_e (t - 2\varpi_p) & \pi / 2\varpi_p \le t \le \pi (1/2\varpi_p + 1/2\varpi_e) \\ 0 & \text{for other values of t} \end{cases} \qquad (A14)$$

By extending the left time limit from $\pi/2\varpi_p$ to $\pi/2\varpi_p - \pi/2\varpi_e$ and then moving the origin of the time forward through $\pi/2\varpi_p$, (A14) becomes

$$f(t) = \begin{cases} P^* \cos \varpi_e t & |t| \le \pi / 2\varpi_e \\ 0 & |t| \ge \pi / 2\varpi_e \end{cases} \qquad (A15)$$

where the maximum contact force is given by (A10) due to the physical argument in which the transition from loading to unloading should be continuous. Hunter (1957) also worked out that for a purely elastic impact the displacement-time relationship can be approximately expressed as

$$\alpha = \alpha^*_e \sin \varpi_e t = \alpha^*_e \sin \left(\frac{\pi}{2.94} \frac{V_{ie}}{\alpha^*_e} t \right) \qquad 0 \le t \le \pi / \varpi_e \qquad (A16)$$

where V_{ie} is the impact velocity which is less than the yield velocity and α^*_e is the maximum displacement during elastic impact, and

$$\alpha^*_e = \left(\frac{15m}{16E^*} \right)^{2/5} R^{-1/5} V_{ie}^{4/5} \qquad (A17)$$

From (A16) the elastic response frequency is

$$\varpi_e = \frac{\pi}{2.94} \frac{V_{ie}}{\alpha^*_e} = \frac{\pi}{2.94} \left(\frac{16E^*}{15m} \right)^{2/5} R^{1/5} V_{ie}^{1/5} \qquad (A18)$$

where R is the radius of contact curvature.

As demonstrated by Hunter (1957) and Reed (1985) the initial kinetic energy loss in elastic wave propagation during pure elastic impacts is not significant and we are justified to assume that the velocity V_{ie} for calculating the response frequency during elastic recovery is

approximately equal to the rebound velocity for an elastic-plastic impact. Based on this assumption we have

$$V_{ie} = V_{nr} = e_n V_{ni} \qquad (A19)$$

where e_n is the normal coefficient of restitution and

$$e_n = \sqrt{\frac{6a_y}{5E^*a^*}} = \sqrt{\frac{3\pi\sigma_y R}{5E^*a^*}} \qquad (A20)$$

Due to the flattening of the contact surfaces under plastic deformation the radius of contact curvature at the transition point from plastic loading to elastic recovery is given by (3.27). By ignoring the initial elastic loading before yield we may rewrite (3.27) as

$$R_p = \frac{4E^*a^{*3}}{3P^*} = \frac{4E^*a^*}{3\pi\sigma_y} \qquad (A21)$$

where the relationship between the maximum contact radius and the impact velocity is

$$V_{ni} = \sqrt{\frac{\pi\sigma_y}{Rm}}\, a^{*2} \qquad (A22)$$

Substituting (A19) and (A21) into (A18) we obtain

$$\begin{aligned}\varpi_e e_n &= \frac{\pi}{2.94}\left(\frac{16E^*}{15m}\right)^{2/5}\left(R_p V_{ni} e_n^6\right)^{1/5} \\ &= \frac{\pi}{2.94}\left(\frac{16E^*}{15m}\right)^{2/5}\left[\frac{36}{125}\left(\pi\sigma_y R\right)^{5/2} E^{*-2} m^{-1/2}\right]^{1/5} \\ &= \frac{4}{5}\frac{\pi}{2.94}\left(\frac{\pi\sigma_y R}{m}\right)^{1/2} \qquad (A23)\end{aligned}$$

Since

$$\varpi_p = \left(\frac{\pi\sigma_y R}{m}\right)^{1/2} \qquad (A24)$$

we have

$$\varpi_e = \frac{4}{5}\frac{\pi}{2.94}\frac{\varpi_p}{e_n} = 0.956\sqrt{\frac{4}{5}}\frac{\varpi_p}{e_n} \qquad (A25)$$

Adopting the same method as for obtaining (3.59), we have the first part of (3.68). From (3.67) we have

$$\varpi_e = \sqrt{\frac{4E^*a^*}{3m}} = \sqrt{\frac{4}{5}}\frac{\varpi_p}{e_n} \qquad (A26)$$

which is very close to (A25) when plastic deformation dominates the loading process. If the impact velocity is below the yield velocity the maximum contact radius produced during impact is given by

$$a^* = \left(\frac{15R^2mV_{ni}^2}{16E^*}\right)^{1/5} \qquad (A27)$$

Therefore the elastic response frequency is

$$\varpi_e = \sqrt{\frac{4E^*a^*}{3m}} = \sqrt{\frac{5}{4}}\left(\frac{16E^*}{15m}\right)^{2/5} R^{1/5} V_{ie}^{1/5} \qquad (A28)$$

which is very close to that given in (A18). Since Hunter's equation of (A18) is an approximation for the analytical solution which governs the elastic impact process we are justified to use

$$\varpi_e = \sqrt{\frac{4E^*a^*}{3m}} \qquad (A29)$$

for the elastic response frequency irrespective of elastic impact or elastic recovery during an elastic-plastic impact.

It is worth noting that the relationship between the elastic frequency and plastic frequency has also been investigated by Hutchings (1979), who simply assumed

$$\varpi_e = \varpi_p / e_n \qquad (A30)$$

which qualitatively agrees well with (A26). It is clear from both Huchings' assumption and (A26) that the elastic frequency is dependent on the severity of plastic indentation and the power law relationship has an exponent of 1/4 because ϖ_p is a constant. Having the equations for plastic and elastic frequencies in the loading and unloading processes respectively, it is now possible to estimate the total energy loss in terms of elastic wave motion and the fraction of initial kinetic energy loss during the impact process. With respect to (A7) the energy loss in the unloading process is

$$W_e = \frac{W}{2} = \frac{\zeta(\nu_2)}{2\rho_2 C_0^3} P^{*2} \varpi_e = \frac{\zeta(\nu_2)}{2\rho_2 C_0^3} P^{*2} \varpi_p \sqrt{\frac{4}{5}} \frac{1}{e_n} \qquad (A31)$$

and the total energy loss is obtained

$$W = W_p + W_e = W_p \left(1 + \sqrt{\frac{4}{5}} \frac{1}{e_n}\right) = \frac{\zeta(\nu_2)}{2\rho_2 C_0^3} P^{*2} \varpi_p \left(1 + \sqrt{\frac{4}{5}} \frac{1}{e_n}\right)$$

$$= \frac{\zeta(\nu_2)}{\rho_2 C_0^3} \pi^2 R^3 \left(\frac{\rho_1 \sigma_y}{3}\right)^3 {}^{1/2} V_{ni}^2 \left(1 + \sqrt{\frac{4}{5}} \frac{1}{e_n}\right) \qquad (A32)$$

Finally the fraction of initial kinetic energy loss is given by

$$W^* = \frac{W}{\frac{1}{2} m V_{ni}^2} = \frac{\zeta(\nu_2)}{\frac{2}{3}\pi\rho_1 R^3 \rho_2 C_0^3} \pi^2 R^3 \left(\frac{\rho_1 \sigma_y}{3}\right)^3 {}^{1/2} \left(1 + \sqrt{\frac{4}{5}} \frac{1}{e_n}\right)$$

$$= \frac{\zeta(\nu_2)}{\rho_2 C_0^3} \pi \left(\frac{3\sigma_y}{4\rho_1}\right)^3 {}^{1/2} \left(1 + \sqrt{\frac{4}{5}} \frac{1}{e_n}\right) \qquad (A33)$$

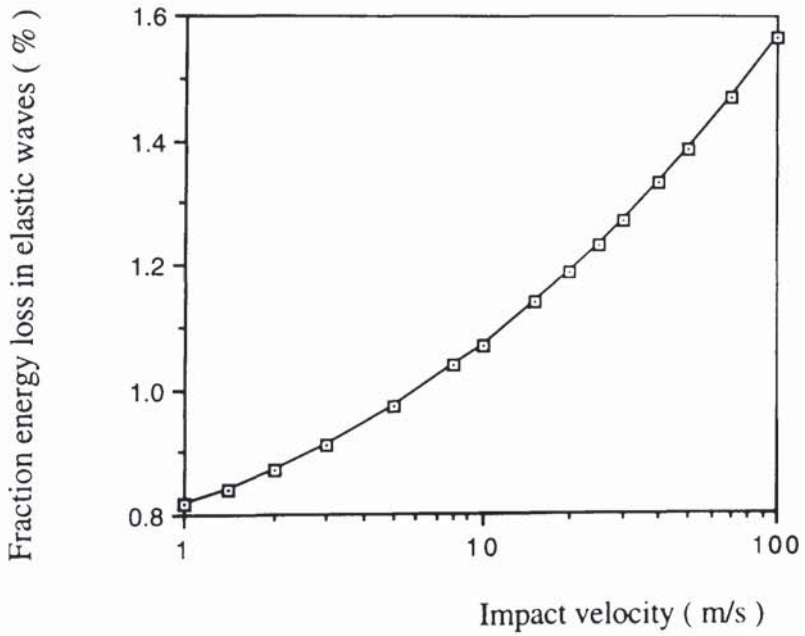

Fig. A2 Variations of the fraction of initial kinetic energy loss through elastic waves with impact velocities when an U_3O_8 particle strikes a steel target surface.

For U_3O_8 particles striking a steel plate, Figure A2 shows the variations of the fraction energy loss in elastic wave propagation with the impact velocity. When V_{ni} = 1.0 m/s, which is slightly above the yield velocity, the percentage energy loss W* is 0.818%; when V_{ni} = 10 m/s equation (A33) predicts that W* = 1.07%; and at V_{ni} = 100 m/s we have W* = 1.564%. In the previous analysis we assume that there is no effects of dynamic yield stress during impact. If this factor is going to be included the situation would be much more complicated. As the fraction of energy loss is very low we are justified to ignore the energy loss in terms of elastic wave propagation during elastic and elastic-plastic impacts irrespective of whether or not we take into account the effects of a dynamic yield strength.

Appendix B Input sample files of commands

Operative commands are used in TRUBAL, performing various functions such as file handling, program execution and control, defining material properties and constants, etc. The format of all input commands is a word followed, in most cases, by a number of parameters, some of which may be words themselves. In computer simulated tests, the input file which contains a series of operative commands is normally used. Only a few commands are introduced in this Appendix and the whole command list is provided by Lian et al (1993). The first command on entering TRUBAL must be either

STArt l_x l_y l_z M_{box} M_{ball} M_{wall} [log]

or **REStart**

where l_x, l_y, l_z, are the components of the three dimensional workspace; M_{box} is the number of the boxes that the workspace can be sub-divided into; M_{ball} and M_{wall} are the maximum number of balls and walls that may be required to be generated. The workspace is divided in TRUBAL into small boxes in a way that the size of a box in each axial direction is the same and normally we have $l_x = l_y = l_z$. The optional keyword **log** allows output information to be written in the output file TRUBAL.OUT. The **REStart** command is used when it is desired to continue a run from the point at which a **SAVe** command was given. It means that **REStart** causes a previously-saved problem to be fetched from a restart file.

The next input command line can consist of any message. For the simulated impact of particles with a wall only one single particle needs to be created. The command to create a particle in a given position is

CREate x y z v_x v_y v_z ω_x ω_y ω_z isize mtyp

where x, y, z are the coordinates of the particle centre; v_x, v_y, v_z, ω_x, ω_y, ω_z are the linear and angular velocity components; **isize** and **mtyp** indicate the particle size type and material type respectively. For an assembly of granular spheres currently TRUBAL allows 5 size-type and 5 material-type particles to be generated.

The simulated assembly can either consist of randomly generated particles or have a regular shape by placing particles together based on a certain rule. In Cundall's 1988 version of TRUBAL particles are generated in such a way that three random numbers are selected from the closed intervals of [0, l_x], [0, l_y], [0, l_z] and are assigned as the coordinates of the centre of the particle. The periodic cell is within the defined workspace. After each new particle is generated there is check in the program to make sure that the newly generated particle will not overlap with previously existing particles or otherwise it is deleted. The process of generation continues until the expected number of particles are generated.

In the present version of TRUBAL particles can be randomly generated either in a specified spherical region or in a limited periodic cell within the workspace. Up to two assemblies can be generated in the workspace in order to perform simulated collisions between agglomerates. The commands for random assembly generation is

DFV styp nagg x_c y_c z_c r_a

GENerate nball isize nagg ntry

where **styp** indicates the sample type, agglomerate or periodic cell (**agm** or **per**); nagg is the number of agglomerates; x_c, y_c, z_c are the coordinates of the agglomerate centre; r_a is the radius of the spherical region; **nball** is the particle number to be generated; **isize** indicates the particle size type and **ntry** is the number of trying to allocate a particle in a random position. During particle generation both location check and overlap check are carried out to make sure that all the particles are generated in the defined region and there is no overlap between the generated particles.

Smooth planar walls are introduced in the current version of TRUBAL. The command for defining planar walls in a 3-D space is

DWAll [P d a b c] [V v_x v_y v_z] [M mtyp]

[FP d a b c x_1 x_2 y_1 y_2 z_1 z_2] [V v_x v_y v_z] [M mtyp]

where P defines the position of the wall with the equation ax + by + cz = d; V gives the translational velocities of the wall (v_x, v_y, v_z) and M indicates the wall material type mtyp. At the moment the program can only handle the walls parallel to one of the three planes x-y, y-x, and x-z. This means that only one of the parameters a, b, c is non-zero for any wall. The " finite wall " option FP defines a plane wall with the same equation but limited to the region defined by the limits (x_1, x_2), (y_1, y_2), (z_1, z_2), with the first value in each pair being the low limit.

The wall generated previously can be moved to another position or given new parameters such as velocity and material type. The command for wall alteration is

AWAll n [P d a b c] [V v_x v_y v_z] [M mtyp]

[FP d a b c x_1 x_2 y_1 y_2 z_1 z_2] [V v_x v_y v_z] [M mtyp]

where n is the number of the wall which has the new position (P/FP), velocity (V) and material type (M).

One sample file used for single particle impact and two files for agglomerate collision are shown below. Sample file 1 provides the information for a single particle impact in which the particle with initial angular velocity of 40000 rad/s will move towards to the target wall at an impact speed of 0.7071 m/s and an impact angle of 45°. The target and particle properties are also defined in the sample file. The commands for the polydisperse agglomerate collision are presented in Sample files 2 and 3. For a start run, the particle sizes and distribution are defined and a centripetal gravity filed is created to bring the particles together. After the contact number reaches a constant value, the target wall is introduced in the restart run and a

velocity is given to the agglomerate. Finally, all the information of agglomerate fragmentation after collision is plotted out.

Sample file 1: Command file for single particle impact

```
START 0.001 0.001 0.001 64 540 4 LOG
Trial single particle impact
* 3-D
FRAC 0.01
YMD 2.15E11 1
YMD 2.15E11 2
YIE 3.04E9 1
YIE 3.04E9 2
PRAT 0.3 1
PRAT 0.3 2
DENS 8.3E3 1
DENS 7.8E3 2
GRAV 0.0 -9.81 0.0
coh 0.1 1
coh 0.1 2
fric 0.35 1
fric 0.35 2
rad 1.0e-5 1
creat 0.0005 0.00051000001 0.0005 0.5 -0.5 0.0 0.0 0.0 40000.0 1 1
dwall pos 0.0005 0.0 1.0 0.0 vel 0.0 0.0 0.0 mat 2
sgm on 100 sim, info, ene
cyc 1800
print info
print ball
plot wall ball
sgm off
stop
```

Sample file 2: Command file for agglomerate collision (start run)

```
START .0001 0.0001 0.0001 64 540 4 log
Trial Agglomerate impact
* 3-D
FRAC 0.05
YMD 2.15E11 1
YMD 2.15E11 2
YIE 1.9E999 1
YIE 1.9E999 2
PRAT 0.3 1
PRAT 0.3 2
```

```
DENS 8.3E10 1
DENS 7.8E10 2
GRAV 9.81 9.81 9.81
*coh 0.1 1
*coh 0.1 2
*fric 0.35 1
*fric 0.35 2
damp 0.1 0.15 0 0 1
rad 1.e-5 1
rad 8.e-6 2
rad 7.e-6 3
rad 6.e-6 4
rad 4.e-6 5
dfv agm 1 0.00005 0.00005 0.00005 0.000032
gen 7 1 1 10000
dfv agm 1 0.00005 0.00005 0.00005 0.000032
gen 11 2 1 10000
dfv agm 1 0.00005 0.00005 0.00005 0.000032
gen 14 3 1 10000
dfv agm 1 0.00005 0.00005 0.00005 0.000032
gen 11 4 1 10000
dfv agm 1 0.00005 0.00005 0.00005 0.000032
gen 7 5 1 10000
sgm on 100 info, ene, str
cyc 100000
print info
cyc 100000
zero
print info
cyc 500
zero
print info
cyc 500
zero
print info
cyc 500
zero
print info
save
plot circ vel
sgm off
stop
```

Sample file 3: Command file for agglomerate collision (restart run)

```
RESTART
* 3-D
FRAC 0.1
YMD 2.15E11 1
YMD 2.15E11 2
YIE 3.04E999 1
```

YIE 3.04E999 2
PRAT 0.30 1
PRAT 0.30 2
DENS 8.3E3 1
DENS 7.8E3 2
GRAV 0.0 -9.8 0.0
coh 0.1 1
coh 0.1 2
fric 0.35 1
fric 0.35 2
damp 0.1 0.15 0 0 1
dwall pos 0.0000226 0.0 1.0 0.0 vel 0.0 0.0 0.0 mat 2
vel 0.0 -0.5 0.0 1
sgm on 50 aim, info, ene, str
cyc 1000
print ball
print cluster
print info
plot cluster 0 0
plot cluster 1 1
plot cluster 2 5
plot cluster 6 9
plot cluster 10 40
plot cluster 41 50
plot cnd
plot wall circ vel
sgm off
save
stop